

# Spectrometer Straw Tracker design studies for the SHiP experiment

## Dissertation

zur Erlangung des Doktorgrades

an der Fakultät für Mathematik, Informatik und Naturwissenschaften

Fachbereich Physik

der Universität Hamburg

vorgelegt von

**Daniil Sukhonos**

Hamburg

2020







## **Eidesstattliche Versicherung / Declaration on oath**

Hiermit versichere ich an Eides statt, die vorliegende Dissertationsschrift selbst verfasst und keine anderen als die angegebenen Hilfsmittel und Quellen benutzt zu haben. Die eingereichte schriftliche Fassung entspricht der auf dem elektronischen Speichermedium. Die Dissertation wurde in der vorgelegten oder einer ähnlichen Form nicht schon einmal in einem früheren Promotionsverfahren angenommen oder als ungenügend beurteilt.

Hamburg, den 22. Oktober 2020

Daniil Sukhonos

Gutachter der Dissertation:

Prof. Dr. Caren Hagner  
Dr. Massimiliano Ferro-Luzzi

Zusammensetzung der Prüfungskommission:

Prof. Dr. Caren Hagner  
Dr. Massimiliano Ferro-Luzzi  
Prof. Dr. Daniela Pfannkuche  
Prof. Dr. Johannes Haller  
Prof. Dr. Peter Schleper

Vorsitzender der Prüfungskommission:

Prof. Dr. Daniela Pfannkuche

Datum der Disputation:

23/11/2020

Vorsitzender Fach-Promotionsausschusses  
PHYSIK:

Prof. Dr. Günter Hans Walter Sigl

Leiter des Fachbereichs PHYSIK:

Prof. Dr. Wolfgang Hansen

Dekan der Fakultät MIN:

Prof. Dr. Heinrich Graener



## Abstract

The SHiP experiment has been proposed in conjunction with a new high-intensity Beam Dump Facility (BDF) at the CERN SPS complex in order to search for neutral “hidden” particles with masses up to a few GeV and feebly interacting with Standard Model particles. Unprecedented sensitivities are expected due to the high intensity of the 400 GeV SPS proton beam ( $4 \cdot 10^{19}$  protons on target per year), a large acceptance detector and careful suppression of background, in particular by using a magnetic Muon Shield behind the production target. A crucial role in the reconstruction of the decays of the signal candidates is played by the Hidden Sector (HS) decay spectrometer of SHiP.

The main subsystem of the HS decay spectrometer is the spectrometer straw tracker (SST) consisting of four tracking stations and a dipole magnet. The SST is a tracking detector conceived to reject background and detect signal events by measuring precisely charged particle momenta, reconstruct decay vertices and the impact parameters to the point of production of hidden particle candidates. The SST needs to cover a large acceptance of  $5 \text{ m} \times 10 \text{ m}$  providing at least  $120 \mu\text{m}$  spatial resolution of track hits and must be made with a minimum amount of material in the acceptance. To satisfy these requirements, an in-vacuum drift detector based on ultralight  $5 \text{ m}$  long and  $2 \text{ cm}$  diameter straw tubes was proposed.

Building on a technology developed by the NA62 collaboration, the cathode straw tubes are made of  $36 \mu\text{m}$  thick biaxially-oriented PET coated with copper and gold on the inner surface of the tube. The anode is a  $30 \mu\text{m}$  diameter wire made of gold-plated tungsten-rhenium alloy. The tube is filled with Ar/CO<sub>2</sub> 70%/30% gas mixture at 1 bar absolute pressure. An applied high voltage of 2.2 kV provides a gas gain between  $10^4$  and  $10^5$ . This design allows to achieve 0.5% of a radiation length per tracking station. However, it brings important challenges in terms of mechanical rigidity and stability of the tubes. The straw tubes undergo significant gravitational sagging, which leads to a non-negligible wire displacement from the tube center, and cannot operate without pretensioning or external supporting structures. Several mechanical designs of the tracking stations are being explored to minimize the magnitude of the sagging of the tubes, while keeping minimal the material amount in the acceptance. The studies presented in this thesis address various aspects related to the characteristics of the straw tubes and their performance within the SST and are intended to guide the engineering design.

One chapter of this thesis covers some key mechanical and electrical properties of the straw tubes. This includes gravitational sagging, 3-dimensional surface scanning, elongation, creep measurements and signal attenuation. Prototypes were built and measurements were performed in the laboratory. The results are compared to theoretical predictions.

A chapter is devoted to the test beam experiment performed with a straw tube prototype and to the associated data analysis. A  $2 \text{ m}$  prototype straw tube was tested with a 150 GeV pion beam at CERN. The goal of the test beam experiment was to measure the spatial resolution of the straw tube with respect to different wire displacement values. The results

show that the spatial resolution of the straw tube does not depend significantly on the magnitude of the wire displacement, and a spatial resolution of less than  $110\text{ }\mu\text{m}$  was obtained. However, the shape of the isochrone relation of the straw tube (the V-shape) depends significantly on the wire eccentricity, indicating that the electric field distortions due to the wire displacement are important. The possibility to extract the wire eccentricity from the drift time spectrum alone, using edge finding algorithms, was also considered and elaborated in this chapter based on the test beam results. Apart from providing a direct measurement of the local wire eccentricity, these algorithms could help to understand the actual straw tubes geometry in SHiP and could provide input to a future geometry-correcting algorithm.

In the last chapter, the results of a few simulation studies are discussed. As already mentioned, the suppression of the backgrounds is essential for the SHiP physics reach. The Muon Shield was developed to deflect out of the acceptance the muons coming out of the production Target and Hadron Absorber of the BDF, thereby keeping as low as possible the background rates in the SHiP detectors. The description of the experiment in the simulation framework was improved to take into account a more realistic field map of the spectrometer magnet and the equivalent mass model of SST frames. The rates of background hits in the SST were verified with this new description. The maximum occupancy in the SST per straw tube obtained for the nominal values of the magnetic fields of the SHiP Muon Shield is  $\approx 10\text{ kHz/tube}$ , which corresponds to an average of 0.01 hits/tube for a  $1\text{ }\mu\text{s}$  time window. This ensures smooth operation of the tubes without saturation under nominal conditions and leaves room to increase significantly the hit rate for the tracker alignment runs, for example, by reducing the Muon Shield field. It was also found that the hit rates are dominated by low energy  $e^+/e^-$  particles (from photon conversions) in the two stations before the dipole magnet, while real muons are the dominant cause of hit rates in the two stations behind the magnet.

An initial simulation study of the effect of straw tube sagging and, hence, of non-zero wire eccentricity was performed in the SHiP simulation framework. The results show that the track fitting quality depends significantly on the spread of the wire eccentricity across the SST, while it is less sensitive to the mean value of this eccentricity. These studies should be elaborated further in order to specify more precisely the acceptable tolerance to the variation of the maximum wire displacements in the straw tubes.

The last simulation study is devoted to the influence of the pile-up in time of the muon background events. So far, SHiP simulation events corresponded to one generated proton interaction and the subsequent Geant4 particle production through the experimental setup. In the real experiment, the data stream will be subdivided in time frames containing detector hits from various sources (several proton interactions, cosmic ray showers, noise, etc). As part of this thesis, a pile-up simulation algorithm was proposed and implemented into the digitization procedure of the SHiP simulation framework. The robustness of the track pattern recognition algorithms was checked on the muon background events without any adaptation of the algorithm. Adding pile-up within a  $3\text{ }\mu\text{s}$  time window provoked a relative drop of the tracks recognition efficiency by 9%, indicating that some adaptation is required.

In summary, a characterization of several aspects of the SHiP straw tubes was performed and studied within the SHiP simulation framework. The results obtained in this work not only confirm the viability of the proposed SST detector concept for the SHiP experiment, in particular the choice of increasing the straw diameter to 2 cm, but also provide a guidance for further development of the engineering design.



## Zusammenfassung

Das SHiP-Experiment wurde im Zusammenhang mit einer neuen Beam Dump Facility (BDF) von hoher Intensität am CERN SPS-Komplex vorgeschlagen, um nach neutralen „versteckten Teilchen“ mit Massen bis zu einigen GeV zu suchen, die nur schwach mit Teilchen des Standardmodells wechselwirken. Aufgrund der hohen Intensität des 400 GeV SPS Protonenstrahls ( $4 \cdot 10^{19}$  p.o.t. pro Jahr), einer großen Akzeptanz des Detektors und einer sorgfältigen Unterdrückung des Untergrunds, insbesondere durch Verwendung eines magnetischen Myonen-Schildes hinter dem Target, werden bislang unerreichte Sensitivitäten erwartet. Eine entscheidende Rolle bei der Rekonstruktion der Zerfälle möglicher Kandidaten spielt das Hidden Sector (HS) Spektrometer von SHiP.

Hauptkomponente des HS-Spektrometers ist der *Spectrometer Straw Tracker* (SST), der aus vier Trackingstationen und einem Dipolmagneten besteht. Der SST ist ein Spurdetektor, welcher konzipiert wurde Untergrund zu verwerfen und Signalereignisse zu erkennen, indem er die Impulse geladener Teilchen präzise misst sowie die Zerfallsvertizes und die Stoßparameter rekonstruiert und so den Entstehungsort der verborgenen Teilchen bestimmt. Anforderungen an den SST sind eine große Akzeptanz von  $5\text{ m} \times 10\text{ m}$  und eine Ortsauflösung von mindestens  $120\text{ }\mu\text{m}$ . Dabei muss die Menge an Material im Akzeptanzbereich auf ein Mindestmaß reduziert werden. Um diese Anforderungen zu erfüllen, wurde ein Drift-Detektor auf Basis ultraleichter, 5 m langer *Straw Tubes* mit einem Durchmesser von 2 cm vorgeschlagen, welcher im Vakuum betrieben werden soll.

Basierend auf einer von der NA62-Kollaboration entwickelten Technologie, bestehen die Kathoden der Straw Tubes aus  $36\text{ }\mu\text{m}$  dünnen, biaxial orientierten PET-Röhren, die auf der Innenseite mit Kupfer und Gold beschichtet sind. Als Anode wird ein Draht aus einer vergoldeten Wolfram-Rhenium-Legierung mit  $30\text{ }\mu\text{m}$  Durchmesser verwendet. Die Röhre ist mit einem Gasgemisch aus Ar/CO<sub>2</sub> im Verhältnis 70%/30% bei 1 bar Absolutdruck gefüllt. Eine Hochspannung von 2.2 kV sorgt für eine Gasverstärkung zwischen  $10^4$  und  $10^5$ . Mit dieser Konstruktion lassen sich Werte von 0.5% einer Strahlungslänge pro Station erreichen. Sie bringt jedoch Herausforderungen in Bezug auf die mechanische Festigkeit und Stabilität der Röhren mit sich. Die Straw Tubes unterliegen einem erheblichen gravitativen Durchhang, welcher zu einer nicht zu vernachlässigenden Verschiebung des Drahtes aus der Röhrenmitte führt, und können nicht ohne Vorspannung oder externe Haltestrukturen betrieben werden. Es werden mehrere mechanische Konstruktionen der Tracking Stationen untersucht, um das Ausmaß des Durchhangs der Röhren zu minimieren und gleichzeitig die Menge an Material im sensitiven Bereich minimal zu halten. Die in dieser Arbeit vorgestellten Studien befassen sich mit verschiedenen Aspekten im Zusammenhang mit den Eigenschaften der Straw Tubes und ihrer Leistungsfähigkeit innerhalb des SST und sollen als Leitfaden für das technische Design dienen.

Ein Kapitel dieser Arbeit behandelt einige wichtige mechanische und elektrische Eigenschaften der Straw Tubes. Dazu gehören gravitativer Durchhang, 3-dimensionale Oberflächenuntersuchungen, Messungen der Elongation, des Fließens und der Signaldämpfung.

Es wurden Prototypen gebaut und Messungen im Labor durchgeführt. Die Ergebnisse werden mit theoretischen Vorhersagen verglichen.

Ein Kapitel widmet sich einem mit einem Straw Tube Prototypen durchgeführtem Teststrahlexperiment und der damit verbundenen Datenanalyse. Ein 2 m langer Straw Tube Prototyp wurde in einem 150 GeV-Pionenstrahl am CERN getestet. Das Ziel des Teststrahlexperiments war die Ortsauflösung der Straw Tube in Abhängigkeit verschiedener Drahtverschiebungen zu messen. Die Ergebnisse zeigen, dass die Ortsauflösung der Straw Tube nicht wesentlich von der Drahtverschiebung abhängt, und es wurde eine Genauigkeit von besser als 110  $\mu\text{m}$  erzielt. Die Form der Driftzeit-Orts-Beziehung („V-Form“) hängt jedoch signifikant von der Drahtexzentrizität ab, was darauf hinweist, dass die Verzerrungen des elektrischen Feldes aufgrund der Drahtverschiebung eine große Rolle spielen. Die Möglichkeit, die Drahtexzentrizität allein aus dem Driftzeitspektrum mit Hilfe von Algorithmen, welche die Form des Spektrums analysieren, zu extrahieren, wird in diesem Kapitel ebenfalls in Betracht gezogen und auf der Grundlage der Teststrahlergebnisse ausgearbeitet. Abgesehen von der direkten Messung der lokalen Drahtexzentrizität könnten diese Algorithmen zum Verständnis der tatsächlichen Straw Tube Geometrie bei SHiP beitragen und einen Input für einen zukünftigen Geometriekorrekaturalgorithmus liefern.

Im letzten Kapitel werden die Ergebnisse einiger Simulationsstudien besprochen. Wie bereits erwähnt, ist die Unterdrückung des Untergrunds für das SHiP Physik Programm wesentlich. Das Myon-Schild wurde entwickelt, um die aus dem Target und Hadronenabsorber der BDF kommenden Myonen aus dem Akzeptanzbereich abzulenken und dadurch die Untergrundraten in den SHiP-Detektoren so niedrig wie möglich zu halten. Die Beschreibung des Experiments im Simulationsframework wurde verbessert, um ein realistischeres Feld des Spektrometernagnetes und die passende Massenverteilung der SST-Rahmen zu berücksichtigen. Die Untergrundraten im SST wurden mit dieser neuen Beschreibung verifiziert. Die maximale Okkupanz im SST pro Straw Tube, die für das nominelle Magnetfeld der SHiP-Myonen-Abschirmung berechnet wurde, beträgt  $\simeq 10 \text{ kHz/Röhre}$ , was einer mittleren Anzahl von 0.01 Treffern/Röhre in einem Zeitfenster von 1  $\mu\text{s}$  entspricht. Dies gewährleistet einen reibungslosen Betrieb der Röhren ohne Sättigung unter nominellen Bedingungen und lässt noch einen Spielraum, die Trefferrate für eine Kalibration des Trackers deutlich zu erhöhen, z.B. durch Reduzierung des Myon Shield Feldes. Es wurde weiterhin gezeigt, dass die Trefferraten in den beiden Stationen vor dem Dipolmagneten von niederenergetischen  $e^+/e^-$ -Teilchen (aus Photokonversion) dominiert werden, während in den beiden Stationen hinter dem Magneten tatsächlich Myonen die dominierende Ursache für die Trefferraten sind.

In der SHiP-Simulation wurde eine erste Studie über die Auswirkung des Durchgangs der Straw Tubes und damit einer von Null verschiedenen Drahtexzentrizität durchgeführt. Die Ergebnisse zeigen, dass die Qualität der Fits signifikant von der Streuung der Drahtexzentrizität innerhalb des SSTs abhängt, während sie weniger empfindlich auf den Mittelwert reagiert. Diese Studien sollten weiter ausgearbeitet werden, um die akzeptable Toleranz für die Variation der maximalen Drahtverschiebungen in den Straw Tubes genauer zu spezifizieren.

Die letzte Simulationsstudie ist dem Einfluss der zeitlichen Anhäufung von Myon-



Untergrundereignissen gewidmet. Bislang wurden in der SHiP-Simulation Ereignisse einzelner Protonenwechselwirkungen und die anschließende Geant4-Teilchenproduktion innerhalb des experimentellen Aufbaus betrachtet. Im realen Experiment werden die Daten in Zeit-Frames eingeteilt, die Detektorsignale verschiedener Herkunft enthalten (mehrere Protonenwechselwirkungen, kosmische Schauer, Rauschen usw.). Als Teil dieser Arbeit wurde ein *Pile-Up*-Simulationsalgorithmus vorgeschlagen und in das Digitalisierungsverfahren des SHiP-Simulationsframeworks implementiert. Die Robustheit der Mustererkennungsalgorithmen wurde ohne jegliche Anpassung an Myon-Untergrundereignissen überprüft. Das Hinzufügen von Pile-Up innerhalb eines Zeitfensters von  $3\text{ }\mu\text{s}$  führte zu einem relativen Abfall der Effizienz der Spurerkennung um 9%, was darauf hinweist, dass eine gewisse Anpassung erforderlich ist.

Zusammenfassend wurde eine Charakterisierung verschiedener Aspekte der SHiP-Straw Tube durchgeführt und im Rahmen der SHiP-Simulation untersucht. Die in dieser Arbeit erzielten Ergebnisse bestätigen nicht nur die Durchführbarkeit des vorgeschlagenen SST-Detektorkonzepts für das SHiP-Experiment, insbesondere im Hinblick auf die Vergrößerung des Röhrendurchmessers auf 2 cm, sondern bieten auch eine Anleitung für die weitere Entwicklung des technischen Designs.



## **Dedication**

I dedicate this thesis to my beloved grandmother, who was always supportive in my pursuit for knowledge. She followed and was proud of all my achievements acquired during doctoral studies and missed only the last moment - my defense. Rest in Peace, my granny.



# Contents

<b>Introduction</b>	<b>1</b>
<b>1 The SHiP experiment and its straw tracker</b>	<b>3</b>
1.1 The SHiP experiment and its subsystems . . . . .	5
1.1.1 The Target complex . . . . .	6
1.1.2 The Muon Shield . . . . .	7
1.1.3 The Scattering and Neutrino Detector . . . . .	7
1.1.4 The Hidden Sector decay spectrometer . . . . .	8
1.1.5 The detector electronics . . . . .	9
1.2 Spectrometer Straw Tracker characteristics and purpose . . . . .	9
1.3 A straw tube as a detector of ionizing radiation . . . . .	13
1.3.1 The effect of the distorted electric field on the wire displacement . .	17
1.3.2 The detection of photons end electrons with the straw tube . . . . .	19
<b>2 Characteristics of the straw tubes</b>	<b>23</b>
2.1 Mechanical properties of the tubes . . . . .	23
2.1.1 Sagging effect and the shape of the straw tubes . . . . .	24
2.1.2 Creep and rupture tests . . . . .	31
2.2 Electrical properties of the tubes . . . . .	40
2.2.1 ANSYS simulation of the electro-magnetic properties of the straw tube . . . . .	42
2.2.2 Signal attenuation measurements . . . . .	44
<b>3 SST 2017 test beam analysis</b>	<b>49</b>
3.1 Overview of the experiment . . . . .	50
3.1.1 Detectors . . . . .	50
3.1.2 Readout and data acquisition system . . . . .	51
3.1.3 Data samples . . . . .	53
3.2 Telescope data analysis . . . . .	57
3.2.1 Beam profiles . . . . .	57
3.2.2 Tracks reconstruction . . . . .	58
3.2.3 Telescope alignment . . . . .	58
3.2.4 Track extrapolation and hit maps . . . . .	61

3.3	Optical measurement of the wire eccentricity . . . . .	65
3.4	Data quality and event selection . . . . .	69
3.4.1	Data rates, pile-up and noise sources . . . . .	69
3.4.2	T0 and DUTs efficiencies . . . . .	76
3.4.3	The isochrone relation and the hit selection algorithm . . . . .	77
3.5	Straw tube spatial resolution . . . . .	83
3.5.1	Resolution from spatial distributions . . . . .	83
3.5.2	Comparison of resolution results . . . . .	92
3.5.3	Systematic effects . . . . .	94
3.6	Drift time distribution analysis . . . . .	98
3.6.1	Two-threshold method . . . . .	99
3.6.2	Canny's edge detection method . . . . .	101
3.6.3	Improved Canny's method . . . . .	103
3.6.4	Laplacian of Gaussian method . . . . .	103
3.7	The results of the edge finding algorithms and their application . . . . .	105
3.7.1	Comparison of the results . . . . .	105
3.7.2	Reconstruction of the isochrone relation . . . . .	108
<b>4</b>	<b>SST studies in FairShip</b>	<b>115</b>
4.1	Muon background studies . . . . .	115
4.1.1	Material frames around the views . . . . .	116
4.1.2	The effects of the realistic magnetic field on the SST occupancy . . . . .	120
4.1.3	The effects of the Scattering and Neutrino Detector magnetic field on the SST occupancy . . . . .	124
4.1.4	Expanding the size of the material frames around the views of the SST tracking stations . . . . .	127
4.1.5	Symmetrical design . . . . .	129
4.1.6	The occupancy of the SST for smaller magnetic fields of the Muon Shield . . . . .	130
4.1.7	The summary tables with the results . . . . .	132
4.2	Misalignment simulation of the straw tubes . . . . .	134
4.2.1	Straw tube wire sagging profile . . . . .	134
4.2.2	The track fitting performance for displaced wires . . . . .	136
4.3	Hits pile-up simulation in the SST . . . . .	142
	<b>Conclusions</b>	<b>153</b>
	<b>Bibliography</b>	<b>157</b>
	<b>List of acronyms</b>	<b>167</b>
<b>A</b>	<b>The evolution of the straw tube rupture process</b>	<b>169</b>

<b>B</b>	<b>Read-out electronics tests</b>	<b>171</b>
B.1	PNPI electronics tests . . . . .	171
B.2	WaveCatcher tests . . . . .	178
<b>C</b>	<b>Synchronization algorithms</b>	<b>183</b>
<b>D</b>	<b>Geometry configuration script for muon background studies</b>	<b>185</b>
<b>E</b>	<b>Momentum distributions of the the SST hits in muon background simulations</b>	<b>187</b>
	<b>Acknowledgements</b>	<b>201</b>





# Introduction

The “Search for Hidden Particles” experiment (SHiP) is an experiment proposed to be built at the Beam Dump Facility at CERN, aiming at searches for hidden sector particles, light dark matter and studies of neutrino physics [1–5]. The hidden particles are neutral but some of them are expected to decay to Standard Model charged particles. The Spectrometer Straw Tracker (SST) is the detector of the SHiP Hidden Sector decay spectrometer that will be used for the reconstruction of the tracks, the positions of the decay vertices and the impact parameters of the Hidden Sector signal candidates. The SST is a tracking detector with a large acceptance of  $5\text{ m} \times 10\text{ m}$ . It is a gaseous drift detector based on straw tubes. The straw tubes meet all the requirements defined for the SST. They are extremely light (made of thin BoPET rolls), close to 100% efficient, they can provide a spatial resolution of  $< 120\text{ }\mu\text{m}$  and are capable to operate in vacuum. However, being made of polymeric material, the straw tubes suffer significant gravitational sagging and creep under load. This brings drastic challenges for the SST mechanical design and has non-negligible influence on the performance of the SST.

In this thesis a number of studies on the straw tubes were performed addressing mechanical and electrical properties of the tubes, measurements of the sagging and the shape of the tube, investigation of the sagging effects on the performance of the straw tube as a detector unit and conducting read-out electronics tests, the simulation of the misalignment (due to the sagging) and hits pile-up effect in the straw tubes and their influence on the performance of the tracks reconstruction in the SST, the hits occupancy simulation (hit rate per tube) due to the muon background in SHiP and investigating the limits for the SST alignment mode hit rates in the straw tubes. Overall, the aim of this thesis is to characterize the straw tubes as detector units of the SST, use and test the obtained information in the SST simulation, find the limits on the straw tubes parameters, when the tracker performance is still tolerable.

In Chapter 1 a brief description of the SHiP experiment and its physics program is provided and the physics of straw tubes as a gaseous detectors is explained. In Chapter 2 the mechanical (strain, creep, elastic modulus, sagging) and electrical (resistance, signal attenuation) properties of the straw tubes are described.

Chapter 3 is focused on the analysis of the beam test carried out at CERN in 2017. The objects of these studies were two straw tube prototypes. The main goal was to obtain the spatial resolution of the studied prototypes and to investigate the possibility to extract the wire displacement value inside the straw tube using only the information from the drift time distributions.

Chapter 4 covers the studies related to the SST performance in the SHiP simulation framework, FairShip, including studies of the muon background hit rates in the SST at different values of the magnetic fields of the SHiP magnets and variations in the geometry of the SST, influence of wire misalignment on the SST track fitting quality and effect of hit pile-up in the SST on the tracks pattern recognition algorithms.

The studies and results described in this thesis are partially presented in the notes: [6–8]. The author of this thesis is the first author in those notes.

# Chapter 1

## The SHiP experiment and its straw tracker

Despite the great success of the Standard Model (SM) [9], and the recent discovery of its last missing building block (the Higgs boson), there are still a few phenomena in the Universe, which cannot be explained in the scope of the SM. These are the non-zero neutrino masses, the existence of dark matter, the baryon asymmetry and the cosmic inflation. In order to be able to theoretically explain all these experimental observations, the SM needs to be extended. However, right now there are no clear hints indicating the possible energy scale for the interactions of the new particles and their coupling strength to the already known ones. Searches for new physics are mostly concentrated on higher energies (*i.e.*, at TeV scale). For example, the ATLAS and the CMS collaborations at CERN conduct activities to search for dark matter using proton-proton collisions at 13 TeV [10] and plan to continue the searches at the High Luminosity LHC [11]. However, the low energy landscape for new physics searches remains almost intact. Even theories that predict new particles at the high energy scale do not completely discard the possibility to have new low-mass feebly interacting particles. For example, some models with a hidden sector [12] predict that dark matter particles interact with SM particles via gravity and potentially through hypothetical mediators (portals) such as dark photons, dark scalars and axion like particles. A theory can explain the massiveness of the neutrinos by introducing right-handed Majorana neutrinos [13], but the mass scale can be extremely wide and calls for searching at both intensity and energy frontiers. To sum up, currently there are large areas of unexplored territory in the parameter phase space of many extensions of the SM. The sensitivity of the current energy frontier experiments does not allow to cover some regions that can be reached by the new intensity frontier SHiP experiment [1–5].

The SHiP experiment consists of a production target and a Hadron absorber (the Target complex), a Muon Shield, a Scattering and Neutrino Detector and a Hidden Sector decay spectrometer (the details are given in Section 1.1). The SHiP experiment has competitive sensitivities to dark photons, dark scalars, heavy neutral leptons (HNLs) and axion like particles coupled to fermions and photons with masses from sub-GeV up to 10 GeV range and with feeble couplings down to  $10^{-10}$  [14–16]. The corresponding

sensitivity plots are shown in Figure 1.1 and 1.2. These plots were calculated using the SHiP simulation framework, FairShip [17], that simulates the SHiP experiment. The evaluation was performed for  $2 \cdot 10^{20}$  incoming protons on the SHiP target, which can be achieved in five years of data taking using slowly extracted proton spills [18] (of  $4 \cdot 10^{13}$  protons per 1 s spill) from the CERN SPS. Such sensitivity reaches are possible due to specifically low background rates achieved in SHiP. For instance, the signal events for fully reconstructible HNL decays such as  $\text{HNL} \rightarrow \mu^\pm \pi^\mp$  or  $\text{HNL} \rightarrow \mu^\pm \rho^\mp (\rightarrow \pi^\mp \pi^0)$  can take advantage of a powerful background rejection by reconstructing a decay vertex and an impact parameter to the production target of the neutral decaying particle. With low, but non-vanishing probability, background tracks can mimic the daughter tracks from a signal event. Three dominant sources of such background were identified: random muon combinations, muon inelastic scattering and neutrino inelastic scattering. The cosmic background contribution was evaluated and is expected to be negligible.

The muon combinatorial background is formed by spurious muons that pass the Muon Shield and reach the HS decay spectrometer. The rate of such muons is expected to be  $26.3 \pm 3.6$  kHz. The combinatorial rate can be heavily suppressed by applying pre-selection cuts [5] requesting additionally the coincidence of muon tracks within a small time window (hundreds of picoseconds) and using the veto information from the Surround Background Tagger (liquid scintillators surrounding the Decay Volume of the HS decay spectrometer). An estimate of 0.042 events in five years of running is obtained from simulation. The contribution of this background muon rate in the Spectrometer Straw Tracker (SST) of the SHiP HS decay spectrometer was thoroughly investigated in this thesis in Chapter 4. To validate the muon background rate simulated in the FairShip framework, an experiment was conducted in 2018 [19] at the H4 beam-line of the SPS North Area<sup>1</sup> at CERN to measure the muon flux generated after the interaction of 400 GeV protons with a replica of the SHiP target. The results of the experiment are in good agreement with the simulations provided by the FairShip framework.

The muon inelastic interactions are expected to produce  $2 \cdot 10^8$  long-lived neutral  $V_0$  particles for  $2 \cdot 10^{20}$  protons on target (after five years of SHiP operation) in the proximity of the Decay Volume of HS decay spectrometer of SHiP. This background source is reduced after applying the pre-selection cuts and using the information from background taggers to  $6 \cdot 10^{-4}$  events for  $2 \cdot 10^{20}$  protons on target.

The last source of the background is neutrino inelastic interaction with the residual gas inside the Decay Volume. This background is rejected using the background taggers (around the Decay Volume) information, time window coincidence and pre-selection cuts to the level of  $< 0.3$  events after five years of SHiP operation. This background process is the main reason for evacuating the Decay Volume to a vacuum pressure of  $< 10^{-2}$  bar.

The SHiP experiment includes also a dedicated detector to search for light dark matter (LDM) and to perform neutrino physics investigations – the Scattering and Neutrino Detector (SND), made of emulsion cloud chambers (ECCs) and target tracker planes to detect and measure the electromagnetic showers created by the recoil electrons

---

<sup>1</sup>Information on Secondary Beams & Areas at CERN: <http://sba.web.cern.ch/sba/>

from the elastic scattering of LDM in the SND ( $\chi e^- \rightarrow \chi e^-$ ). The most significant background source, which can mimic this LDM signal, are the neutrino interactions with a single reconstructed electron at the primary vertex. The quantitative estimation of the contribution of the neutrino background sources was performed using the FairShip framework. The total number of background events for the LDM searches obtained after five years of SHiP operation is  $\sim 800$  for an LDM mass in the range of  $M_\chi \sim \mathcal{O}(1 \text{ GeV}/c^2)$ . The SND platform of SHiP allows also to perform dedicated neutrino physics studies. In particular, the muon identification system of the SND provides the necessary data to distinguish the three flavors of the neutrinos through the flavors of the primary charged leptons produced in the neutrino charged-current interactions. The number of such interactions is expected to be of the order of  $10^6$  for  $\nu_e$  and  $\nu_\mu$ ,  $10^5$  for  $\bar{\nu}_e$  and  $\bar{\nu}_\mu$ ,  $10^4$  for  $\nu_\tau$  and  $\bar{\nu}_\tau$  after five years of SHiP operation ( $2 \cdot 10^{20}$  protons on target). For the first time, the SND magnetic spectrometer can provide the possibility to distinguish between  $\nu_\tau$  and  $\bar{\nu}_\tau$  by measuring the charge of  $\tau$  decay products. One extra topic accessible with the SND platform is the estimation of the number of neutrino induced charmed hadrons. These studies can improve, in general, all studies related to the charm production from the neutrino interactions and grant the access to so far inaccessible channels. The simulation of the charm production in the FairShip framework gives an estimate of  $2 \cdot 10^5$  charmed hadrons produced from the  $2 \cdot 10^{20}$  protons on target after five years of SHiP operation. More details on the physics program of SHiP can be found in [1].

## 1.1 The SHiP experiment and its subsystems

The current 3-dimensional layout of SHiP experiment is shown in Figure 1.3. The layout is extracted from the output of the Event Display script of the FairShip framework. The SHiP experiment consists of the Target complex, the Muon Shield, the Scattering and

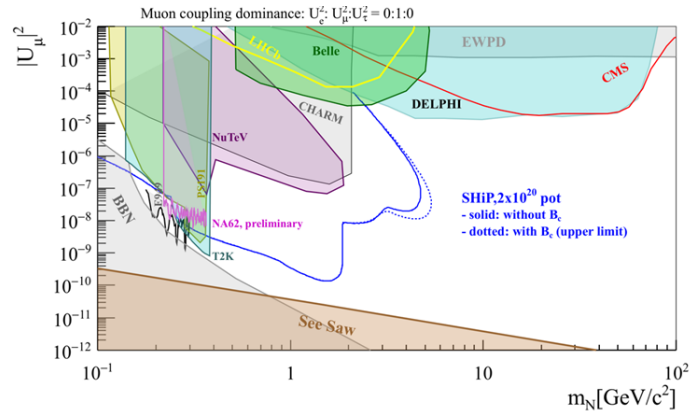


Figure 1.1: SHiP's sensitivity to heavy neutral leptons.  $U_\mu$  is the matrix element parametrizing the mixing of HNLs and muon neutrinos in the dark sector Lagrangian.  $m_N$  is the HNL mass. The figure is taken from [5].

Neutrino Detector, and the Hidden Sector decay spectrometer. The whole SHiP detector will be installed inside the experimental hall of the Beam Dump Facility [20] of 120 m length, 20 m width and at 15 m below the local ground level. In the following subsections more details on the subsystems of SHiP are provided.

### 1.1.1 The Target complex

The main requirements for the SHiP target, driven by the physics performance, are the shortest possible nuclear interaction length (to maximize hadronic interactions and reduce the neutrino flux) and the dimensions large enough to keep much of the hadronic showers inside the target. Thus, the longitudinally segmented hybrid target consists of blocks of four interaction lengths of titanium-zirconium doped molybdenum (TZM) alloy (58 cm) followed by six interaction lengths of pure tungsten (58 cm). A 4.5 m long Hadron absorber, made of iron, is positioned right after the target. Its role is to contain the full hadronic shower. The magnetization of the Hadron absorber has been studied [21] and should permit to move upstream the Muon Shield and the detectors (increasing the geometrical acceptance) and reduce the weight and length of the Muon Shield.

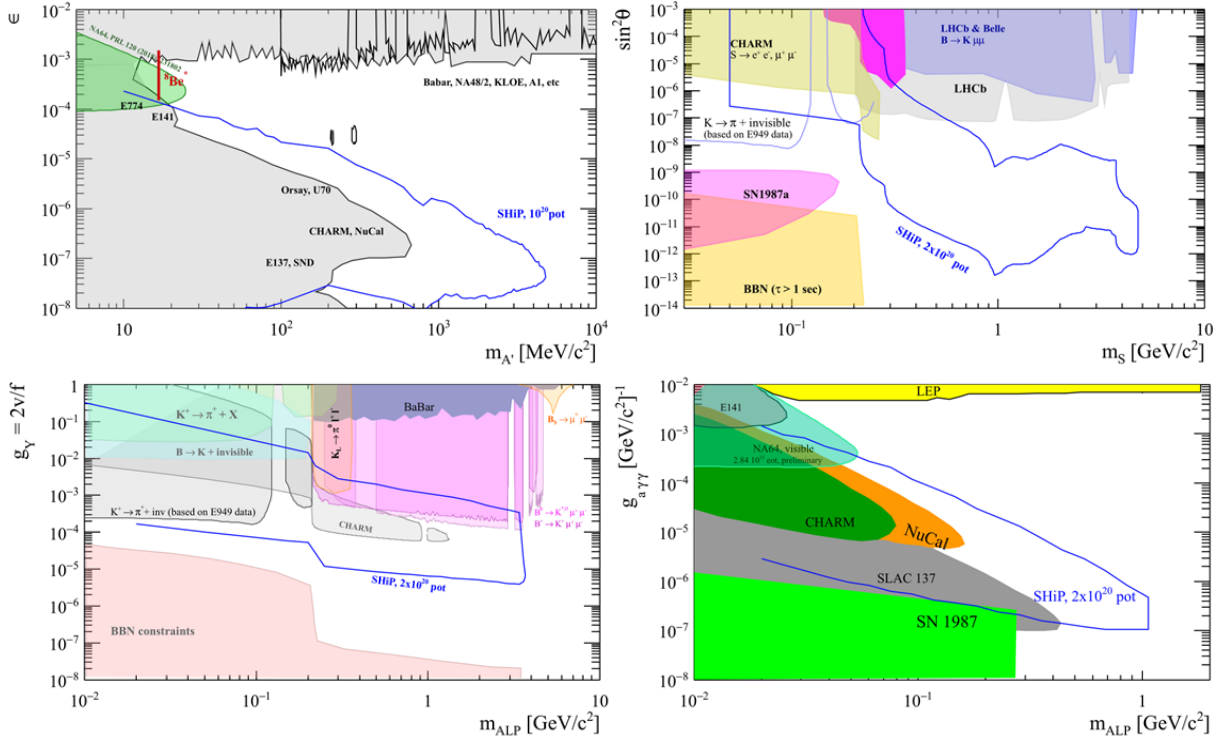


Figure 1.2: SHiP's sensitivity to dark photons (top-left), dark scalars (top-right), axion-like particles coupled to fermions (bottom-left) and to photons (bottom-right). The figures are taken from [5].

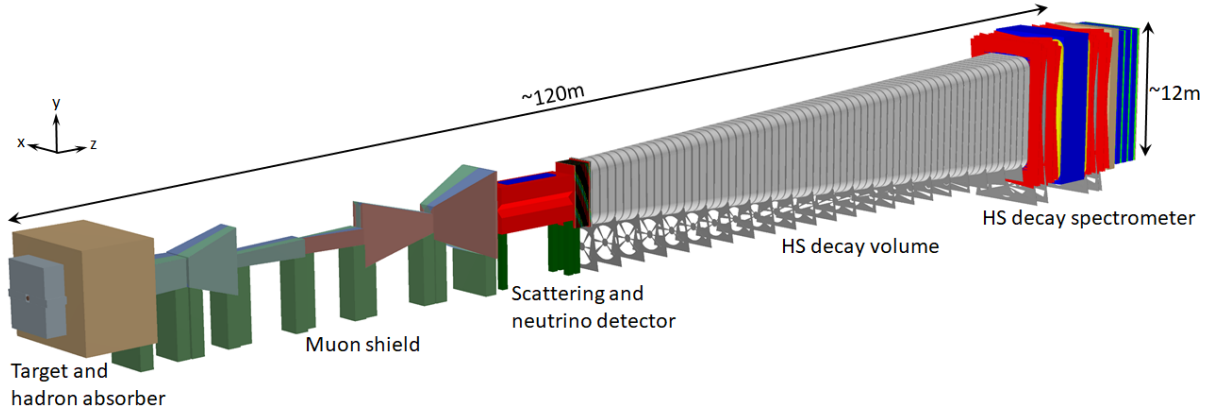


Figure 1.3: The current layout of the SHiP experiment. The figure is taken from [5].

### 1.1.2 The Muon Shield

The main task of the Muon Shield [22] is to deflect the muons that passed through the Hadron absorber to the left and the right sides of the SHiP experiment minimizing the muon flux within the geometrical acceptance. According to the baseline design [23], the warm magnets of the Muon Shield are made of 50 mm thick sheets of CRGO steel [24], which are air-cooled. The current baseline dimensions were calculated after the Bayesian optimization was performed for the muon background simulation within the FairShip framework. The optimized length of the Muon Shield is 35 m and the total mass – 1300 tonnes. The average field gradient across all magnetic volumes of the Muon Shield is 1.7 T. Such configuration allows to reduce the muon flux inside the geometrical acceptance of SHiP by six orders of magnitude.

### 1.1.3 The Scattering and Neutrino Detector

The Scattering and Neutrino detector (SND), as it was mentioned previously in this chapter, is involved in the LDM searches and neutrino physics studies. The SND consists of a precision spectrometer and a muon identification system. The precision spectrometer consists of an emulsion target and a water-cooled dipole magnet with a field of 1.2 T with transverse dimensions that do not exceed the geometrical acceptance of SHiP at the SND location. The emulsion target is a combined device made of modules called “bricks” and compact emulsion spectrometers (CESs). A brick consists of alternating layers of tungsten and nuclear emulsions. A CES is made of a “sandwich” of light material plates (15 mm-thick polymethylmethacrylate spacers) and emulsion films. In between the emulsion target modules the Target tracker (TT) planes [25] are installed. They provide the time stamp for the reconstructed events in the emulsion target modules. In total, the emulsion target consists of 19 bricks and CESs modules, and 19 TT planes reaching a total of 8 tonnes of absorber mass. The precision spectrometer of the SND has sufficient

resolution for  $\nu_\tau$  detection. The muon identification system in the baseline SHiP design consists of eight iron layers interleaved with tracking planes instrumented with Resistive Plate Chambers (RPCs). Two additional downstream layers made of Multi-gap Resistive Plate Chambers (MRPCs), act as an Upstream Background Tagger for the Hidden Sector particles searches (see the following Section 1.1.4). The goal of the muon identification system is to reconstruct the tracks from the precision spectrometer and identify the muons created after neutrino interactions in the emulsion target.

#### 1.1.4 The Hidden Sector decay spectrometer

The Hidden Sector (HS) decay spectrometer is a complex apparatus consisting of the Decay Volume, background taggers, the Spectrometer Straw Tracker (SST), the Spectrometer Magnet, the Timing Detector, The Split Calorimeter and the Muon System. A 50 m long Decay Volume is located in front of the HS spectrometer. The Decay Volume is a huge vacuum vessel with  $< 10^{-2}$  bar pressure made of steel. Its dimensions are defined by the dimensions of the Muon Shield and the SST. For the current baseline design of SHiP, the Decay Volume has upstream and downstream geometrical acceptance of  $1.5\text{ m} \times 4.3\text{ m}$  and  $5.0\text{ m} \times 11.0\text{ m}$ , respectively. The Decay Volume must have as light and as thin walls as possible to minimize neutrino and muon interactions. In order to veto the neutrino and muon background events in the Decay Volume, a Surround Background Tagger (SBT) is installed on the outer walls of the decay vessel. The SBT cells are made of a liquid scintillator in order to cover optimally the surface of the outer walls of the Decay Volume. The SST is made of four stations of straw tubes and is designed to reconstruct charged particle tracks. The SST tracking stations are located inside the vacuum vessel connected to the Decay Volume. More details on the SST are given in the Section 1.2. The Spectrometer Magnet [26] is located in between the two pairs of the tracking stations of the SST. The baseline option is a warm magnet with physical aperture of  $5\text{ m} \times 10\text{ m}$  and a vertical bending power of about 0.65 Tm over the distance between the upstream and the downstream tracking stations. A superconducting option is currently under study. The Timing Detector (TD), situated outside the vacuum vessel downstream the last tracking station of the SST, is responsible for providing a precise reference time ( $T_0$ ) for the SST drift time measurement. The TD must be adequately segmented in order to facilitate matching SST tracks with TD hits. The time resolution required for the effective rejection of background di-muon events is  $\approx 100\text{ ps}$  by far exceeding the precision required by the SST. Two design options are considered for the TD: one option based on plastic scintillators and another one based on time measuring resistive plate chambers (tRPCs). The Split Calorimeter (SplitCal) and the Muon System provide a particle identification, which is essential in discriminating between the very wide range of HS models. The SplitCal consists of layers of lead absorbers and scintillator planes orthogonal to the Z-axis. There are two precision layers inside the SplitCal “sandwich” made of MicroMegas chambers serving to measure precisely the transverse profiles of the showers created in the beginning of the SplitCal and the position of the maximum transverse spread of the electro-magnetic shower. The mutual arrangement of the lead/scintillator



layers and the precision layers of the SplitCal is being optimized to provide the best performance for the reconstruction of the decays of axion-like-particles to photons. The Muon System [27] consists of four  $6\text{ m} \times 12\text{ m}$  stations made of organic scintillating tiles with SiPMs read-out. The active stations are interleaved with passive iron plates of about three nuclear interaction lengths. The scintillating tiles are grouped into modules of 32. The usage of the organic scintillators allows to reach 100–150 ps timing resolution over the four stations. Overall, the constituents of the HS decay spectrometer are designed in a way to maximize the amount of the reconstructed decays of hidden sector particles maintaining ultra-low levels of the backgrounds.

### 1.1.5 The detector electronics

Compared to the LHC experiments there are no strong requirements on the radiation hardness and ultra-fast throughput of the read-out electronics for SHiP. The signals are collected from around 175 000 channels distributed over large distances and the events are built out of the detector hits that have a wide range of response times. The proposed DAQ system architecture [28] is based on common components up to the front-end electronics. The front-end read-out electronics with implemented interfaces to the common DAQ system are required to be developed by the SHiP subdetector teams. There are two main subsystems of the common DAQ: the Control distribution, data Transport and Concentration (CTC) system, and the Timing and Fast Control (TFC) system. A central feature of the DAQ system is that it uses no hardware trigger, all hits will be recorded continuously during an SPS spill. To synchronize all subdetectors, a common clock is distributed from the top-level concentrator through the cascade of the mid-level concentrators to the final front-end read-out boards attached directly to the detectors' outputs. The top-level concentrator is interfaced with the front-end host PC for data readout, slow control and monitoring, and with the TFC master for the clock distribution and synchronization commands. The front-end host PCs transmit the obtained time framed data to the Event Filter Farm, which builds the events.

## 1.2 Spectrometer Straw Tracker characteristics and purpose

The purpose of the Spectrometer Straw Tracker (SST) is to reconstruct the tracks of charged particles from the decay of neutral hidden sector particles with high efficiency while rejecting background events. Additionally, the SST must provide as good as possible measurements of the track momentum and of the particle flight direction originating from the fiducial Decay Volume. The invariant mass, the vertex quality and the value of the reconstructed impact parameter are crucial tools for rejecting background from  $V_0$  meson decays or from random di-muon combinations. The overall physics performance of SHiP depends on a number of requirements for the SST:

- Usage of ultra-light material along the particle trajectory to minimize multiple Coulomb scattering.
- Integration of the SST inside the vacuum vessel to further minimize the multiple scattering and suppress neutrino interactions.
- An intrinsic spacial resolution (at least  $120\ \mu\text{m}$ ) that allows the reconstruction of the decay vertices of the neutral hidden sector particles with a resolution of the order of 1 mm for the  $Y$  vertex coordinate, a factor of two or three more for the  $X$  coordinate. The  $Z$  vertex coordinate resolution is expected to be an order of magnitude worse.
- A hit efficiency close to 100% for signal events.

To fulfill the mentioned performance requirements for the tracking detector with large geometrical acceptance of  $5\text{ m} \times 10\text{ m}$  and adequate cost to performance ratio, a design inspired from the NA62 Straw Tracker [30] was proposed. The SST is located between the Decay Volume and the Timing Detector (see Figure 1.4). It consists of 4 tracking stations (named T1, T2, T3 and T4). A dipole magnet (the Spectrometer Magnet) is situated between the first two and the last two stations with gaps of 2.5 m between the magnet center and the closest tracking stations. The distance between the neighboring

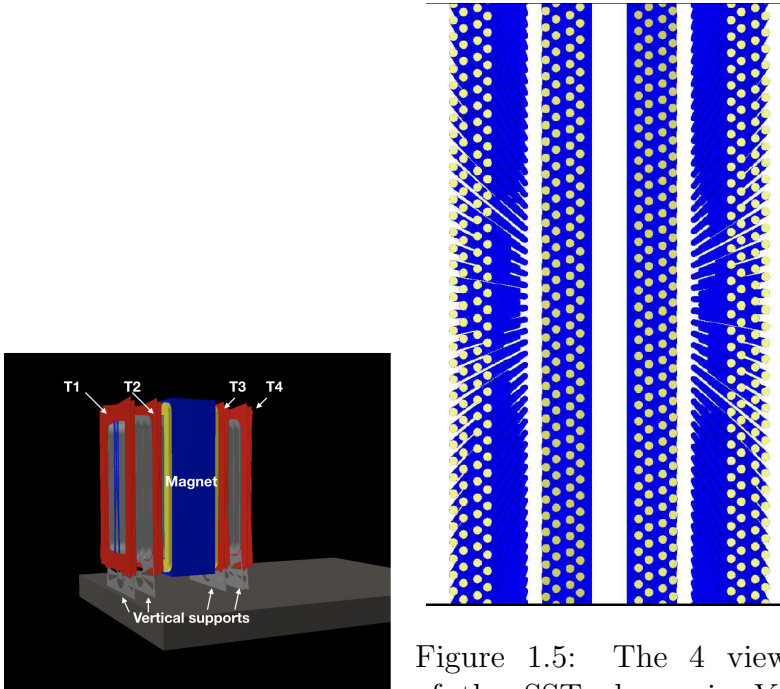


Figure 1.4: The SST geometrical volumes simulated in the FairShip framework.

Figure 1.5: The 4 views of the SST shown in  $YZ$  plane in the FairShip framework. The figure is adapted from [29].

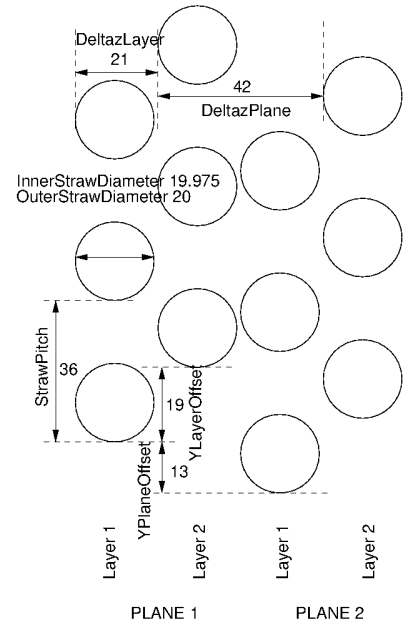


Figure 1.6: Schematic layout of one view of the tracking station implemented in the FairShip framework.

stations upstream and downstream the magnet is 2 m. The magnetic field, oriented along the  $X$ -axis, is about 0.14 T at its maximum and about 0.08 T at the location of the closest tracker stations, outside the magnet. Along the longitudinal axis  $Z$ , the field integral between the second and the third stations is approximately 0.65 Tm. The orientation of the magnetic field drives the design of the tracking stations layout. Each station contains 4 views, each view contains two straw planes and each plane consists of two straw tube layers. The first and the last views are made of horizontal straw tubes to measure precisely the vertical  $Y$  coordinate, while the two middle views are rotated by, respectively,  $+5^\circ$  and  $-5^\circ$  around the  $Z$  axis measuring the  $X$  coordinate, which is a sufficient stereo angle to provide a good measurement of the decay vertex, the opening angle of the daughter particles and the impact parameter at the production target. The height of each view is 10 m, the width is 5 m, the  $Z$  extent is currently 10 cm (see Figure 1.6). Each layer contains an array of the straw tubes aligned vertically. The diameter of each straw tube is 2 cm. There is a constant gap of 36 mm between the straw tubes in the layers (so called “pitch”) that was introduced due to possible mechanical challenges of mounting the tubes inside the stations. Straw tubes in the neighboring layers, which form a straw plane, are displaced in a way to cover the whole geometrical acceptance of the plane (see Figure 1.5). The total number of straw tubes in all stations is 17728. The baseline layout of straw tubes within the views, planes and layers corresponds to the TP [2] configuration except the tube diameter, which was increased. However, other design options are considered and being developed.

The straw tubes design used for the SST is building on the design used in the NA62 experiment [30]. The tubes are made of thin ( $36\text{ }\mu\text{m}$ ) biaxially-oriented PET rolls coated with 50 nm Cu and 20 nm Au on the inner surface of the BoPET film. To make a single tube, the needed length of the metalized BoPET film from the roll is cut. Then the obtained piece is folded along the longitudinal dimension making a cylinder and is weld along the length of the cylinder with ultrasonic welding apparatus [31]. Two end-plugs with gas insertion capillaries are glued at the opposite ends of the tube and a tungsten-rhenium gold plated wire is tensioned in the middle of the tube. Both ends of the wire are attached and fixed with crimped pins in the end-plugs. The crucial differences between the SST straw tubes and NA62 ones are the length of the tubes (5 m instead of 2.1 m), the diameter (2 cm instead of 1 cm) and the end-plug design. The nominal value of the applied high voltage for the SST tubes is 2.2 kV instead of 1.8 kV for the NA62 ones. Higher applied HV in the SST straw tubes compensates the differences in the electric field inside the tubes due to different dimensions comparing to the NA62 tubes. The electric field  $E$  distributions vs. the distance to the wire  $r$  are shown in Figure 1.7 for both the NA62 and SHiP SST tubes for the nominal operating voltages and for an ideally centered wire. The requirement for the SST vacuum vessel pressure  $p$  is few orders of magnitude lower ( $p < 10^{-2}$  bar) than for the NA62 vacuum, thus, relaxing the requirements on vacuum leaks and permeation, when compared to NA62. The main challenges for the SST design arise from the mechanical engineering viewpoint. The straw tubes are made of light organic material, which is a subject to sagging under its own weight and creep under the loads (see Section 2.1). Three competitive SST designs are proposed to address these mechanical issues [32, 33] (the note

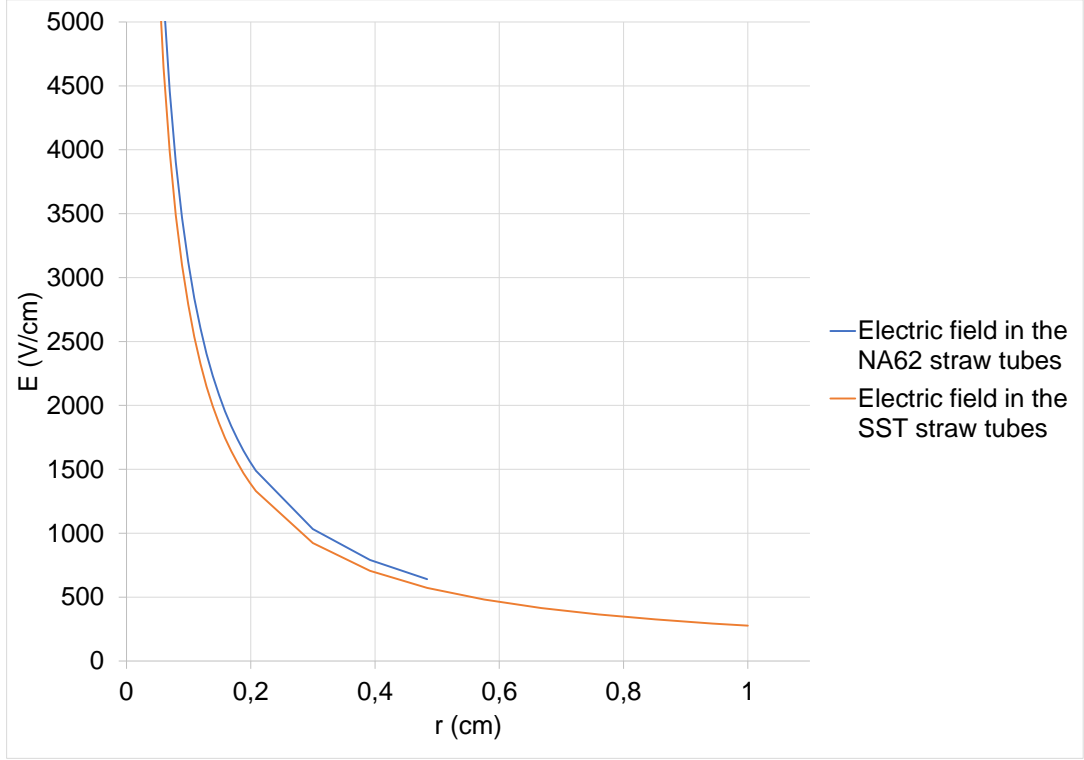


Figure 1.7: The electric field distribution for SST straw tubes (2 cm diameter, orange line) and the NA62 straw tubes (1 cm diameter, blue line) along the radius of the tubes for an ideally centered wire.

on the third design of the SST is in progress [34]). A decision on the final mechanical design is yet to be taken. More comprehensive prototype development and simulation studies should be provided for the engineering design reviews in the coming months.

Currently, only a single straw tubes layout option (the one corresponding to [32]) is implemented in the FairShip framework. The straw tubes and the wires are perfectly aligned in the simulated SST geometry with respect to the layout parameters described earlier. The first trials to simulate the misalignment of the tubes and the wires due to the sagging are shown in Section 4.2. The isochrone relation  $r(t)$  for the straw tubes is set to be linear in FairShip by default. This is a simplification, because according to the test beam results described in Chapter 3 the isochrone relation is non-linear. The attempts to implement the non-linear isochrone relation into the digitization procedure of the FairShip were taken in [35]. Such implementation can be integrated in future when more testing is performed.

To study the efficiency of the SST three track pattern recognition methods were implemented in FairShip [36]. The investigations on their recognition efficiency for the signal events and the muon background (see Section 4.3) are ongoing.

### 1.3 A straw tube as a detector of ionizing radiation

The straw tube is a gaseous detector working in proportional operation mode. It has cylindrical shape with the wire tensioned along the cylinder axis. A picture of a straw tube is shown in Figure 1.8. The straw tubes are filled with Ar/CO<sub>2</sub> gas mixture in 70%/30% proportion. The operational pressure is 1 bar absolute, which means also 1 bar overpressure in the SHiP experiment as the tubes will be installed inside the vacuum vessel. The nominal HV value applied during operation is 2.2 kV, which results in a gas gain for a given pressure and gas mixture in the range of 10<sup>4</sup>–10<sup>5</sup>. The main purpose of the straw tube is to detect charged particles passing through it (mainly muons and pions) with a time delay correlated to the minimal distance between the wire and the trajectory of the passing particle (see Figure 1.9). When a charged particle penetrates the tube, it creates the electron-ion pairs from the atoms and molecules of the gas along its trajectory. The mean energy that a particle loses in the gas volume along its trajectory is calculated with Bethe formula [37]:

$$\left\langle -\frac{dE}{dx} \right\rangle = K z^2 \frac{Z}{A} \frac{1}{\beta^2} \left[ \frac{1}{2} \ln \frac{2m_e c^2 \beta^2 \gamma^2 W_{max}}{I^2} - \beta^2 - \frac{\delta(\beta\gamma)}{2} \right], \quad (1.1)$$

where  $K$  is a coefficient equal to  $4\pi N_A r_e^2 m_e c^2 \approx 0.307075 \text{ MeV} \cdot \text{mol}^{-1} \cdot \text{cm}^2$ ,  $z$  is the charge number of the incident particle,  $Z/A$  is the charge number to atomic number ratio of the target material,  $W_{max}$  is the maximum energy transfer in a single collision equal to  $W_{max} = \frac{2m_e c^2 \beta^2 \gamma^2}{1+2\gamma m_e/M + (m_e/M)^2}$ , where  $M$  is the mass of the incident particle.  $I$  in the equation (1.1) is the mean excitation energy,  $\delta(\beta\gamma)$  is a function taking into account the density effect correction.

The number of primary electron-ion pairs  $n_p$  created by passing charged particle is Poisson distributed with a mean number of primary electron-ion pairs  $\tilde{n}_p$  equals to  $LN\sigma_i$ , where  $L$  is the thickness of the traversed gas segment,  $N$  is the concentration of gas and  $\sigma_i$  is the ionization cross section. Most primary electrons have enough energy to ionize and excite other atoms (within 10  $\mu\text{m}$  range on average), thus, creating ionization clusters along the particle trajectory. The total number  $n_t$  of primary and secondary electrons produced after the charged particle has traveled a certain distance  $\Delta L$  in the gas volume of the straw tube can be estimated from the mean energy loss of this particle in the gas  $\langle \frac{dE}{dx} \rangle$  calculated using equation (1.1) and the average energy  $W_I$  needed to produce an electron-ion pair in the gas:

$$n_t \approx \frac{\langle \frac{dE}{dx} \rangle \Delta L}{W_I} \quad (1.2)$$

For a minimum-ionizing particle (MIP) values of  $n_p$  and  $n_t$  for argon under NTP (normal temperature and pressure) conditions are  $n_p = 25 \text{ cm}^{-1}$  and  $n_t = 97 \text{ cm}^{-1}$ , respectively [37]. For carbon dioxide  $n_p = 35 \text{ cm}^{-1}$  and  $n_t = 100 \text{ cm}^{-1}$ . The average energy to produce the electron-ion pair  $W_I$  in argon is 26 eV, for CO<sub>2</sub> 34 eV. The probability for an electron released during the ionization process to have energy  $E$  in the wide range of energies follows a  $\sim 1/E^2$  dependence. According to [37] around 0.6% of released primary electrons



Figure 1.8: The photo of a prototype of a straw tube.

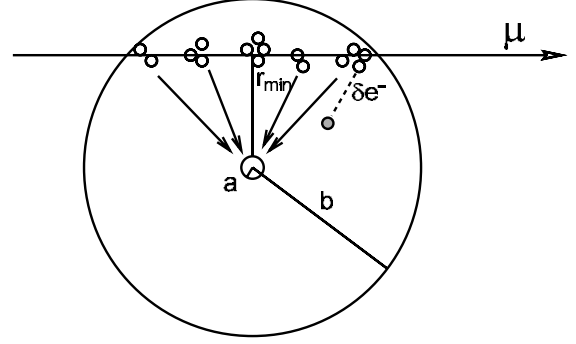


Figure 1.9: Ionization clusters created in the straw tube gas by a passing muon through the tube. The figure is taken from [38].

can have the energy above 1 keV. Such electrons can travel significant distances (*i.e.*, hundreds of microns) and ionize further the gas volume of the straw tube. They are commonly called  $\delta$ -electrons.

All electrons and ions created after the primary and the secondary ionization immediately start to drift: the electrons towards the anode, the ions to the cathode wall of the tube. The drift velocity of the electrons inside the tube depends on the properties of the gas and the electric field value:  $v = e\tau E/m_e$ , where  $\tau$  is the mean collision time in the gas. The electric field  $E$  inside the straw tube depends on the distance  $r$  from the wire. If the wire is perfectly centered, then:

$$E(r) = \frac{CV_0}{2\pi\epsilon_0} \frac{1}{r}, \quad (1.3)$$

where  $C$  is the capacitance per unit length of the tube  $C = \frac{2\pi\epsilon_0}{\ln(b/a)}$ ,  $b$  is the inner radius of the tube and  $a$  is the radius of the wire,  $V_0$  is the applied HV. As the electric field magnitude increases towards the wire, the electrons start to accelerate. At some distance from the wire  $r_{min}$  (a few micrometers for the SST straw tubes) they gain enough energy to excite and eventually ionize the atoms of the gas on their way creating an avalanche of the electrons. The number of electrons  $dN$  released per unit length  $dr$  is proportional to the total number of released electrons  $N(r)$  and the first Townsend coefficient  $\alpha(r)$ :

$$\frac{dN}{dr} = N(r)\alpha(r). \quad (1.4)$$

From the solution of the differential equation (1.4) the gas gain coefficient  $G$  can be derived:

$$G = \frac{N}{N_0} = e^{\int_a^{r_{min}} \alpha(r) dr}, \quad (1.5)$$

where  $r_{min}$  is the minimal distance to the wire, where the electron avalanche starts,  $N_0$  is the initial number of drifting electrons.

If the straw tube is filled with argon only, a few issues related to the drifting electrons and the avalanche creation arise. The first issue is related to the accelerated electrons. According to the argon-electron interactions cross sections dependence (see Figure 1.10a), the electrons with energy  $< 11.6$  eV have a large probability to undergo elastic interactions with argon and the resulting trajectory of drifting deflects significantly from the shortest distance to the wire. This introduces the fluctuations that worsen the spatial resolution of the tube. Both transverse and longitudinal diffusion in the gas are affected. According to [39] the standard deviation of the transverse diffusion for electrons per 1 cm of drift at NTP conditions in pure argon at 2.2 kV/cm electric field is  $\approx 1$  mm. Another issue is the excitation of argon atoms with drifting electrons. The argon has a variety of excited states with decay times from tens of picoseconds to hundreds of nanoseconds. The photons emitted by argon atoms can either ionize or excite another atom of the gas or extract electrons from the tube wall due to the photoelectric effect (which is mostly evident for the tracks passing in the vicinity of the tube inner wall). All these processes eventually lead to the creation of extra electrons that can create delayed avalanches in the tube and, hence, induce delayed signals in the anode wire or cause a continuous discharge in the tube, if larger HV is applied.

To address the mentioned issues, polyatomic gases (*e.g.*,  $\text{CH}_4$ ,  $\text{CO}_2$  or  $\text{CF}_4$ ) are added to the noble gas inside the straw tube. In case of the SST carbon dioxide is added to argon to reach the 70%/30% proportion at NTP conditions. The cross sections for electron- $\text{CO}_2$  interactions are shown in Figure 1.10b. The cross-sections for inducing vibrational and rotational excited states of  $\text{CO}_2$  are relatively large in the energy range 0.1–10 eV. Thus, carbon dioxide molecules can absorb photons emitted by excited argon atoms and, also, due to the large inelastic cross section, slow down electrons to the Ramsauer-Townsend minimum ( $\sim 0.5$  eV) of the argon elastic cross section (see Figure 1.10a). The drifting electrons at energies close to 0.5 eV have a significantly smaller probability to undergo the elastic interaction with argon and can reach higher and more stable drift velocities for given applied HV. Varying the fraction of  $\text{CO}_2$  in the gas mixture, one can reach the desired drift velocity for different HV values. For Ar/ $\text{CO}_2$  (70%/30%) mixtures, the drift velocity of electrons for 2.2 kV/cm electric field (at 1.2 mm from the wire) and NTP conditions reaches the plateau of  $\approx 6.5$  cm/ $\mu\text{s}$  [37].

Adding another gas and, hence, creating a mixture (in our case adding  $\text{CO}_2$ ) introduces other effects, most notably the Penning effect [41]. The argon atoms can be excited to states with energy higher than the first ionization potential of  $\text{CO}_2$  (13.8 eV). These excited atoms of argon can collide with molecules of  $\text{CO}_2$  and transfer their excitation energy leading to the release of an electron from  $\text{CO}_2$ :

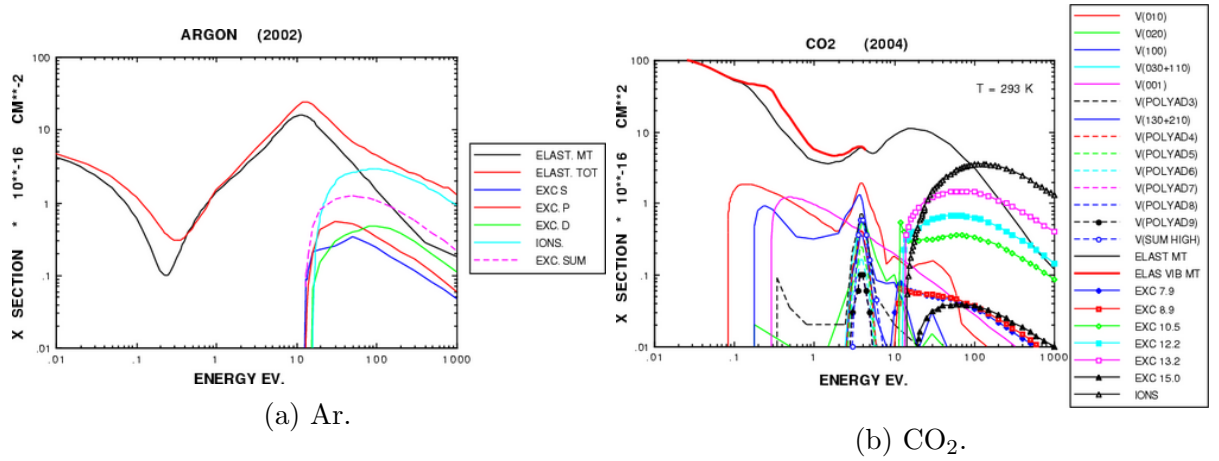
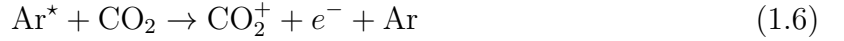


Figure 1.10: The measured cross sections of Ar and CO<sub>2</sub> gases at NTP conditions. The figures are adapted from [40].



The Penning mean collision time in Ar/CO<sub>2</sub> mixtures is of the order of a hundred picoseconds, thus, the released electrons cannot create measurable delayed signals in the straw tube. The probability of the Penning effect occurring in the 70%/30% Ar/CO<sub>2</sub> mixture at NTP conditions is 57% according to the measurements in [42]. Another possibility to release electrons from the CO<sub>2</sub> atoms is photo-ionization caused by the photons from the decay of higher excited states of argon. The decay times of higher excited states of argon (*e.g.*,  $3p^54d$ ,  $3p^55p$ ,  $3p^56s$ ) vary from 75 ns to 360 ns. The emitted photons from long-living excitation states of argon can create the coherent delayed signals in the straw tubes, which are also observed in the 2017 test beam data (see Section 3.4).

The signal in the anode wire is induced when the electrons and ions from different ionization clusters start to move apart (Ramo's theorem). However, the signal induced by a few hundreds of electrons and ions is very weak (*i.e.*, a few microvolts) and is masked within the electronics noise. The theoretical estimations of the induced signal inside the wire can be performed in the following way. The infinitesimal charge  $dq$ , which is induced in the wire due to the charges passing infinitesimal distance  $dr$  along the radius of the straw tube, can be calculated using the formula [39]:

$$dq = Q \frac{dV}{dr} dr, \quad (1.7)$$

where  $Q$  is the charge of either moving electron or ion in the tube,  $V$  is the electric potential inside the tube  $V = \frac{CV_0}{2\pi\epsilon_0} \ln(\frac{r}{b})$ , where  $C$  is the capacitance of the tube per unit length. The main contribution to the induced charge  $q^-$  due to the moving electrons in the tube is coming from the electrons released in the avalanche process. The step-by-step avalanche development is shown in Figure 1.11. The electrons released in the avalanche



move a short distance from  $r_{min}$  (*i.e.*, the distance to the starting position of an avalanche) to  $a$  and induce the following charge in the wire:

$$q^- = \frac{Q}{V_0} \int_a^{a+r_{min}} \frac{dV}{dr} dr = -\frac{QC}{2\pi\epsilon_0} \ln\left(\frac{a+r_{min}}{a}\right) \quad (1.8)$$

The ions created during the avalanche process start moving from the  $r_{min}$  to the cathode (*i.e.*, the inner conductive wall of the straw tube) at  $b$  distance from the wire. So, the contribution to the induced charge in the wire from the moving ions is:

$$q^+ = \frac{Q}{V_0} \int_{a+r_{min}}^b \frac{dV}{dr} dr = -\frac{QC}{2\pi\epsilon_0} \ln\left(\frac{b}{a+r_{min}}\right) \quad (1.9)$$

The ratio between the total induced charge contributions  $q^-$  from electrons and  $q^+$  from ions can be calculated using relations (1.8) and (1.9):

$$\frac{q^-}{q^+} = \frac{\ln(a+r_{min}) - \ln(a)}{\ln(b) - \ln(a+r_{min})} \quad (1.10)$$

Substituting  $a$ ,  $b$  and  $r_{min}$  from the equation (1.10) with the real SST straw tube values  $a = 0.015$  mm,  $b = 9.92$  mm and  $r_{min} = 1$   $\mu$ m, the one can obtain  $\frac{q^-}{q^+} \approx 0.01$ . This means that the total induced charge in the wire is formed mainly by the ions, but the fast leading edge time of a few nanoseconds is provided by the short electrons induced signal. The electrons from other clusters created along the trajectory of passing charged particle create subsequent peaks in the induced signal on top of the ion tail. The length of the induced signal depends on the time of travel for ions from the wire to the inner wall of the straw tube:

$$t_{max} = \frac{(b^2 - a^2) \ln(b/a)}{\mu^+ V_0}, \quad (1.11)$$

where  $\mu^+$  is the ion mobility in the gas mixture under NTP conditions. For  $\text{Ar}^+$  ions, the mobility is  $\mu_{\text{Ar}^+}^+ = 1.54 \text{ cm}^2 \text{ V}^{-1} \text{ s}^{-1}$  and for  $\text{CO}_2^+$  ions in the  $\text{Ar}/\text{CO}_2$  gas mixture  $\mu_{\text{CO}_2^+}^+ = 1.72 \text{ cm}^2 \text{ V}^{-1} \text{ s}^{-1}$ . Thus, the maximum drift time for the  $\text{Ar}^+$  ions is 1.9 ms and for  $\text{CO}_2^+$  ions 1.7 ms. In reality, the ion tail drops below the electronics background noise level after few hundreds of nanoseconds.

### 1.3.1 The effect of the distorted electric field on the wire displacement

If the wire inside the tube is displaced by the value  $d$  (*e.g.*, due to the gravitational sagging) along vertical  $Y$  axis, the potential  $V$  in the tube will be perturbed [43]:

$$V(r, \phi) = \frac{CV_0}{2\pi\epsilon_0} \ln\left(\frac{r}{b}\right) - \frac{CV_0}{2\pi\epsilon_0} \frac{dr}{b^2} \sin \phi, \quad (1.12)$$

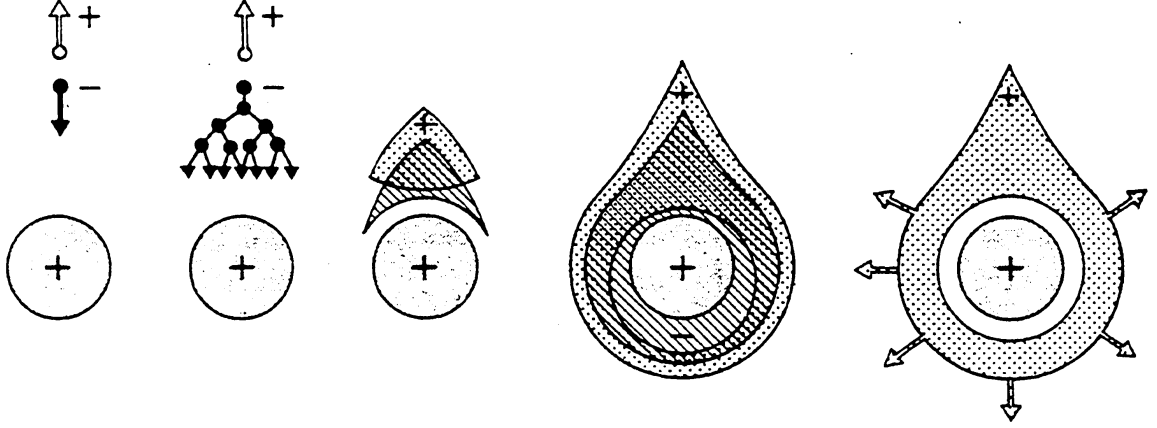


Figure 1.11: Time development of an avalanche in a straw tube. A single primary electron proceeds towards the anode, in the regions of high electric field, experiencing ionizing collisions; due to the lateral diffusion, a drop-like avalanche, surrounding the wire, develops. Electrons are collected in a very short time ( $\sim 1$  ns) and a cloud of positive ions is left, slowly migrating towards the cathode. The figure is adapted from [39].

where  $\phi$  is the polar angle changing from 0 to  $2\pi$  in the cross section plane inside the tube,  $C$  is the capacitance of the straw tube per unit length:  $C = \frac{2\pi\epsilon_0}{\ln(b/a)}$ . Thus, the total electric field perturbed due to the wire displacement is equal to:

$$E(r, \phi) = -\frac{\partial V}{\partial r} - \frac{\partial V}{r\partial\phi} \quad (1.13)$$

Taking into account the conversion from cylindrical coordinates to Cartesian ones,  $y = r \sin(\phi)$ , the perturbed part of  $E(r, \phi)$  acts only along  $y$  axis with the opposite sign. The value of the perturbed part of  $E(r, \phi)$  can be easily calculated:

$$E_p(y) = -\frac{CV_0}{2\pi\epsilon_0} \frac{d}{b^2} \quad (1.14)$$

The electric force pulling the displaced wire per unit length in the same direction as the gravitational one is equal to:

$$F_{el} = \frac{(CV_0)^2}{2\pi\epsilon_0} \frac{d}{b^2} \quad (1.15)$$

The gravitational force acting on the wire per unit length is:

$$F_g = \rho g A = \rho g \pi a^2, \quad (1.16)$$

where  $\rho$  is the density of the wire,  $g$  is the gravitational constant and  $A$  is the area of the wire cross section. According to the calculations from the textbook [43], the magnitude of the wire sagging due to the gravitational force is equal to:

$$s = \frac{\rho g A L^2}{8T}, \quad (1.17)$$

where  $L$  is the length of the tube,  $T$  is the wire tension. Inserting the values corresponding to the SST straw tubes ( $L = 5$  m,  $a = 15$   $\mu$ m,  $b = 9.92$  mm,  $T = 1$  N,  $\rho = 19.22$  g/cm<sup>3</sup>) the one can obtain the maximum sagging magnitude  $s = 0.42$  mm. The contribution from the perturbed electric field will further amplify the sagging magnitude of the wire. The total magnitude of wire sagging with both extra electrical and gravitational forces applied is equal to:

$$s_k = \frac{C_g}{k^2} \left( \frac{1}{\cos(kL/2)} - 1 \right), \quad (1.18)$$

where  $C_g = \rho g A / T$ ,  $k = \sqrt{\frac{2\pi\epsilon_0}{T}} E(b)$ .  $E(b)$  is the value of the electric field in the straw tube, when the wire is perfectly centered (see equation (1.3)). For the straw tubes used in the SST,  $V_0 = 2.2$  kV,  $C = 8.57$  pF/m,  $C_g = 1.33 \cdot 10^{-4}$  m<sup>-1</sup>,  $k = 0.25$  m<sup>-2</sup> and the maximum sagging magnitude  $s_k = 0.5$  mm. The extra electrical force amplified the maximum magnitude of the gravitational sagging of the wire by 19%.

### 1.3.2 The detection of photons and electrons with the straw tube

The electrons and positrons can ionize the gas inside the straw tube when they pass through the tube, like the heavier charged particles (muons, pions and other mesons) described in the beginning of the Section 1.3. However, their mean energy loss due to the ionization deviates from the Bethe formula (1.1). During the process of the gas ionization, the impinging electrons interact with the atomic electrons, which are identical to the impinging electrons, meaning that the maximum energy transfer in a single collision can reach the half of the kinetic energy of the incoming electron:  $W_{max} = m_e c^2 (\gamma - 1) / 2$ . The effects related to a spin and a charge of incoming particle also introduce the corrections to the mean energy loss. For electrons, the large energy transfers to the atomic electrons are described by the Møller cross section. The formula for the mean energy loss of electrons in the matter is the first moment of this cross section [37]:

$$\left\langle -\frac{dE}{dx} \right\rangle = \frac{1}{2} K z^2 \frac{Z}{A} \frac{1}{\beta^2} \left[ \ln \frac{2m_e c^2 \beta^2 \gamma^2 (m_e c^2 (\gamma - 1) / 2)}{I^2} + 1 - \beta^2 - \frac{2\gamma - 1}{\gamma^2} \ln 2 + \frac{1}{8} \left( \frac{\gamma - 1}{\gamma} \right)^2 - \delta \right], \quad (1.19)$$

The positrons-electrons interaction is described by the Bhabha cross section. The interacting particles are not identical, so  $W_{max} = m_e c^2 (\gamma - 1)$ . The first moment of the

Bhabha cross section provides the mean energy loss during the collision of positrons and electrons [37]:

$$\left\langle -\frac{dE}{dx} \right\rangle = \frac{1}{2} K z^2 \frac{Z}{A} \frac{1}{\beta^2} \left[ \ln \frac{2m_e c^2 \beta^2 \gamma^2 (m_e c^2 (\gamma - 1))}{I^2} + 2 \ln 2 - \frac{\beta^2}{12} \cdot \left( 23 + \frac{14}{\gamma + 1} + \frac{10}{(\gamma + 1)^2} + \frac{4}{(\gamma + 1)^3} \right) - \delta \right], \quad (1.20)$$

However, the electrons and positrons that have the energy larger than the critical energy for the material, which they penetrate through, lose their energy mostly by bremsstrahlung. During this process, the emitted high-energy photons lose their energy mainly via the  $e^+$ ,  $e^-$  pairs production. The critical energy for Ar is 38.03 MeV for  $e^-$  and 37.06 MeV for  $e^+$ , for CO<sub>2</sub>– 86.17 MeV for  $e^-$  and 84.25 MeV for  $e^+$  according to [37]. The total stopping power of electrons in the Ar/CO<sub>2</sub> 70%/30% gas mixture is shown in Figure 1.13.

In Chapter 2 the DAQ system tests with the real prototype of a straw tube are described. As a source of charged particles for the measurement  $^{90}\text{Sr}$  was used. It is a pure  $\beta^-$  radioactive source emitting electrons with a maximum energy of 2280.1 keV and an average energy of  $\approx 900$  keV according to [44]. The electrons in the mentioned energy range are MIPs and lose their energy mainly through the collisions and their mean energy lost  $\langle dE/dx \rangle$  in the gas mixture is equal to  $1.5 \text{ MeV} \cdot \text{cm}^2/\text{g}$ . The total number of electrons released in the ionization clusters in the given gas mixture at NTP conditions by electrons from the  $^{90}\text{Sr}$  source passing through it is  $\approx 91 \text{ cm}^{-1}$ . The trajectory of electrons inside the gas volume is not a straight line and has significant deflections. This leads to inducing longer in time signals in the anode wire than heavier charged particles do, because of larger spatial spread of ionization clusters along the electron path. Some fraction of electrons (low energetic part of a decay spectrum) cannot penetrate through the tube and are stopped within the gas volume.

The photons passing through the straw tube can undergo photo-absorption, Compton scattering or produce the  $e^+$ ,  $e^-$  pairs. The cross sections for these processes depend on the energy of the incoming photons (see Figure 1.12). Photons with the energy between 1 keV and 100 keV undergo mostly photo-absorption. For energies from 100 keV to 10 MeV, the incoherent Compton scattering is dominating the interaction cross section in Ar/CO<sub>2</sub> gas mixture used for the SST tubes. From 10 MeV and further, the pair production has the largest contribution to the total cross section (the threshold for pair production is  $\approx 1 \text{ MeV}$ ). The commonly used metric related to the interaction of photons with matter is attenuation  $\mu$ . The attenuation  $\mu$  is related to the cross section  $\sigma$  in the following way:

$$\mu = \frac{N\sigma}{\rho}, \quad (1.21)$$

where  $N$  is the concentration of the gas molecules,  $\rho$  is the density of the mixture. The mean free path of photons  $\lambda$  can be extracted from the photon attenuation  $\mu$ :

$$\lambda = \frac{1}{\mu\rho} \quad (1.22)$$

A typically used electron source for various tests of the straw tube prototypes is  $^{55}\text{Fe}$ . It emits X-ray photons of 5.9 keV and 6.5 keV [44]. The most probable way of interaction with gas molecules in the straw tube for these photons is the photo-absorption according to Figure 1.12. The released electron from the inner shells of the gas mixture atoms has enough energy to ionize the surrounding atoms and create the localized cluster of electrons. The size of such ionization cluster is larger than the mean size of the clusters created by the charged particles passing through the tube. According to [47], the mean number of electrons created in the ionization cluster after emitted from the  $^{55}\text{Fe}$  source photon interacts with atoms of the Ar/CO<sub>2</sub> 70%/30% gas mixture at NTP conditions is  $\approx 198$ , which is significantly larger than the mean number of electrons produced during the ionization of the gas mixture with charged particles. Thus, the electrons from a single ionization cluster will induce a sharp signal with a large single peak. Such signals are useful for attenuation and gain measurements. The attenuation measurement of a straw tube prototype is described in Section 2.2.2. The photons with larger energies, for example, 660 keV from the Cs<sup>137</sup> radioactive source [44] can undergo Compton scattering a few times inside the tube and escape creating a few distant ionization clusters, which induce a signal with a few peaks, but the overall shape of the collected signal from the wire of the straw tube becomes more stochastic.

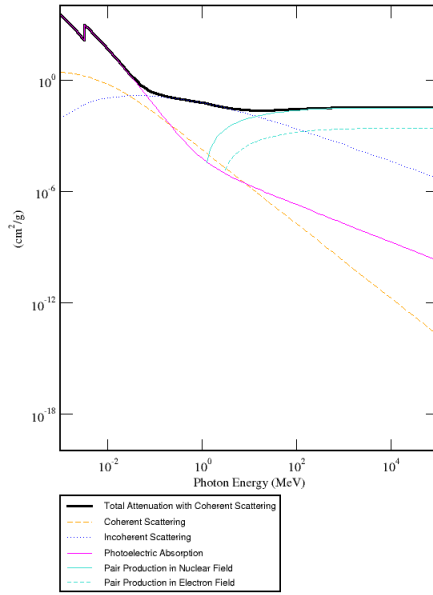


Figure 1.12: The total attenuation of the photons in the Ar/CO<sub>2</sub> (70%/30%) gas mixture at NTP conditions. The contribution from each process is shown with dashed lines of different colors. The data is obtained from [45].

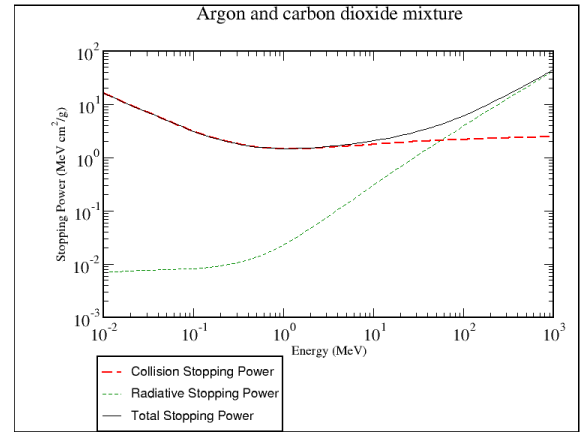


Figure 1.13: The stopping power for electrons passing through the Ar/CO<sub>2</sub> (70%/30%) gas mixture at NTP conditions. The contribution from collision and radiative stopping power is shown with dashed lines of different colors. The data is obtained from [46].

# Chapter 2

## Characteristics of the straw tubes

The performance goals for the SST are described in Section 1.2. Accomplishing of these goals brings drastic mechanical challenges in constructing straw tubes, uniting them into the detector modules and maintaining their stability over time. In this chapter some mechanical and electrical properties of straw tubes are described. The mechanical studies include the measurements of gravitational sagging of a tube under its own weight, the scanning of a shape of the fully assembled straw tube, the creep and rupture tests of the tubes. The studies of electrical properties of straw tubes are focused on signal attenuation measurement and characteristic impedance estimation. Also, two DAQ systems were tested with straw tubes prototypes (see Appendix B).

### 2.1 Mechanical properties of the tubes

As it was mentioned in the previous chapter, the straw tubes are designed to be 5 m long, 2 cm diameter and made of BoPET (Hostaphan RNK 2600 [48]) 36  $\mu\text{m}$  thin rolls welded using ultrasonic techniques along the longitudinal dimension of the tube and coated with the metalization layers on the inner surface: 50 nm of Cu and 20 nm of Au. The tubes are supposed to operate in vacuum under 1 bar absolute pressure. Each tube is closed with the plastic end-plugs, which are also supposed to hold the special crimped pin fixing the pretensioned wire inside the tube. The tube is a very fragile object and it can buckle, when it is put in horizontal position (when the tube axis is parallel to the ground) and it is not supported and pressurized. All mechanical stresses, which appear in the tube under various conditions are described in this paper [49]. The most crucial effect happening in the horizontally aligned straw tube is its sagging due to the gravitational force. One of the complications arising for the sagging problem is the fact that the tube has different maximum amplitude of sagging comparing to the wire inside (the tube bends more than the wire). This issue affects the performance of the tube: the drift time distribution becomes longer in time and, if the displacement of the wire with respect to the tube center is too large, a discharge can occur inside the tube, when operating at high voltages (2.2–2.6 kV).

In order to minimize the sagging effect and optimally arrange the tubes inside the

tracking stations, several design options were proposed. There are three competitive design options considered by the SST group. One of them is being developed in Hamburg University [33]. Its main features are special horizontal carbon fibers tensioned along the two neighboring tubes, which hold the plastic external supports glued to those neighboring tubes (so called “suspension bridge” design). These supports are supposed to minimize the sagging magnitude of the tubes.

At CERN two other design options are developed simultaneously. The first one [32] utilizes the idea of pulling the tubes to counter sagging effect instead of supporting them, which can be practically realized in a way that one side of the rectangular supporting frame with the tubes’ end-plugs attached to it can be pulled applying the sufficient force. The magnitude of the applied force should increase in time, because the BoPET under constant loads is a subject to the relaxation effect (its elastic modulus changes with time).

The third design option developed at CERN is so called “cemented pack” design. It is inspired by the design of the STT (straw tubes tracker) of PANDA experiment [50]. In this design the pressurized tubes are glued side-by-side and layer on top the previous one forming a module (see Figure 2.1). The advantage of such module is that the straw tubes after gluing start to support each other. According to the calculations [34], the pack of 8 tubes already has reduced magnitude of sagging effect being  $< 2$  mm. On the current stage of R&D all 3 possible design options are not finalized and they require further prototypes development to prove their theoretical concepts. The studies in this chapter are related to single straw tubes. The investigations on the mechanical properties of a module of tubes are planned in the future.

### 2.1.1 Sagging effect and the shape of the straw tubes

The effect of the tube sagging is of a great importance and is a crucial obstacle for the SST mechanical designs to overcome. Also, the theoretical models (see [49]) do not take into account the fact that the straw tube is not a perfect cylinder and has a welding seam along the longitudinal dimension that was created after the ultrasonic welding of



Figure 2.1: The image of 5 straw tubes glued together à la PANDA STT design [50].



the BoPET roll. To study the influence of the seam on the sagging magnitude of the horizontally installed tube, the experimental measurements were performed<sup>1</sup>. The detailed report about the measurement can be found here [51]. In what follows, the obtained results are discussed and the conclusions are made.

The straw tube was installed horizontally on V-shaped metal supports (see Figure 2.2). It was closed from the ends with specially designed reusable end-plugs. These end-plugs are made of metal with the flanges for the gas connection. The important note about the end-plugs is that their mass is much larger than the mass of the tube. So, their positioning on the V-shaped supports can influence the sagging behavior of the tube. In order to minimize their influence, the end-plugs were always positioned in a way that the center of their mass (the balance point) is located at the edge of the V-shaped support. Depending on the pressure value inside the tube the position of the V-shaped supports was adjusted to fulfill the balance point location condition (the tube elongates, when the pressure inside increases and the metal end-plugs should be shifted). Leica NA2 optical levels [52] were used to measure the positions of the edges of the 2.40 m tube and the position of the middle point located at 1.175 m distance from the V-shaped supports. Additionally, the two reference points on the opposite walls of the room were measured to control the possible systematic shifts occurring during the measurement. The measurement plan was to fill the tube with compressed air at 1220 mbar, measure the position of 5 points mentioned previously and calculate the sagging magnitude of the tube. In order to check, if the seam position has any effect on the sagging magnitude, those points were measured 4 times for different seam positions with respect to the laboratory environment: on top of the tube (facing the ceiling), rotated by 90° (facing the doors), on the bottom of the tube (facing the floor) and rotated by 270° (facing the windows). The reference point and two straw tube positions are shown in Figure 2.2.

The results of the sagging magnitude measurements of the straw tube are shown in Table 2.1. The tube was not pretensioned, the only possible tension source could be the traction between the V-shaped supports and the metal end-plugs. This traction couldn't be measured precisely, also the slightest deviation from the balance position of the end-plugs could lead to sizable changes in the measured absolute values of the tube maximum sagging magnitude. The instrumental precision achieved by the optical levels for the vertical measurement is 0.1 mm at  $2\sigma$  significance level. The most important values derived from Table 2.1 are the relative differences between the displacement values of various seam positions. It is clearly seen that the existence of the welding seam brings the asymmetry to the results, especially when the tube is turned the seam side to the top (facing the ceiling). This means that the welding seam has a larger elastic modulus than the rest of the tube and, thus, the entire tube has smaller strain in the longitudinal dimension, when the tube is positioned in a way that the seam is on top. So, the welding seam can help to counter sagging effect, when the straw tube is positioned with the seam on top (opposite side to the direction of the gravitational force). However, there is no any measured data concerning the reliability of such orientation over the time (*i.e.*, how the

---

<sup>1</sup>The help of Dirk Mergelkuhl (CERN, EN-SMM) and Vitali Batusov (CERN, EP-UAT) is highly appreciated

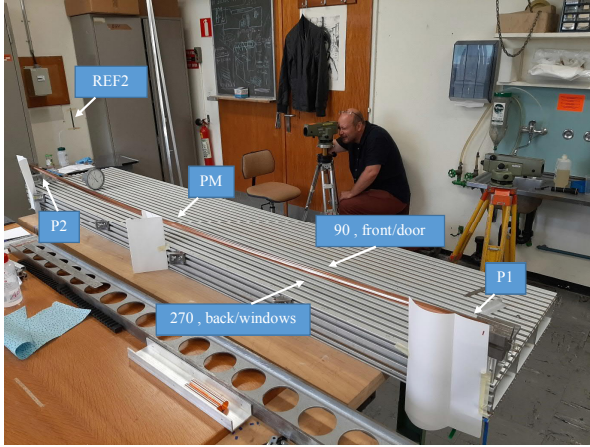


Figure 2.2: The photo of the arrangement of the instruments, the positioning of the straw tube, the location of temporary reference point “REF2” and view points of the tube. The figure is adapted from [51].

Table 2.1: Vertical displacements of a center point “PM” to the reference line “P1–P2”. The table is adapted from [51].

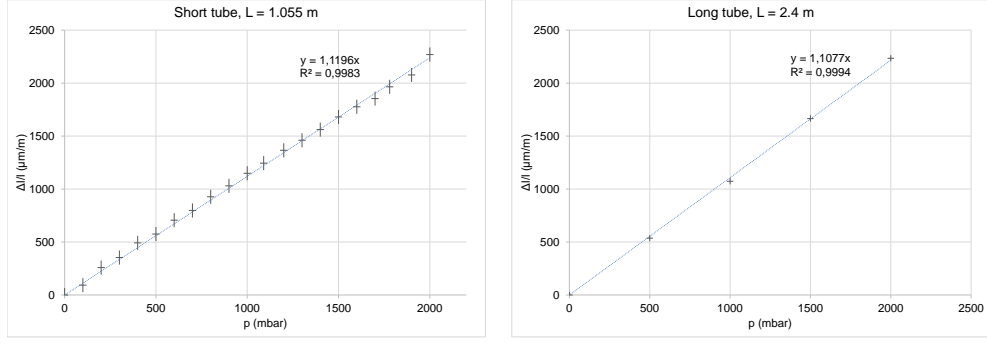
Position of the seam w.r.t. the lab environment	Displacement (m)
Seam on Top ( $0^\circ$ )	0.03129
Seam on Front/Door ( $90^\circ$ )	0.03312
Seam on Bottom ( $180^\circ$ )	0.03387
Seam on Back/Windows ( $270^\circ$ )	0.03301

welding seam can handle continuous load over long periods of time).

Other important effects occurring in the tube under the internal gas pressure are the elongation of the tube and the hoop effect. The theoretical model describing both effects is elaborated in this document [49]. In order to check the validity of the model, the uncoated straw tubes (transparent tubes without the metalization) were used for the laboratory tests (carried out in the laboratory 15/1-006 at CERN). Three specimens of different length were chosen: the tube 1 (1.055 m), the tube 2 (2.40 m) and the tube 3 (0.97 m). Each tube was closed with metal end-plugs (they were used earlier for the sagging effect measurements). One of the end-plugs was fixed to the laboratory table, the other one was left freely sliding on the table. The tubes were connected to a gas bottle with compressed air inside. The pressure values inside the tubes were measured with two types of pressure gauges: a class 1 accuracy gauge with 0–2000 mbar overpressure range and a class 2.5 accuracy gauge with 0–6 bar overpressure range. The relative elongation  $\Delta l$  was measured with a calibrated Dino-Lite digital microscope (model AM7515MZTL-Edge [53]) and its proprietary software with the precision of 0.07 mm. The results of the elongation measurements are shown in Figure 2.3. The elongation of the tubes increases linearly with the pressure until  $\approx 2$  bar. After a 2 bar overpressure value, the tubes’ response becomes non-linear and permanent deformation appears.

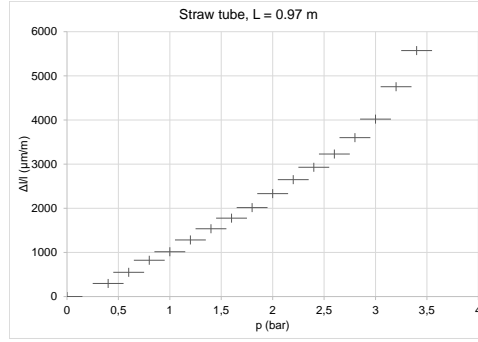
During the elongation measurement, it was observed that the tube experiences axial torque<sup>2</sup> with the increasing pressure inside. The relative rotation angle of tube 3 was measured (see Figure 2.5). The behavior of the relative angle *vs.* the pressure dependence is similar to the elongation (see Figure 2.3). It is linear up to  $\approx 2$  bar too. The theoretical

<sup>2</sup>It was at first observed by Temur Enik from Dubna (Russia), but was not documented.



(a) Tube 1,  $L = 1.055$  m.

(b) Tube 2,  $L = 2.40$  m.



(c) Tube 3,  $L = 0.97$  m.

Figure 2.3: The strain  $\Delta l/l$  vs. the internal overpressure  $p$  measurements for 3 different uncoated (transparent) straw tubes.

model of the tube [49] does not predict and explain the axial torque appearing in the tube under the internal overpressure, because it was elaborated without taking into account any anisotropy of the tube material. The similarity of the two plots mentioned earlier can point to the material features, which could cause extra torque applied on the tube under the load. Indeed, the BoPET is not an isotropic material due to the manufacturing techniques used to produce it. So, the behavior of the tube under the stress can depend on the molecular orientation inside the material and the direction of the applied forces to it.

The measured elongation of the straw tubes allows to find the elastic modulus of the tubes and crosscheck the obtained value with the one from the data sheet provided by the manufacturer [48]. According to the model of the tube described in [49] the elastic modulus  $E$  can be calculated using the formula:

$$E = (\sigma_l - \nu\sigma_h)/\epsilon_l \quad (2.1)$$

where  $\sigma_l$  is a longitudinal stress and it is equal to  $\sigma_l = pb/2t$ , where  $p$  is the gas pressure inside the tube,  $b$  is the radius of the tube (10 mm),  $t$  is the wall thickness (0.036 mm);  $\nu$  is the Poisson coefficient equal to 0.34 for PET,  $\sigma_h$  is the hoop stress and it is equal to  $\sigma_h = pb/t$  for the case of the tube with a thin wall comparing to its diameter size (the

condition is fulfilled in our case). The calculated elastic modulus *vs.* different pressure values is shown in Figure 2.4. According to the plot, the measured experimentally elastic modulus value converges within the errors to the data sheet [48] value of 4.5 GPa in the machine direction for the overpressure up to  $\approx 2$  bar. After achieving an overpressure of 2 bar, the deformation of the tube becomes plastic, which can be observed from the plot (the elastic modulus decreases) in Figure 2.4. The data for the tube 3 has large uncertainties for the small values of pressure, because of the precision of the pressure gauge used (a class 2.5 with 6 bar limit instead of a class 1 with 2 bar measurement limit). Other tubes were measured with more precise pressure gauge (a class 1 with 2 bar limit), so their uncertainties are smaller and the data for the small pressure values ( $< 1$  bar) has smaller discrepancy with respect to the value from the data sheet [48] of 4.5 GPa.

According to equation (2.1) the stress induced in the tube due to the hoop effect has a significant contribution to the total stress in the tube walls caused by the internal gas pressure. The increase of the hoop stress leads to increase of the circumferential strain, which causes the increase of the tube diameter. In order to study the change of the diameter of the tube along its length because of the hoop stress, another laboratory test was performed. One of the most precise ways to study the shape of the tube as a whole is a laser scanning technique<sup>3</sup>. This technique allows to scan the surface with laser profiles and create the cloud of points in the places, where the laser profiles are reflected from the surface of the tube. The scanning tool, Leica Absolute Scanner (LAS) with Leica tracker AT960 [54], is capable to create the points on the surface of the tube with 50–100  $\mu\text{m}$  precision (it varies because of the high reflectivity of the tube's surface). The plan of the

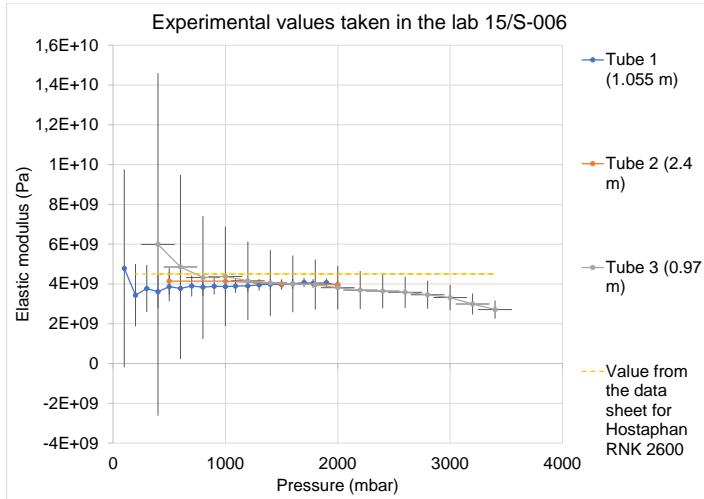


Figure 2.4: The elastic modulus of the tubes *vs.* the internal overpressure values. The data sheet [48] value is shown with a yellow dashed line (4.5 GPa).

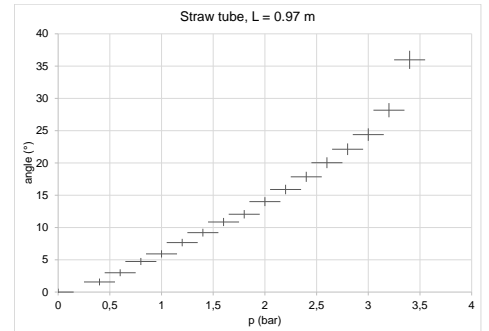


Figure 2.5: The relative rotation angle in degrees *vs.* the overpressure values for the tube 3.

<sup>3</sup>The help of our colleagues from EN-SMM department (CERN), Dirk Mergelkuhl and Kostantinos Nikolitsas, is highly appreciated.

measurement was to scan the fully assembled (with the tensioned wire inside) metalized tube, which is hanging vertically fixed at one end in the top (see Figure 2.6). The top end of the tube was firmly fixed with the clamp, the bottom end was very gently supported with a steel block in order to prevent microscopical movements of the tube during the scanning because of the weak air flows in the laboratory room. The tube was connected to the gas system through the top end-plug and it was possible to vary the air pressure inside. The tube was scanned 3 times for the selected overpressure values: 840 mbar, 1040 mbar and 1280 mbar. The tube was scanned manually using Leica Absolute Scanner (LAS) in his hand, so the density of the cloud of points is not uniform and fluctuates along the length of the tube. The report on the measurement can be found in [55] The local coordinate system, which was used as a reference for the point clouds, was defined in the following way [55] (see Figure 2.7):

- Origin: the upper base center of the nearest slice to the supporting clamp (at the top end of the tube).
- $X$ -axis: horizontal and roughly passing from the middle of the gap of the supporting clamp.
- $Y$ -axis: horizontal and perpendicular to the  $X$ -axis in a right handed Cartesian coordinate system.
- $Z$ -axis: perpendicular to the  $XY$ -plane positive to the top (vertical).

The result of each laser scanning for different pressure values is a cloud of points (points with  $X$ ,  $Y$ ,  $Z$  coordinates) containing approximately 15 million points. Such large data sample cannot be analyzed within adequate CPU time, so an additional treatment on the raw data was applied. 90% percent of the points were randomly removed from the raw data leaving 1.5 million points. The data was also segmented into 237 slices, each slice is 1 cm long in  $Z$  direction. The slices were also cleaned from so called “spikes” – the artifacts of the scanning (the outliers located further than 1 mm from the tube’s surface). The data samples after the initial treatment are ready for further processing. Each slice was fitted using the tools of special PYTHON package: `cylinder_fitting` [56]. The fitting methods in this package were developed according to this paper [57]. The slices were fitted with the cylinders of 1 cm length. The results of the fits are the arrays containing the coordinates of the centers of the cylinders, the radii of the fitted cylinders, the directions of the cylinders’ axes and the fitting errors (so called G-function). The dependencies of the fitting results *vs.* the length of the tube are shown in Figure 2.8 and in Figure 2.9.

The variation of the radius of the tube for different pressure values shown in Figure 2.8 is within 0–3.5% range from the nominal 10 mm. The behavior trend of the absolute deviations of the estimated radius from the nominal value is close to the parabolic shape having a maximum in the middle of the tube. During the scanning of the tube for 840 mbar overpressure value, the tube was accidentally displaced and it affected the final scanning result reflected in the radius estimation. The last 40 slices with the cloud points for 840 mbar overpressure value were not analyzed, because they contained spoiled data.

In Figure 2.9 the coordinates of the centers of the fitted cylinders depending on  $Z$  coordinate are shown. From Figure 2.9 (a) and (b), it is clearly seen that there is a certain offset in  $XZ$ -plane of  $\approx 27\text{--}30\text{ mm}$  and in  $YZ$ -plane of  $\approx 6\text{--}8\text{ mm}$ . These offsets are caused not due to the mechanical properties of the straw tube itself, but by the clamp, which was holding the tube at the top. The alignment of this clamp was roughly performed after the tube was attached to it, but the precise vertical positioning of the tube was not guaranteed. Another fact arising from the Figure 2.9 (a) and (b) is that the position of the fitted cylinder centers changes non-linearly along  $Z$  axis. The dashed lines in the plots are the lines connecting the first and the last data points. They were used to calculate the residuals between the points along the dashed lines and the measured data. The residuals are shown in Figure 2.9 (c) and (d). The one can observe from the plots that the tube bends more for greater overpressure values. This fact can be related to the difference in longitudinal stiffness of the welding seam on the tube's surface and the straw tube itself. This was also observed during the straw tube sagging measurements (see Table 2.1). The last plot obtained during the analysis of the shape of the straw tube is the RMS of the distances (RMSD) between the data points and the fitted cylinders axes within the tube slices (see Figure 2.10). This plot shows how the measurement precision is getting worse, when the tube is scanned from the top to the bottom. This happens, because of the small air turbulences occurring around the tube during the scanning. The tube is very light (a few milligrams) and even very weak air flows from the movement of the hand with

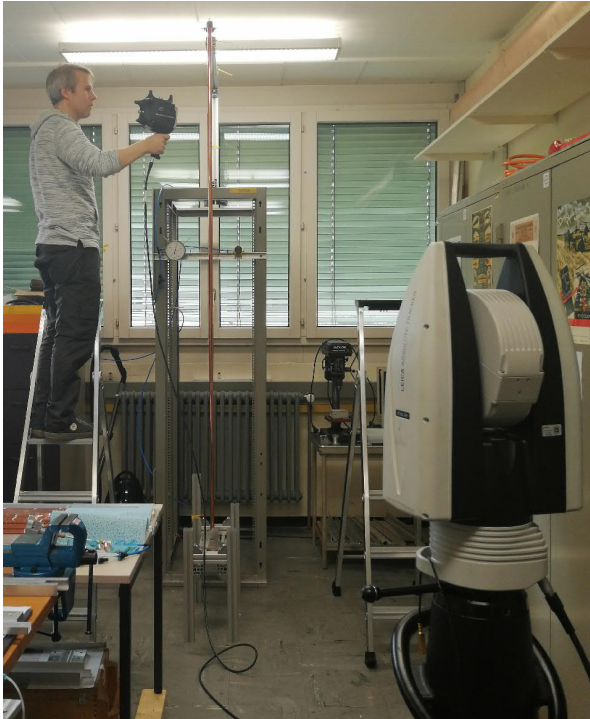


Figure 2.6: The process of laser scanning in the laboratory. The photo is taken from [55].

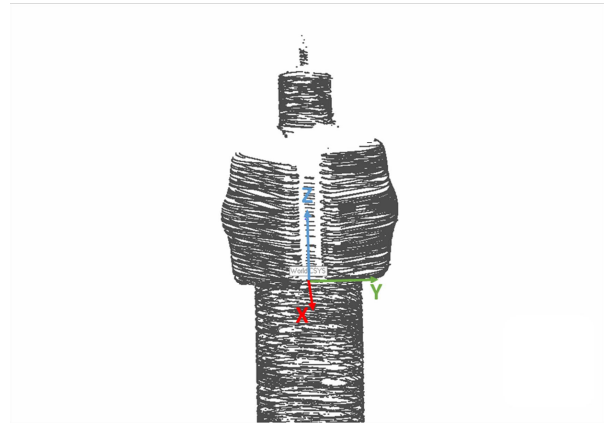


Figure 2.7: The coordinate system defined during the measurement. The figure is adapted from [55].

a scanner can influence the result, which is clearly seen on the plot. The RMSD gets better at the bottom of the tube (large  $Z$  values), because the tube, as it was mentioned earlier, was gently supported by the metal block in the bottom in order to suppress the accidental movements of the tube during the laser scanning and prevent evolving of the tube oscillation around the fixed top point.

### 2.1.2 Creep and rupture tests

As the straw tubes are going to operate in the vacuum chambers, they have to withstand the internal gas overpressure of 1 bar for the required operational time (up to few years

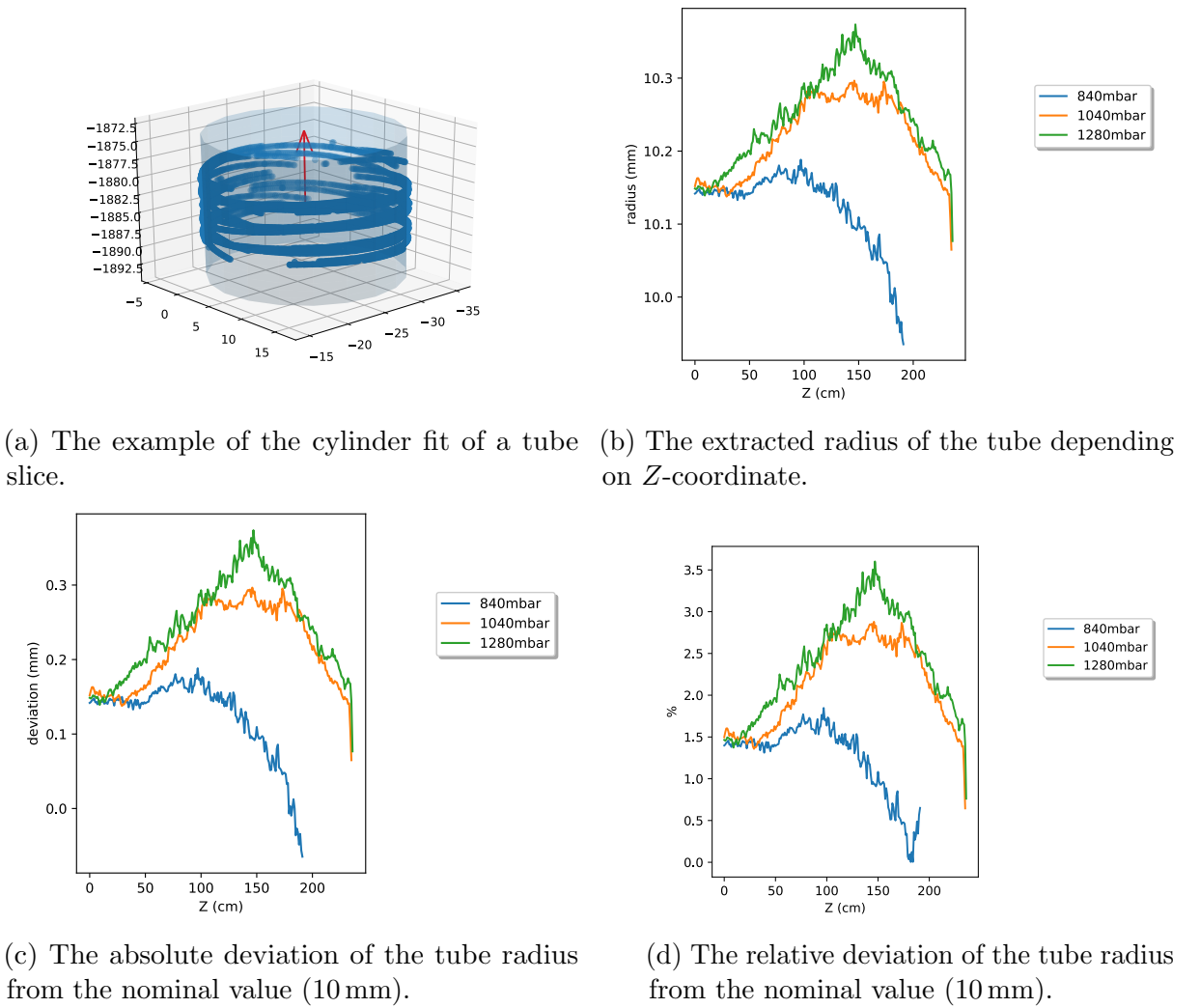
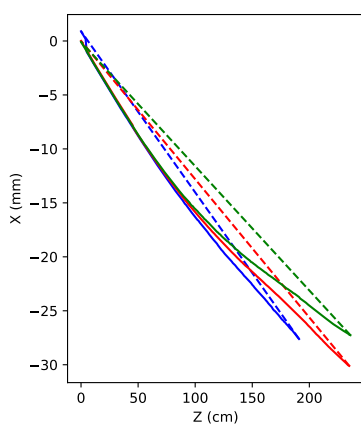


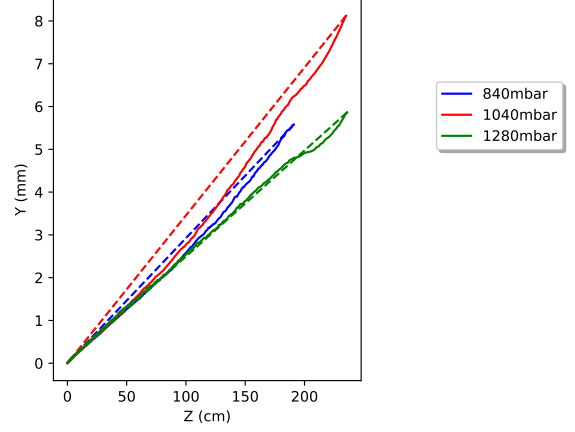
Figure 2.8: The results of the analysis of the measured cloud points with the laser scanning of the straw tube.  $Z$  dependence of the radii of the fitted cylinders in the tube slices is shown alongside the calculated uncertainties.



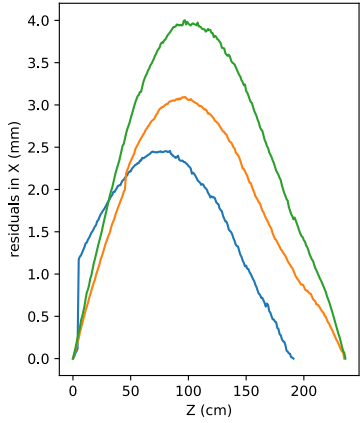
in a row). This means that they will stay under constant stress for years. The elastic modulus of the straw tube walls (made of BoPET) is not stable over the time under the load. According to theoretical calculations [49], due to the effect of material relaxation over the time of 10 years, the elastic modulus of the tube wall will decrease by more than a half to  $\approx 2.1$  GPa. This happens because the polymers (plastics) are creeping under a constant load. Their strain increases with time to a certain extent, which depends on the type of material, the magnitude of the load, the temperature of the environment and the



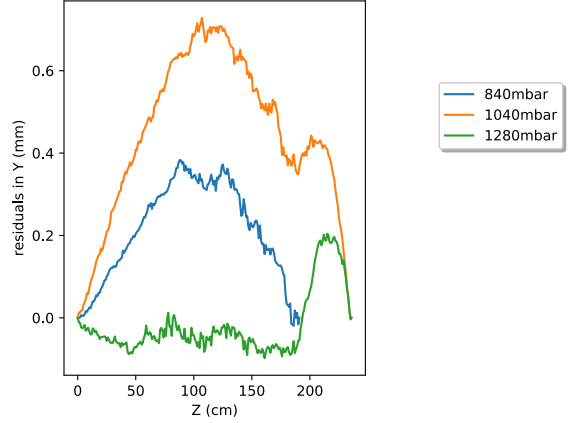
(a) The  $X$  coordinates of the centers of the fitted cylinders per slice.



(b) The  $Y$  coordinates of the centers of the fitted cylinders per slice.



(c) The differences between the points located on the line going through the first and the last data point in  $XZ$ -plane and the measured data points.



(d) The differences between the points located on the line going through the first and the last data point in  $YZ$ -plane and the measured data points.

Figure 2.9: The results of the analysis of the measured cloud points with the laser scanning of the straw tube. The coordinates of the centers of the fitted cylinders in the tube slices and their residuals are shown.



time duration of the applied load. As soon as the load is released the creep process stops, the polymer immediately recovers the elastic deformation up to the elastic limit, but the permanent deformation to its shape remains, if the material was deformed plasticly. If hypothetically the load stress would have stayed applied for infinite amount of time, the polymer eventually ruptured. So, in order to be sure that the straw tubes of the SST will operate under the safe mechanical stress conditions and will have enough safety margin, the creep and rupture tests were performed<sup>4</sup>. The detailed report on the measurement can be found in [58].

Some tubes prepared for the rupture tests were covered with the stripes of cyanoacrylate glue on their surface (not on the welding seam). The straw tubes with the stripes of cyanoacrylate were prepared to check how the glue can affect the stresses induced in the walls of the tubes. This particular glue was chosen, because it is commonly used to attach the neighboring tubes to each other like in “cemented pack” SST design [50]. In the laboratory 15/S-006 at CERN a prototype of a module with 5 straw tubes glued together with cyanoacrylate was produced (see Figure 2.1). During the assembly of the module, the tubes were glued at 1 bar overpressure. The module was kept under this pressure value for several weeks. One day, the overpressure was accidentally increased to 1.7 bar of overpressure and after staying approximately 12 hours at this pressure value the module exploded. The exact reasons of the accident are unknown. One hypothesis suggests that the rupture happened at such small overpressure value, because of additional stresses occurring in the module along the lines of cyanoacrylate glue that fixes neighboring tubes together. To check this hypothesis, the rupture and creep tests were performed with

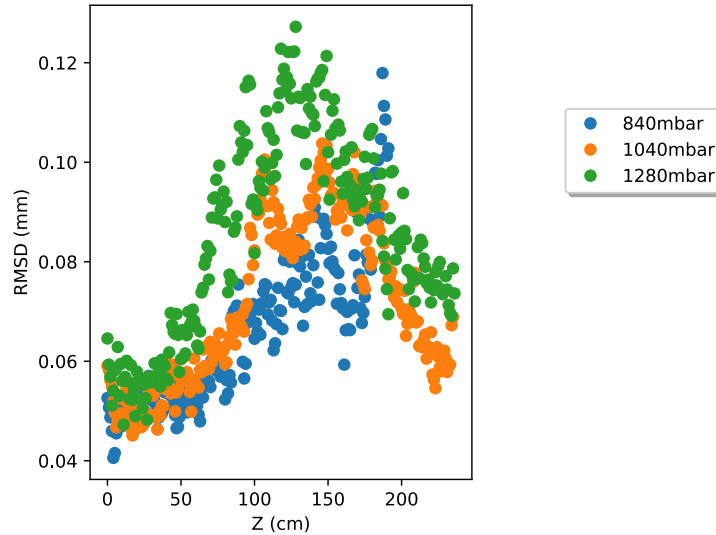


Figure 2.10: The RMS of the distances between the data points and the fitted cylinders axes inside the tube slices (RMSD).

<sup>4</sup>The help of our colleagues from EN-MME department at CERN by Antonio Carvalhosa and Óscar Sacristan de Frutos is gratefully acknowledged.

pristine tubes and with the ones that have the stripe of glue on their surface.

The following equipment was prepared to conduct the tests:

1. The transparent (without the metalization) straw tubes (10 pieces) of short length (from 10 cm to 15 cm) and 2 cm diameter. 4 straw tubes had also stripes of cyanoacrylate glue on their surface. The glue was poured on the surfaces of the tubes in a way to form the narrow stripe ( $\approx 0.5$  cm width) along the longitudinal dimension of the tube trying not to intercept the welding seam.
2. The gas pressure inside the tubes was measured with the CTE9005AQ4 pressure sensor [59]. The tubes were filled with compressed air during the test.
3. The Digital 3D Image Correlation System Q-400 [60] was used to measure the strain induced in the walls of the tubes. A photo of the experimental setup is shown in Figure 2.11.

The digital 3D image correlation system (DIC) is a powerful tool, which has various applications starting from the material testing to the high-speed dynamic measurements. This device is designed to perform a true full-field, non-contact, three-dimensional measurement of a shape, displacements and strains on components and structures made of almost any material [60]. The DIC system, which was used for the measurements of the straw tubes, consists of two cameras attached to a stand recording the tube surface from different angles. A monochromatic ambient light source (an array of red LEDs) is also attached to the stand in a way that it illuminates homogeneously the surface of the tube (see Figure 2.11). When the proper lighting conditions are established, the two cameras are adjusted to focus on the surface of the studied object. The crucial principle of the measurement is to assign the infinitesimal pieces of the object surface to the pixels in the obtained image of the object. In order to do this association correctly, the surface of the studied object should be mat and needs to have a random surface reflection pattern to achieve different intensity levels in neighboring pixels of the images and, hence, a maximum precision of the measurement. The straw tubes used for the measurement are transparent and have polished reflective surfaces, so, before the measurement they were covered with a special paint, which creates the random pattern of different shades of gray on their surfaces. Then, when the first tube is installed, the cameras needed to be calibrated with special plates at different angles in order to calculate their intrinsic parameters (a focal length, a principal point, a distortion) and their respective orientations in space to determine the reference coordinate system. The knowledge of the calibration parameters allows to create the 3-dimensional map of the recorded part of the tube's surface assigning for each pixel certain coordinates. If the points of straw tube displace from their initial position due to any influence, their new positions will be recorded immediately creating the displaced contour of the tube's surface. The correlation algorithm [60] is then applied to associate the pixel maps from the previous video frame with the current one and, thus, calculate the displacements for every pixel and their strains. In the end the temporal 3-dimensional strain map of the tube's surface is created. The analysis software installed in the host PC allows to transform the obtained map of strains into the map of principal strains:

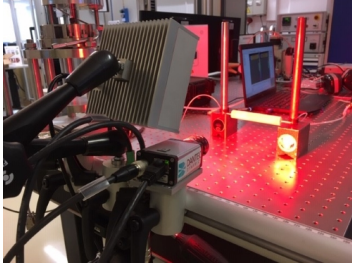


Figure 2.11: The experimental setup constructed to record the changes of the tube shape under the load. The DIC system is in front, the straw tube under study is fixed to the stands and the host PC is located behind the tube. The photo is taken from [58].

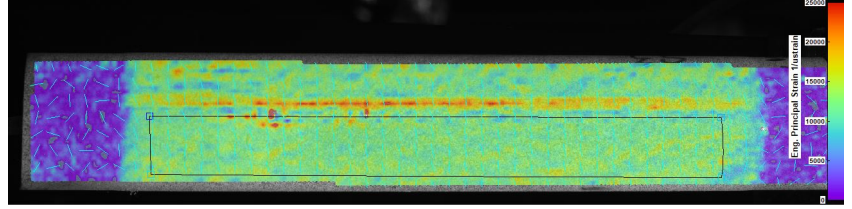


Figure 2.12: The image obtained from the DIC analysis of the straw tube under pressure. The area below the seam line (cropped with the rectangular selection) is used to calculate the mean of the principal strain. The figure is adapted from [58].

longitudinal and circumferential (hoop). The example of the principal strain map is shown in Figure 2.12. The principal strain values inside the rectangle selection are averaged and extracted. The area of the tube along the welding seam has the largest principal strain values under the load (red areas in the figures) and was not taken into account for the calculation of the average principle strain.

For the rupture tests, the measurement plan was to measure the circumferential strain (principal strain 1) induced in the tube walls for various values of gas overpressure inside the tube until the tube fails. Seven tubes were selected for the test: four tubes were in pristine conditions and three tubes had the stripe of cyanoacrylate glue. The tubes were inflated with the compressed air up to 2.5 bar at first, then deflated to 0.5 bar and inflated again until the rupture happened. The speed of the measurements was relatively high: the measurement plan for every tube was executed within maximum 8 minutes. The results of the rupture tests are presented in Table 2.2.

The pristine straw tubes failed on average at  $4.79 \pm 0.35$  bar, while the straw tubes with a glue stripe on their surface failed on average at  $4.63 \pm 0.24$  bar. The stripe of glue on the surface of the tubes did not influence significantly the overall stiffness of the tubes. The strain was smaller locally, where the glue was applied, but the contribution to the mean value of the strain over the surface of the tube was negligible. The distribution of circumferential strain of the tube with the applied glue compared to the pristine one is showed in Figure 2.13. The existence of stripes of cyanoacrylate glue on the surface of single tubes did not have any influence on the rupture behavior. The tests with a module of a few tubes glued together should be carried out in the future to investigate more on the influence of the glue. In the images from Figure 2.13 the one can observe that the tube

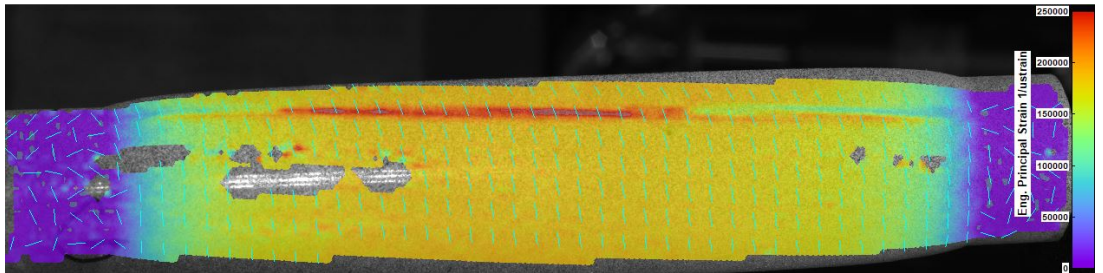
Table 2.2: The results of the rupture tests performed using the digital image correlation technique [60].

Straw tube ID	Rupture overpressure ( bar)	Principal strain 1 (%)	Remarks
Pristine tubes			
3	4.56	16.9	The tube didn't explode, but started leaking through the seam
4	4.62	18.6	
6	4.66	No data	The tube rotated after the first inflation stage (2.5 bar) and the image correlation failed
9	5.3	13.1	
Tubes with the glue			
5	4.76	17.5	
7	4.77	20	
10	4.35	14.2	The glue stripe was not strait and partially covered the welding seam

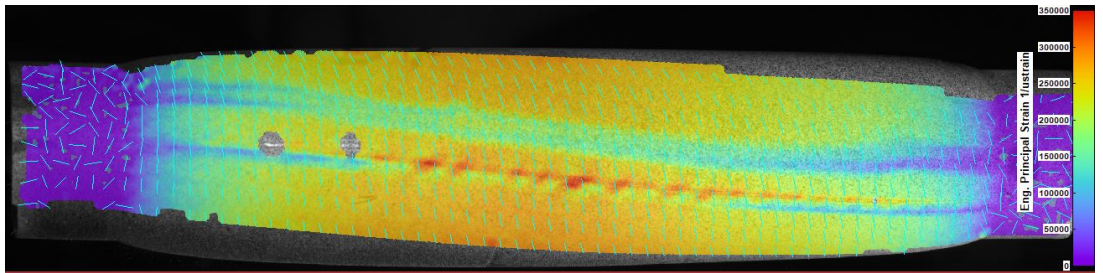
experience the rotation under the load, which was previously shown during the laboratory tests in Figure 2.5. For two straw tubes (number 4 and 7) the principle strain 2 (the longitudinal strain) *vs.* overpressure was calculated and compared to the results obtained during the laboratory tests (see Figure 2.3). The scatter plots are shown in Figure 2.14. The one can notice the systematic difference between the measurement techniques used: the distributions of points have different slopes for the two methods. In general, both measurement methods are consistent and the observed systematic discrepancy is tolerable. In Figure 2.15 the two principal strain components are shown in the same plot in order to compare their absolute values. The circumferential strain is higher than the longitudinal one meaning that the straw tube tends to form the shape of a “barrel”, when it is inflated. A few stages of creeping process can be observed in the plots in Figure 2.15: the elastic deformation (from 0 bar to 2 bar), the yielding of the material (from 3.5 bar to 4 bar) and the final plastic deformation until the rupture. The tubes didn't reach the point when the BoPET itself fails during the measurement. The weak spot of all tubes was the welding seam and they ruptured along it. This process is very fast. It takes  $\approx 0.12$  ms to tear the seam of 15 cm long straw tube and a special ultrafast camera is needed to record the process. The photos of the rupture evolution are showed in Appendix A.

For the creep test, three tubes were prepared. Two tubes (number 1 and 2) were in pristine conditions, the third one (number 8) had the stripe of cyanoacrylate glue on its surface. The tubes were fixed horizontally on top of each other (leaving a gap in between) and were recorded simultaneously using the digital image correlation system [60] (see Figure 2.16). The tubes were connected to the gas delivery manifold in parallel having always equal overpressure during the measurement. Initially, the tubes were inflated to 1 bar of overpressure and left intact for 1 hour, then they were inflated to 2 bar overpressure and left for another 1 hour. The last measurement pressure value was 2.5 bar. The tubes were left for 17 hours under this value of gas pressure. During 19 hours of the creep measurement the digital image correlation system was recording the changes of the shapes of the studied tubes. The stability of the pressure values was maintained during the test, because the main valve to the gas manifold was left open to the global compression air

system. The tube 2 suffered the leakage issue after 1 hour and 19 minutes from the start of the test being at 2 bar overpressure. In the resulting plots (see Figure 2.18) the strain values for the tube 2 drop to zero at some point and maintain this value until the end of the measurement. A small leak also appeared in the straw tube 8 after approximately 15 hours of the test, which led to a systematic shift of the strain values for this tube observed in the resulting plots (see Figure 2.18). The elastic modulus was calculated for the tubes under the test in order to quantify its time dependence. The resulting plot is shown in Figure 2.17. The elastic modulus values start at 4.4–4.8 GPa and decrease with time to 2.7 GPa for the straw tube 1 and to 3.1 GPa for the tube 8. Such high material degradation after the test is equal to the theoretically calculated [49] elastic modulus value of the straw tube operating at nominal 1 bar overpressure for half a year. In general, the strain of the tubes changed over time with the rate depending on the gas pressure inside. For 1 bar overpressure the strain was almost constant during 1 hour of measurement, but for 2 bar and especially for 2.5 bar the strain changed significantly. For 2.5 bar overpressure, the strain increased in almost 2.5 times after 17 hours of measurement comparing to the initial value right after the tube was inflated to this value of pressure. This means that the operation of the straw tubes at more than 2 bar overpressure is already not safe and leaving them at such pressure values even for few days may lead to their failure. The straw tube with cyanoacrylate glue on its surface behaved similarly to the pristine tube during the creep test. The hypothesis stating that the module of five tubes



(a) The pristine tube.



(b) The tube with the the stripe of cyanoacrylate glue.

Figure 2.13: The distributions of the principal strain 1 (the circumferential strain) calculated using the DIC analysis right before the point of failure of the straw tube specimens. The figures are adapted from [58].

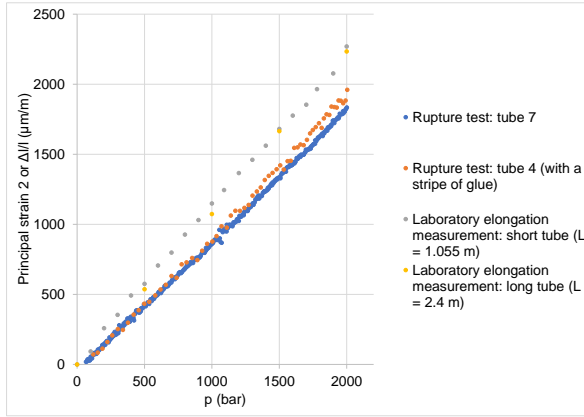


Figure 2.14: The comparison between the longitudinal strain distributions measured in the lab 15/S-006 using the digital microscope and measured with DIC technique in the Mechanical Measurements Laboratory.

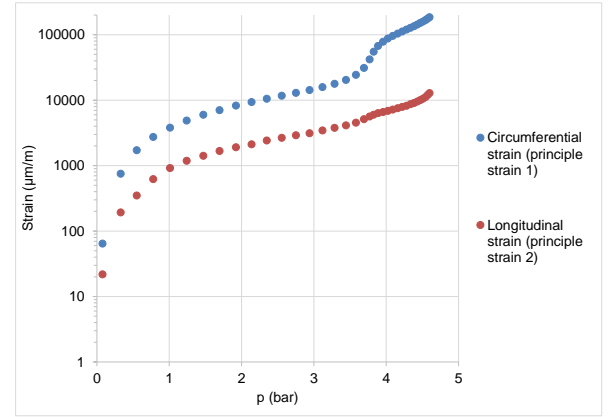


Figure 2.15: The principal strain components of the surface of the straw tube *vs.* the gas overpressure inside.

showed in Figure 2.1 was destroyed because of the stresses induced with the glue was not confirmed. There is another hypothesis stating that the tube exploded because of the shock wave, which appeared when one of the wires inside the straw tubes ruptured after experiencing the excess elongation. This event could cause the rapid local movement of the tubes and tear them apart, because they are made of very thin, light and fragile material. However, this process should be repeated in the controlled laboratory conditions to prove its sustainability.

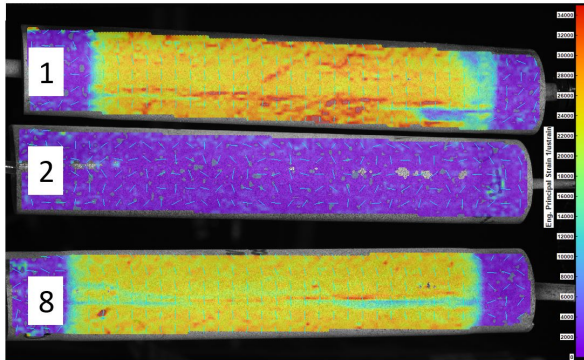


Figure 2.16: The circumferential strain (principal strain 2) distributions for the tubes under creep test after 17 hours of measurement at 2.5 bar. The tube 2 leaked earlier during the measurement and was deflated. The figure is adapted from [58]

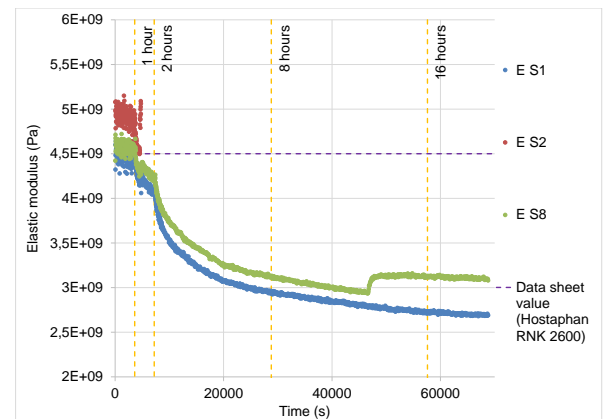
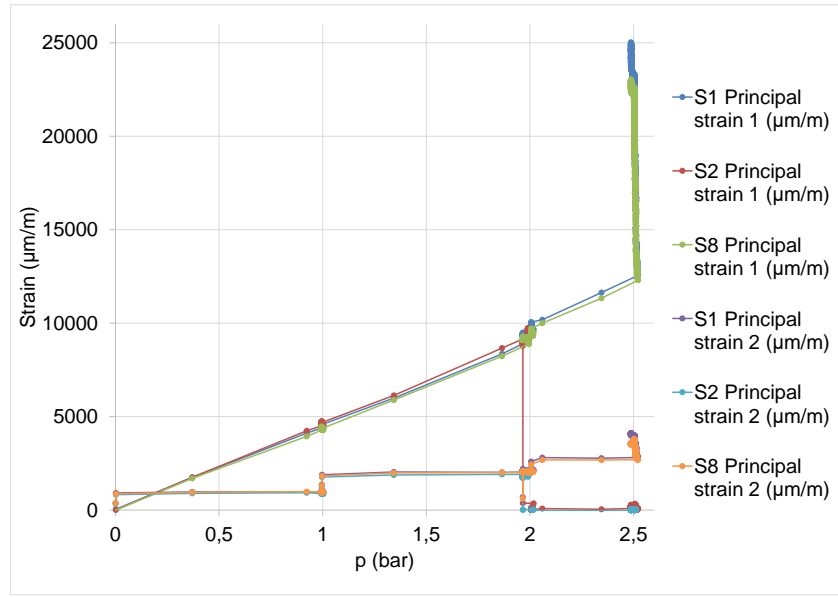
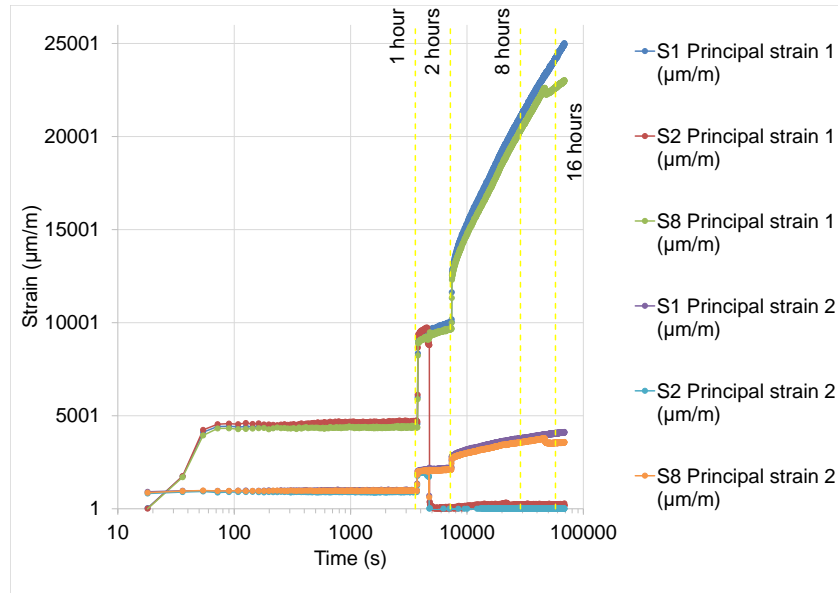


Figure 2.17: The dependence of the estimated elastic modulus of the tube *vs.* the measurement time. The steps in the distributions reflect the gas pressure changes.



(a) The dependence of the principal strain components *vs.* the gas overpressure inside the tubes.



(b) The dependence of the principal strain components *vs.* the measurement time.

Figure 2.18: Measured principle strain values during the creep tests. The principal strain 1 is the circumferential strain and the principle strain 2 – the longitudinal one.



## 2.2 Electrical properties of the tubes

From the point of view of transmitting high frequency ( $> 1$  MHz) electro-magnetic signals, a straw tube acts as a lossy transmission line. Indeed, the wire inside the tube is the inner conductor of the line, the gas mixture inside is a dielectric material and the metalized inner surface of the tube is a grounded shielding, which keeps the electro-magnetic excitations inside the gas volume of being radiated into the environment. The inner metal coating is rather thin ( $< 100$  nm), so the losses of the electro-magnetic energy through the walls of the tube are possible. Also, the DC resistances of the wire and the tube metalization layers are not negligibly small, which influences the characteristic impedance of the tube. The resistivity  $\rho$  of the tungsten-rhenium gold coated wire provided by the manufacturer [61] is  $0.092 \Omega \cdot \text{mm}^2/\text{m}$ . Thus, the DC wire resistance  $R_w$  can be calculated using the formula:

$$R_w = \rho \frac{l}{S} = \rho \frac{2l}{\pi d^2} \approx 312.5 \Omega, \quad (2.2)$$

where  $l$  is the length of the wire equal to 2.4 m,  $d$  is the wire diameter of 0.03 mm. The DC resistance of the wires of the fully assembled tubes was measured experimentally with a regular multimeter with the best resistance measurement accuracy of 1%. The mean value of the DC wire resistance for 6 fully assembled straw tubes is equal to  $318 \pm 3 \Omega$ . The discrepancy with respect to the theoretical resistance values origins from the fact that the wire inside the tube is pretensioned. The cross section  $S$  of the wire becomes smaller and the resistance according to the equation (2.2) increases.

Resistivity values of the thin metal films differ from the bulk values for copper ( $1.67 \cdot 10^{-8} \Omega \cdot \text{m}$ ) and gold ( $2.2 \cdot 10^{-8} \Omega \cdot \text{m}$ ) at  $20^\circ$ . The resistivity of the films, which have the thickness of the order of few tens nanometers, increases, when the mean free path for electron-phonon interactions inside the thin film is similar or larger than its thickness. The mean free path of electrons in copper is 39 nm, in gold 37.7 nm. The standard thickness of the metalization layers on the surface of straw tubes is 50 nm and 20 nm, which means that the bulk resistivity values are not applicable in our case.

The quality of a metalized film and the uniformity of its thickness also contribute to the total resistivity value of the given film. The metalization layers on the inner surface of straw tubes are created by a vapor deposition of thin metal films of evaporated copper and gold. The quality of metal deposition is not uniform and the thickness is not the same for all metalized tubes available in the laboratory. To find the tubes with standard metalization thickness, the DC resistance measurements were performed. The same multimeter was used to measure the DC resistance of the metalized layers on the inner surfaces of the tube walls as for the wire DC resistance measurements. The obtained results are shown in a histogram in Figure 2.19. The tubes, which were measured, had different metal coating thickness varying from 50 nm to 150 nm of total thickness. All tubes have 20 nm gold coating layer, but a thickness of copper layers can be different: 30 nm, 50 nm and 130 nm. A major fraction of the available tubes constituted the standard tubes with 70 nm coating thickness. This majority can be observed in the histogram in Figure 2.19 as a peak



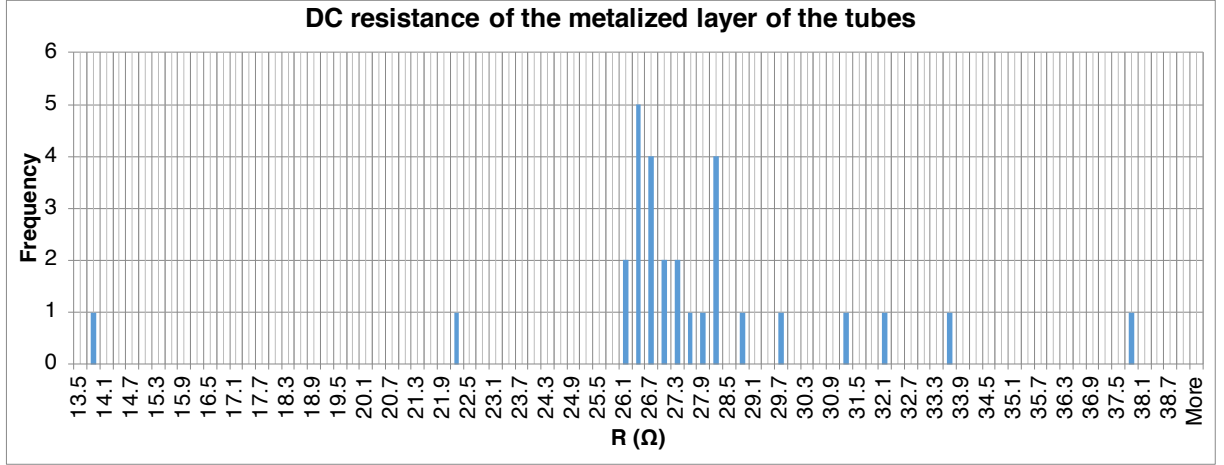


Figure 2.19: The DC resistances of the metalized layers on the inner surface of the straw tubes walls. Data is extracted from [62]

Table 2.3: The electrical resistivity of thin copper films measured experimentally in [62].

Film thickness (nm)	Electrical resistivity ( $\Omega \cdot \text{m}$ )
30	$4-8 \cdot 10^{-8}$
50	$3-6 \cdot 10^{-8}$
130	$2-5 \cdot 10^{-8}$

between  $25.94 \Omega$  and  $28.32 \Omega$ . The tubes with larger coating thickness values had smaller resistance down to  $13.7 \Omega$  and, correspondingly, the ones with thinner coating had larger resistances up to  $37.5 \Omega$ . The mean value of measured DC resistances is  $27.29 \pm 3.75 \Omega$ .

According to the measurements conducted in [62] and [63], the electrical resistivity of a 20 nm thick gold film is  $6.9 \cdot 10^{-8} \Omega \cdot \text{m}$  and the electrical resistivity values of copper films for different thickness values are given in Table 2.3. The electrical resistivity values for particular thickness values vary depending on the quality of the metal deposition.

The DC resistance of the layers can be calculated using equation (2.2), substituting the cross section  $S$  of a conductor with  $S = 2\pi bt$ , where  $b$  is the inner radius of a straw tube equal to 9.92 mm,  $t$  is the thickness of a metalization layer on the inner surface of the tube. Then, a DC resistance  $R_{\text{Au}}$  of a gold layer with thickness  $t_{\text{Au}}$  of 20 nm is equal to  $132.8 \Omega$ . A DC resistance  $R_{\text{Cu},30}$  of a 30 nm copper layer varies in the range  $51.3-102.7 \Omega$ , for a 50 nm layer the DC resistance  $R_{\text{Cu},50}$  varies in the range  $23.1-34.7 \Omega$ , for a 130 nm layer the DC resistance  $R_{\text{Cu},130}$  changes in the range  $5.9-13.3 \Omega$ , respectively. The total DC resistance of two metalization layers deposited on the inner surface of straw tubes can be calculated assuming that these layers act as parallel conductors:  $R = R_{\text{Au}} R_{\text{Cu}} / (R_{\text{Au}} + R_{\text{Cu}})$ . The estimated values of total DC resistances for different thickness values of straw tube metalization layers are:  $37-58 \Omega$  for 50 nm total thickness,  $19.7-27.5 \Omega$  for 70 nm and

5.6–13.3  $\Omega$  for 150 nm. The estimated values of DC resistance are consistent within the variations with the results from the measurements performed in the laboratory 15/S-006 at CERN. More precise estimations of DC resistances can be made, once the exact electrical resistivity values are provided by the BoPET film manufacturer.

### 2.2.1 ANSYS simulation of the electro-magnetic properties of the straw tube

The theoretical calculation of the DC resistance of the tube’s metalization layers and, ultimately, the impedance of whole straw tube is complicated and requires deep investigation of the electron-phonon interactions occurring inside the thin metalization layers of the tube coating. In the scope of this thesis, it was decided to perform the simulation of the electro-magnetic properties of the straw tube using the ANSYS [64] software (HFSS module). The simulation of the whole 2.4 m straw tube is not possible, because it would need to create trillions of mesh points due to the existence of such thin metalization layers (70 nm), which are 6 orders of magnitude smaller than the gas volume radial size of 2 cm. The only stable simulation configuration was achieved for a small piece of the tube of 15 mm length instead of 2.4 m of the real one. Such simulation will not be accurate for the frequencies smaller than 10 MHz, but for larger values of signal frequencies the extracted  $S$ -parameter values and the characteristic impedance values are close to the real ones. In order to make the correction for the length of the tube, the post-processing de-embedding algorithm for excited wave port (assigned to the gas volume face at one of the sides of the straw tube in our case) is executed after the main electro-magnetic simulation run. This algorithm exploits the cylindrical symmetry of the modeled geometry and renormalizes the electro-magnetic solution over the increased distance to the simulated volumes. Eventually, the corrected values of the  $S$ -parameter and the characteristic impedance are calculated.

The simulated tube model is simplified. The end-plugs are not modeled, so the gas inside the tube has a contact surface with the air of the environmental cylinder, but the diffusion of the gases is not simulated and the gases remain in the dedicated volumes. This specific contact face is set to be radiative in order to simulate the open end of the transmission line. There are the options to short cut this face or set the termination impedance too. Inside the tube the air at 1 bar absolute pressure is used instead of Ar/CO<sub>2</sub> mixture. The electrical permeability of the air is approximately equal to the one of the Ar/CO<sub>2</sub> mixture, so it can be used for the model to a certain extent. The opposite face of the tube, which shares the border with the bottom face of the environmental cylinder (the face of the gas volume of the tube), is assigned as the excitation wave port meaning that the excitation of a certain frequency is set as the border condition for this side of the model. The mesh of the model is created for the highest simulation frequency (5 GHz in our case) and then the electro-magnetic solutions are calculated for the smaller frequencies in the sweep. The de-embedding distance parameter for the post-processing of the simulation results is set in the wave port properties too (-2.4 m for the straw tube prototype). The image of the isometric projection of the described 3-dimensional simulation model is shown

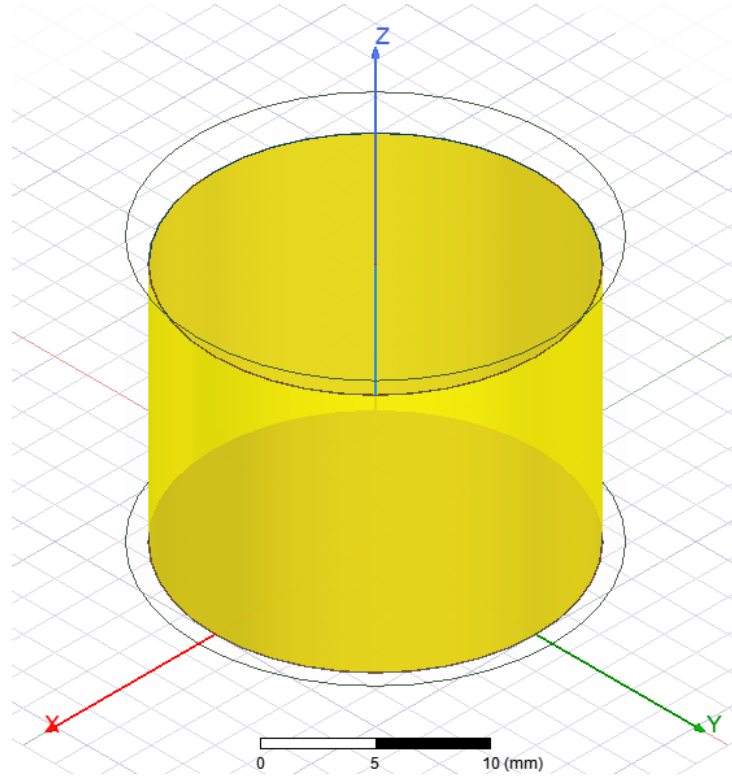


Figure 2.20: The model of the part of the straw tube created in the ANSYS HFSS design editor [64].

in Figure 2.20.

The number of mesh points needed to find the electro-magnetic solutions within the desired precision ( $\Delta S = 0.02$ ) is optimized for 5 GHz frequency. Then the frequency sweep between 100 Hz and 5 GHz is performed with a step of 500 kHz. The plots of the  $S_{11}$ -parameter *vs.* the frequency of the signal and the characteristic impedance *vs.* the frequency are created as the output results of the electro-magnetic simulation. The plots are shown in Figure 2.21.

The  $S_{11}$ -parameter in Figure 2.21 is the ratio between the power of the forward signal passing through the tube and the reflected one in dB. The plot in Figure 2.21 shows how the reflected signal becomes significantly attenuated for  $> 1$  MHz frequency of the excited signal inside the tube. The characteristic impedance of the tube is high for small frequencies, up to 5500  $\Omega$  for  $< 40$  MHz, and drops to 395  $\Omega$  for higher excited signal frequency (from 200 MHz onwards). According to the simulation results, if the straw tube is terminated with 395  $\Omega$  load resistance, then the contribution of the higher frequency ( $> 100$  MHz) reflections will be suppressed, which should remove extra sharp peaks (FWHM  $\approx 5$ –10 ns) from the output signal, but the lower frequency contribution will remain. The characteristic impedance value for a simulated tube for frequencies larger than 200 MHz tends to a characteristic impedance  $Z_0 = \sqrt{\frac{L}{C}}$  value calculated for a coaxial

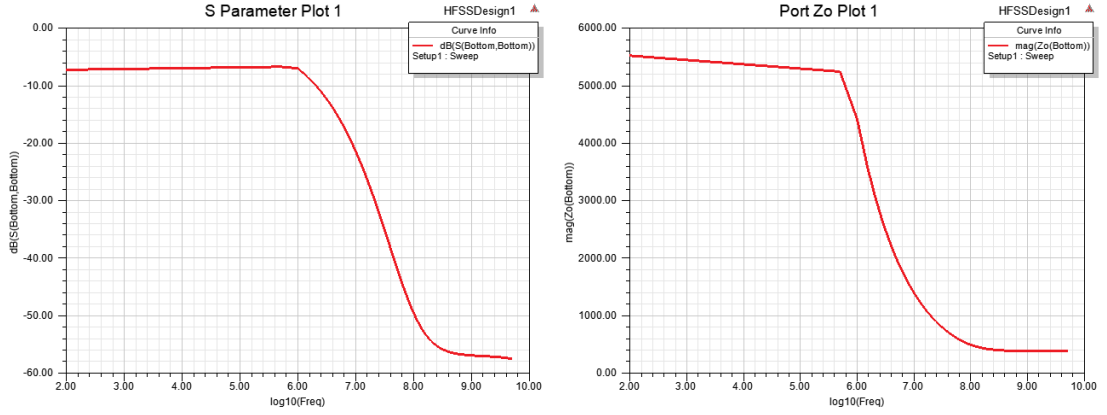


Figure 2.21: The left figure: the plot of the  $S_{11}$ -parameter values depending on the frequency of the excited signal in the tube volumes. The right figure: the characteristic impedance of the tube depending on the frequency of the excited signal in the tube volumes.

line with straw tube parameters:  $\epsilon_r \approx 1$  (a relative permittivity),  $b = 9.92$  mm (an inner tube radius) and  $a = 0.015$  mm (a wire radius).

$$Z_0 = \sqrt{\frac{L}{C}} = \frac{138 \cdot \log_{10}(b/a)}{\sqrt{\epsilon_r}} \quad (2.3)$$

Inserting the straw tube parameters mentioned earlier,  $Z_0 = 390 \, \Omega$ , which is consistent with the simulated value in a high frequency range.

## 2.2.2 Signal attenuation measurements

The attenuation of the signal propagating through the tube can be measured experimentally. The experimental setup for such measurement was assembled in the laboratory 15/S-006 at CERN and is schematically illustrated in Figure 2.22. A fully assembled straw tube filled with the gas mixture of Ar/CO<sub>2</sub> in 70%/30% proportion with the HV decoupling interface attached was connected to the HV power supply. The signal output from the wire was connected through the 50  $\Omega$  coaxial cable directly to one of the inputs of the oscilloscope (LeCroy waveSurfer 44Xs, 2.5 GS/s, 400 MHz bandwidth) (see Figure 2.22). In order to be able to detect the weak straw tube signals with the scope without the pre-amplification, the applied HV to the anode wire was set to higher value of 2300 V than the nominal one of 2200 V. The trigger threshold for the input channel of the scope was set to -2 mV. The signals were averaged over 1000 sweeps. As a source of the ionization radiation the <sup>55</sup>Fe was used. This particular radioactive source according to [44] emits Auger electrons of 5.19 keV (60% of the decay intensity) and X-rays of 5.9 keV and 6.5 keV (27.25% of the intensity) energy. The Auger electrons of 5.19 keV are very unlikely to penetrate through the wall of the straw tube (the continuous slowing down approximation range of the electrons of  $\approx 10$  keV in the BoPET is  $\approx 2 \, \mu\text{m}$ ). The advantage of irradiating

the straw tubes with the X-rays instead of charged particles is that the mean number of primary electrons can be estimated for the X-rays of low energy, because of the high probability of a full absorption of an X-ray in the gas. According to Section 1.3.2, the mean number of electrons released in the ionization cluster from single photon interaction with gas atoms is 198. Also, the  $\delta$ -electrons are not produced for the X-rays in keV energy range. The output signal induced in the wire (after the absorption of an X-ray) of the tube should always have similar characteristics (an amplitude, a rise/fall time, a length) not depending on the distance from the primary ionization cluster to the wire. The attenuation of the signals can be measured with the described above experimental setup by placing

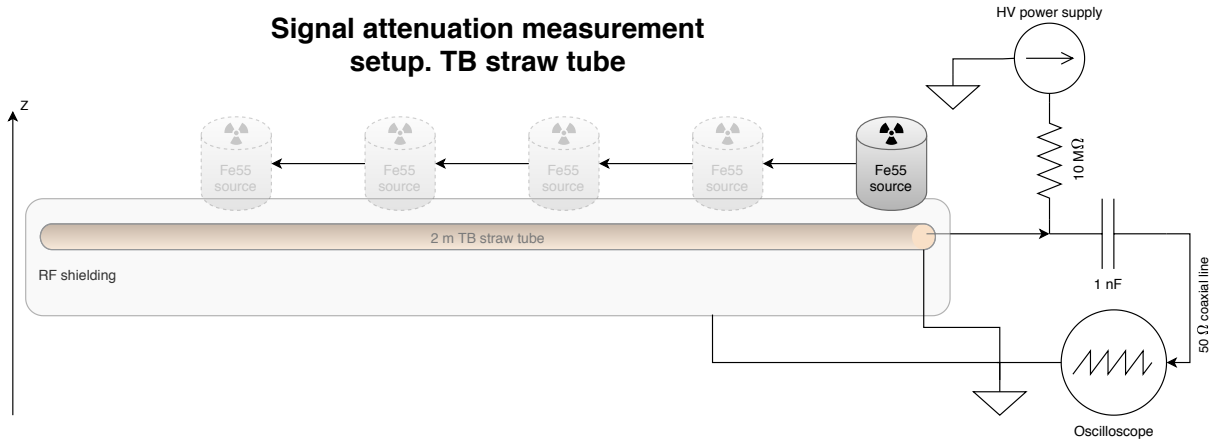


Figure 2.22: The experimental setup built for the signal attenuation measurements. The radioactive source of  $^{55}\text{Fe}$  is moved further (the transparent dashed images of the source) along the tube to measure the output signal at various distances.

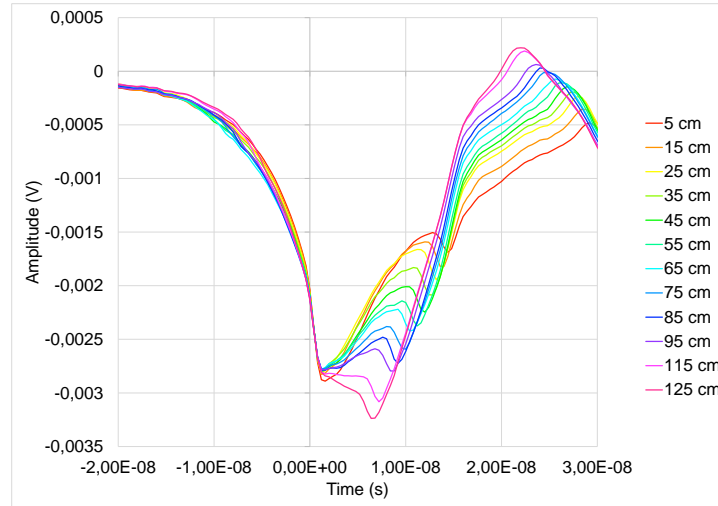


Figure 2.23: The plot showing the output signals from the straw tube acquired for various positions of the  $^{55}\text{Fe}$  source from the read-out end of the tube.

the radioactive  $^{55}\text{Fe}$  source at different distances from the tube's read-out side until the two output signals (a forward and a reflected one) measured with the scope are merged into a single large signal. The output signal for each position of the radioactive source is the sum of the forward and the reflected signals from both the far end of the tube and the near end (read-out side of the tube). The first reflected signal appears because the far end of the tube is open. The second reflection occurs on the read-out side, because there is an impedance mismatch between the tube output and the read-out interface. The reflections of those signals of higher order contribute to the output signal, but they vanish after a few iterations due to the attenuation. The first two peaks (the ones with the largest amplitudes) of the output signal are the forward signal and the reflected from the tube's far end one. The part of the output signal, which corresponds to the sum of the first two signals, is shown in Figure 2.23 for all positions of the source along the tube, which were used during the measurement. The one can observe that the two peaks are shifting towards each other with the growing distance of the source placement. At the far end of the tube the 2 contributions merge into a single larger peak, because in this case both peaks travel the same distance to the read-out electronics.

The output signals shown in Figure 2.23 are fitted with a combination of two Voigtian distributions. A Voigtian distribution is a convolution of a Breit-Wigner distribution and a Gaussian distribution. The Voigtian distributions are used to model the peaks of forward and reflected signals in each data sample. The sum of the distributions with coefficients reflecting the contribution of each peak forms the final fit function:

$$\begin{aligned}
 U(t) &= N_1 \cdot V(t, \mu_1, \sigma, \gamma) + N_2 \cdot V(t, \mu_2, \sigma, \gamma), \text{ where} \\
 V(t, \mu_i, \sigma, \gamma) &= \int_{-\inf}^{+\inf} G(t, \mu_i, \sigma) B_w(t - t', \mu_i, \gamma) dt', \quad i = 1, 2; \text{ where} \\
 G(t, \mu_i, \sigma) &= \frac{1}{\sigma\sqrt{2\pi}} \exp\left(-\frac{(t - \mu_i)^2}{2\sigma^2}\right) \text{ and} \\
 B_w(t, \mu_i, \gamma) &= \frac{\gamma}{\pi((t - \mu_i)^2 + \gamma^2)}, \quad i = 1, 2;
 \end{aligned} \tag{2.4}$$

where  $\mu_i$  is the location parameter of each peak,  $\sigma$  and  $\gamma$  are the scale parameters: smaller  $\gamma$  makes the distribution sharper, larger  $\sigma$  makes the distribution more flat. The approximation is performed using the RooFit [65] subroutine of the ROOT [66] framework. This subroutine allows to fit the data samples with the combinations of complicated functions, which do not converge well within standard gradient methods used in the ROOT. The results of the fits are shown in Figure 2.24 for 3 different positions of the radioactive source. The ratio of the amplitudes ( $N_1/N_2$ ) of two Voigtian distributions obtained from the approximations of the output signal are used for the  $S_{11}$ -parameter calculation (see formula (2.5)). The evolution of the ratio between the components of the acquired straw tube signal is shown in Figure 2.25. The first value at 5 cm distance is the closest approximation of the theoretical  $S_{11}$ -parameter and it is equal to  $-7.5 \pm 0.8$  dB, which is close to the simulated value from the straw tube model simulated with HFSS for  $\approx 1.5$  MHz frequency.

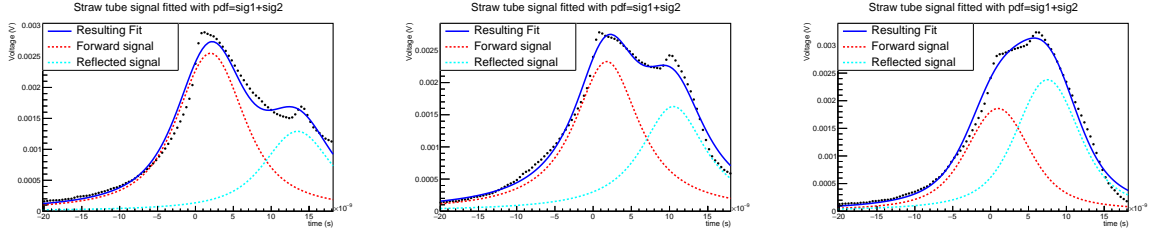


Figure 2.24: The output signals from the straw tube recorded for three positions of the radioactive source. The signals are fitted with (2.4). The left plot: the source is placed at 5 cm from the read-out side of the tube; the middle plot: at 65 cm from the read-out side; the right plot: at 125 cm from the read-out side.

$$S_{11} = 20 \log_{10} \left( \frac{N_r}{N_f} \right) [\text{dB}], \quad (2.5)$$

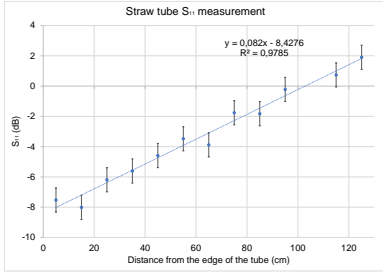


Figure 2.25: The dependence of the  $S_{11}$ -parameter on the distance of the radioactive source from the read-out side. The plot is fitted with the linear model.

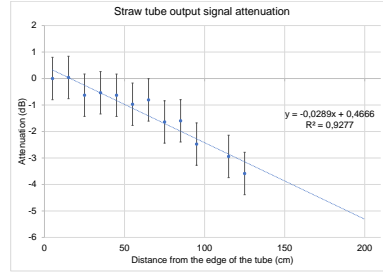


Figure 2.26: The attenuation of the forward signal depending on the distance from the read-out side in dB. The plot is fitted with the linear model, which predicts the attenuation of the signal at the far end of the tube.

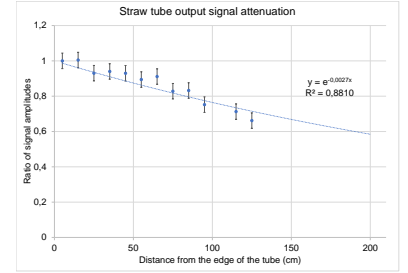


Figure 2.27: The ratio of the amplitude of a forward signal measured at the closest distance to the read-out side to the amplitudes of forward signals further along the length of a straw tube. The plot is fitted with exponential model.

where  $N_f$  and  $N_r$  are the fractions of each Voigtian distribution describing the forward and the reflected signals obtained from the fit (2.4). The signal attenuation per unit length is then calculated in dB according to the formula (2.5), but instead of the ratio  $\frac{N_r}{N_f}$  the ratio between the  $N_{f,1}$  parameter of the forward signal obtained for the closest position of the radioactive source to the read-out side (5 cm) and the consecutive values  $N_{f,i}$  in each point further along the tube are used. As it was mentioned previously the two peaks are getting closer to each other in time with respect to the increasing distance from the read-out electronics side. At the far end of the tube the two signals completely merge. At

some point, in the second half of the tube (before the tube's end) the fitting algorithms are not anymore able to disentangle the two signals, that is why the measurements were not performed after 125 cm distance from the read-out side. The length of the tube under study was 2 m. The plot of the signal attenuation vs. the distance from the read-out side is shown in Figure 2.26. The plot is fitted with the linear model and it is extrapolated to the far end of the tube in order to predict the maximum attenuation. The predicted value of signal attenuation at the tube's end (2 m) is  $-5.31 \pm 0.54$  dB. As alternative, the fit parameter of exponential function from Figure 2.27, where the ratio  $\frac{N_{f,i}}{N_{f,1}}$  is built *vs.* the distance from the read-out side, can provide an attenuation length parameter  $\lambda$  for a straw tube, *i.e.* a length of the tube sufficient to suppress the induced signal by  $e$  times. This parameter is equal to the inversed coefficient 0.0027 at “x” variable from the fit function from Figure 2.27:  $\lambda = 1/0.0027 \approx 370.4 \pm 25.6$  cm.

The fit parameters, which describe the location of each signal in the data sample (each Voigtian distribution),  $\mu_f$  and  $\mu_r$ , can be used to estimate the signal propagation velocity inside the wire. As the distance between the radioactive source positions is known, it can be related to the difference in time between the combination of parameters  $\mu_r - \mu_f$  for every measured position:  $\mu_{r,1} - \mu_{f,1} - (\mu_{r,i} - \mu_{f,i})$ . Index 1 refers to the first measurement at 5 cm from the read-out side and indices  $i = 2, \dots, N - 1, N$  - to the rest of the measurements further along the tube. Then, the signal propagation velocity can be calculated using the formula:

$$\beta_i = \frac{v}{c} = \frac{d}{c \cdot (\mu_{r,1} - \mu_{f,1} - (\mu_{r,i} - \mu_{f,i}))}, \quad (2.6)$$

where  $c$  is the speed of light in vacuum,  $d$  is the distance between the points of the signal measurement along the tube. The average of the obtained  $\beta_i$  values is equal to  $0.68 \pm 0.03$ , which is comparable to the velocity factors of typical coaxial lines.

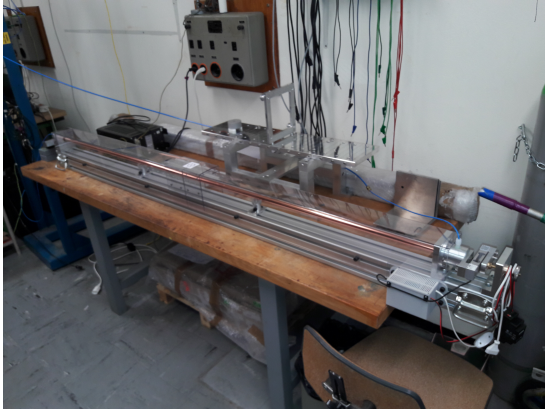


# Chapter 3

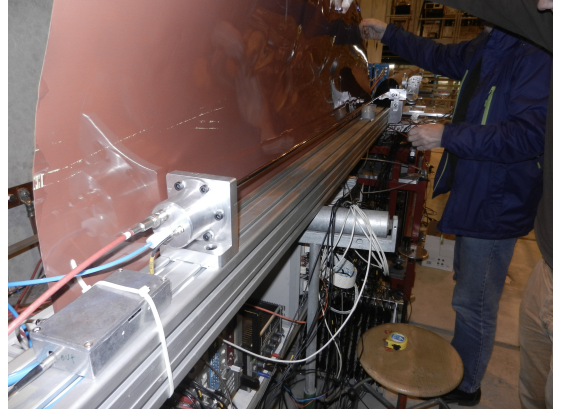
## SST 2017 test beam analysis

An experiment was carried out at the SPS H2 beam line of the CERN North Area<sup>1</sup>, in September-October 2017 by the SHiP Spectrometer Straw Tracker (SST) group to test two straw tube prototypes, one with a diameter of 10 mm and a length of 5 m and the second one with 20 mm and 2 m. The emphasis in the analysis was put on the second one, given that the new baseline diameter of the SST straws is now 20 mm (instead of 10 mm). The prototypes are shown in Figure 3.1.

The main goal of the test beam experiment was to study the drift time distribution and spatial resolution of the straw tubes for different wire eccentricities, by which one means here the vertical offset distance of the wire relative to the tube center. The experimental setup was situated on the beam line in PPE172 (H2B). During this SST test a secondary pion beam with momentum  $p = 150 \text{ GeV}/c$  was used. The intensity of the beam varied



(a) “Short”: 2 m length, 20 mm diameter.



(b) “Long”: 5 m length, 10 mm diameter.

Figure 3.1: Straw tube prototypes.

---

<sup>1</sup>Information about the beam lines in North Area (CERN): <https://edms.cern.ch/document/1605378/1>

between  $10^5$  and  $1.3 \cdot 10^5$  particles per spill, with a spill duration of about  $4.72 \text{ s}^2$ . In order to cover the full 2 cm diameter of the straw tube, the transverse beam profile was enlarged to have root mean squares (RMS)  $\sigma_x \approx 9 \text{ mm}$  and  $\sigma_y \approx 13 \text{ mm}$  (here  $x$  is the transverse horizontal axis, along the straw, and  $y$  is the transverse vertical axis).

A silicon microstrip sensor telescope from Milano University [67] was used to reconstruct precise tracks and link them to the measured drift time of hits in the straws with an extrapolated vertical position resolution ( $50\text{--}60 \text{ }\mu\text{m}$  at the straws) conveniently smaller than the expected spatial resolution of the drift detector.

## 3.1 Overview of the experiment

### 3.1.1 Detectors

The experimental layout is sketched in Figure 3.2. The detectors were assembled on a  $1.8 \text{ m} \times 1 \text{ m}$  table and visually aligned to the beam line, at a height of 2.46 m above the floor level. The most upstream and downstream detectors were two  $15 \text{ cm} \times 15 \text{ cm}$  plastic scintillators (T1 and T2), 7 mm thick, used for triggering the passage of charged particles from the beam. A  $5 \text{ cm} \times 6 \text{ cm}$  plastic scintillator (labeled T0 on Figure 3.2), 2.5 cm thick, was used for defining the arrival (reference) time of the particles.

The telescope, located in a dark box, consisted of 8 identical microstrip sensors of  $94 \times 92 \text{ mm}^2$  size,  $500 \text{ }\mu\text{m}$  thickness and  $183 \text{ }\mu\text{m}$  strip pitch [67]. Half of the sensors were oriented with the strips vertical (measuring the  $x$  coordinate), the other half with the strips horizontal (measuring the  $y$  coordinate), as indicated on the sketch (Figure 3.2). The gap between sensors was approximately 10 cm. The 512 strips of each sensor were read out by four Beetle front-end chips [68].

The two devices under study (DUT) were located horizontally, perpendicular to the beam, in sequence on the beam path, as shown in Figure 3.2, between the T0 detector and the Milano telescope. The main DUT was a 2 cm diameter straw prototype of 2 m length made with the NA62 technique [31, 69–71]. The straw cathode (tube) consists of a  $36 \text{ }\mu\text{m}$  thick PET ribbon coated with copper (50 nm) and gold (20 nm), formed into a cylinder shape and welded with an ultrasonic head. The anode wire consists of a  $30 \text{ }\mu\text{m}$  diameter tungsten-rhenium alloy coated with gold. The tube wall was tensioned with 4 kg, the wire with 90 g. An older and similar tube, of 5 m length and 1 cm diameter, was also exposed to the beam. This tube was tensioned with 2 kg and its wire with 90 g. The two prototypes are shown in Figure 3.1. Each straw was read out on one side with a single-channel discrete component (custom made<sup>3</sup>) amplifier. The high voltage (HV) for the 2 m straw tube was 2.2 kV and 1.8 kV for the 5 m straw. The operating gas mixture was 70% argon (Ar) and 30% carbon dioxide ( $\text{CO}_2$ ) from a pre-mixed bottle.

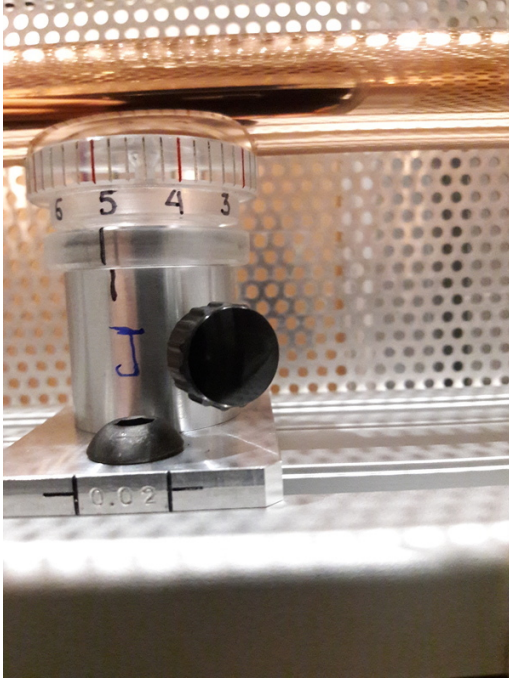
The main goal of the test beam experiment was to study the drift time distribution and spatial resolution for different wire eccentricities. In order to change the wire eccentricity,

---

<sup>2</sup>Information on Secondary Beams & Areas at CERN: <http://sba.web.cern.ch/sba/>

<sup>3</sup>Special thanks to Pavel Shatalov, ITEP Moscow, for providing these two circuit boxes.





(a) Offset adjuster (Jura side).



(b) Offset adjuster (Salève side).

Figure 3.3: The adjusters used during the test beam for the short straw (2 cm diameter).

was read out by two silicon photomultipliers (SiPMs), which formed a coincidence in a dedicated CAEN SiPM readout unit (model CAEN SP5602). The T1 and T2 coincidence signals were sent to a NIM coincidence unit. The output of this NIM coincidence unit was then used to trigger both the VME and MAMBA boards. The MAMBA board propagated the trigger to the Beetles, from which it received the associated microstrip analog data. The MAMBA board performed a digitization, common-mode and zero suppression, before sending the data to a dedicated PC. The signals from the T0 scintillator and the two DUTs were sent to a VME constant-fraction discriminator (CFD) unit<sup>4</sup> and subsequently to a TDC VME board<sup>5</sup>. The CFD threshold was usually set to -15 mV (or other values for specific tests). Data was recorded and sent to a separate PC in a time window broad enough ( $1.5\text{ }\mu\text{s}$ ) to record the signals from the straw tubes which were delayed due to the electrons drifting to the anode wires. Upon reception of a trigger by the VME control unit (CES RCB 8047) a busy signal was generated and sent to the NIM crate to veto the coincidence triggers in order to stop the acquisition from the telescope during the  $1.5\text{ }\mu\text{s}$  time window. Both the MAMBA and VME data were time-stamped with internal clocks. The recorded data were then time-matched in the offline analysis.

<sup>4</sup>CAEN model V812.

<sup>5</sup>CAEN V1290A, least significant bit (LSB) is 25 ps (21 bit resolution, 52  $\mu\text{s}$  full scale range (FSR)).

### 3.1.3 Data samples

The VME output files were created in a ROOT tree format [72]. The MAMBA data files were saved in a custom format ('\*.dat') and converted into a ROOT tree by a dedicated software package<sup>6</sup> provided by the Milano telescope group. This software package subtracts the pedestal from each readout channel (silicon strip) and applies a common-mode subtraction algorithm over groups of 32 Beetle channels, forming then strip clusters. Several Beetle pedestal files were acquired separately, when the beam was switched off, by sending a periodic trigger to the systems (rate of the order of 100 Hz). The VME and MAMBA systems had their own internal clocks for time stamping (27-bit counter of 800 ns ticks for the VME and 48-bit counter of 2.5 ns ticks for MAMBA). An algorithm was applied offline to match events by the time stamp (see Appendix C). The software package also reconstructs tracks from the clusters using the artificial retina algorithm [73] and provides alignment parameters of the telescope, as briefly discussed in a subsection below. The output '\*.root' files containing the tracks were created using the alignment corrections. The tracks obtained from the MAMBA files were then extrapolated to the position of the DUT. The extrapolated tracks were correlated to hits (drift times) of the DUTs obtained from the VME '\*.root' file.

Several measurements were performed. At a fixed short straw HV of 2200 V, event data were collected for different settings of the straw height adjusters. This measurement is called an “offset scan”. The list of files taken for this scan is given in table 3.1. The two offset scales (for the long and short straws) have an arbitrary origin and are given here in  $\mu\text{m}$  (with an accuracy of the order of 20  $\mu\text{m}$ ).

Because the adjusters did not allow us to move the short straw downward relative to its unsupported position, weights were added to the straw and offset scans repeated. These are called “offsets scans with applied weights”, see table 3.2. “High voltage scans” were also performed at two fixed wire offsets (applied offset value -400 and -700) by varying the HV, as listed in table 3.3. The CFD threshold was different for the two scans (-15 mV and -30 mV respectively). In order to study the effect of the threshold as well, a few “threshold scans” were performed.

In all these measurements the gas flow and gas pressure inside the straw tubes were kept constant to approximately 2  $\ell/\text{h}$  and 1.08 bar absolute.

Table 3.1: Wire offset scans without weights on the short tube. Useful runs with offset scans are: 159 to 221. Short straw HV: 2200 V, long straw HV: 1800 V. CFD thresholds for both tubes were set to -15 mV.

Short straw offset	Long straw offset	Number of a measurement	MAMBA file name	VME file name	Statistics	Total statistics per measurement
1500	0	0	test_hadrons—159.dat	ADC_170916_202138	2.00E+05	2.20E+06
			offsetScan_hadrons—160.dat	ADC_170916_203530	5.00E+05	
			offsetScan_hadrons—161.dat	ADC_170916_205827	0.00E+00	
			offsetScan_hadrons—163.dat	ADC_170916_211826	5.00E+05	
			offsetScan_hadrons—164.dat	ADC_170916_213838	5.00E+05	

<sup>6</sup>The software can be downloaded from a GitHub repository: [https://gitlab.cern.ch/mpetruzz/Sbt\\_Milano](https://gitlab.cern.ch/mpetruzz/Sbt_Milano)

Table 3.1: Wire offset scans without weights on the short tube. Useful runs with offset scans are: 159 to 221. Short straw HV: 2200 V, long straw HV: 1800 V. CFD thresholds for both tubes were set to -15 mV.

Short straw offset	Long straw offset	Number of a measurement	MAMBA file name	VME file name	Statistics	Total statistics per measurement
1300	100	1	offsetScan_hadrons—165.dat	ADC_170916_215551	5.00E+05	2.17E+06
			offsetScan_hadrons—166.dat	ADC_170916_223022	1.00E+05	
			offsetScan_hadrons—167.dat	ADC_170916_224132	7.00E+04	
			offsetScan_hadrons—168.dat	ADC_170916_233307	5.00E+05	
			offsetScan_hadrons—169.dat	ADC_170917_000327	5.00E+05	
1100	200	2	offsetScan_hadrons—170.dat	ADC_170917_002316	0.00E+00	1.17E+06
			offsetScan_hadrons—171.dat	ADC_170917_004212	5.00E+05	
			offsetScan_hadrons—172.dat	ADC_170917_010015	5.00E+05	
			offsetScan_hadrons—173.dat	ADC_170917_013805	5.00E+04	
			offsetScan_hadrons—174.dat	ADC_170917_014543	5.00E+05	
900	300	3	offsetScan_hadrons—175.dat	ADC_170917_023001	0.00E+00	1.52E+06
			offsetScan_hadrons—176.dat	ADC_170917_030815	3.50E+05	
			offsetScan_hadrons—177.dat	ADC_170917_034509	2.70E+05	
			offsetScan_hadrons—178.dat	ADC_170917_041940	5.00E+04	
			offsetScan_hadrons—179.dat	ADC_170917_042235	5.00E+05	
700	250	4	offsetScan_hadrons—180.dat	ADC_170917_045253	0.00E+00	2.05E+06
			offsetScan_hadrons—181.dat	ADC_170917_053503	4.70E+05	
			offsetScan_hadrons—182.dat	ADC_170917_060340	5.00E+05	
			offsetScan_hadrons—183.dat	ADC_170917_063227	5.00E+04	
			offsetScan_hadrons—184.dat	ADC_170917_063537	5.00E+05	
500	150	5	offsetScan_hadrons—185.dat	ADC_170917_065254	5.00E+05	2.14E+06
			offsetScan_hadrons—186.dat	ADC_170917_070950	5.00E+05	
			offsetScan_hadrons—187.dat	ADC_170917_072629	0.00E+00	
			offsetScan_hadrons—188.dat	ADC_170917_074323	5.00E+05	
			offsetScan_hadrons—189.dat	ADC_170917_081704	1.40E+05	
300	50	6	offsetScan_hadrons—190.dat	ADC_170917_082845	5.00E+05	1.50E+06
			offsetScan_hadrons—191.dat	ADC_170917_090540	5.00E+05	
			offsetScan_hadrons—192.dat	ADC_170917_093617	5.00E+05	
			offsetScan_hadrons—193.dat	ADC_170917_095341	5.00E+05	
			offsetScan_hadrons—194.dat	ADC_170917_102135	5.00E+05	
400	-50	7	offsetScan_hadrons—195.dat	ADC_170917_103859	5.00E+05	2.00E+06
			offsetScan_hadrons—196.dat	ADC_170917_105528	5.00E+05	
			offsetScan_hadrons—198.dat	ADC_170917_113915	5.00E+05	
			offsetScan_hadrons—199.dat	ADC_170917_115621	5.00E+05	
			offsetScan_hadrons—200.dat	ADC_170917_121254	5.00E+05	
600	-150	8	offsetScan_hadrons—201.dat	ADC_170917_122957	5.00E+05	1.91E+06
			offsetScan_hadrons—202.dat	ADC_170917_125734	5.00E+05	
			offsetScan_hadrons—203.dat	ADC_170917_131403	4.10E+05	
			offsetScan_hadrons—204.dat	ADC_170917_133031	5.00E+05	
			offsetScan_hadrons—205.dat	ADC_170917_134743	5.00E+05	
800	-250	9	offsetScan_hadrons—206.dat	ADC_170917_141256	5.00E+05	2.00E+06
			offsetScan_hadrons—207.dat	ADC_170917_142938	5.00E+05	
			offsetScan_hadrons—208.dat	ADC_170917_144629	5.00E+05	
			offsetScan_hadrons—209.dat	ADC_170917_150315	5.00E+05	
			offsetScan_hadrons—210.dat	ADC_170917_152949	5.00E+05	
1000	-200	10	offsetScan_hadrons—211.dat	ADC_170917_155003	5.00E+05	2.00E+06
			offsetScan_hadrons—212.dat	ADC_170917_160805	5.00E+05	
			offsetScan_hadrons—213.dat	ADC_170917_163112	5.00E+05	
			offsetScan_hadrons—214.dat	ADC_170917_170700	5.00E+05	
			offsetScan_hadrons—215.dat	ADC_170917_173017	5.00E+05	
1200	-100	11	offsetScan_hadrons—216.dat	ADC_170917_174954	5.00E+05	2.00E+06
			offsetScan_hadrons—217.dat	ADC_170917_180801	5.00E+05	
			offsetScan_hadrons—218.dat	ADC_170917_184121	5.00E+05	
			offsetScan_hadrons—219.dat	ADC_170917_185828	5.00E+05	
			offsetScan_hadrons—220.dat	ADC_170917_191914	5.00E+05	
1400	0	12	offsetScan_hadrons—221.dat	ADC_170917_195645	5.00E+05	2.47E+07
					Total:	

Table 3.2: Wire offset scans with extra weights on the short tube. Useful runs with offset scans are: 222 to 236. Short straw HV: 2200 V, long straw HV: 1800 V. CFD thresholds for both tubes were set to -15 mV.

Short straw offset	Long straw offset	Number of a measurement	MAMBA file name	VME file name	Statistics	Total statistics per measurement
-500	30	13	offsetScan_hadrons—222.dat	ADC_170917_210435	5.00E+05	1.50E+06
			offsetScan_hadrons—223.dat	ADC_170917_213614	5.00E+05	
			offsetScan_hadrons—224.dat	ADC_170917_215257	5.00E+05	
			offsetScan_hadrons—225.dat	ADC_170917_220941	0.00E+00	

Table 3.2: Wire offset scans with extra weights on the short tube. Useful runs with offset scans are: 222 to 236. Short straw HV: 2200 V, long straw HV: 1800 V. CFD thresholds for both tubes were set to -15 mV.

Short straw offset	Long straw offset	Number of a measurement	MAMBA file name	VME file name	Statistics	Total statistics per measurement
-800	80	14	offsetScan_hadrons—228.dat offsetScan_hadrons—229.dat offsetScan_hadrons—230.dat	ADC_170917_225625 ADC_170917_231428 ADC_170917_233425	5.00E+05 5.00E+05 5.00E+05	2.00E+06
500	130	15	offsetScan_hadrons—231.dat offsetScan_hadrons—233.dat offsetScan_hadrons—234.dat offsetScan_hadrons—235.dat offsetScan_hadrons—236.dat	ADC_170918_001615 ADC_170918_011820 ADC_170918_015641 ADC_170918_021732 ADC_170918_023441	5.00E+05 5.00E+05 5.00E+04 5.00E+05 5.00E+05	1.55E+06
500	300	20	test-pions—318.dat test-pions—319.dat test-pions—320.dat	ADC_170930_013724_318 ADC_170930_014602_319 ADC_170930_024212_320	5.00E+04 5.00E+05 5.00E+05	1.05E+06
200	200	21	test-pions—322.dat test-pions—323.dat test-pions—324.dat test-pions—325.dat test-pions—326.dat test-pions—327.dat	ADC_170930_031626_322 ADC_170930_032220_323 ADC_170930_042139_324 ADC_170930_051534_325 ADC_170930_052229_326 ADC_170930_062026_327	5.00E+04 5.00E+04 0.00E+00 5.00E+04 9.00E+04 0.00E+00	1.00E+05
0	100	22	test-pions—328.dat test-pions—329.dat	ADC_170930_071724_328 ADC_170930_074344_329	5.00E+05 5.00E+05	1.40E+05
-700	0	23	test-pions—328.dat test-pions—329.dat	ADC_170930_071724_328 ADC_170930_074344_329	5.00E+05 5.00E+05	1.00E+06
					Total:	7.34E+06

Table 3.3: High Voltage scans with extra weights on the short straw. Useful HV scan runs: 288–298.

Short straw (V)	Long straw (V)	Number of run	MAMBA file name	VME file name	Statistics	Total
Short straw offset: “-400”, long straw offset: “30”. CFD thresholds for both tubes are set to -15 mV.						
2100	1850	283	test-hadrons—283.dat	ADC_170924_000524_run283	0.00E+00	1.00E+06
		288	HVscan-hadrons—288.dat	ADC_170924_024940_run288	5.00E+05	
		289	HVscan-hadrons—289.dat	ADC_170924_035116_run289	5.00E+05	
1900	1700	290	HVscan-hadrons—290.dat	ADC_170924_043747_run290	5.00E+04	5.50E+05
		291	HVscan-hadrons—291.dat	ADC_170924_044110_run291	5.00E+05	
		298	HVscan-hadrons—298.dat	ADC_170924_074736_run298	0.00E+00	
2000	1750	292	HVscan-hadrons—292.dat	ADC_170924_051937_run292	5.00E+04	1.05E+06
		293	HVscan-hadrons—293.dat	ADC_170924_052433_run293	5.00E+05	
		297	HVscan-hadrons—297.dat	ADC_170924_071336_run297	5.00E+05	
2200	1800	294	HVscan-hadrons—294.dat	ADC_170924_055855_run294	5.00E+04	5.50E+05
		295	HVscan-hadrons—295.dat	ADC_170924_060658_run295	0.00E+00	
		296	HVscan-hadrons—296.dat	ADC_170924_064021_run296	5.00E+05	
Short straw offset: “-700”, long straw offset: “30” CFD thresholds for both tubes were set to default: -30 mV.						
2200	1800	238	offsetScan_hadrons—238.dat	ADC_170918_040326	1.00E+04	2.01E+06
		239	offsetScan_hadrons—239.dat	ADC_170918_040957	5.00E+05	
		240	offsetScan_hadrons—240.dat	ADC_170918_043505	5.00E+05	
		241	offsetScan_hadrons—241.dat	ADC_170918_045951	5.00E+05	
		242	offsetScan_hadrons—242.dat	ADC_170918_052423	5.00E+05	
2000	1750	244	offsetScan_hadrons—244.dat	ADC_170918_055527	0.00E+00	5.00E+05
		245	offsetScan_hadrons—245.dat	ADC_170918_061952	5.00E+05	
		246	offsetScan_hadrons—246.dat	ADC_170918_065735	0.00E+00	
		247	offsetScan_hadrons—247.dat	ADC_170918_072436	0.00E+00	
					Total:	5.66E+06

Table 3.4 summarizes the statistics collected in the various scans. The total number of events recorded during the test beam for all measurements is also shown.

Table 3.4: Total statistics acquired during the test beam experiment.

Type of measurement	Number of events (millions)
Offset scans	24.66
Offset scans with applied weights	7.34
HV scans	3.15
Thresholds scans	2.51
Total number of events recorded	37.66



## 3.2 Telescope data analysis

### 3.2.1 Beam profiles

The connection between the real position of each sensor of the telescope and their identifier (ID) in the reconstruction software is shown in Table 3.5. The “0” Z position represents the closest “Y” sensor of the telescope to the straw tubes according to the experimental setup shown in Figure 4.3.

The tracks in the telescope are fitted using the measured clusters of each tracking plane. A cluster is formed from several neighboring strips where a signal is measured. Figure 3.4 shows typical distributions of the number of clusters per sensor. Only one sensor, the last “Y” tracking plane (Det 7), exhibits a distribution with sensibly larger RMS and mean than others, which on average have around 1 cluster per sensor. However, this does not have a significant influence on the track fitting quality, because the clusters from all 8 tracking planes are used to make a track. The distribution of the total number of clusters per event is shown in Figure 3.5. The peak at a value of “8” reflects the fact that, in a large sample of events, there is 1 hit per tracking plane.

The distribution of the cluster position per sensor in Figure 3.6 shows essentially the beam profile in each tracking plane. Only the clusters which are associated to a track were used. The last sensor (Det 7) has a similar distribution compared to the others, which supports the above statement about the negligible influence of the excess cluster multiplicity in this sensor on the track quality.

Figure 3.7 shows the MAMBA time difference between two consecutive triggers. The distribution is dominated by the VME system busy time (of the order of 0.5 ms). The small peak at  $\approx 1.6 \cdot 10^5 \mu\text{s}$  is due to the MAMBA being busy writing out buffers to disk. The temporal spill profile taking into the account dead time of the whole system is shown in Figure 3.8. There are periodic dips in each temporal profile. The distance between the consecutive dips is 0.64 s. The width of each gap is 0.16 s, for the reason explained above.

Table 3.5: The software detector IDs and their real arrangement along the beam.

Detector Z position (cm)	ID in decoding software	The measured coordinate
0	Det1	Y
20	Det0	Y
50	Det2	Y
70	Det3	Y
10	Det4	X
30	Det5	X
40	Det6	X
60	Det7	X

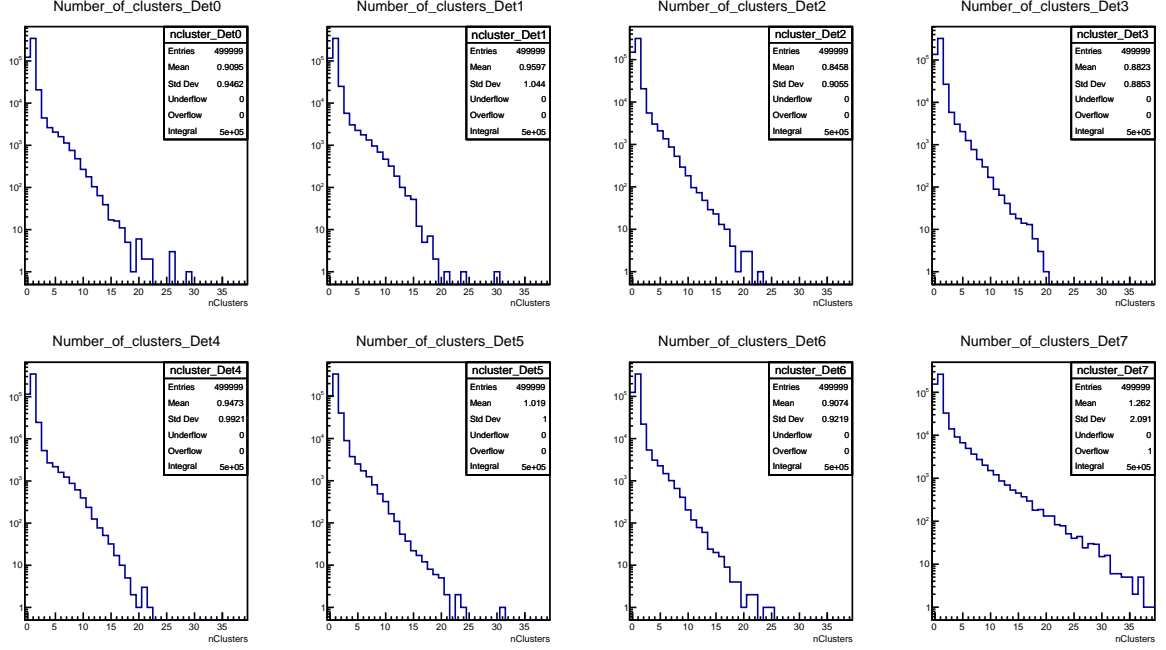


Figure 3.4: Number of clusters per event per sensor.

### 3.2.2 Tracks reconstruction

The tracks are reconstructed using the artificial retina algorithm [73]. The minimum number of clusters per event required to run the track reconstruction was set to 8. In addition, at least 1 cluster per sensor was requested. The distribution of the total number of tracks per event obtained with these settings is shown in Figure 3.9. In the further analysis only the events with exactly one track were used (about half of the reconstructed events).

### 3.2.3 Telescope alignment

The alignment of the telescope was checked using a dedicated software tool<sup>7</sup>. This software tool corrects the misalignment parameters, here the most sensitive ones being the sensor offsets ( $\Delta X$  and  $\Delta Y$ ) in the  $XY$  plane and a possible rotation ( $\phi$ ) around the  $Z$  axis (the  $Z$  positions were measured by hand and kept constant).

Typical distributions of the track residuals<sup>8</sup> in the sensor planes after the alignment corrections are shown in the plots of Figure 3.10.

In Table 3.6 the alignment corrections obtained for our run are summarized.

<sup>7</sup>The software can be downloaded from a GitHub repository: [https://gitlab.cern.ch/mpetrzz/Sbt\\_Milano](https://gitlab.cern.ch/mpetrzz/Sbt_Milano)

<sup>8</sup>These are biased residuals, with the considered hit used also in the track fit.

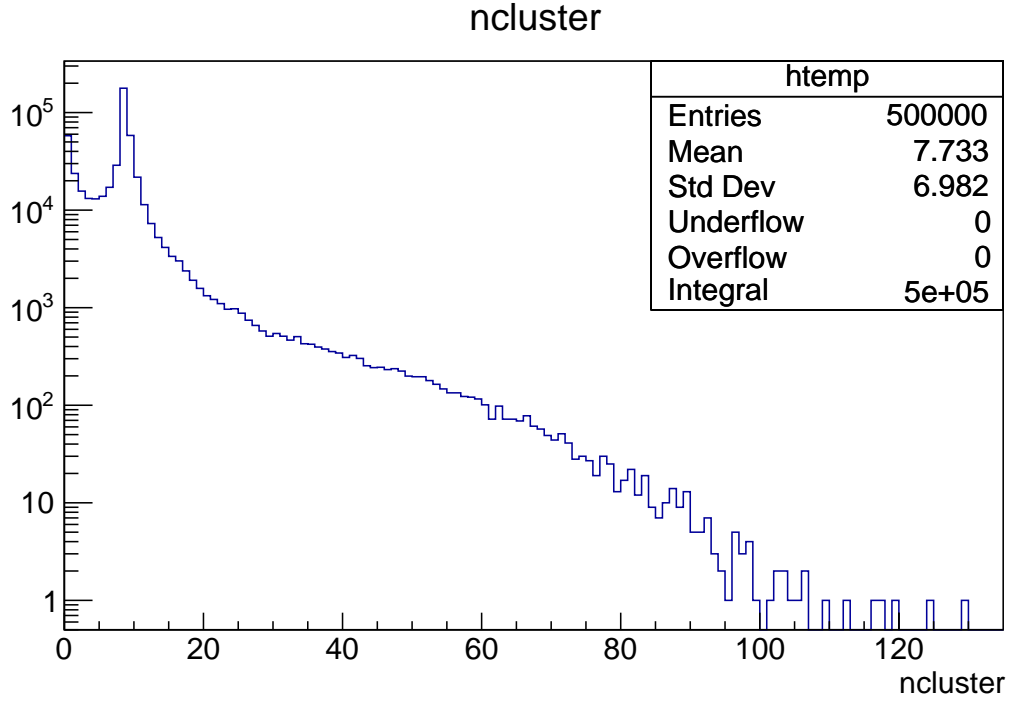


Figure 3.5: Total number of clusters per event.

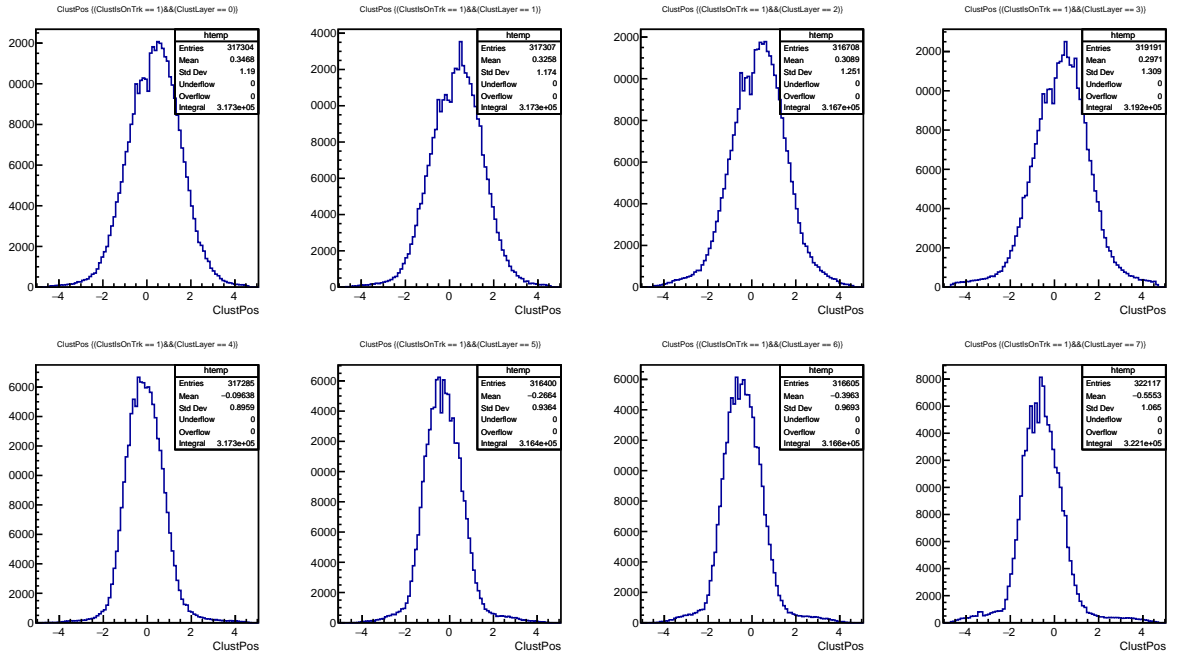


Figure 3.6: The distribution of cluster position in cm for each sensor.

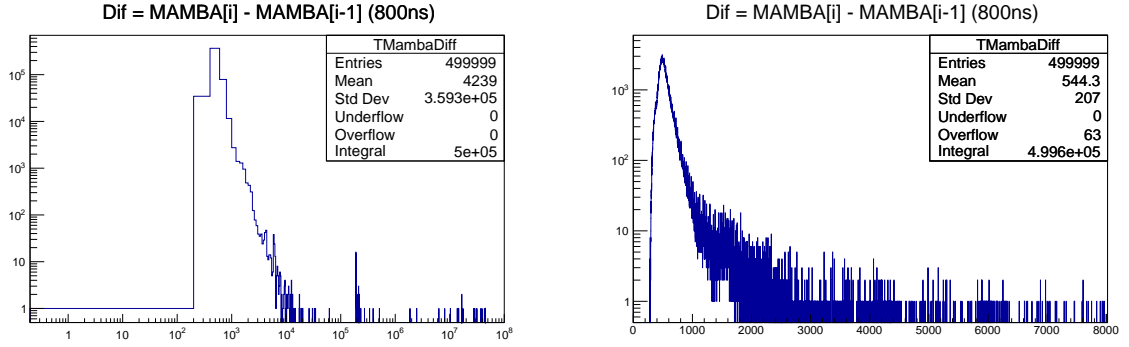


Figure 3.7: Difference in MAMBA time (in units of 800 ns) between consecutive triggers. The left histogram is in full range Log-Log scale. The right one is a zoomed version showing the first peak.

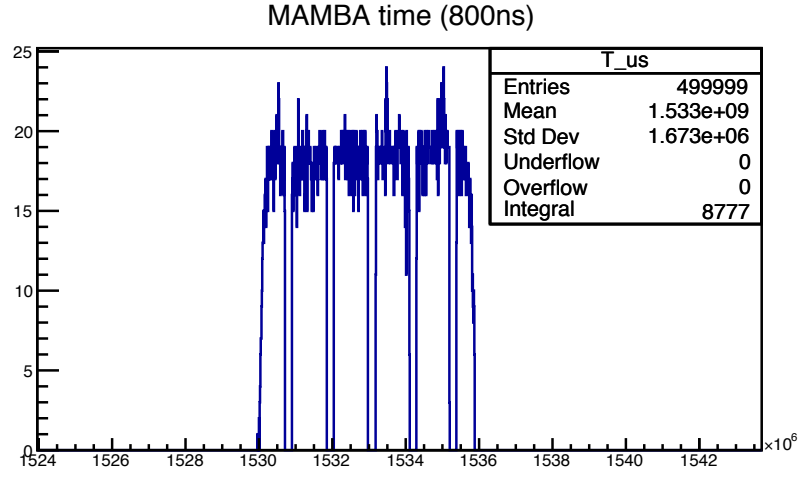


Figure 3.8: Typical temporal beam spill profile in units of 800 ns.

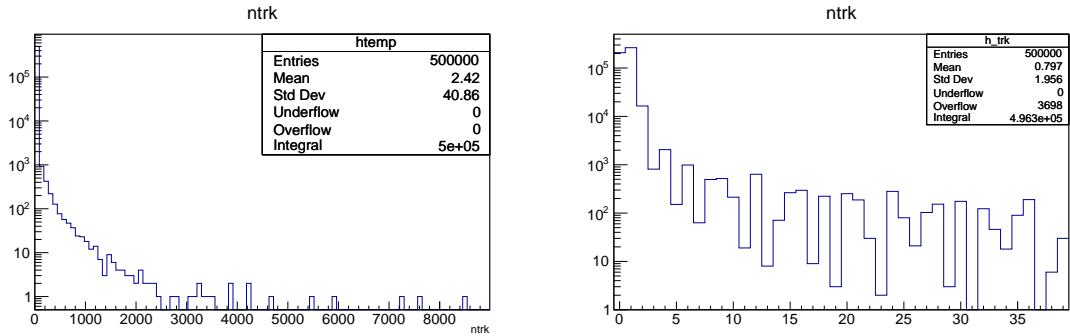


Figure 3.9: The total number of tracks per event.

Table 3.6: Telescope alignment parameters in our experiment (see text).

Plane	$\phi$ ( $^\circ$ )	$\Delta X$ (cm)	$\Delta Y$ (cm)
0	0.171	-0.000	-0.019
1	-0.055	0.000	0.014
2	-0.206	-0.000	-0.001
3	0.097	0.000	0.006
4	-0.010	-0.002	0.000
5	-0.013	-0.014	0.000
6	0.045	0.026	0.000
7	-0.024	-0.010	0.000

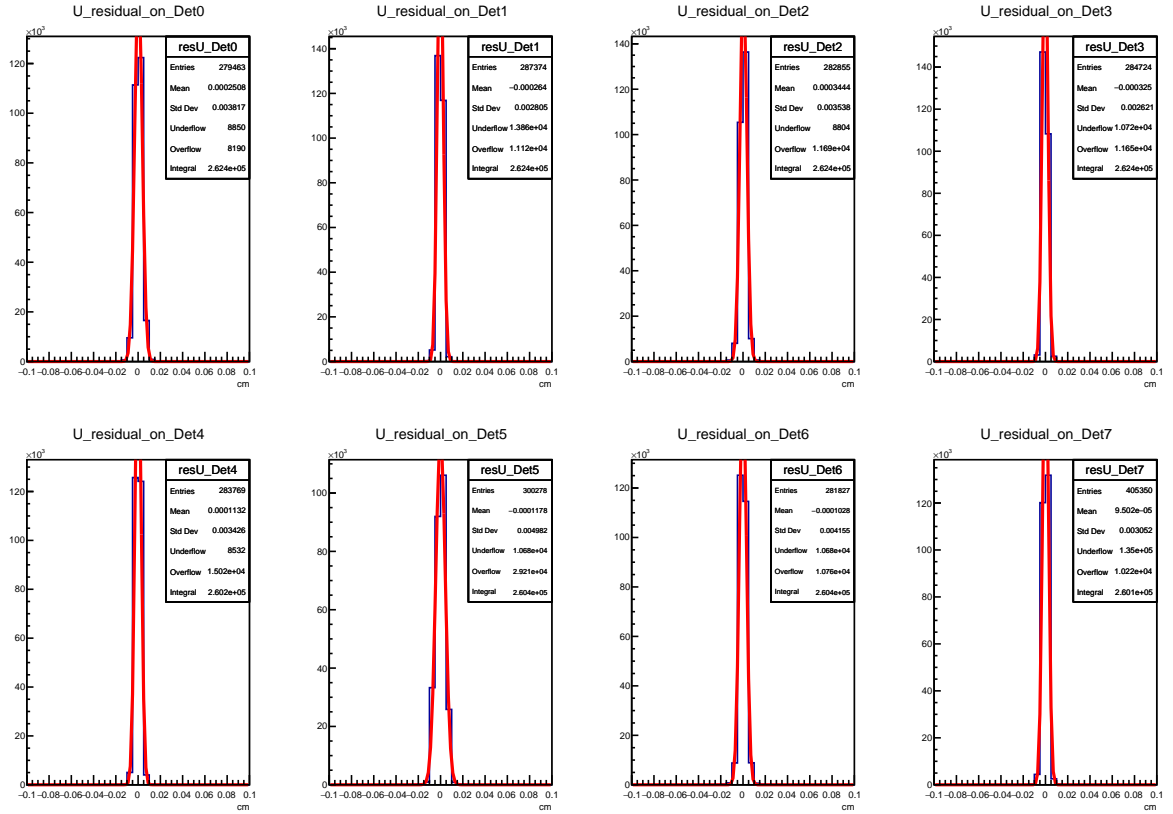


Figure 3.10: Track residuals per plane of the telescope.

### 3.2.4 Track extrapolation and hit maps

The information about the tracks is stored in the MAMBA tree. It contains  $b_U$ , the initial position of the tracks at  $z = 0$ , and  $a_U$ , the slope of the track in the  $UZ$  plane. Here, the  $U$  coordinate stands for either  $X$  or  $Y$ . Using those values one can extrapolate

the tracks and evaluate their errors at the DUT positions. Some extrapolated tracks are shown for illustration in Figure 3.11. The extrapolation errors are calculated as follows.

$$\sigma_{DUT}^2 = \left( \frac{\partial U}{\partial b_U} \right)^2 \sigma_{b_U}^2 + \left( \frac{\partial U}{\partial a_U} \right)^2 \sigma_{a_U}^2 + \sum_{i \neq j} \text{cov}(b_{U,i}, a_{U,j}) \frac{\partial U, i}{\partial b_{U,i}} \frac{\partial U, j}{\partial a_{U,j}}, \quad (3.1)$$

where  $U = a_U \cdot Z + b_U$  is the extrapolated coordinate of the track,  $\sigma_{b_U}$  is the error of  $b_U$  and  $\sigma_{a_U}$  is the error of  $a_U$ ,  $\text{cov}(b_{U,i}, a_{U,j})$  is the non-diagonal value of the covariance matrix for  $b_U$  and  $a_U$ .

For the analysis described in this thesis expression (3.1) can be simplified using the definition of  $U$ :

$$\sigma_{DUT}^2 = \sigma_{b_U}^2 + Z^2 \sigma_{a_U}^2 + \sum_{i \neq j} Z \text{cov}(b_{U,i}, a_{U,j}). \quad (3.2)$$

From expression (3.2) the extrapolated error at the short straw tube position is found to be about  $60 \mu\text{m}$  and at the long one about  $50 \mu\text{m}$ .

Using the obtained extrapolated coordinates and the constrains described above one can build the beam profiles at the DUT positions, see Figure 3.12(a) for the short straw

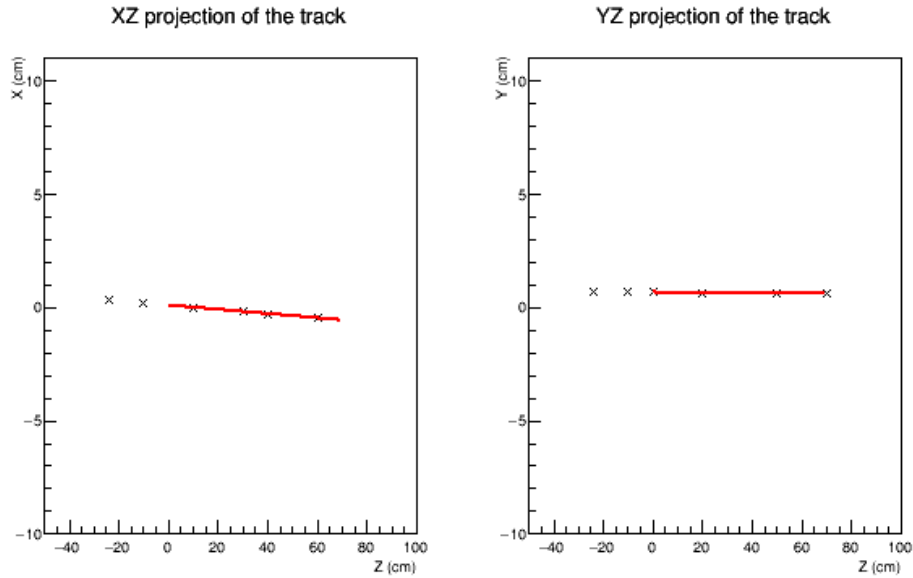
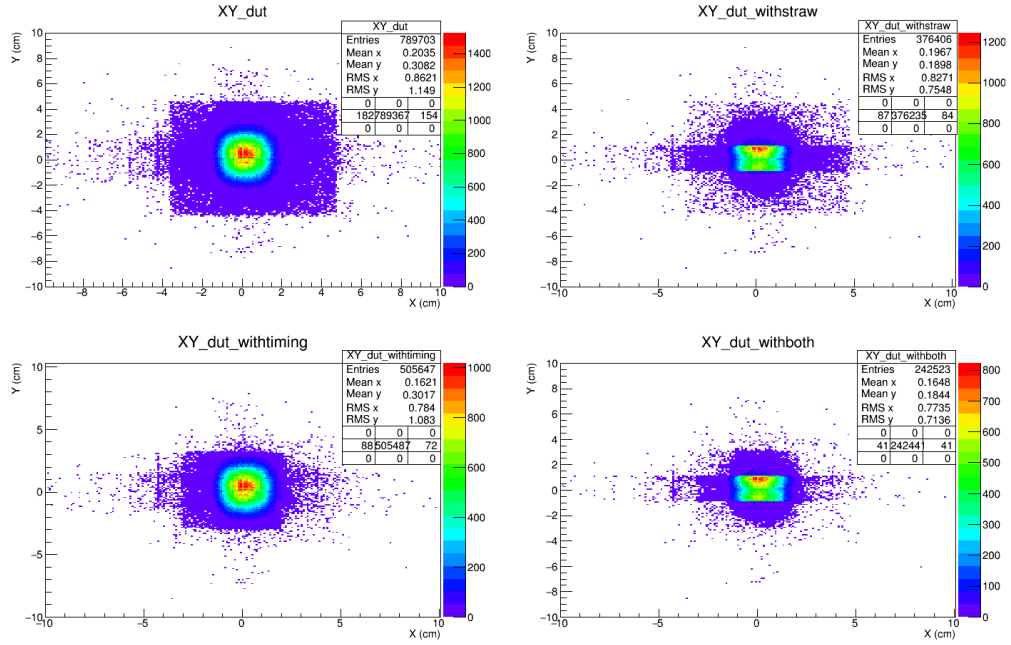


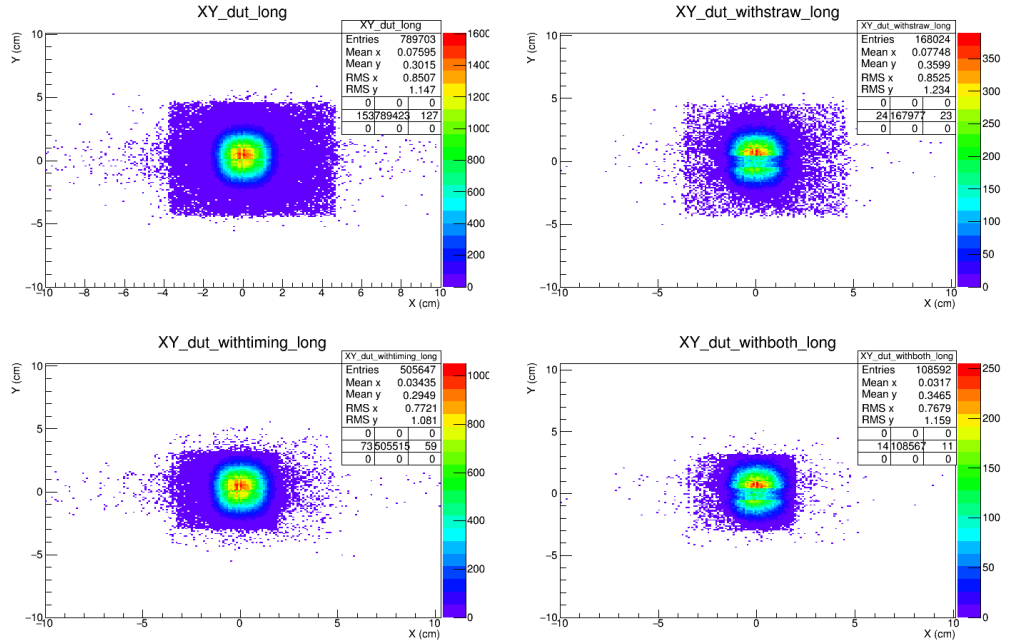
Figure 3.11: Extrapolated tracks projections onto  $XZ$  and  $YZ$  planes. The red line shows the track within the telescope. The crosses are intersects inside the telescope planes. The points outside the red line range are extrapolated intersects at the position of the short (-24 cm) and long (-10 cm) straw tubes.

and 3.12(b) for the long straw. The raw distributions are shown for the extrapolated tracks positions in the  $XY$  plane (top right), and after requiring one straw hit (top right) or one timing scintillator hit (bottom left), or both together (bottom right).

The shape of the short straw tube is clearly seen in the corresponding beam profiles. For the long straw tube the distribution is different. There are many hits outside the straw tube geometrical position, due to noise, as is further discussed in Section 3.4.



(a) Beam profiles at short straw tube position.



(b) Beam profiles at long straw tube position.

Figure 3.12: Beam profiles at DUT positions at the (a) short and (b) long straws based on triggered events with a single track. Top left: extrapolated track positions. Top right: with requirement of exactly 1 hit in the DUT. Bottom left: with requirement of exactly 1 hit in the T0 detector. Bottom right: with both requirements applied.



### 3.3 Optical measurement of the wire eccentricity

One of the tasks performed during the test beam was to measure the detector response for different applied offsets on the straw tubes. The offset was applied using special graduated holders (see Figure 3.3). The precision of those instruments allowed to adjust the position of the tube within  $20\text{ }\mu\text{m}$  uncertainty. It is important to note that, when the tube was shifted by a certain value, the wire was displaced as well due to the different electric field configuration. Therefore, the change in tube offset (also called “applied offset”) is *not* identical to the change in wire eccentricity.

In order to prove the validity and consistency of the wire eccentricity values extracted from tracking and drift time data, a direct measurement was performed during a pause of the test beam run. The straw tube walls are sufficiently thin ( $36\text{ }\mu\text{m}$ ) to allow seeing through the wall, when an adequate light source is used to shine from the other side of the straw. This feature was used to determine the position of the wire inside the straw tube. As a light source, 5 LEDs were used. The straw and wire images were captured with a Dino-Lite AM7515MZTL-Edge digital microscope [53]. This microscope has 5M pixels resolution, adjustable magnification of 10x–140x, 8 white LEDs for lighting and can be calibrated with a special calibrating plate. The image obtained from the microscope shows the dimensions of the straw tube and, due to the transparency feature of the tube walls, the shadow of the wire (see Figure 3.13b). A proprietary image processing tool of the digital microscope was used to measure distances on the image. The tool was calibrated using a special calibrating plate with a ruler provided by the manufacturer of the microscope. The uncertainty of the digital microscope measurements is  $\sim 20\text{ }\mu\text{m}$ . The complete optical setup is shown in Figure 3.13a.



(a) Optical setup installed around the short straw tube. The digital microscope is visible on the right, the LEDs on the left (opposite side of the straw).



(b) Sample image obtained from the digital microscope. The shadow of the wire can be observed in the middle of the tube and is highlighted by the LED spots.

Figure 3.13: Pictures illustrating the optical measurements of the wire eccentricity.

Table 3.7: Applied straw offset and wire eccentricity as extracted from the isochrone relation (V-shape) analysis and compared to the optically measured wire eccentricity for the short straw tube. The values on the left are for the short tube and have a precision of about  $450\text{ }\mu\text{m}$ . The values for the long tube are shown on the right for the sake of completeness, although the precision of the measurement was considerably poorer due to the noise ( $\sim 1\text{ mm}$ ).

Short straw tube			Long straw tube	
Applied offset ( $\mu\text{m}$ )	V-shape extracted eccentricity ( $\mu\text{m}$ )	Optically measured eccentricity ( $\mu\text{m}$ )	Applied offset ( $\mu\text{m}$ )	V-shape extracted eccentricity ( $\mu\text{m}$ )
1500	2053	2388	0	-127
1400	2080	2323	100	150
1300	1963	2146	200	452
1200	1965	2178	300	849
1100	1987	1907	250	563
1000	1787	1952	150	346
900	1762	1709	50	38
800	1565	1709	-50	-253
700	1566	1495	-150	-579
600	1467	1499	-250	-923
500	1317	1269	-200	-774
400	1266	1160	-100	-373
300	1318	1180	0	-169
500	1167	1269	30	-81
500	1116	1269	80	28
0	869	671	130	219
-500	225	275	300	510
-700	106	-61	100	-22
-800	-71	-117	0	-348

The data analysis of the straw drift time distributions and isochrone relation (also called “V-shape”) allow one to quantitatively estimate the wire eccentricity value with respect to the straw tube axis, as explained in details later (see Section 3.4). The results of such analysis are given in Table 3.7.

The results of the wire eccentricity measurements using the optical setup and the results of the test beam data analysis are shown in Figure 3.14. Due to time constraints, only the short straw tube was investigated using the optical method. The blue circles show the optical results obtained, when not applying the weights to the straw tube. The corresponding results obtained from the V-shape analysis are shown by the green circles. One clearly sees that, for negative values of the adjuster offset, the measured wire eccentricity is constant, indicating that the supports detach from below the straw. For this reason the weights were added on the short straw. With these weights added one could reach meaningful adjuster offsets down to  $-0.8\text{ mm}$  and thus make the wire eccentricity cross the zero value, as shown by the circles in red (optical result). The reference line showing the accordance between the optically measured wire eccentricities and the ones

obtained from the V-shape analysis is shown in Figure 3.15. Overall, the optical results are in agreement with the values obtained from the V-shape analysis. A linear fit of the optically measured wire eccentricity as a function of the applied offset gives a slope of  $1.12 \pm 0.02$ . It is larger than 1 due to the electric force acting on the wire. A linear fit of the measured wire eccentricity from the V-shape analysis has a slope of  $0.96 \pm 0.15$ . The linear fit deviates from the one of the optical measurement for the large values of the wire eccentricity meaning that the apex position estimation for the V-shape analysis is less precise for large wire eccentricities.

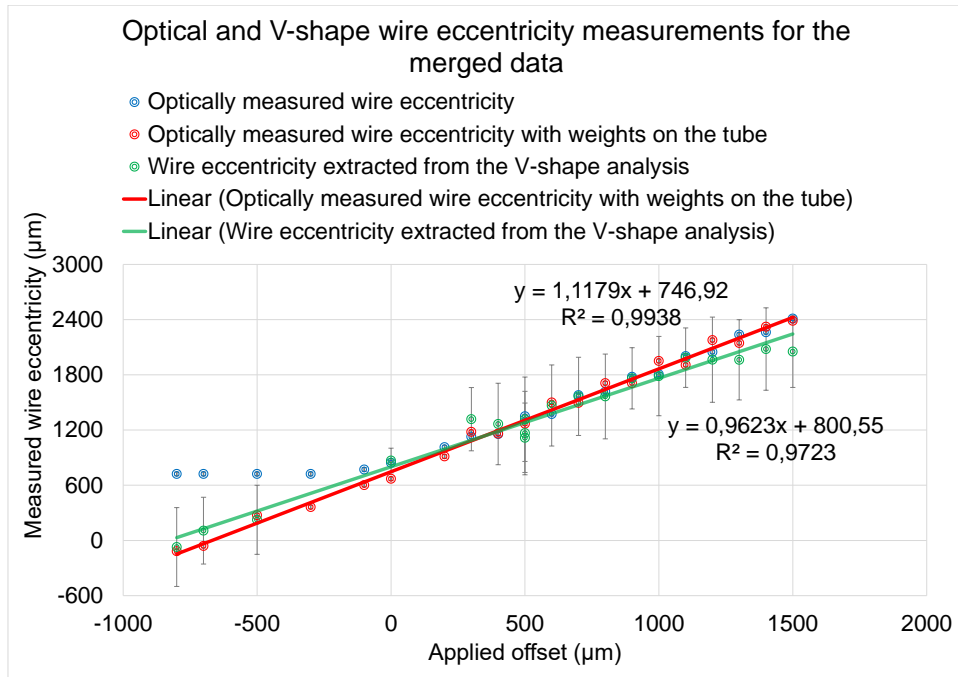


Figure 3.14: Comparison between optical measurements of the wire eccentricity and the values obtained from the V-shape data analysis for the short straw tube.

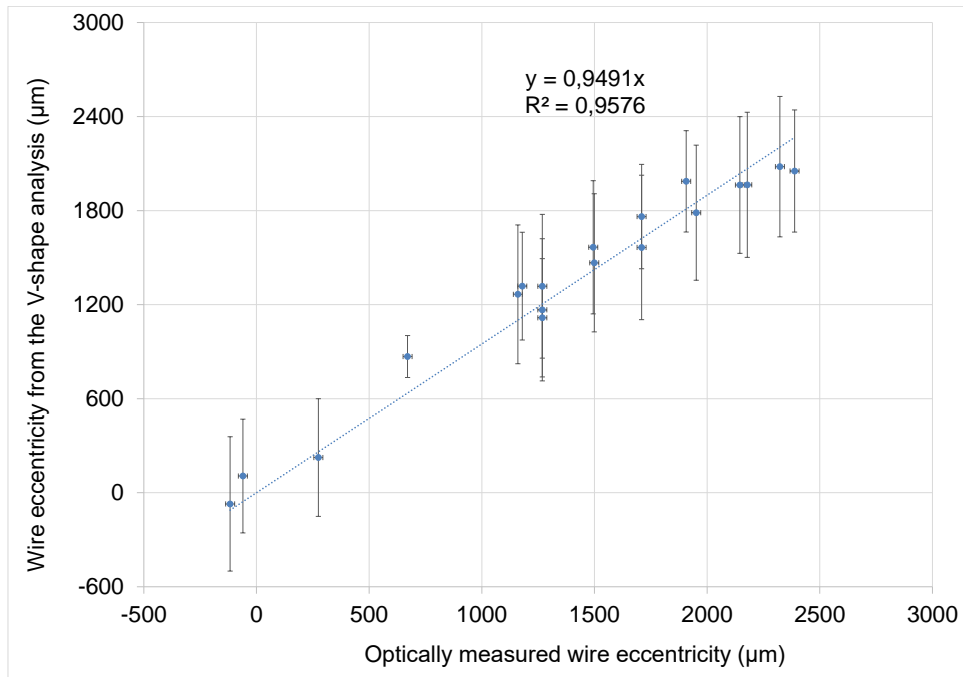


Figure 3.15: The reference line relating the optically measured wire eccentricities and the ones obtained from the V-shape analysis.

## 3.4 Data quality and event selection

The goal of the analysis is to evaluate the resolution of straw tubes depending on the wire eccentricity and the high voltage applied on the tubes. In this section, various features of the data quality and event selection are discussed. For the sake of simplicity, a run (nr. 222) is used, where the wire eccentricity was relatively small (0.19 mm) and the run nr. 239 with the similar offset value (0 mm), but with the CFD threshold value of -30 mV instead of the default -15 mV. The runs with larger wire eccentricities are discussed in Section 3.5.

### 3.4.1 Data rates, pile-up and noise sources

The hit rate measured by the closest scintillator along the H2 beam line (XSCI.021.528) was  $\approx 10^5$  hits per SPS spill. The spill length is 4.72 s, so the hit rate per second is  $10^5/4.72 \approx 21.2$  kHz. According to the Figure 3.7 the mean dead time of the DAQ system is  $\approx 435$   $\mu$ s. Assuming a non-paralyzable DAQ system the recorded hit rate should be equal to:

$$m = \frac{n}{1 + \tau_{dead}n} = \frac{21.2}{1 + 435 \cdot 0.0212} \approx 2.1 \text{ kHz}, \quad (3.3)$$

where  $m$  is the recorded rate (events per second) with the DAQ,  $n$  is the rate from the beam line scintillator and  $\tau_{dead}$  is the mean dead time of the system from Figure 3.7. The recorded event rate is close to the obtained theoretical value. One can extract the recorded event rate using Figure 3.8 and it is  $\approx 1.9$  kHz. Some particles, especially from the beam halo, are lost, because the last 20 m upstream the test beam setup the beam traverses through the air outside the beam pipe and the halo particles can escape the acceptance of the experimental setup due to the elastic scattering. Also each 0.64 s the MAMBA board reads out its buffers to the PC and thus the whole DAQ is dead for 0.16 s. All these facts make the real event rate smaller than theoretically predicted.

According to Figure 3.8 the event rate is constant along the spill duration and this means that the particles arrival time during the spill will follow the Poisson distribution. The  $\lambda$  parameter (the mean) of the Poisson distribution is equal to the original rate  $n$  multiplied by the time window width  $\Delta t$ , when the DAQ system records hits in the DUTs, the T0 detector and the telescope planes. The event in the DAQ is created, when the coincidence signal from the trigger scintillators is received. Assuming the fact that the trigger scintillators are located 1.5 m apart from each other and both have double SiPMs read-out, the probability of getting random coincidence signal is negligibly small. So, it is possible to assume that the DAQ is triggered most probably due to the real track passing through the experimental setup. After the scintillators are triggered the system records all the hits in the detectors within the  $\Delta t = 1.5$   $\mu$ s time window. According to the Poisson distribution the probability of getting a single track within such a window is:

$$p_1(\Delta t) = n\Delta t \exp(-n\Delta t) = 0.0308 \quad (3.4)$$

The probability of getting more than one track within such a window is:

$$p_{>1}(\Delta t) = 1 - p_0(\Delta t) - p_1(\Delta t) = 1 - \exp(-n\Delta t) \cdot (1 + n\Delta t) = 0.0005 \quad (3.5)$$

These probabilities are used below to understand triggered event track multiplicities.

### Silicon telescope

If the telescope planes had the same area as the trigger scintillator and had 100% hit efficiency and track reconstruction efficiency, the probability of reconstructing a single track within the  $\Delta t = 1.5 \mu\text{s}$  time window of a trigger would be  $p(N_{\text{track}} = 1) = p_1(\Delta t)/(p_1(\Delta t) + p_{>1}(\Delta t)) = 0.984$  and the probability of reconstructing more than one track would be equal to  $p(N_{\text{track}} > 1) = p_{>1}(\Delta t)/(p_1(\Delta t) + p_{>1}(\Delta t)) = 0.016$ . Naturally, the silicon tracking planes are not 100% efficient. There are noise hits in the strips, some strips do not respond or are continuously fired due to the high baseline offset, but the main contribution to the global inefficiency of the telescope comes from the track reconstruction algorithms. Those algorithms have many parameters, which are configured by the developer of the software and allow for getting tracks of good quality, but at the same time they reduce the overall efficiency. The mentioned features of the track reconstruction lead to the fact that in the real data samples taken with the telescope only 52.71% of the events have a single track reconstructed, 5.74% are the events with multiple tracks (more than one), the rest of the events do not have any reconstructed track. According to Figure 3.6 the beam is almost centered in each tracking plane (as much as it was possible to adjust its position with collimators and magnets of the H2 beam line) covering more than  $3 \cdot \text{RMS}$  of the beam profile. This means that the geometrical acceptance of the telescope can be assumed to be close to 100% of all incoming particles of the beam. The ratio between single track events in the telescope and multiple track events is  $0.902 : 0.098$ , which deviates from the theoretically expected  $0.984 : 0.016$  from the estimated event pile-up. A part of this excess can be explained by particles interacting in the materials of our experimental setup. This is already hinted at by the distribution of track multiplicity shown in Figure 3.9: the contribution from the events with 4 and more tracks does not drop as quickly as expected from a Poisson distribution for the incoming rate of 21.2 kHz. The rate of nuclear interactions in the T0 detector can be roughly estimated. The probability for a charged particle to undergo inelastic nuclear interaction according to [74] after passing through the material of a thickness  $l$  is equal to:

$$P(l) = 1 - \exp\left(-\frac{l}{\lambda_I}\right), \quad (3.6)$$

where  $\lambda_I$  is the nuclear interaction length. A typical  $\lambda_I$  value for commonly used plastic scintillators and charged pions having the momenta in GeV/c range is  $\approx 100 \text{ cm}$  [37]. The thickness of our T0 scintillator is 2.5 cm, so the probability of an inelastic nuclear interaction is 0.025. Taking into account that the beam size is somewhat larger than the T0 scintillator this value is reduced to  $0.9442 \cdot 0.025 = 0.024$ . Therefore, about a third

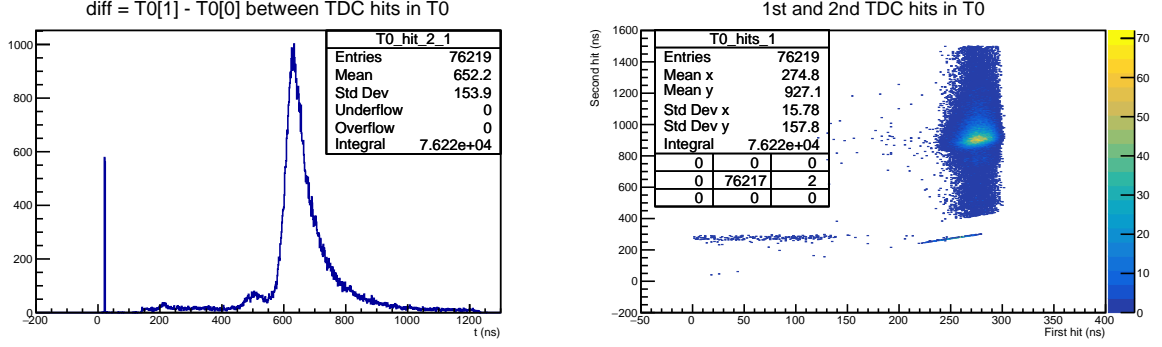


Figure 3.16: The histogram on the left: the time difference between the first and the second hit in the T0 for events with at least two T0 hits. The scatter histograms on the right: the first hit in T0 *vs.* the second hit in T0 shown one against the other with the same event selection.

of the above excess may be explained by interactions in the T0 detector alone. The rest of the excess of multiple track events might be explained by other materials and also by noise hits or split clusters in the telescope producing more reconstructed tracks.

### T0 detector and DUTs

The T0 detector has a sensitive area ( $5 \times 6 \text{ cm}^2$ ) smaller than the telescope planes, but still covers most of the beam profile: 92.84% of single track events have at least 1 hit in T0 and 94.42% of all triggered events with at least 1 track. The hit rate  $n$  in the T0 is affected by the (configurable) dead time of the CFD<sup>9</sup>. According to the CFD specifications the minimal dead time is 150 ns per channel and it was configured by the DAQ software to be 160 ns. Using equation (3.3) and substituting  $\tau_{dead}$  with 160 ns the hit rate  $m$ , which the T0 can record, is 21.13 kHz. Taking into account the geometrical acceptance and the calculated hit rate  $m$ , the average number of tracks passing through the T0 in  $\Delta t = 1.5 \mu\text{s}$  time window becomes smaller:  $m\Delta t \cdot 0.9442 = 0.0299$ . From equations (3.4) and (3.5), the Poisson probabilities of getting a single particle and many particles through the T0 during  $\Delta t$  are 0.0290 and 0.0004. The measured fraction of triggered events with a single hit in T0 is 0.6432 and for more than 1 hit it is 0.3112, the rest being with no hits. If, in addition, a single reconstructed track is requested which extrapolates through T0, then these fractions become 0.6984 and 0.3008 (showing that the T0 detector is efficient). In order to understand the significant discrepancy in the ratio between single hit events and multiple hit events (almost 70 in theory and about 2 in the measurement), the processes inside the PMT are invoked. A first contribution comes from the dark count rate (the intrinsic characteristic of the chosen PMT) and the exterior light coming through the holes in the insulation covering the photocathode window of the PMT and the plastic scintillator. These signals are random and uniformly distributed within the selected time window of

<sup>9</sup>CAEN model V812

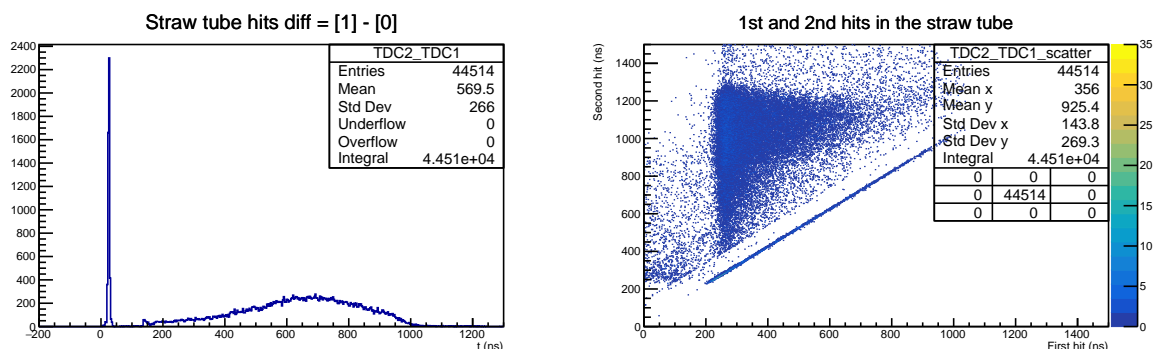


Figure 3.17: Left: the difference between the 2<sup>nd</sup> and the 1<sup>st</sup> consecutive hits in the short straw tube for  $N_{tube} \geq 2$ . Right: the scatter histogram for the 2<sup>nd</sup> and the 1<sup>st</sup> consecutive hits in the short straw tube. Considering triggered events with a single reconstructed track extrapolating through the nominal diameter of the tube.

1.5  $\mu$ s. Another significant contribution to the multiple hits rate in the T0 comes from the afterpulses formed, when the residual gas in the PMT gets ionised with electrons and those ions travel back to the photocathode and release the new electrons. The afterpulses from ions can arrive in a time range from hundreds of nanoseconds to tens of microseconds depending on the type of the ions, the internal structure and dimensions of the PMT. The contribution from both random background and afterpulses is shown in Figure 3.16. In the first histogram the difference in time between the first and the second consecutive hits in the T0 detector for single tracks, which penetrated through the T0 detector, is shown. The random noise forms a plateau starting from 160 ns. On top of the plateau there is a huge peak representing the afterpulses from the ion feedback inside the PMT. There is a highly correlated narrow peak in the beginning of the distribution at  $\approx 25$  ns, which is related to the issues at the TDC input (sometimes the signal is duplicated with a constant time shift).

The DUTs cover a smaller fraction of the beam profile than the T0 detector: about 73.51% (40.82%) of all reconstructed tracks pass through the short (long) tube. Both tubes are read out with the same CFD as the T0 detector meaning that the dead time per channel is also 160 ns. Thus, following the same reasoning as above, the expected mean number of particles passing through the short tube in a  $\Delta t = 1.5 \mu$ s time window of triggered events is  $m\Delta t \cdot 0.7351 = 0.0233$ , and  $m\Delta t \cdot 0.4082 = 0.0129$  for the long tube. Thus, the Poisson probabilities of getting a single particle and multiple particles passing through the tubes in the 1.5  $\mu$ s time window are 0.0228 and 0.00027 for the short one, 0.0127 and 0.00008 for the long one. Considering triggered events with a single reconstructed track extrapolating through the nominal diameter of the DUT, for the CFD threshold setting of -15 mV, the measured fractions of events with a single hit and more than 1 hit in the short tube are 0.7144 and 0.2272, the rest being with no hits. For the long tube these fractions are 0.1248 and 0.8741. The data taken with the CFD threshold of -30 mV per channel and the same event selection give different fractions: 0.8623 and 0.1258 for the short tube, 0.7440 and



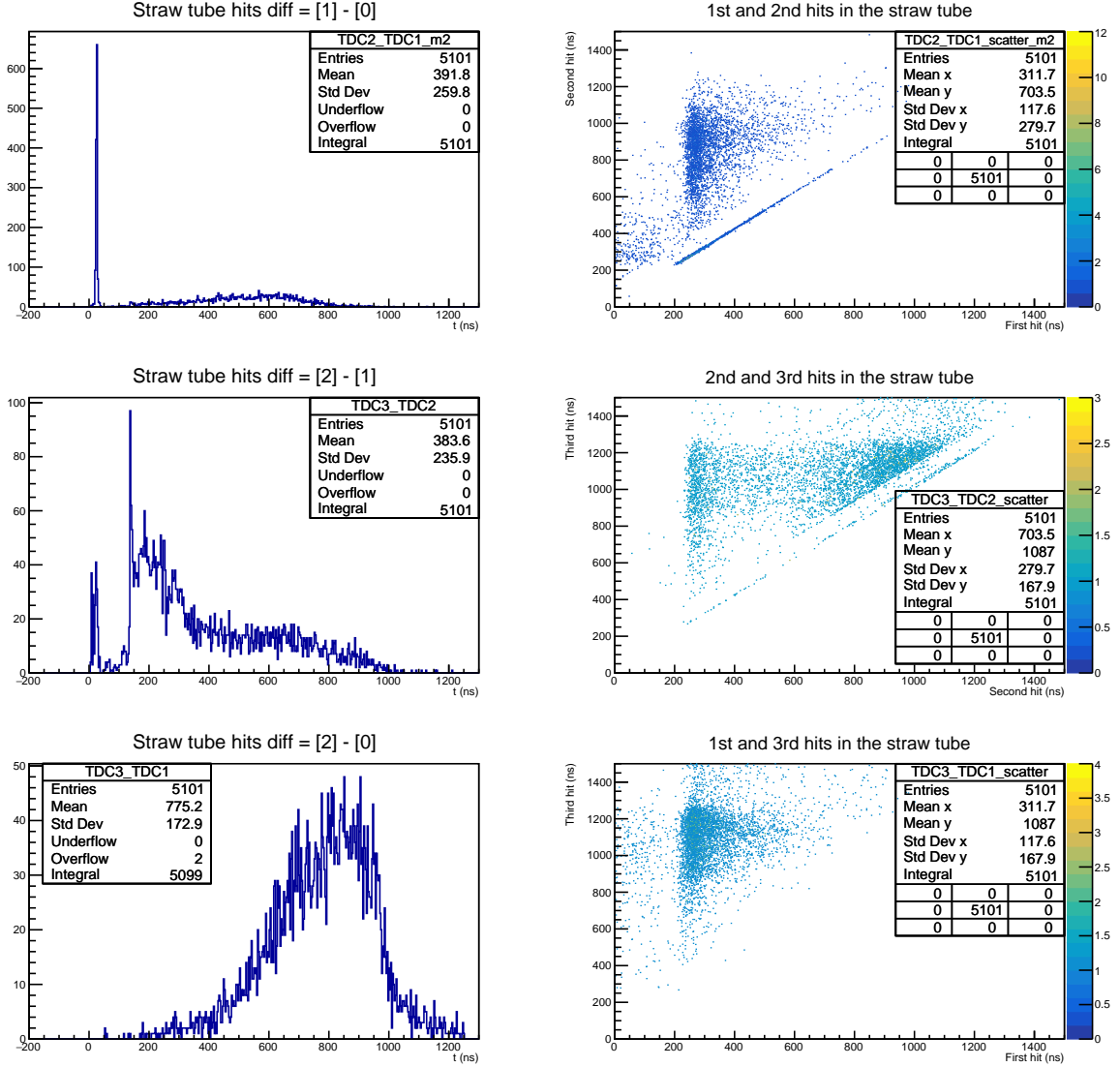


Figure 3.18: The difference between the consecutive hits in the short straw tube for  $N_{tube} > 2$ , considering triggered events with a single reconstructed track extrapolating through the nominal diameter of the tube. The left column of histograms shows the differences between the 2<sup>nd</sup> and the 1<sup>st</sup>, 3<sup>rd</sup> and the 2<sup>nd</sup>, 3<sup>rd</sup> and the 1<sup>st</sup> consecutive hits in the short straw tube. The right column of scatter histograms shows the corresponding consecutive hits one against the other.

0.2071 for the long one. Applying a higher CFD threshold affects significantly the rate in the long tube suppressing the electronics noise contribution, but the ratios between single and multiple hits in the tubes still do not converge to theoretically estimated ones. Other effects need to be invoked.

The signals induced in the anode wire of the straw tube have a sharp ( $\approx 5$  ns) leading

edge due to the fast electrons movement towards the wire and a long trailing edge (up to few milliseconds) formed by the ions drifting to the wall of the tube. If the amplifier and read-out electronics have a shaping time of the order of few nanoseconds, then the contribution from the primary ionization clusters can be observed in the signal (separate peaks appear). As it was mentioned above, the CFD had a dead time of 160 ns, which, in general, is not sufficient to suppress the remaining signal and the CFD can trigger again on the same signal contributing to multiple hits in the tube. The re-triggering effect generates the uniform noise after  $\approx 160$  ns in the consecutive hits differences in Figure 3.17 and Figure 3.18. Some events have purely correlated consecutive hits (a straight inclined line below the rest of the data can be observed in the scatter histograms in Figure 3.17 and Figure 3.18). These correlations have the same origin as the one observed for the T0 detector hits. Thus, a small fraction of consecutive hits have the value of their predecessor shifted by a constant value. However, the distributions of the difference between the second and the first hit and the third and the first signals in the short straw tube in Figure 3.17 and Figure 3.18 have wide peaks (RMS  $> 170$  ns) at  $\approx 680$  ns and  $\approx 850$  ns. These peaks can be explained by the decay of the excited argon states with the energy higher than the first ionization potential of the CO<sub>2</sub>. The excited states have life times up to few hundreds of nanoseconds (see Section 1.3) and created photons can ionize the atoms of CO<sub>2</sub> and create the coherent delayed avalanches. The fraction of such additionally released electrons to the total number of released electrons in the gas mixture can be estimated for the 150 GeV pion beam. The mean energy loss of 150 GeV pion in Ar is  $dE/dx = 2.4 \text{ MeV} \cdot \text{cm}^2/\text{g}$  and in CO<sub>2</sub> is  $dE/dx = 3.4 \text{ MeV} \cdot \text{cm}^2/\text{g}$  at NTP conditions [37]. The total number of electrons produced in either Ar or CO<sub>2</sub> is:

$$n_T = \frac{dE/dx}{W_I} \cdot \rho, \quad (3.7)$$

where  $\rho$  is the density of the gas and  $W_I$  is the average energy required to produce the electron-ion pair, 26 eV for Ar and 34 eV for CO<sub>2</sub> (see Section 1.3). These numbers, strictly speaking, are valid for a pure gas sample, while in the test beam setup a mixture was used of Ar (70%) and CO<sub>2</sub> (30%). However, a rough value for the total number of electrons can be evaluated assuming a simple density scaling and adding a correction for the fast Penning transfer<sup>10</sup>. For a rough estimate it is assumed that about 57% of the excited Ar atoms decay promptly by the fast Penning transfer [41], thus contributing to the total number of emitted electrons, and 43% through slow photon emission followed by ionization of CO<sub>2</sub>.

With the given gas mixture at NTP conditions, one estimates from (3.7)  $n_{T,\text{Ar}} \approx 107 \text{ cm}^{-1}$  and  $n_{T,\text{CO}_2} \approx 55 \text{ cm}^{-1}$ . The ratio between the total number of electrons in the ionization clusters  $n_T$  and the number of primary electrons  $n_p$  is similar for Ar (3.88) and CO<sub>2</sub> (2.86), see Section 1.3. Assuming this ratio does not depend on the energy of the impinging particle at high energy, one can estimate that  $n_{p,\text{Ar}} \approx 28 \text{ cm}^{-1}$ . The

---

<sup>10</sup>Fast Penning transfer occurs in mixture and is of the type  $A^* + B \rightarrow A + B^+ + e^-$ . It can deplete a selective fraction of the  $A^*$  population very rapidly, with life times below 1 ns for specific excited levels, see [75].

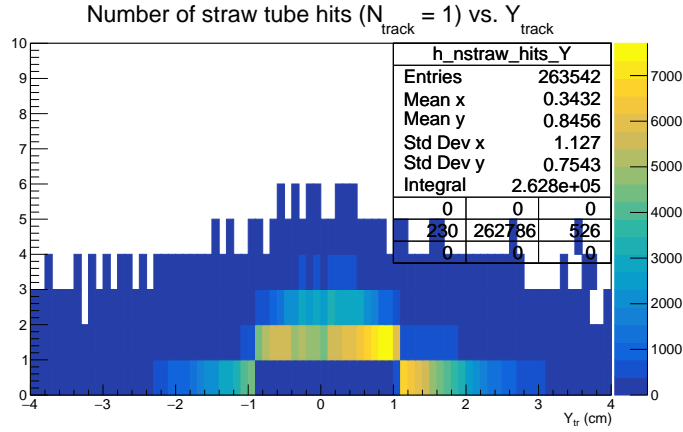


Figure 3.19: The number of hits in the short straw tube depending on the coordinate of reconstructed track at the position of the tube.

primary electrons have an average energy of about hundred eV and can either ionize or excite other atoms. Neglecting the mixture effects, the number of secondary electrons from Ar is  $n_{sec,Ar} = n_{T,Ar} - n_{p,Ar} \approx 79 \text{ cm}^{-1}$ . Since the ratio between ionization and excitation cross sections for electron-Ar interactions at 100 eV is about 3 (see Figure 1.10a in Section 1.3), the mean number of Ar atoms excited by the primary electrons can be expected to be roughly given by  $n_{exc,Ar} \approx n_{sec,Ar}/3 \approx 26 \text{ cm}^{-1}$  and it is assumed that 57% of those contribute to the prompt ionization by fast Penning transfer to  $\text{CO}_2$ , while 43% of those remain and induce a “delayed”  $\text{CO}_2$  ionization (a few hundred nanoseconds later, by photon radiation). Therefore, the number of “prompt” electrons (primary and secondary electrons) is in the order of  $n_{T,Ar} + n_{T,\text{CO}_2} + 0.57 \cdot 26 \text{ cm}^{-1} \approx 177 \text{ cm}^{-1}$ , while the number of delayed electrons is in the order of  $0.43 \cdot 26 \text{ cm}^{-1} \approx 11 \text{ cm}^{-1}$ . It is believed that this effect can explain, at least partially, the wide peak in Figure 3.17. It is also compatible with (a) the fact that an early decay is likely to be masked by the tail of the original pulse, as seen in Figure 3.17, and (b) the fact that some drift time values of the second hit go beyond the maximum drift time of the short straw tube (about  $1 \mu\text{s}$ ).

Another effect contributing to the events with multiple hits in the straw tubes is the production of  $\delta$ -electrons inside the primary electron clusters, which can further ionize the gas and produce the signal earlier, if their trajectory is closer to the wire than the one of the primary track. The signal becomes very long (up to 600–800 ns) and the CFD can re-trigger on this signal due to the peaks from the primary ionization. According to [37] the probability of getting at least 1 electron of 1 keV per incoming track is  $\approx 0.6\%$  for argon. Also there is a tiny probability of an X-ray photon feedback at the straw tube wall, which contributes to the events with multiple hits inside the tubes too.

### 3.4.2 T0 and DUTs efficiencies

The efficiency of the T0 detector and the straw tubes within the test beam setup can be defined as a ratio between the number of single tracks passing through the geometrical acceptance of the detectors creating a single hit in the detector and the total number of single tracks passing through the corresponding geometrical acceptance:

$$\epsilon(N_{detector} = 1) = \frac{N'(N_{track} = 1 \& N_{detector} = 1)}{N(N_{track} = 1)} \quad (3.8)$$

However, this definition gives only a lower bound for the efficiencies, because, as shown in Section 3.4.1, an event with a correctly detected hit can be lost due to the presence of a second (noise or background) hit in the same triggered event. Figure 3.20 shows the dependence of the efficiencies along the  $Y$  coordinate of the reconstructed single tracks at the position of the DUT. With the above definition, the efficiency is significantly smaller than 100% within the sensitive area of the straws, especially in case of the long straw tube, where the level of the side bands (the efficiency outside the sensitive area) is higher than the values of the efficiency inside the geometrical acceptance of the tube representing the noise hit dominance in this tube. Given the large probability of having more than one hit, the following alternative definition of the efficiency is of interest

$$\epsilon(N_{detector} \geq 1) = \frac{N'(N_{track} = 1 \& N_{detector} \geq 1)}{N(N_{track} = 1)}, \quad (3.9)$$

where one now requires, in the numerator, *at least* one hit in the DUT, which gives now an *upper bound* to the “real” efficiency of detecting the “correct” hit. However, as discussed in the previous section, and according to the Figure 3.19, in the case of multiple hits in the straw tube there is a high chance that at least one hit corresponds to the signal from the track passing through the tube (the overestimation of the “real” efficiency is believed to be negligible). Figure 3.21 shows  $\epsilon(N_{detector} \geq 1)$  versus the extrapolated position for the T0 detector and the two straw tubes. The average values of the so-defined efficiency in the sensitive areas are more than 99% for all 3 detectors. The level of the side

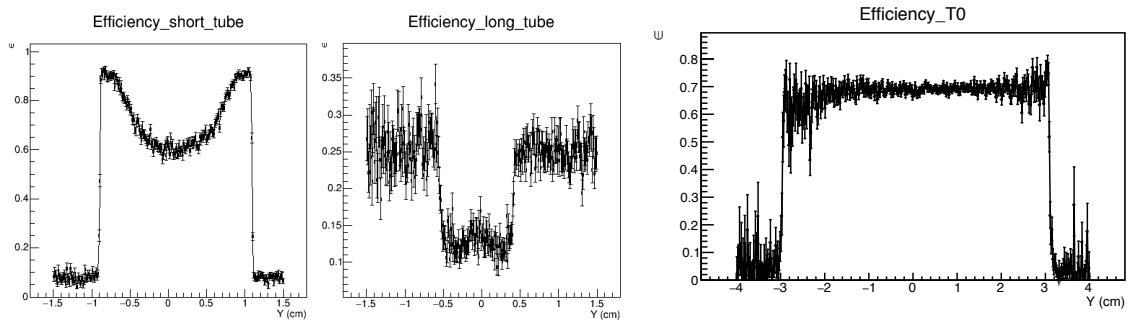


Figure 3.20: Efficiency plots for the short, the long straw tubes and the T0 detector, requesting  $N_{tube} = 1$  for the tubes and  $N_{T0} = 1$  for T0.

bands indicates the combined noise and background contribution in each detector. The side bands level for the T0 is  $< 5\%$ , for the short straw tube about  $10\%$ . For the long tube it is close to  $80\%$ , i.e. too noisy to extract a meaningful efficiency (with the used CFD threshold of  $-15\text{ mV}$ ).

In order to use the maximum number of such hits, which can correspond to the real reconstructed tracks in the telescope, and reduce the fraction of the noise and the background hits, a specific hit selection algorithm for the tubes is proposed and used in this work, as described in the next Section 3.4.3.

### 3.4.3 The isochrone relation and the hit selection algorithm

In order to describe the hit selection algorithm for the tubes the concept of the isochrone relation needs to be introduced at first.

#### Isochrone relation

The main characteristic of the straw tube as a charged particle tracking detector and a component of the future SST subdetector of SHiP is the isochrone relation,  $r(t)$ , the relation between the radial position  $r$  (relative to the wire) of the production of an electron cluster by instantaneous ionization and the electron drift time  $t_{drift}$ . This relation is often referred to as “V-shape” for a reason that will become clear when plotting the measured drift time against the spatial coordinate. Assuming cylindrical symmetry of the straw detector, the charged particle trajectories are tangent to a coaxial circle of radius  $r$ , the distance of closest approach to the wire, which directly translates into a drift time. In the test beam experiment, the charged particles impinge on the straw at an almost perpendicular angle and the tracking telescope returns  $X$  and  $Y$  coordinates of the tracks at the position of the tube. The track location ambiguity (above or below the wire) is resolved. In the SHiP experiment this ambiguity will be resolved using a pattern recognition algorithm and track fit, using many hits from many different straws.

The drift time of the tubes is obtained from

$$t_{drift} = t_{T0} - t_{tube} \quad (3.10)$$

where  $t_{T0}$  is the hit time registered with the TDC unit from the T0 scintillator signal and  $t_{tube}$  is the time of the arriving signal registered in either the short or the long straw tube. The drift time can only be unambiguously calculated for those events, which have a single hit in T0 detector and at least 1 hit in the tube. The measured  $t_{drift}$  then needs to be associated with the track coordinates, which can be done unambiguously only in the case of a single track being delivered by the telescope (using the telescope cuts described in Section 3.2). This naturally leads to the following event selection cuts:  $N_{track} = 1$  &  $N_{T0} = 1$  &  $N_{tube} \geq 1$ . In the presence of more than one hit in the DUT (tube), a choice needs to be made. For simplicity, at first the V-shapes for  $N_{tube} = 1$  are considered and are shown in Figure 3.22 for the short and the long straw tubes. The noise and background contribution in the histograms is represented as uniform random hits outside the V-shape.

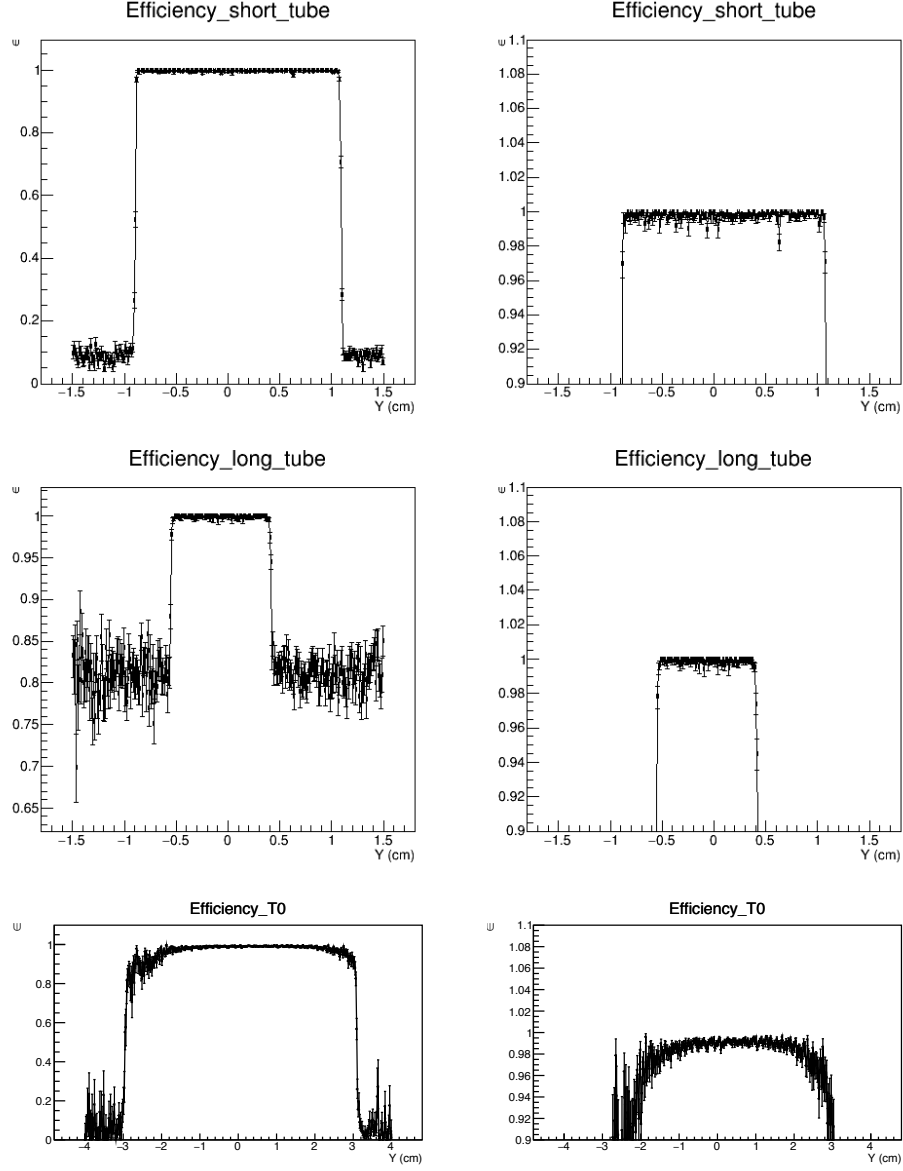


Figure 3.21: Efficiency plots for the short, the long straw tubes and the T0 detector, requesting  $N_{tube} \geq 1$  for the tubes and  $N_{T0} \geq 1$  for T0. The plots on the right are a zoom of the efficiency around the value of 1.

They also make the contribution in the V-shape region (below and above the curve). There is a stripe with random events under the V-shape (seen the best in the bottom histogram for the long straw tube, but also present in the top histogram). The width of this stripe is  $\approx 160$  ns (matching the CFD dead time). The noise hits should contribute evenly to the area above the V-shape as well. However, due to the long signals (few hundreds of nanoseconds) produced in the tube, they are merged with (i.e. hidden by) the tail of the signal from the track hit. So, the noise rate above the V-shape is highly suppressed. In the

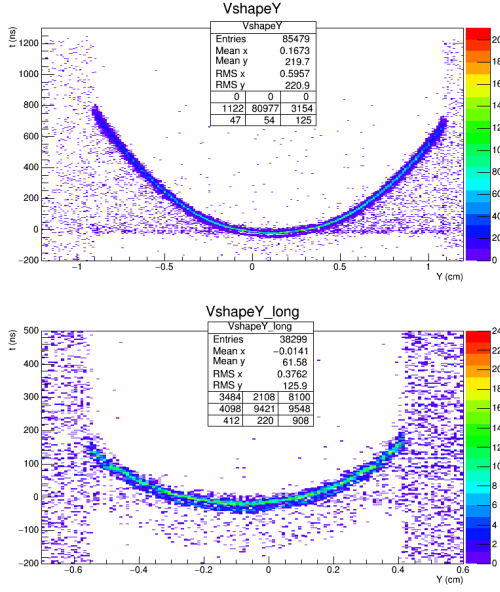


Figure 3.22: The drift time vs. the  $Y$  coordinates of the extrapolated tracks at the position of the straw tubes (V-shapes). The top distribution is created for the short tube, the bottom one – for the long tube. In both distributions a single hit in the tube is requested ( $N_{tube} = 1$ )

top histogram of the Figure 3.22 the hits from  $\delta$ -electrons can be observed. They populate the area below the V-shape up to  $\approx 0$  ns drift time. If the trajectory of the  $\delta$ -electron is closer to the wire than the trajectory of the primary track, then the hit in the tube will be registered earlier than the primary one. The cutoff at 0 ns is present, because the signal from the  $\delta$ -electrons for the primary tracks, which passed through the wire, physically cannot arrive earlier than the primary signal. Another notable feature of both V-shapes is a shadow shifted by  $\approx 20$ – $30$  ns to the negative side of the drift time axis. This feature was investigated more comprehensively. The possible cause is the issue with the TDC inputs, which lead to the duplication of the signals with a fixed time shift. The evidences of such assumption can be found in the correlation histograms between the first and the second hits in the T0 too (see Figure 3.16). The narrow peak at  $\approx 25$  ns contains the events, which created the shadow below the V-shape in Figure 3.22. The number of events inside the V-shape shadow is at least the order of magnitude smaller than the number of the real hits, but they still contribute to the spatial resolution calculations.

### Straw tube hit selection algorithm

A straw tube hit selection algorithm was used to recover events with more than one DUT hit, which allows to increase the statistics for resolution analysis with good reconstructed tracks passing through the tubes. It takes the advantage of a rough knowledge of the V-shape of the tube and selects the hit among several by their distance to this V-shape curve. Possible systematic effects or biases on the resolution turn out to be negligible and are discussed in Section 3.5.3.

Among events with a single track ( $N_{track} = 1$ ) and a single hit in the T0 detector ( $N_{T0} = 1$ ), the selection algorithm is only applied to the events which have  $N_{tube} > 1$ . The steps of the algorithm are the following:

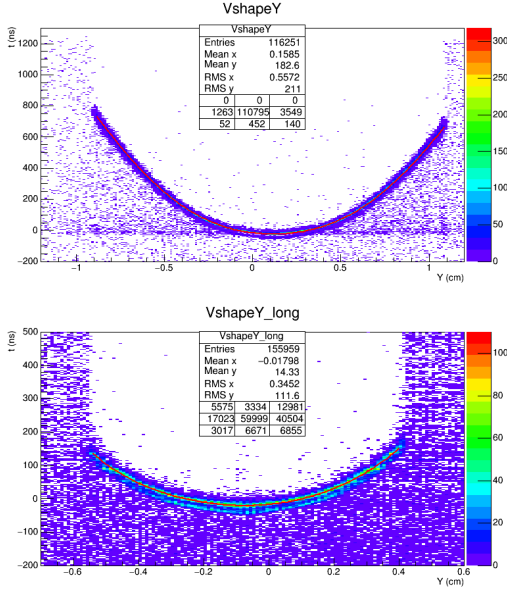


Figure 3.23: Fitted V-shapes for the short (top) and the long (bottom) straw tubes. The event selection algorithm was applied to produce them.

1. In a first pass, using only events with  $N_{tube} = 1$ , find a parametrization of the isochrone relation (V-shape function):
  - (a) Divide the 2-dimensional V-shape distribution into slices of  $Y$  coordinate (with a given bin width).
  - (b) Create for each  $Y$  slice a drift time distribution.
  - (c) Define a  $Y$  range by checking the condition on the Kurtosis,  $Kurt[t_{drift}] \geq 0$ , for each slice, starting from the middle of the  $Y$  range. The edges of the range are given by the last slices that satisfy this condition.
  - (d) Find the drift time value in each  $Y$  slice, where the distribution has the maximum of entries. Assign an error equal to the standard deviation of the core of this histogram (arbitrarily chosen to be about  $\pm 9$  ns). Extract the obtained drift time values and their errors.
  - (e) Fit the mean values (with the errors) of the drift time distributions per slice with a user defined function (*e.g.* parabola or other  $n$ -th degree polynomial)
2. In a second pass, and only if  $N_{tube} > 1$ , select the straw tube hit, which has the closest drift time value to the one calculated using the V-shape parametrization (obtained in step 1) without applying any cut on the distance to the V-shape.

The V-shape data with  $N_{tube} = 1$  were shown in Figure 3.22. The new V-shape data, populated with the extra entries obtained using the hit selection algorithm are shown in Figure 3.23. A comparison shows that the selection algorithm allows one to increase the useful statistics by almost 50% for the short tube and by a factor 5 for the long tube. The noise density outside the straw acceptance and below the V-shape increased, but less than the increase of data on the V-shape. The noise density above the V-shape didn't change.



Figure 3.24 shows the V-shape distributions for the cases with exactly 2 hits (a) and more than 2 hits (b), including all hits of each event. The bottom graphs (c) and (d) show the same distribution, but restricted to the first hit in those events. One extracts from these plots that the selection algorithm picks in 90% of cases the first (earliest) TDC hit in the tube.

The spatial distribution analysis (see Section 3.5) and the drift time spectrum studies (see Section 3.6) were performed only for the short straw tube (2 m length and 2 cm diameter). The long straw tube suffered huge electronic noise oscillations (see Figure 3.25), which had the magnitude comparable to the magnitude of the real signal. This issue led to the unrealistic results of the spatial resolution for this tube (more than  $250\text{ }\mu\text{m}$ ). During the test beam it was not possible to fix this issue and the off-line analysis methods could not help either. Taking into account the fact that the long tube has the diameter of 1 cm instead of the baseline 2 cm for the SST, it was decided to abandon the analysis of the long tube and concentrate the work on the short straw tube.

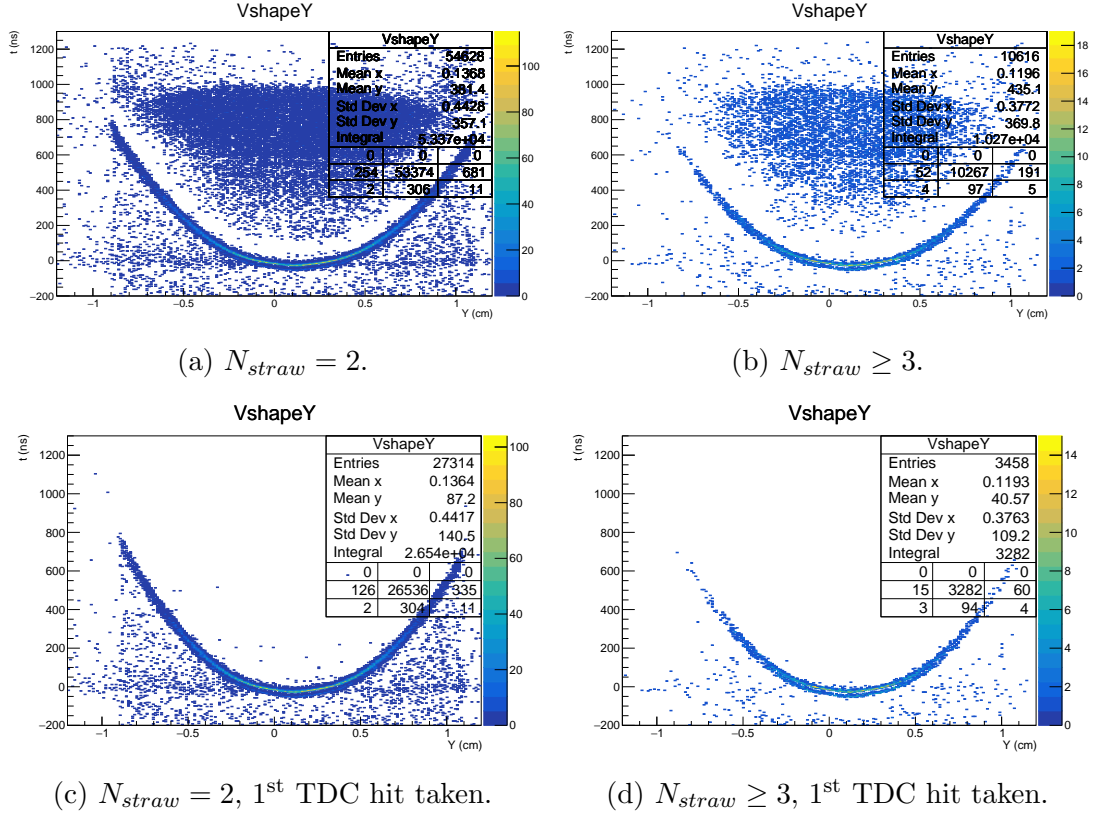


Figure 3.24: The top row: the V-shapes of the short straw tube created for  $N_{straw} = 2$  and  $N_{straw} \geq 3$  conditions. The bottom row: the V-shapes of the short straw tube created for the same conditions, but using only the first TDC hit of the tube.

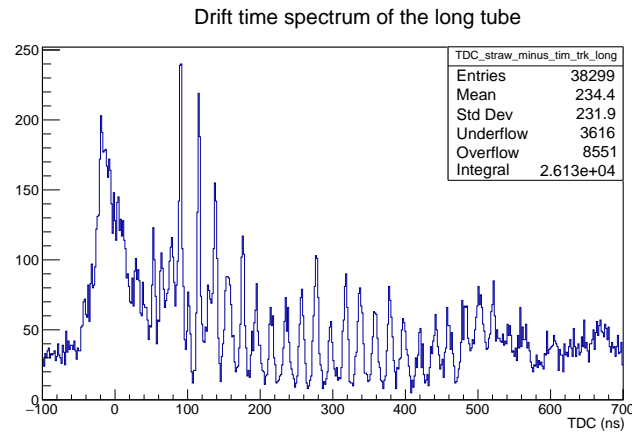


Figure 3.25: The drift time distribution for the long straw tube.

## 3.5 Straw tube spatial resolution

The idea of the spatial resolution analysis is to translate a drift time into a spatial coordinate value according to a V-shape function (comparing three possible parametrisations) and then evaluate the residual to the extrapolated track coordinate,  $Y_{tr}$ . The analysis is described in the following subsections.

### 3.5.1 Resolution from spatial distributions

The first coarse analysis was performed using a parabolic fit of the V-shapes. As will be shown, this parametrization does not satisfactorily describes the V-shapes, especially for large wire eccentricity. The analysis was improved by using a degree 6<sup>th</sup> polynomial fit, which provides a better description, but still shows imperfections. Finally, a numerical interpolation method was used to describe the V-shape, which provides the best results. The generic analysis scheme used for all methods is similar to the hit selection algorithm described earlier in Section 3.4.3 and consists of the following steps:

1. Slice the data in  $Y_{tr}$  slices and extract the drift time  $t_{drift}$  of the maximum of the 1-dimensional distribution for each slice and assign an error equal to the standard deviation of the core of this histogram (arbitrarily chosen to be about  $\pm 9$  ns).
2. Fit or interpolate the extracted  $t_{drift}$  versus  $Y_{tr}$  using the chosen function: parabola, 6<sup>th</sup> degree polynomial or linear interpolation between the points. Calculate the inverse function  $Y(t_{drift})$  either numerically or analytically (for parabolic parametrization). The branches are split at the apex position  $Y_0$ . The apex definition depends on the method used. The range of validity in  $Y$  ( $Y_-$  and  $Y_+$ ) for the all methods is defined in the same way as in the step (c) in Section 3.4.3.
3. Build distributions of residuals  $Y - Y_{tr}$  versus  $Y$  for the straw tube, where  $Y$  is the value from the inverse V-shape function and  $Y_{tr}$  is the extrapolated coordinate of the tracks at the DUT position. If the  $t_{drift}$  is below the apex value  $t(Y_0)$  the apex value of  $t$  is assigned to the point. The points, which exceed the parametrization  $Y$  range defined in the previous step are skipped. The specific branch of the inversed function  $Y(t_{drift})$  used to plot the distribution of residuals  $Y - Y_{tr}$  is selected depending on the closest distance to the track point  $Y_{tr}$  from the obtained  $Y$  coordinate.
4. Slice the data in  $Y$  bins and fit the 1-dimensional distributions of residuals within the range from -0.4 cm to 0.4 cm in each bin with a “linear plus Gaussian” fit function and use the  $\sigma$  value of the Gaussian as a measure of a spatial resolution.

In what follows, the three spatial resolution calculation methods are described in more details.

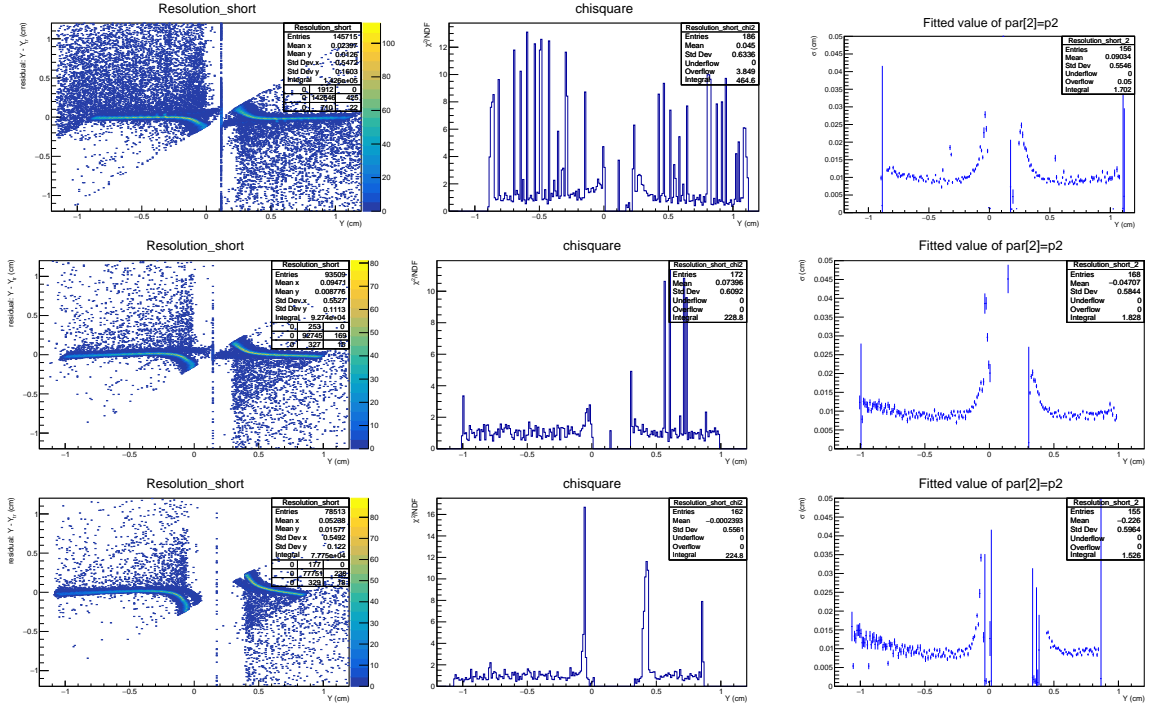


Figure 3.26: Three resolution analysis results for the short tube with a wire eccentricity of 0.02 mm (top row), 1.10 mm (middle row) and 1.97 mm (bottom row), see table 3.7, and using a parabolic parametrization of the V-shape. The graphs in the leftmost column show the distributions of the residual  $Y - Y_{tr}$  versus  $Y$ . The middle column shows the corresponding  $\chi^2/\text{NDF}$  of the  $Y$ -slice fits value versus  $Y$ , using a Gaussian + linear fit in each  $Y$  slice. The rightmost column shows the extracted Gaussian  $\sigma$  parameter value versus  $Y$ , after discarding points with  $\chi^2/\text{NDF} > 5$ .

### Using a parabolic fit of the V-shape

The parametrization obtained for V-shapes, shown in Figure 3.41, can be used as a starting point for an evaluation of straw tube spatial resolution. The procedure described in Section 3.5.1 was applied. In this method the  $t_{drift}(Y_{tr})$  distribution is fitted with the parabolic function:

$$t_{drift} = a \cdot (Y - Y_0)^2 + c. \quad (3.11)$$

In equation (3.11) the parameter  $Y_0$  is the apex position of the V-shape,  $c$  is the arbitrary drift time offset and the parameter  $a$  defines the curvature of the parabola. In order to proceed further with the analysis procedure the inverse fit function is calculated:  $Y = Y_0 \pm \sqrt{\frac{t_{drift} - c}{a}}$ . The residual plots  $Y - Y_{tr}$  vs.  $Y$  built using the inverse parabolic function and the Gaussian  $\sigma$  vs.  $Y$  graphs are shown in Figure 3.26 for the cases with small wire eccentricity (0.02 mm), intermediate value (1.10 mm) and large wire eccentricity (1.97 mm) of the short straw tube. Two examples of the fitted slices are shown in Figure 3.27

showing the distribution of data in blue and the linear+Gaussian fit result (red curve). One can observe that the slices closer to the tube wall have better fit quality than the slices created near the wire location, which is also seen in the  $\chi^2/\text{NDF}$  plots in Figure 3.26. The leftmost graphs in Figure 3.26 show the 2-dimensional distributions of the residuals  $Y - Y_{tr}$  versus  $Y$  coordinate of the inverse V-shape parametrization function  $Y(t_{drift})$ . The resulting dependence on  $Y$  of the Gaussian  $\sigma$  fit parameter (the spatial resolution) and fit quality  $\chi^2/\text{NDF}$  are shown in the middle and rightmost plots respectively. A cut on  $\chi^2/\text{NDF} < 5$  is applied for the  $\sigma$  distribution in order to skip the bins, where the fit did not converge well.

A plateau of the spatial resolution  $\sigma$  is observed on each side of the wire's  $Y$  position. Near the wire location the resolution blows up, as expected. The plateau value of the spatial resolution of the short straw tube is  $\approx 110 \mu\text{m}$ . The  $\sigma$  plateau for the short straw tube is slightly tilted. This originates from the non-perfect match of the fit function to the V-shape points. With a more asymmetrical V-shape (see Figure 3.26 cases with 1.10 mm and 1.97 mm eccentricity), the tilt of the  $\sigma$  distribution exhibits a more pronounced slope for the long “arm” of the V-shape.

The same analysis was repeated for all runs with different wire eccentricities (see table 3.7). The weighted mean of the spatial resolution as a function of wire eccentricity is discussed later, in Section 3.5.2. In addition, when the  $a$  parameter is left free, its value changes considerably as a function of  $Y_0$ , as shown in Ideally, in order to simplify the detector description in the real SHiP experiment, one would wish to be able to use a V-shape parametrization with a fixed curvature parameter  $a$ , independent of the wire eccentricity. However, distortions of the electric field increase with increasing wire eccentricity and may break this idealistic parametrization. Figure 3.28 shows how this parameter depends on the wire eccentricity, as extracted from the fits, indicating that a fixed value of  $a$  would not be ideal. This is further supported by Figure 3.29 which shows the parametrization quality ( $\chi^2$ ) as a function of wire eccentricity for the two cases, with a free  $a$  parameter (bottom graph) and with an  $a$  parameter fixed to the value obtained

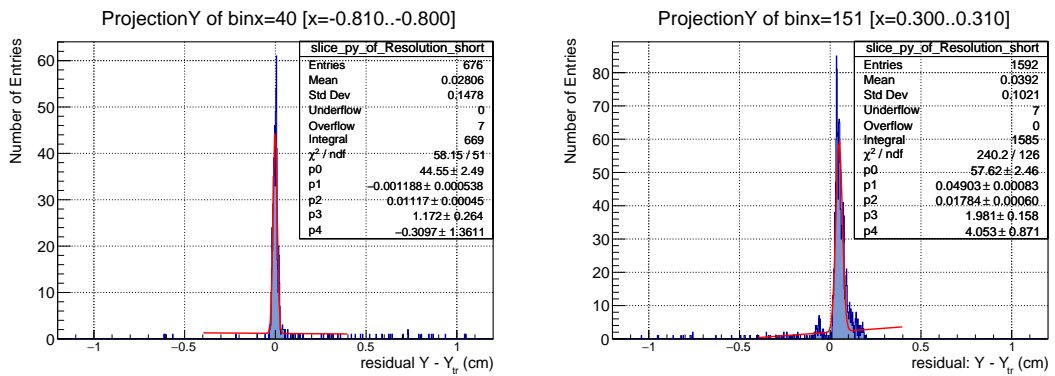


Figure 3.27: The residual distributions  $Y - Y_{tr}$  for a  $100 \mu\text{m}$  wide slice in  $Y$ , centered at  $-0.805 \text{ mm}$  (left) and  $0.305 \text{ mm}$  (right) and for  $0.02 \text{ mm}$  wire eccentricity. The red curve and text insert are the result of a linear+Gaussian fit (within the range  $-0.4$ – $0.4 \text{ cm}$ ).

for the minimal eccentricity (top graph). The fit quality is worse in the latter case, but also that it degrades in both cases with increasing eccentricity.

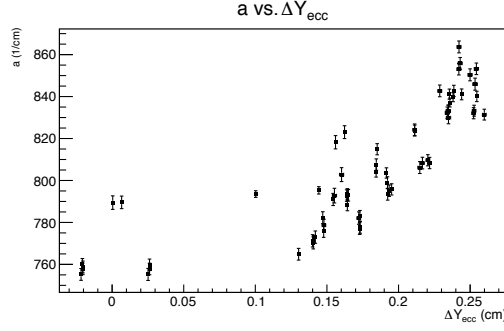


Figure 3.28: Relation between the free parameter  $a$  and  $\Delta Y_{ecc} = Y_0 - (Y_r + Y - l)/2$  calculated from the parabolic fit  $Y_0$  parameter for the short straw tube.

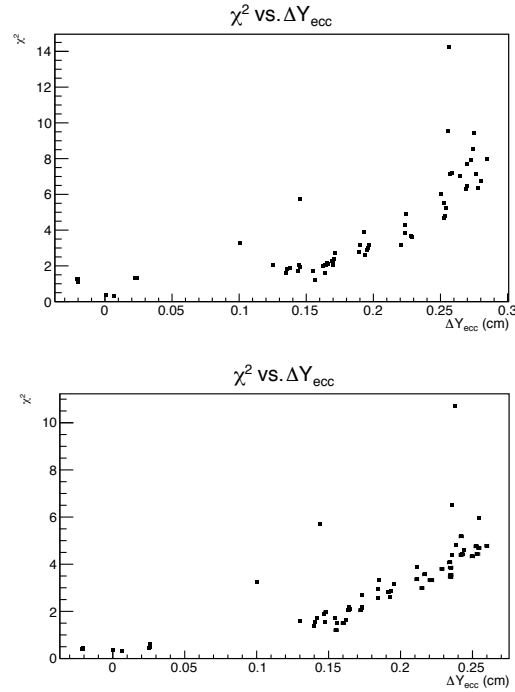


Figure 3.29:  $\chi^2$  value of the parabolic fit as a function of  $\Delta Y_{ecc} = Y_0 - (Y_r + Y - l)/2$  obtained from the parabolic apex  $Y_0$  parameter in the short straw tube, while keeping the parabolic fit parameter  $a$  fixed (top) or free (bottom).

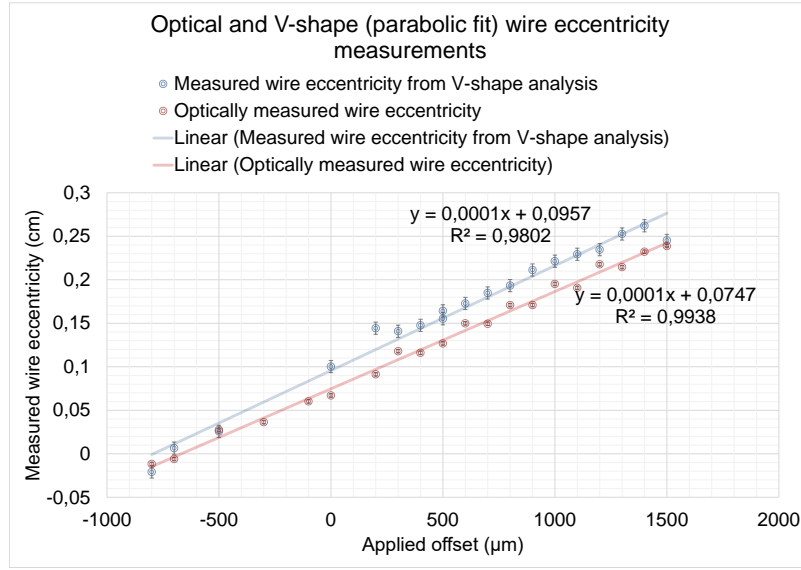


Figure 3.30: The comparison between the optically measured wire eccentricity with obtained from the V-shape parabolic fit.

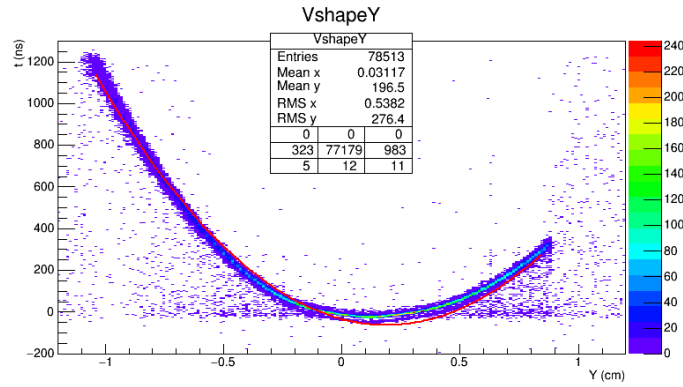


Figure 3.31: V-shape distribution for the short straw tube with 2.05 mm wire eccentricity fitted with a parabolic function. The result of the fit is shown by the red curve.

Figure 3.30 shows the extracted wire eccentricity as a function of applied offset in comparison to the optically measured eccentricity with the method described in Section 3.3. There appears to be a difference between the two methods rising up to 0.4 mm for the largest eccentricity.

Figure 3.31, where the V-shape distribution and fit result are plotted for the case with the largest wire offset, shows what is happening. Due to the asymmetry of the V-shape across the apex (different curvature on each side of the apex), a parabola cannot describe the distribution satisfactorily. This is the main motivation for attempting different parametrizations.

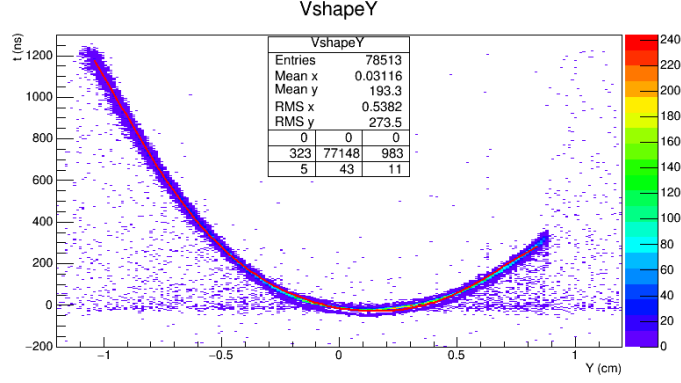


Figure 3.32: V-shape for the short straw tube with 2.05 mm wire eccentricity fitted with a degree 6 polynomial. The result of the fit is shown by the red curve.

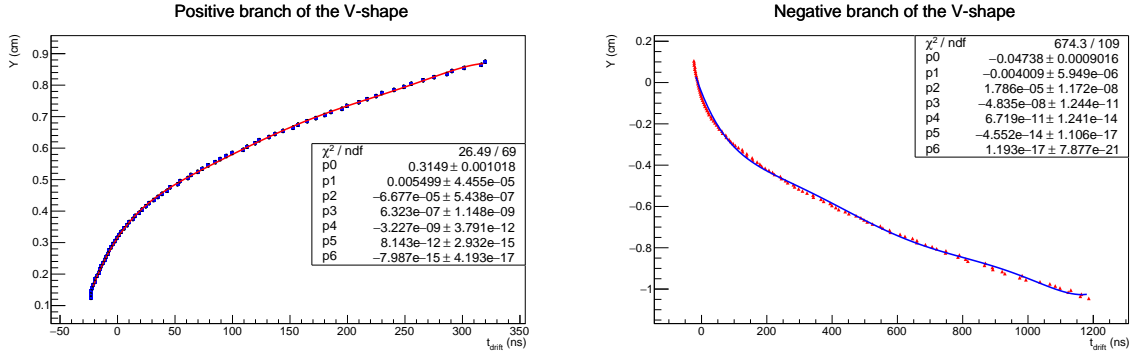


Figure 3.33: Example of degree 6 polynomial fit of the inverted relation  $Y$  versus  $t_{drift}$  for the short straw tube and a wire eccentricity of 2.05 mm.

### Using a 6-degree polynomial fit of the V-shape

An improved functional parametrization can be obtained by using a higher degree polynomial. Beyond the parabola, polynomials of degree 4, 6 and 8 were tried. The degree 6 polynomial gives better performance than the degree 2 and 4, while the degree 8 does not give substantial improvements when compared to the degree 6. Therefore, the following degree 6 polynomial was used:

$$t_{drift} = a_6 \cdot Y^6 + a_5 \cdot Y^5 + a_4 \cdot Y^4 + a_3 \cdot Y^3 + a_2 \cdot Y^2 + a_1 \cdot Y^1 + a_0 . \quad (3.12)$$

Figure 3.32 shows, as an example, the result of the fit with eq. (3.12) for a large wire eccentricity (2.23 mm), to be compared with Figure 3.31. However, this parametrization introduces a complication, since the inverse function is needed to assign a  $Y$  value to a  $t_{drift}$  value for the straw tube resolution studies. In the case of a degree 6 polynomial the analytical solution for the inverse function is not readily available. The method utilises the



generic algorithm scheme described in Section 3.5.1, but has the following modifications:

1. Fit the extracted  $t_{drift}$  versus  $Y_{tr}$  with the degree 6 polynomial, see equation 3.12, and extract the  $a_i$  parameters ( $i = 0, 1, \dots, 6$ ).
2. The apex position  $Y_0$  of the V-shape is obtained by fitting the vicinity of the V-shape with parabolic function (3.11) with initial  $Y_0$  value extracted from ROOT (the minimum (apex) of this polynomial (3.12)) and the range  $[Y_0 - 0.15; Y_0 + 0.15]$  cm.
3. Build two new distributions, with swapped axes ( $t_{drift} \longleftrightarrow Y$ ), split at the apex  $Y_0$  in order to get rid of the ambiguity of the fit function definition.
4. Fit each branch with a degree 6 polynomial.
5. Extract the arrays of the fit parameters  $a_-[7]$  and  $a_+[7]$  which define the inverse fit function.

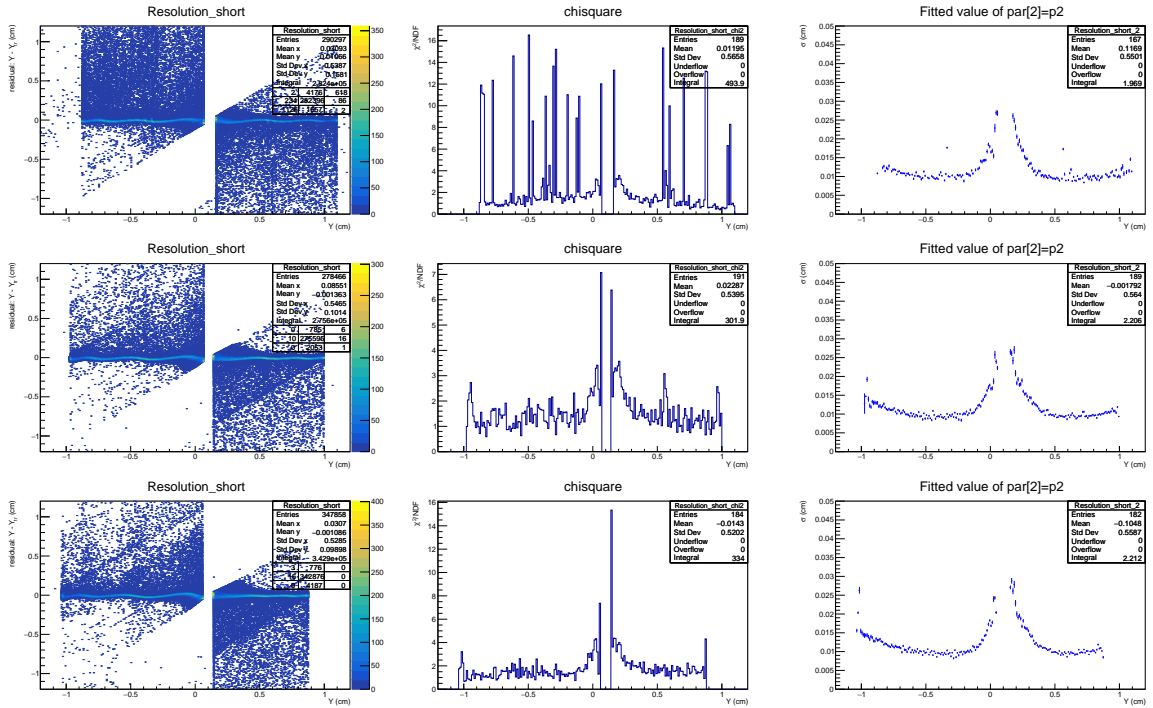


Figure 3.34: Three resolution analysis results for the short tube with a wire eccentricity of 0.02 mm (top row), 1.10 mm (middle row) and 1.97 mm (bottom row), see table 3.7, and using a degree 6 polynomial parametrization of the V-shape. The graphs in the leftmost column show the distributions of the residual  $Y - Y_{tr}$  versus  $Y$ . The middle column shows the corresponding  $\chi^2/\text{NDF}$  of the  $Y$ -slice fits value versus  $Y$ , using a Gaussian + linear fit in each  $Y$  slice. The rightmost column shows the extracted Gaussian  $\sigma$  parameter value versus  $Y$ , after discarding points with  $\chi^2/\text{NDF} > 5$ .

During the event loop to form the residuals, drift times are translated into  $Y$  coordinates using the branch that contains the corresponding  $Y_{tr}$  of the event.

The results obtained with the degree 6 polynomial for three different wire eccentricities of the short straw tube are shown in Figure 3.34. The plateau value of the spatial resolution of the short straw tube is  $\approx 100 \mu\text{m}$ . Like in case of the parabolic fit the  $\sigma$  value increases closer to the edges of the tube. The  $\sigma$  distributions along  $Y$  were made using  $\chi^2/\text{NDF} < 5$  cut in order to reject poorly converged fits.

The degree 6 polynomial used to approximate the inverted V-shape branches gives better results than the parabolic fit, but still doesn't perfectly describe the V-shape. From Figure 3.33 one can see that the approximation functions oscillate around the points. This leads to the oscillations in the residual plots shown in Figure 3.34. The resolution results are also affected by these oscillations, because the slices of the residual plot are vertical ( $Y$ -axis projection per bin) and those, which contain the parts of the distribution with higher slopes, end up having a larger RMS. In order to improve the V-shape description, yet another approach was tried, which is based on interpolation.

### Using an interpolation

In order to improve further the V-shape description, an interpolation approach is tried. First, the same value of the apex,  $Y_0$ , as found with the degree 6 polynomial method, is used to separate the V-shape data shown in Figure 3.33 in two branches. Then, starting from the apex, the space between the points of the two branches is interpolated with a straight line, skipping those points which do not comply with a strict monotonousness (increasing or decreasing, depending on the branch). The two obtained sets of line segments define unambiguously for each branch the relation between drift time and  $Y$  coordinate. As before, the  $Y_{tr}$  value in the event is used to choose the branch.

The histograms with residuals along with the corresponding spatial resolution distributions are shown in Figure 3.35.

In this case the residuals between the real hit coordinate and the interpolated value for a certain drift time no longer have the oscillation effects, as seen in the left column graphs of Figure 3.35. This also leads to a fact that the resolution of the straw tube calculated from the slices extracted from the residual distribution becomes free of the slope effect at both branches, see the middle column graphs of Figure 3.35.

The results of the weighted mean resolution versus extracted wire eccentricity for the short straw tube using the interpolation approach are shown and discussed in Section 3.5.2.

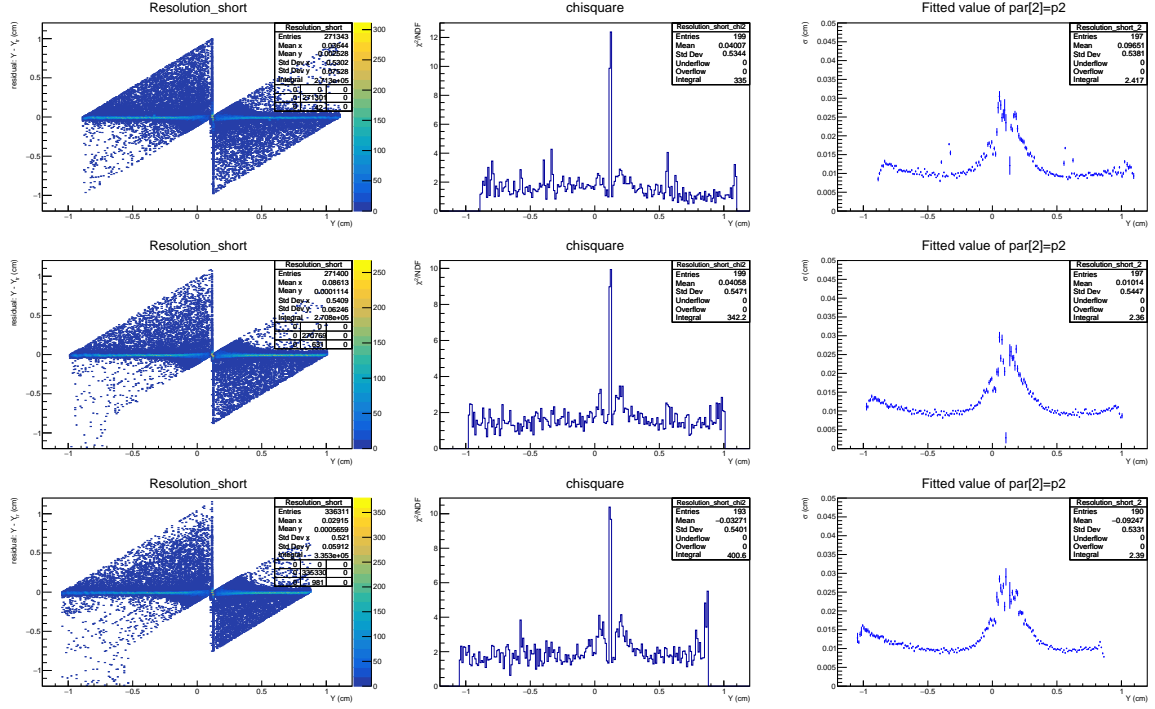


Figure 3.35: Three resolution analysis results for the short tube with a wire eccentricity of 0.02 mm (top row), 1.10 mm (middle row) and 1.97 mm (bottom row), see table 3.7, and using an interpolation of the V-shape points. The graphs in the leftmost column show the distributions of the residual  $Y - Y_{tr}$  versus  $Y$ . The middle column shows the corresponding  $\chi^2/\text{NDF}$  of the  $Y$ -slice fits value versus  $Y$ , using a Gaussian + linear fit in each  $Y$  slice. The rightmost column shows the extracted Gaussian  $\sigma$  parameter value versus  $Y$ , after discarding points with  $\chi^2/\text{NDF} > 5$ .

### 3.5.2 Comparison of resolution results

The results obtained with the 3 V-shape analysis methods described in the previous section can be compared. Additionally, for the comparison the spatial resolution of the straw tube obtained using the drift time distribution is used in the plots. The drift time distribution method is described in [8]. The main idea behind this method is to translate the extrapolated track coordinate into an “expected” drift time and evaluate the residual to the measured drift time, subsequently transforming the obtained drift time resolution back into a spatial resolution using the local slope of the V-shape. Fig 3.36 presents in the same graphs the resolution values versus the  $Y$  coordinate across the straw for 3 representative wire eccentricities, 0.02 mm (left), 1.10 mm (middle) and 1.97 mm (right). There is an overall agreement between the different methods.

In addition, a weighted mean value of the resolution is defined as

$$\sigma_{mean} = \frac{\sum_i \sigma_i \Delta\sigma_i^{-2}}{\sum_i \Delta\sigma_i^{-2}} \quad (3.13)$$

where  $\sigma_i$  is the resolution of the straw tube in bin  $i$  and  $\Delta\sigma_i$  is the statistical error of each resolution value in bin  $i$ . The weighted mean resolution is calculated for each applied offset and displayed in Figure 3.37 in a cumulative plot showing the comparison between the results of the 4 different analysis approaches. These results gather within the range of the weighted spatial resolution values between  $104 \mu\text{m}$  and  $118 \mu\text{m}$  and, within the obtained spread, show little dependence on the wire eccentricity.

The parabolic approximation of the V-shape represents well the rising trend in the resolution of the tube closer to its borders, but each resolution value along  $Y$ , which was obtained after fitting the slices of the residual plot with a combination of Gaussian and linear function, has the  $\chi^2/\text{NDF} > 5$  near the wire position. This means that the distributions in the slices near the wire were not very well described by the fit. This can be explained by the slope in the residual plots (see Figure 3.26) near the wire location, which leads to the distortions of the distributions in the slices and deviation from the Gaussian

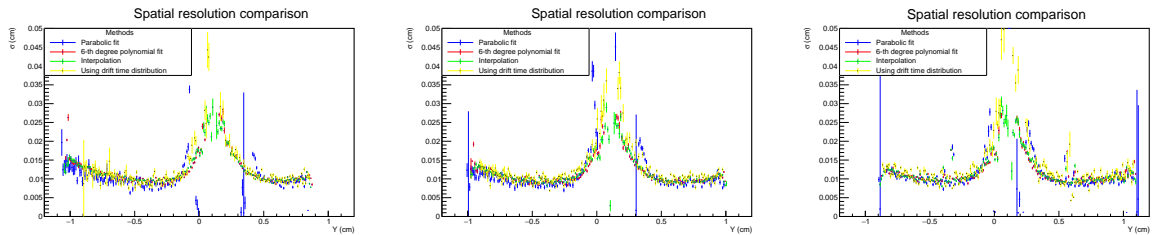


Figure 3.36: Resolution versus  $Y$  for different wire offsets of the short straw tube using three different V-shape parametrisation methods (parabolic fit, 6-degree polynomial fit and interpolation) and drift time distribution approach. Left: 1.97 mm, middle: 1.10 mm, right: 0.02 mm.

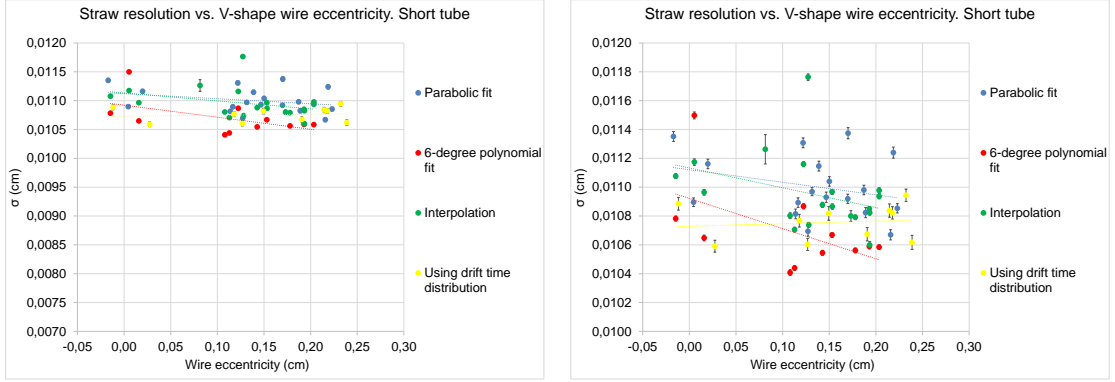


Figure 3.37: The weighted mean of the resolution for the short straw tube as a function of the wire eccentricity. All 4 analysis methods are compared in the left graph (the right graph is a zoom around 100–120  $\mu\text{m}$ ).

shape. The gap in the  $\sigma$  distribution (see Figure 3.36) near the wire location is more pronounced for the data with larger wire displacements (1–2 mm), which is related to the fact that the parabolic fit of the V-shape data degrades with increasing wire eccentricity.

The degree 6 polynomial fit of the V-shape matches the V-shape much better (see Figure 3.32), but it has 7 free parameters. Despite the smaller  $\chi^2/\text{NDF}$  values, the obtained fit function oscillates around the data points' main trend. In particular, the oscillations propagate to the residuals along the  $Y$  plots (see Figure 3.34). The high variability of the mean in the residual plots is also transferred to the resolution ( $\sigma$ ) plots (see Figure 3.34) due to the “slope” effect described earlier. There is no significant effect of the oscillations in the resolution data on the final weighted  $\sigma_{\text{mean}}$  vs. wire eccentricity value (see Figure 3.37), but they mimic the trends in the resolution vs  $Y$  plots (see Figure 3.36).

The interpolation method, to a certain extent (for a distance of 100  $\mu\text{m}$  between the nodes), doesn't have any of the drawbacks described in the two previous approaches. The results for the other methods (parabolic and 6-degree polynomial V-shape fits) lay in the 5% uncertainty range, so they can be taken into account too.

The approach based on the drift time distributions is an alternative to the 3 described above methods, because it operates in the time domain instead of coordinate space as others. The results obtained through this method are similar to the interpolation approach values, thus such analysis option can be considered as consistent too. The bottleneck in the drift time method is the calculation of the derivative of the isochrone relation  $t_{\text{drift}}(Y)$ . It strongly depends on the size of the  $Y$  bins (see [8] for the details), so the systematic contribution in this case is larger than for other methods.

Some possible systematic effects on the resolution results are discussed next.

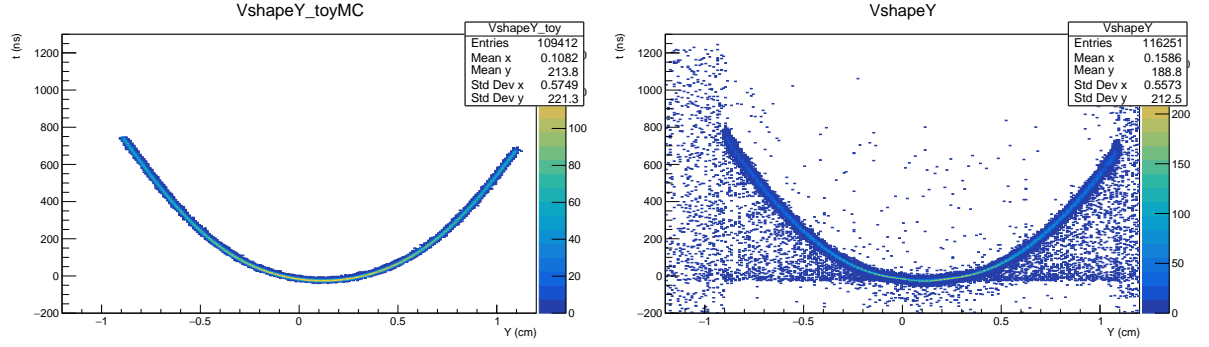


Figure 3.38: Left: MC simulated V-shape based on the parametrization from the 0.02 mm wire eccentricity data. Right: the real V-shape for the 0.02 mm wire eccentricity.

### 3.5.3 Systematic effects

#### Effects due to the slice size

The calculation of the straw tube resolution using the approaches described in this thesis may depend on the width of the residual distribution slices. In order to study the systematic influence on the result of the analysis using the approaches described in this thesis, the straw tube resolution values were obtained for various sizes of the  $Y$  coordinate bins in the V-shape distribution and the residuals plots. The array of the bin sizes selected for the test were the following: 30, 40, 50, 60, 80, 100, 150, 200 and 400  $\mu\text{m}$  (100  $\mu\text{m}$  being the value used for the standard analysis shown in the previous section). This check was performed for all four methods. However, here only the results for the interpolation method are shown. Similar effects in size are seen for the parabolic and the degree 6 polynomial methods.

Additionally, a toy Monte Carlo (MC) simulation was used to determine the pure influence of the bin size and thus the systematic error introduced. In the toy MC simulation, an artificial V-shape was generated based on the V-shape parametrization results obtained with the 6<sup>th</sup> degree polynomial fit function from the real data. The reference study was performed for several wire eccentricities. The true  $Y$  coordinates were generated uniformly within the straw tube edge and the ideal (true) drift time  $t$  was calculated according to the artificial V-shape parametrization. Then, the  $t$  and  $Y$  values were separately and randomly spread according to Gaussian distributions. In  $Y$  the values were spread with a  $\sigma_Y = 60 \mu\text{m}$  taken from the telescope extrapolation error at the short tube position. In time space the points were spread with a Gaussian with  $\sigma_t = 5 \text{ ns}$ , chosen to be similar to the experimental data (for tracks passing in the vicinity of the wire). The details of the generated V-shapes is not crucial, as the main goal here is just The generated V-shape is shown next to the real one in Figure 3.38. Subsequently, the same analysis procedures were applied to the artificial V-shape as the ones for the real data.

The analysis results are shown in Figure 3.39 (top) for the measurement data and (bottom) for the MC simulation. The study shows that the resolution results obtained

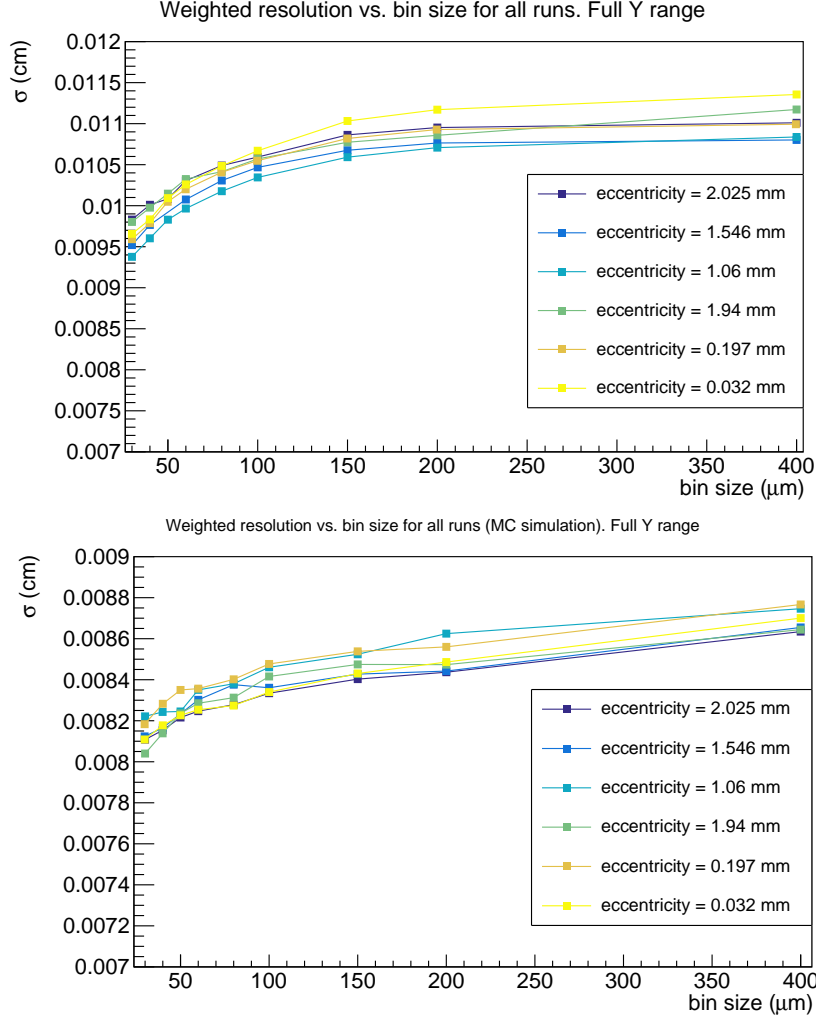


Figure 3.39: The weighted mean resolution of the short straw for different wire eccentricities as a function of  $Y$  coordinate binning size. Top: results from the measured data using the degree 6 polynomial fit. Bottom: results from the MC simulation.

with smaller or larger bin sizes, as compared to the standard bin size value ( $100 \mu\text{m}$  in case of the 3 spatial distribution methods), are with  $\pm 5\%$  of the results with the standard bin size, in both cases of the measurement results and MC simulation results. Given the input values and simplicity of the model, the absolute values of the resolution between the two plots (data and MC) should not be directly compared. Only the relative change as a function of bin size is of interest.

Globally, a systematic error of 5% can be attributed to the weighed mean resolution results due to the bin size dependence.

### Effects due to the track extrapolation errors

The propagated errors of the coordinates of the track at the position of the DUTs were discussed in Section 3.2 and are calculated using expression (3.2). The results of this calculation are shown in Table 3.8.

Table 3.8: The propagated error of the tracks in  $XY$  plane at the position of the DUTs.

DUT	Y error (um)	X error (um)
Short straw tube	60	86
Long straw tube	49	67

To put in perspective the size of the contribution of the telescope resolution  $\sigma_{DUT}$ , this quantity can be subtracted from the weighted mean spatial resolution results  $\sigma_{mean}$  using

$$\sigma_{corr} = \sqrt{\sigma_{mean}^2 - \sigma_{DUT}^2} . \quad (3.14)$$

The weighted mean resolution values presented in Section 3.5.2 varied between  $104 \mu\text{m}$  and  $118 \mu\text{m}$ . After subtraction of the telescope resolution using (3.14) the corrected resolution ranges from  $85 \mu\text{m}$  to  $102 \mu\text{m}$ .

### Effects due to the hit selection

As it was described in the analysis procedure for the spatial distributions approaches (see Section 3.5.1) of the spatial resolution estimation, the events with the number of hits

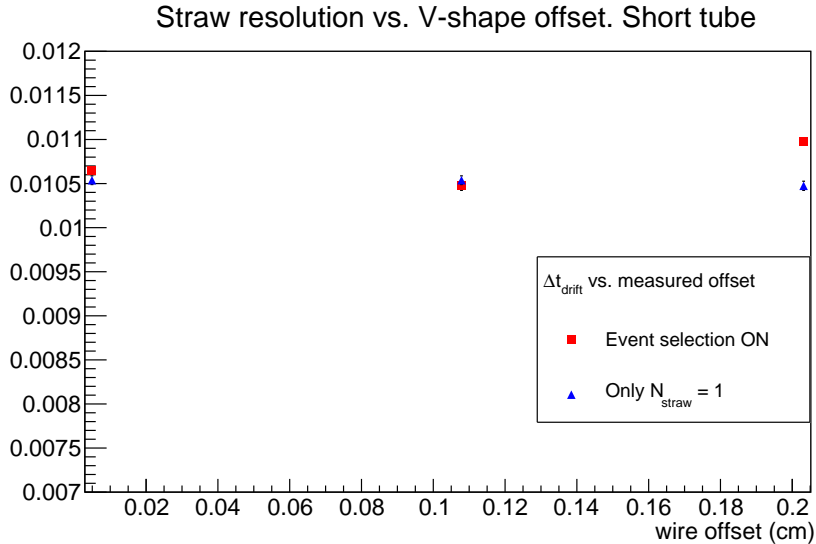


Figure 3.40: The comparison of the straw tube resolution values for 3 typical values of the wire eccentricity ( $\approx 0 \text{ mm}$ ,  $1.17 \text{ mm}$  and  $2.08 \text{ mm}$ ).



in the straw tube larger than one ( $N_{tube} > 1$ ) were considered too. For such events only the hit with the closest drift time to the V-shape parametrization curve for the extrapolated  $Y_{tr}$  coordinate of the track were retained, which, in principle, could affect the resolution result. The probability to get a hit between the correct hit and the drift time value from the V-shape parametrization can be estimated. Within a time window of  $\pm 25$  ns the probability is  $\approx 1.3\%$ , for  $\pm 50$  ns it is  $\approx 2.7\%$ . Therefore the contribution of such hits into the core of the V-shape is negligibly small and cannot affect the spatial resolution of the tube significantly.

It was shown in Section 3.4 that the first hit in the straw tube for the majority of the events with  $N_{tube} > 1$  is likely to be the real one. The rest is mostly caused by the CFD re-triggering issue and the decay of the higher excited states of argon atoms in the gas. This means that such selection should have a negligible influence on the estimated resolution value. In Figure 3.40 the spatial resolution versus the wire eccentricity dependence is shown for the analysis of 3 representative eccentricities performed using all events ( $N_{tube} \geq 1$ , with hit selection for  $N_{tube} > 1$  events), red squares, and compared to the case using only events with a single hit ( $N_{tube} = 1$ ) in the straw tube, blue triangles. The plots show that the relative difference between the approaches is almost identical. A maximum relative deviation of  $\approx 5\%$  is observed at the largest wire eccentricity. This proves the minor influence of the hit selection on the final result for the spatial resolution calculation.

### 3.6 Drift time distribution analysis

The methods shown in this section exploit the properties of the drift time of the charges inside the tube (created after the ionization with the impinging particles) in order to make the calibration curves needed to determine the intermediate values of the wire eccentricities inside the tubes. The curves constructed once for a single tube can be applied to other tubes (if they share the same mechanical design, applied HV and a gas pressure), hence the obtained array of the wire displacements inside the tubes can be used for improving the track fitting precision by modifying the hit coordinates inside the tubes.

In the Spectrometer Straw Tracker (SST) of the SHiP experiment there is no external telescope, which can measure the coordinates of the tracks hitting the straw tubes. Thus, the straw tubes themselves should provide enough information to find the location of the hits inside each tube. The measured drift time  $t$  of the charges (more correctly, the arrival time of the first amplified electrons cloud from the first ionization cluster) is used to obtain the distance of the closest approach  $r$  of the high energy particle trajectory to the cathode wire. The  $r(t)$  relation of our straw tube prototype, especially its dependence on a possible wire eccentricity, has been already studied in detail in the previous sections. For illustration, Figure 3.41 shows two measured V-shape distributions for the case of a small (0.02 mm) and large (1.97 mm) wire eccentricity. In this experimental configuration  $Y$  (up to a trivial sign) can be identified with  $r$ . In this section the study concentrates on the analysis of the drift time distribution alone, with the aim to extract information on the wire eccentricity without the knowledge of  $r$  from an external detector. To build the drift time distribution, only the TDC measurement from the tube itself  $t_{tube}$  and from the T0 detector  $t_{T0}$  are used. The drift time is defined as  $t_{drift} = t_{T0} - t_{tube}$ . Figure 3.42 shows the drift time distributions corresponding to the two cases of Figure 3.41. The event sample used for the plots in this figure was obtained by selecting test beam triggered events with a single hit in the T0 detector and a single hit in the short straw tube. This event selection is used throughout the study presented in this section. The drift time distributions can be imagined by projecting the data of Figure 3.41 onto the  $t$  axis and forgetting about  $Y$ . The comparison of the two figures helps to understand the shape of the drift time distribution. The sharp peak at small drift time values appears due to the reduced slope near the apex of the V-shape. The step at the tail of the distribution, at the largest drift time values, corresponds to the maximum extent in  $t$  of the two branches of the V-shape. In case of zero wire eccentricity, the two branches are symmetric across the apex of the V-shape and there is no other step in the drift time distribution. In case of a non-zero wire eccentricity, one branch will extend further and the other one will be shortened. This results in a step in the middle of the drift time distribution, clearly visible in Figure 3.42 (right) and indicated by the leftmost red arrow.

The scope of this study is to find a robust method to identify the presence of a second step, if any, extract the  $t$  values of the first peak and steps in the distribution and correlate these with the wire eccentricity. Several techniques were explored. First a basic manual method using two thresholds is presented in Section 3.6.1. Then, building on the experience from edge detection algorithms widely used in the image processing field, a few other

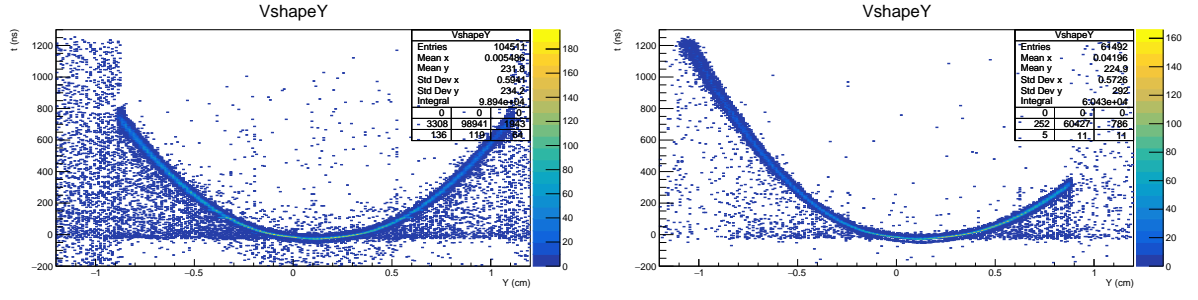


Figure 3.41: Two dimensional distribution of the measured drift time  $t$  versus the extrapolated telescope track position  $Y$  for short straw tube in the case of a 0.02 mm wire eccentricity (left) and 1.97 mm wire eccentricity (right).

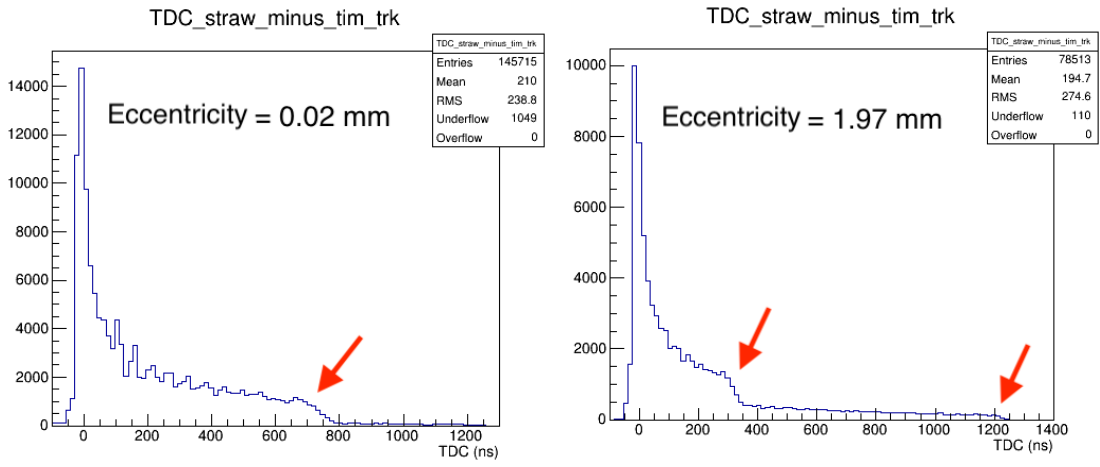


Figure 3.42: The drift time distributions for two values of wire eccentricities. The distribution on the left has only one step (shown by a red arrow), owing to the small wire eccentricity (0.02 mm). The distribution on the right has two steps (shown with two red arrows), due to the large eccentricity (1.97 mm).

methods are tried: Canny's method and an improved version of it, see Section 3.6.2 and 3.6.3, and a Laplacian of Gaussian (LoG) method, described in Section 3.6.4. The V-shape data (i.e. the measured drift time combined with track information from the telescope) is solely used in this last section in order to compare the performance of the various methods used to analysis the drift distribution.

### 3.6.1 Two-threshold method

The principle of our two-threshold method is as follows. In order to define the location of a step on the drift time axis, a threshold is chosen empirically by adjusting to the data. The position of the step is defined by the coordinate of the last histogram bin, which has a value above the defined threshold. If the wire is displaced from the center of the straw, one

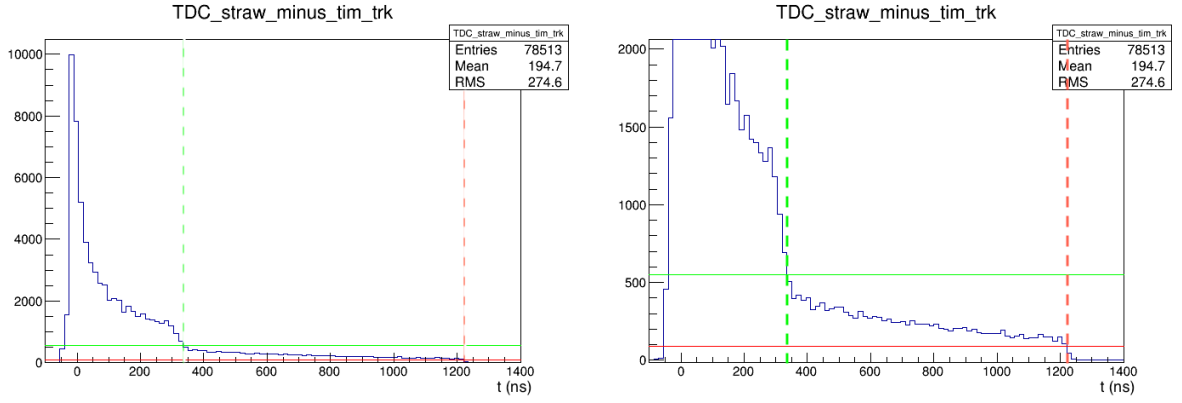


Figure 3.43: Drift time distribution for a large wire eccentricity (1.97 mm) with applied thresholds  $Thr_1$  (green horizontal line) and  $Thr_2$  (red horizontal line) and the extracted locations (green and red dashed vertical lines). The right plot is a zoom around the step.

expects two steps in the drift time distribution. In this case, two thresholds are needed to identify the locations of each step. For the test beam data the following choice of threshold values,  $Thr_1 = 5.5\%$  and  $Thr_2 = 0.9\%$  of the maximum of the drift time distribution produced stable results. Figure 3.43 shows for illustration the time distribution for a large wire eccentricity (1.97 mm) along with the threshold values (horizontal lines) and the extracted locations of the two steps (vertical lines).

The simplicity of the method is counterbalanced by a few shortcomings:

1. Unreliable results are obtained for small eccentricities. Even for zero eccentricity (a single step), the method still returns (artificially) two different step locations, given the inherent difference between the thresholds, see Figure 3.44.

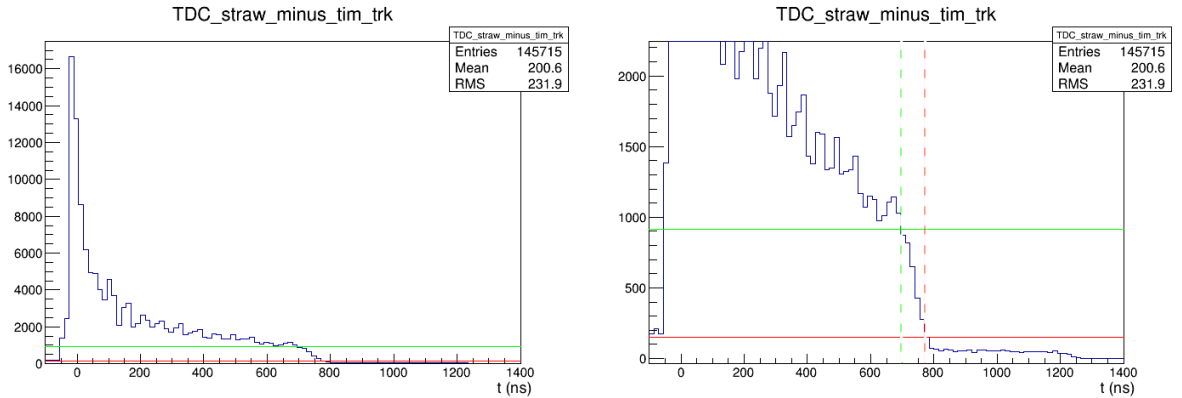


Figure 3.44: A. drift time distribution for a small wire eccentricity (0.02 mm) with applied thresholds:  $Thr_1$  (a green horizontal line) and  $Thr_2$  (a red horizontal line) and the extracted locations (green and red dashed vertical lines). The right plot is a zoom around the step.

2. The choice of thresholds is arbitrary and depends on the shape of the distributions, amount of entries, noise rate, etc.

Some tricks could be tried to address these shortcomings, but this was not further investigated.

### 3.6.2 Canny's edge detection method

The next study is based on Canny's edge finding algorithm. In general Canny's edge detection method [76] is a 2-dimensional (2D) algorithm used for finding edges in images. It can be adapted to the 1-dimensional (1D) case. Here, the following procedure was applied, using a 1D Canny's algorithm, and it is illustrated in Figure 3.45.

1. Smooth the drift time histogram  $h_i(t_i)$  by convolving it with a Gaussian kernel as described below (an example of the original and smoothed histograms is shown in Figure 3.45 top left and right).
2. Produce numerically the first derivative  $h'_i(t_i)$  of the smoothed histogram (Figure 3.45 bottom left).
3. Apply a cut on the differentiated distribution ( $t_{drift} > 250$  ns) in order to skip the large peak around 0 ns.
4. In the kept part of the histogram find the positions  $t_i$  of all local minima, where a local minimum is here defined as a bin with value  $h'_i$  below empirically defined threshold and with neighbors that have both a larger (more positive) value.
5. The  $t_i$  with the most negative  $h'_i$  value is identified as  $t_{step1}$ , the position of the first step.
6. Set a threshold for a peak finding procedure (the choice of threshold is discussed later).
7. The  $t_i$  with the second most negative  $h'_i$  values is identified as  $t_{step2}$ , the position of the second step, provided it fulfills  $t_{step2} > t_{step1}$ , otherwise it is discarded and possibly the next candidate  $t_i$  is considered.

The convolution of the discrete data with a Gaussian kernel of a range  $\pm M$  is defined as:

$$h_s[i] = \sum_{j=-M}^M h[j] \cdot g[i-j], \quad \text{where } g[i-j] = \frac{1}{\sqrt{2\pi} \cdot \sigma} \cdot e^{-\frac{(t_i-t_j)^2}{2\sigma^2}}. \quad (3.15)$$

In Canny's 1D adapted edge finding method there are two parameters to vary. The first parameter is the  $\sigma$  of the Gaussian kernel. Its best value is chosen empirically after running the algorithm a few times over the test beam data. A large  $\sigma$  makes the histogram

smoother and the position of the edges more uncertain, a small value of the  $\sigma$  leads to leaving some remnant noise in the distribution and can fake peaks in the differentiated histogram. In order to speed up the algorithm, smoothing and differentiation operations can be combined using the following property of convolutions

$$\begin{aligned} \frac{d}{dx}g(x) \star h(x) &= \frac{d}{dx} \int g(x-y)h(y)dy = \\ \int h(y) \frac{d}{dx}g(x-y)dy &= h(x) \star \frac{d}{dx}g(x), \end{aligned} \quad (3.16)$$

i.e. the differentiated histogram can be obtained by convolving the original histogram with the derivative of the Gaussian kernel.

The second parameter is the threshold level. For the test beam data it was found empirically and converged to 6% of the magnitude of the first found (global) minimum. The performance comparison with other methods is shown and discussed later (Figure 3.49 and Section 3.7).

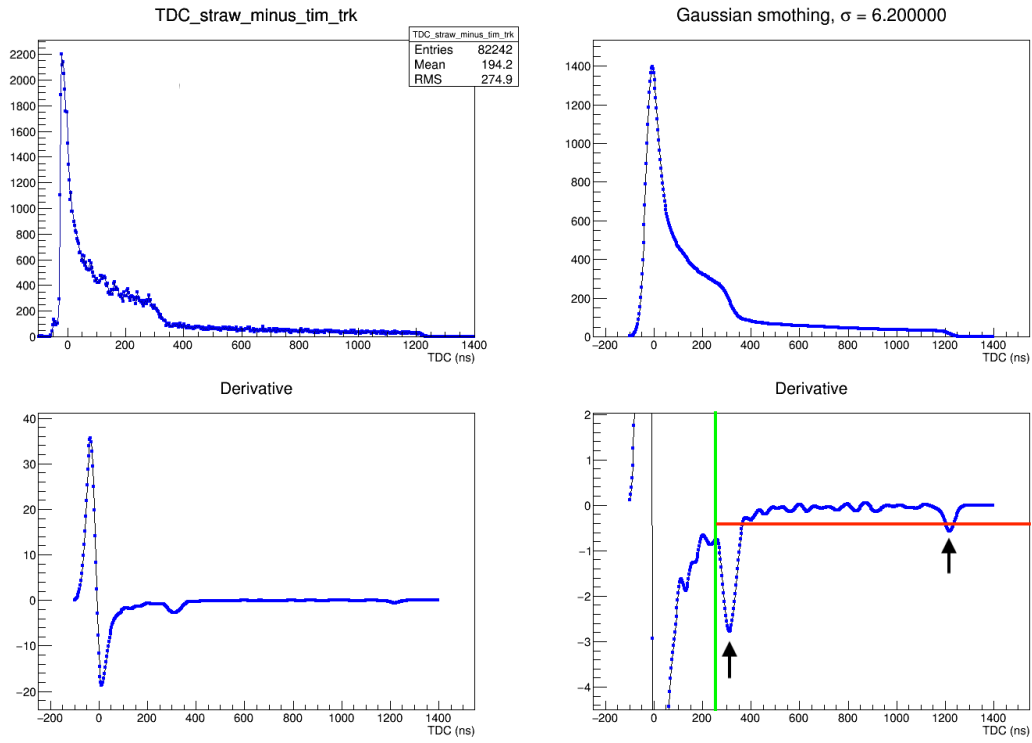


Figure 3.45: Illustration of the results obtained with a 1D Canny's method. Top left: the original drift time distribution for 1.97 mm wire eccentricity. Top right: the smoothed distribution with  $\sigma = 15.5$  ns. Bottom left: the first derivative of the smoothed distribution. Bottom right: zoom of the first derivative with the cut and the thresholds displayed (green and red lines respectively). The black arrows show the position of the found edges.

### 3.6.3 Improved Canny's method

Instead of running Canny's algorithm multiple times, as described in the previous section, in order to find best values for the  $\sigma$  and the threshold, the following solution can be used. The first step is to run the Canny's method with larger  $\sigma$ , for example 23.8 ns (according to Section 3.6.2). This results in a worse edge localization and merging of close edges, but at the same time in a favorable noise suppression. The positions of the edges found during the first step are used as a rough estimation of the real edge locations. The second step is to define subranges of the original distribution with their centers at the estimated edge locations. A subrange width of 50 ns in the vicinity of each edge gives the best results for the test beam data. Canny's algorithm is executed again exclusively over the chosen subranges and with a smaller  $\sigma$  (12.5 ns). As shown in Figure 3.46, the minima inside the subranges have larger magnitudes than in Figure 3.45 and the noise peaks outside the selected ranges become highly suppressed. This leads to more precise localization of the edges and extra reduction of the probability to identify the noise peaks as the real edges of the distribution. The performance comparison of this method with original Canny's and other methods described in the following subsections is shown in Figure 3.49 and discussed in Section 3.7.

### 3.6.4 Laplacian of Gaussian method

This method [77] utilizes a double differentiation of the smoothed histogram. Using the convolution property shown in equation (3.16), the smoothing and the differentiation can be combined into a single operation, but now with the Gaussian kernel differentiated twice. This is the reason why this approach is called Laplacian of Gaussian. The algorithm itself can be described by the following steps:

1. Convolve the original histogram  $h$  with the double derivative of a Gaussian kernel, following expression (3.15).
2. Apply a cut on the resulting distribution  $h''$  (using  $t_{drift} > 250$  ns) in order to skip the large peak around 0 ns.
3. Find the ascending zero crossings of  $h''$ , which correspond to the middle of the descending slopes (steps) of the original distribution.
4. For each entry  $h''_k$  calculate a local variance as  $v_k = \frac{1}{2m+1} \sum_{l=k-m}^{l=k+m} (h''_l - h''_k)^2$
5. In order to get rid of noise crossings, select zero crossings which have a  $v_k > v_{thr}$ . Both  $m$  and  $v_{thr}$  are chosen by trial.

The method has three parameters: the  $\sigma$  of a Gaussian kernel, the range of the variance and the variance threshold. For the test beam data  $\sigma = 18$  ns is chosen. The variance range is set to be 12.5 ns per histogram bin. The variance threshold is defined empirically

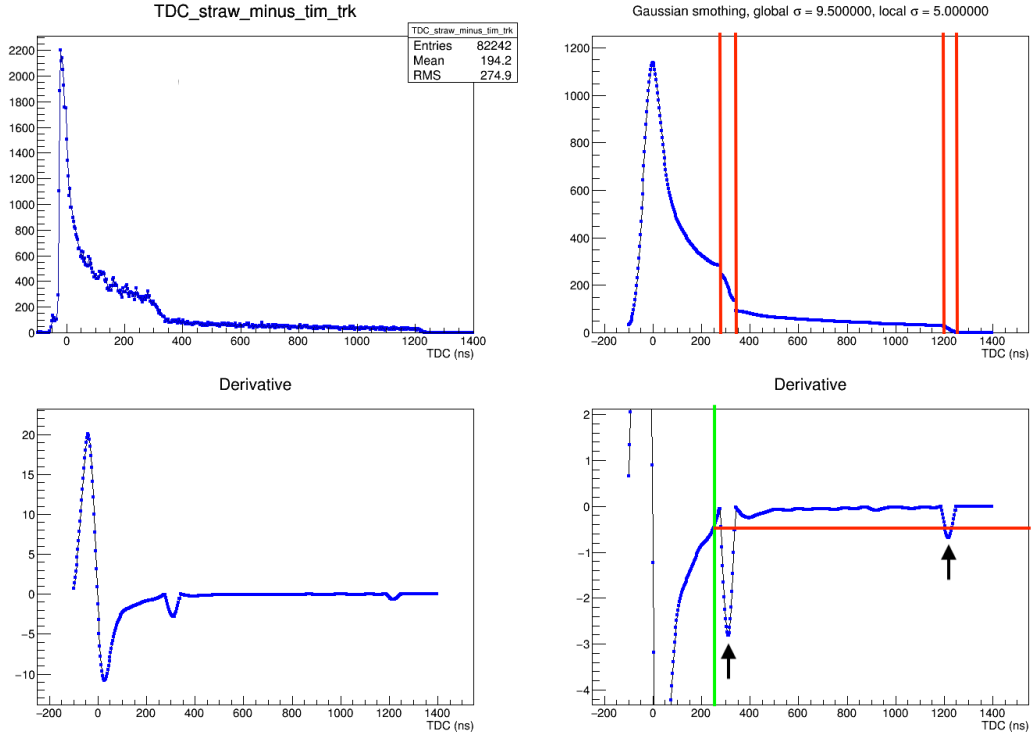


Figure 3.46: Illustration of the results obtained with the improved Canny's method. Top left: the original drift time distribution for 1.97 mm wire eccentricity. Top right: the smoothed distribution with  $\sigma = 12.5$  ns for the subranges (defined by the vertical red lines) and  $\sigma = 23.8$  ns for the rest of the histogram. Bottom left: the first derivative of the smoothed distribution. Bottom right: a zoom of the first derivative with the cut and the threshold displayed (green and red lines respectively). The black arrows show the position of the found edges found.

after running the algorithm a few times. The procedure is illustrated in Figure 3.47 which shows the original drift time distribution  $h$  for 1.97 mm wire eccentricity (top left graph), the resulting distribution  $h''$  after convolving with the double derivative of a Gaussian kernel with  $\sigma = 18$  ns (top right graph), a zoom of the same graph after removing the left peak (bottom left graph), and the variance  $v_k$  with the threshold (red line) applied to select the zero crossings (bottom right graph).

The comparison of the results obtained with LoG method to other methods is shown in Figure 3.49 and discussed in Section 3.7.



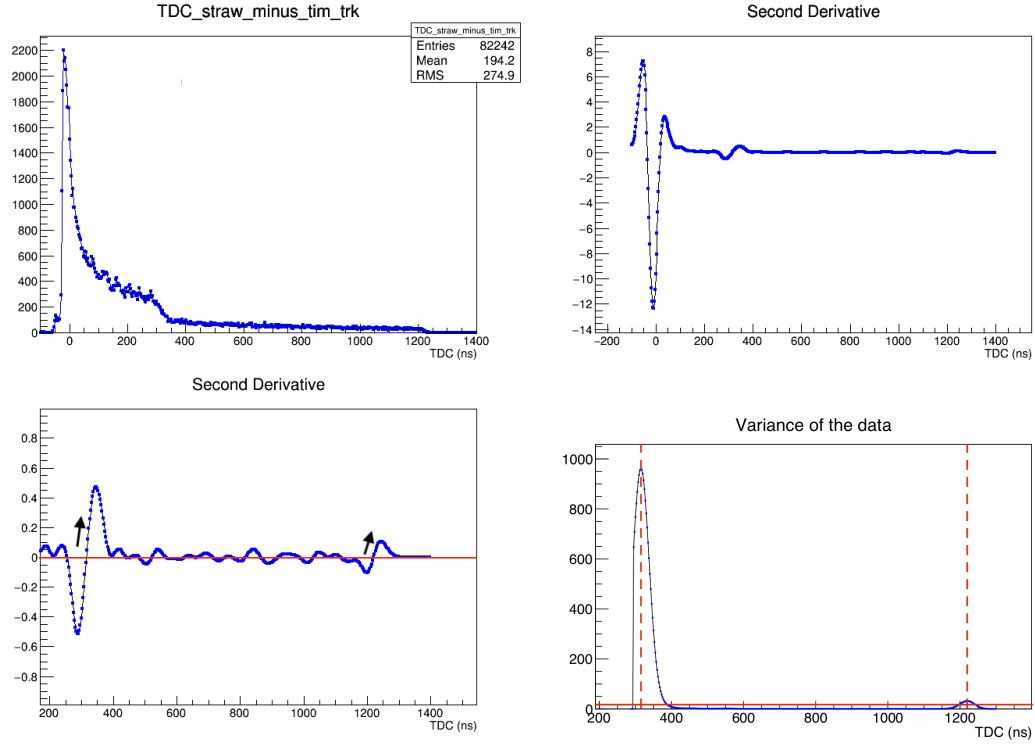


Figure 3.47: Illustration of the results obtained with the Laplacian of Gaussian method. Top left: original drift time distribution for 1.97 mm wire eccentricity. Top right: distribution convolved with the double derivative of a Gaussian kernel with  $\sigma = 18$  ns. Bottom left: a zoom of convolved distribution with the cut applied to remove the left peak. The black arrows show the ascending zero crossings. Bottom right: a variance of the convolved distribution and the threshold (a red line) applied to select the zero crossings. The vertical dashed red lines showed the localized peak positions.

## 3.7 The results of the edge finding algorithms and their application

### 3.7.1 Comparison of the results

To compare the performance of the various edge finding methods, the wire eccentricity  $\Delta Y_{ecc}$  is directly used. A reference relation between the drift time difference of the two steps,  $\Delta t_{drift}$ , and the wire eccentricity  $\Delta Y_{ecc}$  is first obtained from the V-shape data. This association is shown in Table 3.9. The negative values in the bottom of the table mean that the apex of the V-shape curve (which is the wire position) has moved to the other side of the straw tube axis  $Y_{tube}$  (in the vertical direction, given our test beam setup). Explicitly, the wire eccentricity was calculated from the apex position  $Y_0$  and the  $Y$  edges of the two branches of the V-shape,  $Y_-$  and  $Y_+$ , which are extracted by analysis of the

Table 3.9: Wire eccentricities  $\Delta Y_{ecc}$  extracted from V-shapes and from the direct optical measurements  $\Delta Y_{ecc,opt}$  (see Section 3.3) and drift time differences between the edges of the V-shape  $\Delta t_{drift}$ . Here,  $\Delta Y = Y_+ - Y_-$ .

$Y_-$ (cm)	$Y_+$ (cm)	$\Delta Y$ (cm)	$Y_0$ (cm)	$Y_{tube}$ (cm)	$\Delta Y_{ecc}$ (cm)	$\Delta t_{drift}$ (ns)	$\Delta Y_{ecc,opt}$ (cm)
-1.045	0.875	1.920	0.120	-0.085	0.205	879.415	0.239
-1.045	0.895	1.940	0.121	-0.075	0.196	860.443	0.232
-1.065	0.915	1.980	0.124	-0.075	0.199	824.786	0.215
-1.045	0.935	1.980	0.121	-0.055	0.176	740.948	0.218
-1.025	0.955	1.980	0.122	-0.035	0.157	660.780	0.191
-1.005	0.985	1.990	0.122	-0.010	0.132	546.713	0.195
-0.985	1.005	1.990	0.122	0.010	0.112	440.789	0.171
-0.985	0.995	1.980	0.122	0.005	0.117	470.417	0.171
-1.015	0.965	1.980	0.122	-0.025	0.147	611.439	0.149
-1.025	0.955	1.980	0.121	-0.035	0.156	665.380	0.150
-1.045	0.925	1.970	0.119	-0.060	0.179	750.143	0.127
-1.065	0.915	1.980	0.121	-0.075	0.196	829.820	0.116
-1.065	0.895	1.960	0.123	-0.085	0.208	867.076	0.118
-0.895	1.095	1.990	0.122	0.100	0.022	65.199	0.127
-0.865	1.125	1.990	0.123	0.130	-0.007	-79.915	0.127
-0.995	0.985	1.980	0.122	-0.005	0.127	524.875	0.067
-1.005	0.985	1.990	0.122	-0.010	0.132	569.119	0.027
-0.955	1.025	1.980	0.122	0.035	0.087	325.657	-0.006
-0.885	1.105	1.990	0.121	0.110	0.011	2.836	-0.012

V-shape as explained in Section 3.4.3. The wire eccentricity is calculated from

$$\Delta Y_{ecc} = Y_0 - Y_{tube} \quad \text{with } Y_{tube} = (Y_- + Y_+)/2 \quad (3.17)$$

and the reference drift time difference from

$$\Delta t_{drift} = t_- - t_+ \quad (3.18)$$

where  $t_{\pm} = f(Y_{\pm})$  and  $f(Y)$  is the parametrization of the V shape (here the degree 6 polynomial fit results were used from the Section 3.5.1).

In Figure 3.48 the optically measured reference wire eccentricity  $\Delta Y_{ecc,opt}$  is shown as a function of the corresponding reference drift time difference. The slope is about  $2.49 \mu\text{m/ns}$ .

The drift time differences obtained using the edge finding algorithms are then compared to the differences from the reference drift time in Table 3.9. They are shown also as separate plots with linear fits in Figure 3.49.

In general, all methods show consistent results in finding the drift time differences between the steps of the drift time distribution. This is shown by the obtained value of the slope fit parameter, which is  $\approx 1$  for all methods. However, Canny's method has better

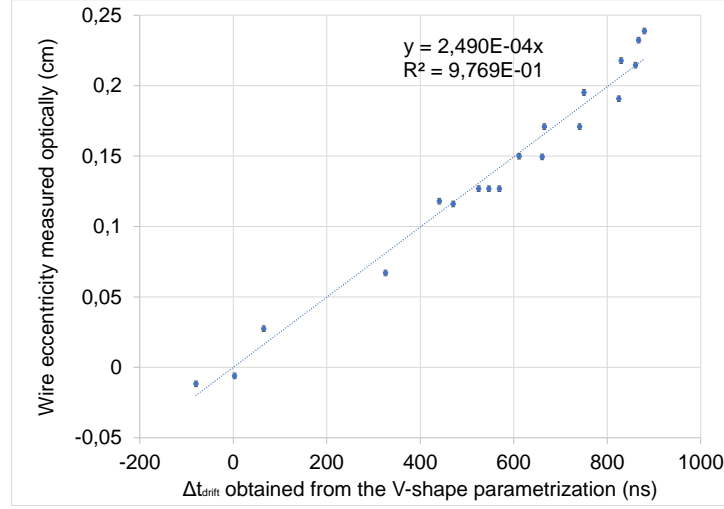


Figure 3.48: The optically measured wire eccentricity as a function of the drift time differences.

edge localization than the two-threshold method, but it is more sensitive to noise. The algorithm needs to be executed a few times in order to find the optimal values of the  $\sigma$  and threshold. Another disadvantage is that Canny’s method cannot distinguish edges which are too close to each other, because after smoothing they can merge into a single broader edge. The advantage of the Laplacian of Gaussian method is that it grants the best edge localization with smaller uncertainties. It requires larger  $\sigma$  value for smoothing than Canny’s algorithm, because the noise is amplified after the 2<sup>nd</sup> differentiation, so it requires fine tuning of the variance thresholds.

The robustness against statistical starvation of the described methods can be tested by varying the number of events in the drift time distribution histogram. As an example, the merged runs Nr. 233–236 are taken, corresponding to an intermediate wire eccentricity of 1.22 mm and a reference  $\Delta t_{drift}$  value of 525 ns, see table 3.9. The total amount of events in the data sample with a single hit in T0 and the straw tube is 440 077. In order to simulate the lack of statistics in the data sample, during the analysis some fraction of the events were skipped. The selection of skipped events was randomized. Figure 3.50 shows the result of this study, with the “residual” on the ordinate axis defined as the  $\Delta t_{drift}$  difference between the reference value and the value obtained with the reduced sample. The point with the largest number of events on each plot corresponds to the full data sample, then it was randomly divided by random sub-samples corresponding to 1/2, 1/4, 1/8, 1/16 and 1/32 of the full sample. As expected, the worst robustness is seen for the two-threshold method, because it is applied on the raw drift time distribution without smoothing. The distribution becomes noisy, when the number of events is small, and the method starts picking wrong edges. The other methods show remarkable stability against the reduction of the event sample, keeping the distribution of the residual values almost

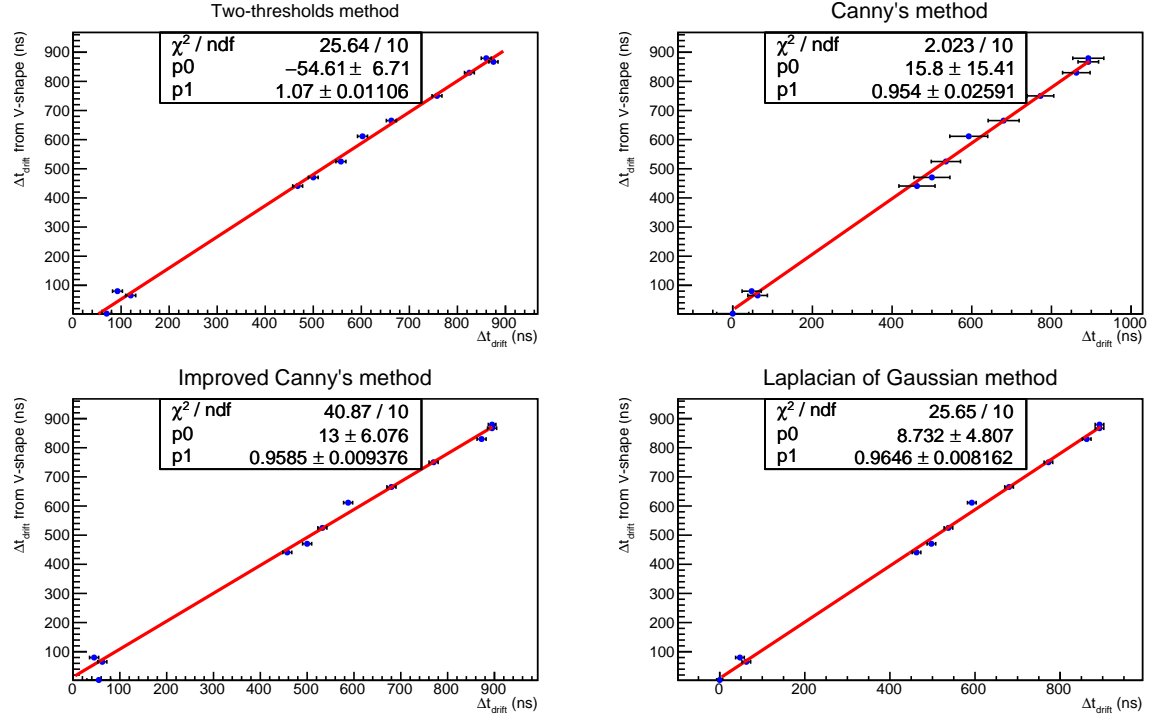


Figure 3.49: Performance of the edge finding algorithms. The reference drift time differences calculated from the V-shapes directly (along vertical axes of the plots) are compared to the drift time differences obtained with the edge finding algorithms from the drift time distributions alone. Top left: simple 2-threshold method. Top right: Canny's method. Bottom left: improved Canny's method. Bottom right: Laplacian of Gaussian method. In each plot the red line is the result of a linear fit.

flat.

The results presented here show that, with some variation in performance, the edge finding methods can be used for the SHiP SST, together with a reference calibration curve, to determine the wire eccentricity down to about  $\sim 0.1$  mm with a precision of the order of  $50 \mu\text{m}$ , depending on the statistics available. These methods are rather generic and can be exploited for arbitrary straw tube detector with own properties (gas mixture, pressure, high voltage, etc.).

### 3.7.2 Reconstruction of the isochrone relation

The other application of the edge finding results is the reconstruction of the  $r(t)$  isochrone relation for the straw tube, even in the presence of a wire eccentricity. The connection between the drift time distribution and the distance to the center of the tube can be derived with some approximations. Defining  $r$  as the distance of closest approach (DOCA) of the charged particle trajectory relative to the wire, the drift velocity can be related to  $\frac{dN}{dr}$  (the distribution of DOCA) and  $\frac{dN}{dt}$  (the drift time distribution) using:

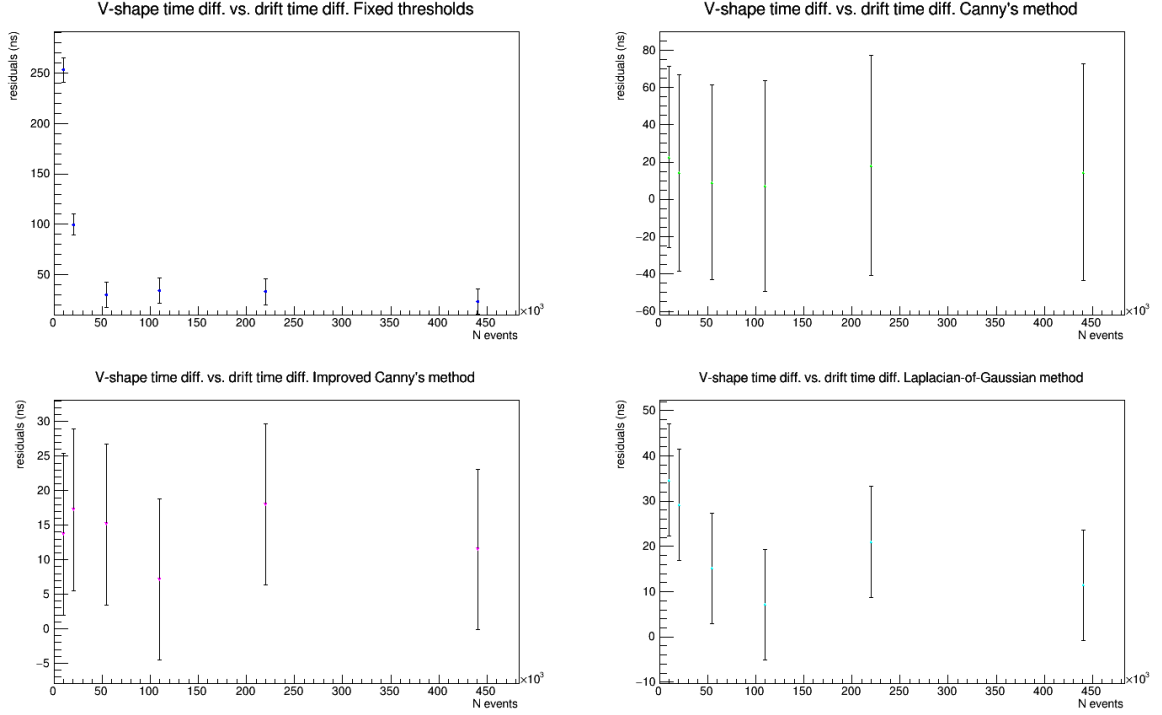


Figure 3.50: Robustness against statistical starvation for the two-thresholds method (top left), Canny’s method (top right), improved Canny’s method (bottom left) and a Laplacian of Gaussian method (bottom right). The residual is the difference between the values of  $\Delta t_{drift}$  obtained with reduced statistics,  $N_{events}$ , and the reference value (which was 525 ns for the considered wire eccentricity of 1.22 mm).

$$v_{drift} = \frac{dr}{dt} = \frac{dr}{dN} \cdot \frac{dN}{dt} \quad (3.19)$$

For a homogeneous illumination (by  $N_{tracks}$  particles) of the straw tube across its diameter, i.e. with trajectories following an axis  $Z$  perpendicular to the straw axis  $X$  and uniformly distributed along the other perpendicular axis  $Y$ , like in our test beam setup,  $\frac{dN}{dr}$  is equal to  $\frac{N_{tracks}}{R_{in}}$ , where  $R_{in}$  is the inner radius of the tube (assumed to be much larger than  $R_{wire}$ , the radius of the wire).

Assuming first zero wire eccentricity,  $r(t)$  can be derived from

$$r(t) = \int_0^t v_{drift}(t') dt' = \frac{R_{in}}{N_{tracks}} \int_0^t \frac{dN}{dt'} dt' , \quad (3.20)$$

i.e. from an integration of the drift time distribution.

In case of non-zero eccentricity the  $\frac{dN}{dr}$  distribution becomes wider (up to  $R_{in} + \Delta Y_{ecc}$ ) and gets a singularity at  $R_{in} - \Delta Y_{ecc}$ , so the  $\frac{dN}{dr}$  drops to the  $\frac{N_{tracks}}{2R_{in}}$  at the singular point, because the events from only longer branch of a V-shape populate the tail of a drift time

distribution between  $t_{step1}$  and  $t_{step2}$ . The correction  $\Delta r(t)$  to  $r(t)$  for  $t > t_{step1}$  should be calculated using

$$\Delta r(t) = \frac{2R_{in}}{N_{tracks}} \int_{t_{step1}}^t \frac{dN}{dt'} dt' \quad (3.21)$$

where  $t_{step1}$  is the position of the first step of the drift time distribution. The total  $r(t)$  becomes a sum of two integrals with different coefficients

$$r(t) = \frac{R_{in}}{N_{tracks}} \int_0^{t_{step1}} \frac{dN}{dt'} dt' + \frac{2R_{in}}{N_{tracks}} \int_{t_{step1}}^t \frac{dN}{dt'} dt' \quad (3.22)$$

where it is meant that the second integral is only added if  $t > t_{step1}$ .

The wire eccentricity itself can be extracted after integration of the equation (3.21) up to  $t_{step2}$ , which is the second step of the drift time distribution:

$$\Delta Y_{ecc} = \frac{\Delta r(t_{step2})}{2} = \frac{R_{in}}{N_{tracks}} \int_{t_{step1}}^{t_{step2}} \frac{dN}{dt'} dt' . \quad (3.23)$$

In order to estimate the effect of a non-homogeneous illumination along the  $Y$  coordinate, a test is made which uses the actual beam profile as measured during the test beam with the telescope tracker. As before, the tracks are considered to be parallel to the beam axis ( $Z$ ), so that the obtained  $\frac{dN}{dY}$  can be simply converted to the  $\frac{dN}{dr}$  distribution. The  $r(t)$  dependence cannot be obtained directly when an arbitrary illuminations is used. The integral equation relating  $r$  to  $t$  should be solved numerically:

$$\int_0^r \frac{dN}{dr'} dr' = \int_0^t \frac{dN}{dt'} dt' \quad (3.24)$$

The conversion of  $\frac{dN}{dr}$  into  $\frac{dN}{dY}$  can be inserted explicitly into the equation (3.24):

$$\int_0^r \frac{dN}{dr'} dr' = \begin{cases} \pm \int_{Y_0}^Y \frac{dN}{dY'} dY' \pm \int_{2Y_0-Y}^{Y_0} \frac{dN}{dY'} dY' & Y \in \begin{cases} [Y_0, Y_+] & (+) \\ [2Y_0 - Y_+, Y_0] & (-) \end{cases} \\ \int_{2Y_0-Y_+}^{Y_+} \frac{dN}{dY'} dY' + \int_Y^{2Y_0-Y_+} \frac{dN}{dY'} dY' & Y \in [Y_-, 2Y_0 - Y_+] \end{cases} \quad (3.25)$$

where  $Y_+$  and  $Y_-$  are the coordinates of the tube borders. The array of  $r$  values is calculated from the equation (3.24) using the bisection method [78] starting with the interval  $[0, 2 \cdot R_{in}]$ .

In Figure 3.51 the comparison is shown between the  $r(t)$  relations obtained from the numerical integration of the drift time distribution using equation (3.22) (assuming a flat beam profile) and (3.24) (folding in the beam profile). The left graph is for a large wire eccentricity (1.97 mm), the right graph for a small wire eccentricity (0.02 mm). For reference, also the two branches of the V-shape are shown which were obtained with a

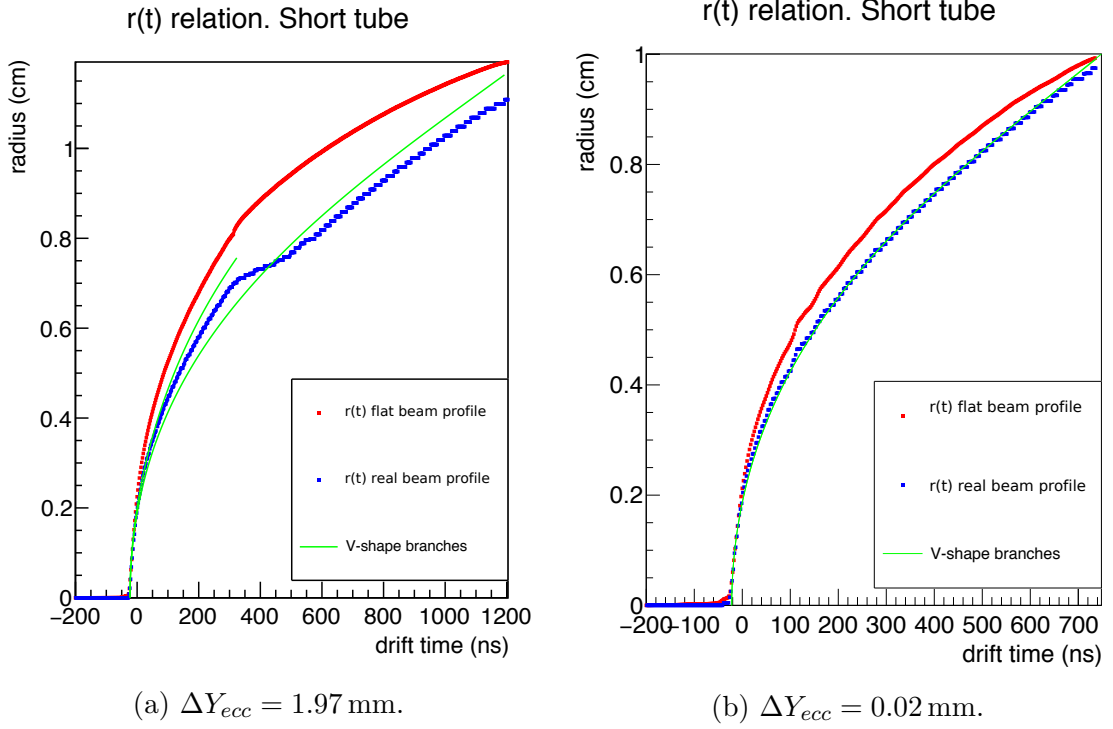


Figure 3.51: The graph on the left shows the comparison between the  $r(t)$  relations, in red obtained using the equation (3.22), in blue obtained using the equation (3.24) from the experimental data, the green lines show the parametrized V-shape branches with 6<sup>th</sup> degree polynomial for a short straw tube with large eccentricity (1.97 mm). The plot on the right shows the same comparison as the left one, but for the short straw tube with the wire almost centered inside the tube (0.02 mm eccentricity).

degree 6 polynomial fit (see Section 3.5.1). One notes, especially for the small eccentricity, that the effect of the non-homogeneous beam profile is not negligible and it is correctly accounted for when extracting  $r(t)$  with equation (3.24). However, a small part of the discrepancy between the two  $r(t)$  results may also be due to the fact that, for the value of  $R_{in}$  entering in equation (3.22), a nominal value of 10 mm was used, which is an overestimation of the sensitive radius of the tube (the sensitive radius, depending on definition, is a few hundred micrometers smaller than the physical tube radius).

#### **$r(t)$ relation for a straw tube in case of pure homogeneous illumination**

The tracks from charged particles in some use cases of the detector can penetrate the tube from any direction contrary to the test beam setup, when all the tracks were almost perpendicular to the longitudinal cross section of the straw tube. Such tracks will create a uniform distribution of the hits inside the whole volume of the tube leading to the fact that the distribution of the tracks along the radius-vector inside the transverse plane will

not be flat like it should be for a homogeneous illumination from a single direction.

In order to simplify the problem and exploit the axial symmetry of the straw tube the transverse cross section of the tube is observed. In case of the tube with the wire perfectly located in the center the cumulative distribution function (CDF)  $N(r)$  of the uniformly distributed distances to the wire is proportional to the area of the tube covered by a circle with the radius of  $r$ :

$$N(r) = \mathcal{P}(r' \leq r) \sim r^2 \quad (3.26)$$

Thus the probability density function (PDF) as a derivative is proportional to the  $r$  (linear dependence). Indeed, the  $\frac{dN}{dr}$  is proportional to the arc length ( $2\pi r$ ), which forms the infinitesimally thin ring of width  $dr$ , where a certain number of points  $dN$  are positioned. When the radius  $r$  increases, the number of points inside each ring grows linearly:

$$\frac{dN}{dr} = \mathcal{P}(r' = r) = \alpha r \quad (3.27)$$

The  $\alpha$  coefficient can be calculated from the border conditions and it is equal to  $\frac{2N_{tracks}}{R_{in}^2}$ . The  $r(t)$  relation according to formula (3.19) and (3.20) is:

$$r(t) = \sqrt{\frac{R_{in}^2}{N_{tracks}} \int_0^t \frac{dN}{dt'} dt'} \quad (3.28)$$

The next step is to add the wire displacement  $\Delta Y_{ecc}$ . In this case any radius vector built towards any ring inside the tube has a shifted starting point to  $(0, \Delta Y_{ecc})$ . As a starting point is moved from the center of the coordinate system the radius vector  $r$  can point outside of the fiducial volume of the straw tube, when its length becomes larger than  $R_{in} - \Delta Y_{ecc}$ . This means that the PDF  $\frac{dN}{dr}$  will start to decrease, because there will be less random points belonging to the arc at distance  $r$  than in case of  $r < R_{in} - \Delta Y_{ecc}$ . For smaller values of  $r$  the dependence of the PDF is the same as for a case with symmetrical wire arrangement (3.27). This issues with large  $r$  described above are illustrated clearly in Figure 3.52. In order to calculate the length of the part of the arc, which lies inside the volume of the tube (from point  $A$  to the diameter  $OO'$  of the tube), the one should apply the law of cosines on the triangle  $OAO'$ . The cosine of the angle *alpha* is equal to:

$$\begin{aligned} \cos(\alpha) &= \frac{r^2 - R_{in}^2 + \Delta Y_{ecc}^2}{2r\Delta Y_{ecc}} \\ \alpha &= \arccos\left(\frac{r^2 - R_{in}^2 + \Delta Y_{ecc}^2}{2r\Delta Y_{ecc}}\right) \end{aligned} \quad (3.29)$$

The arc length  $l$  between the point  $A$  and the diameter  $OO'$  is  $l = r \cdot \alpha$ . The PDF  $\frac{dN}{dr}$  is proportional to the length of the arc  $l$  doubled (because of a symmetry) and for the range  $[R_{in} - \Delta Y_{ecc}, R_{in} + \Delta Y_{ecc}]$  is the following:



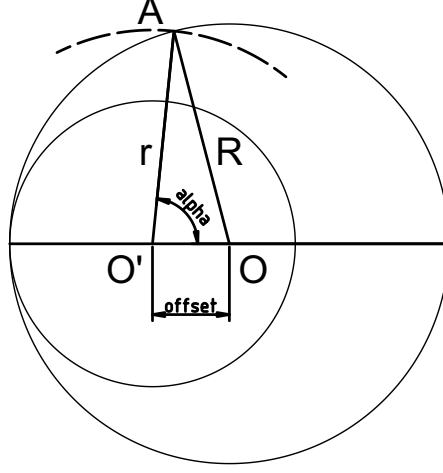


Figure 3.52: The straw tube cross section with displaced wire to the point  $O'$  from the original center  $O$ .  $r$  is the radius-vector from point  $O'$  to the arc, which intersects the straw tube wall in the point  $A$ .

$$\frac{dN}{dr} = 2\beta r \arccos \left( \frac{r^2 - R_{in}^2 + \Delta Y_{ecc}^2}{2r\Delta Y_{ecc}} \right) \quad (3.30)$$

The coefficient  $\beta$  can be calculated from the border conditions and is equal to  $N_{tracks}/(\pi R_{in}^2)$ . In order to find the  $r(t)$  the PDF needs to be integrated along  $r$  according to (3.24). With the linear part there is no problem and it is equal to (3.28), when  $r < R_{in} - \Delta Y_{ecc}$ . The rest of a PDF can be analytically integrated, but in order to simplify the final relation for the  $r(t)$  the arccos can be expanded to Taylor series at point  $r = R_{in}$ . The expansion to the first term of the series has enough precision for the approximation:

$$\arccos \left( \frac{r^2 - R_{in}^2 + \Delta Y_{ecc}^2}{2r\Delta Y_{ecc}} \right) \approx \arccos \left( \frac{\Delta Y_{ecc}}{2R_{in}} \right) - \frac{(2R_{in}^2 - \Delta Y_{ecc}^2)(r - R_{in})}{2R_{in}^2 \Delta Y_{ecc} \sqrt{1 - \left( \frac{\Delta Y_{ecc}}{2R_{in}} \right)^2}} \quad (3.31)$$

The last step is to integrate the (3.30) along the radius  $r$  starting from  $R_{in} - \Delta Y_{ecc}$  and extract the  $r(t)$ . The integration of (3.30) and inserting the obtained answer to the (3.24) gives a 3-degree polynomial equation, which can be solved when the numerical values of all coefficients are inserted:

$$\beta(a + bR_{in})(r^2 - (R_{in} - \Delta Y_{ecc})^2) - \frac{2\beta b(r^3 - (R_{in} - \Delta Y_{ecc})^3)}{3} = \int_0^t \frac{dN}{dt'} dt' \quad (3.32)$$

$$\text{where } \beta = N_{tracks}/(\pi R_{in}^2), \quad a = \arccos \left( \frac{\Delta Y_{ecc}}{2R_{in}} \right), \quad b = \frac{(2R_{in}^2 - \Delta Y_{ecc}^2)}{2R_{in}^2 \Delta Y_{ecc} \sqrt{1 - \left( \frac{\Delta Y_{ecc}}{2R_{in}} \right)^2}}.$$



# Chapter 4

## SST studies in FairShip

The simulation of the SHiP experiment is performed in the FairShip framework [17]. FairShip is based on the FairRoot package [79] and is developed by the SHiP collaborators. The Geant4 package [80] is implemented into FairShip to simulate the passage of particles through the Target, the Hadron Absorber, the Muon Shield and the detector subsystems located downstream in the experimental hall. The detector description has been implemented into FairShip up to digitization, and the magnets are implemented with field maps from simulations with OPERA 3D package [81]. PYTHIA8 [82] is used for the generation of primary proton fixed-target interactions, PYTHIA6 [83] for muon deep inelastic scattering simulation, and the GENIE MC [84] generator for interactions of neutrinos. The production and the decays of Hidden Sector particles are handled by PYTHIA8. If the HS particle is produced from the decays of charm and beauty hadrons, then the cascade production of these hadrons from secondary interactions is simulated.

In this chapter several studies related to the SST performance within the FairShip simulation framework are described. The Section 4.1 is focused on studies of the SST occupancy with muon background hits depending on various SST geometry configurations and different magnetic field maps of the SHiP magnets implementations. In the second Section 4.2, the wire displacement simulation algorithms are proposed for the FairShip implementation followed with the related SST track fitting performance tests. In the last Section 4.3, the simulation of hits pile-up in the SST is developed and its effect on the tracks pattern recognition efficiency is shown and discussed.

### 4.1 Muon background studies

The current layout of the straw tubes of the SST stations was chosen according to the results of a simple toy Monte Carlo based simulation<sup>1</sup> and will be further optimized in the future. The original design of the SST is described in the SHiP Technical Proposal (TP) [2]. The tubes layout is shown in Figure 4.2 and Figure 4.3. In the following subsections the

---

<sup>1</sup>The simulation results were shown in slides: <https://indico.cern.ch/event/636443/contributions/2596063/attachments/1464271/2262988/plans.pdf>

effects on the hit rates per straw tube due to three changes are discussed. The first one is the effect of adding extra material around the stations. The second one – the effect due to a new and more realistic field in the spectrometer magnet is considered. The third one comes from introducing the new and realistic field map for the magnet of the SHiP Scattering and Neutrino Detector (SND) located upstream with respect to the SST position. In Section 4.1.5 the effect of symmetrizing the longitudinal positions of the stations around the SST magnet is presented.

#### 4.1.1 Material frames around the views

The material mass around the straw tubes may affect the background rate in the detector. One of the purposes of this study is to add a more realistic material distribution around the acceptance of the SST and study the impact on the rates. The old description of the TP [2] (see Figure 4.1) had aluminum frames (one per view) of 10 cm width and 1 cm lateral extent and with a total mass of 324.4 kg per station. Since then, preliminary conceptual designs of the station mechanics have been proposed [33] and [32]. Based

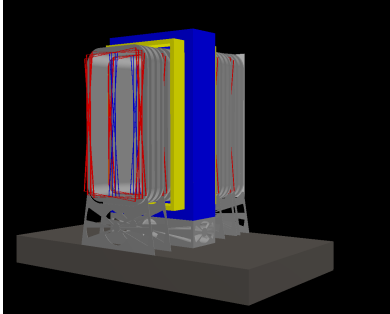


Figure 4.1: Old geometry of the SST with aluminum frames around the stations (obtained using Event Display script).

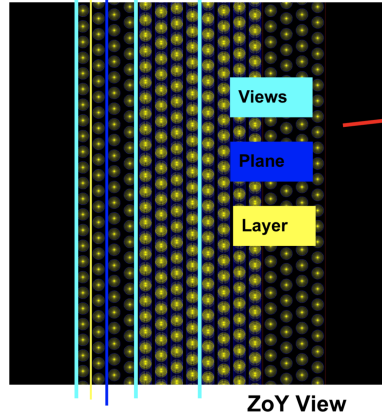


Figure 4.2: The schematic side view of the station showing its composition. Cyan lines separate the views, blue - the planes and yellow - the layers<sup>1</sup>.

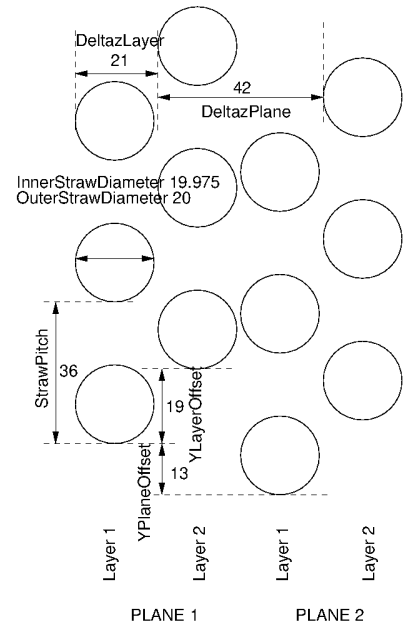


Figure 4.3: Schematic layout of one view with indicated new geometrical parameters used in FairShip.

<sup>1</sup>The figure is adapted from slides: [https://indico.cern.ch/event/660895/contributions/2696928/attachments/1510839/2356021/SST21Aug\\_Solovev.pdf](https://indico.cern.ch/event/660895/contributions/2696928/attachments/1510839/2356021/SST21Aug_Solovev.pdf)

on the heaviest of the proposed designs, stainless steel frames were implemented in the FairShip framework [2] around each view with a total mass of about 32 tonnes per station<sup>2</sup>, in place of the aluminum frames. The stations frame geometry proposed by D. Bick is shown in Figure 4.4 with dimensions. The lateral extent is 1.2 m. The material is steel and the density is 7.874 tonnes/m<sup>3</sup>. For simplicity, one frame per view was implemented with each frame following the orientation of the embedded view. The size of each frame is  $7.4 \times 12.4 \text{ m}^2$  with a hole in the middle of  $5 \times 10 \text{ m}^2$ . The thickness of the frames is 2.5 cm and the total number of them is 16 (one per view). Each of these frames weighs about 8.22 tonnes. The parameters of the frames are configurable through a geometry configuration script included in the FairShip (see Appendix D). The updated geometry with the material frames is shown in Figure 4.5.

FairShip simulations of the muon background were performed using 67 pre-generated muon files available in the SHiP EOS storage. These files were generated using the version of FairShip from October 27, 2017. The muons were produced through various channels including the primary 400 GeV proton interaction with the SHiP target, cascade interactions and showering up to the end of the hadron absorber, decays of kaons, pions, charm and beauty hadrons (see also [85] and [86]). To save CPU time, only particles with an energy above 10 GeV were transported in Geant4 [80] to the exit from the Hadron absorber and only generated events with at least one muon coming out of the absorber were saved. The files contain coordinates, momenta and time of these muon events. For the muon background simulation, each muon is placed again at its production place with

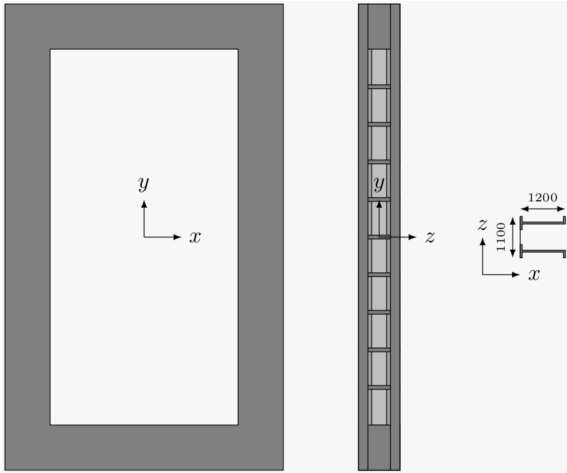


Figure 4.4: One of the proposed conceptual designs of the supporting frames and vacuum envelope for one station<sup>1</sup>.

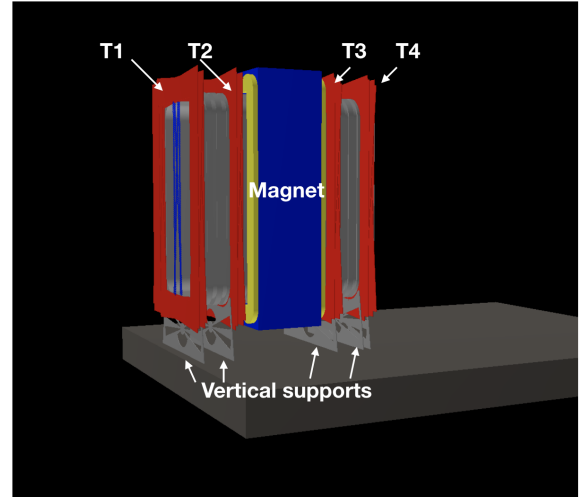


Figure 4.5: The updated geometry with the material frames added, in red (one per view, obtained using Event Display script).

<sup>1</sup>The figure is adapted from slides: [https://indico.cern.ch/event/704472/contributions/2890094/attachments/1603293/2542588/status\\_hamburg.pdf](https://indico.cern.ch/event/704472/contributions/2890094/attachments/1603293/2542588/status_hamburg.pdf)

<sup>2</sup>This is may be an overkill. Lighter frames may be possible.

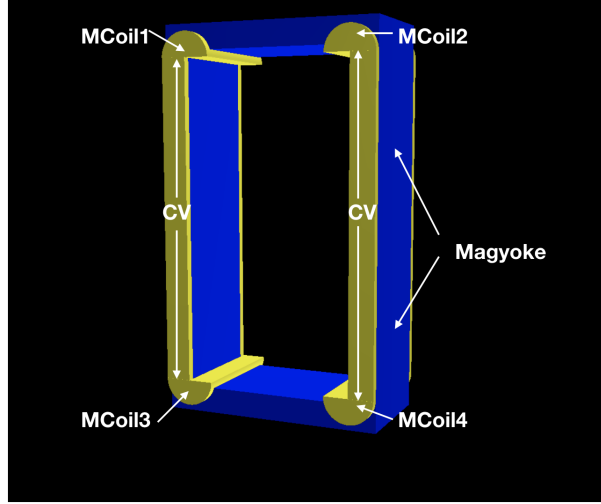


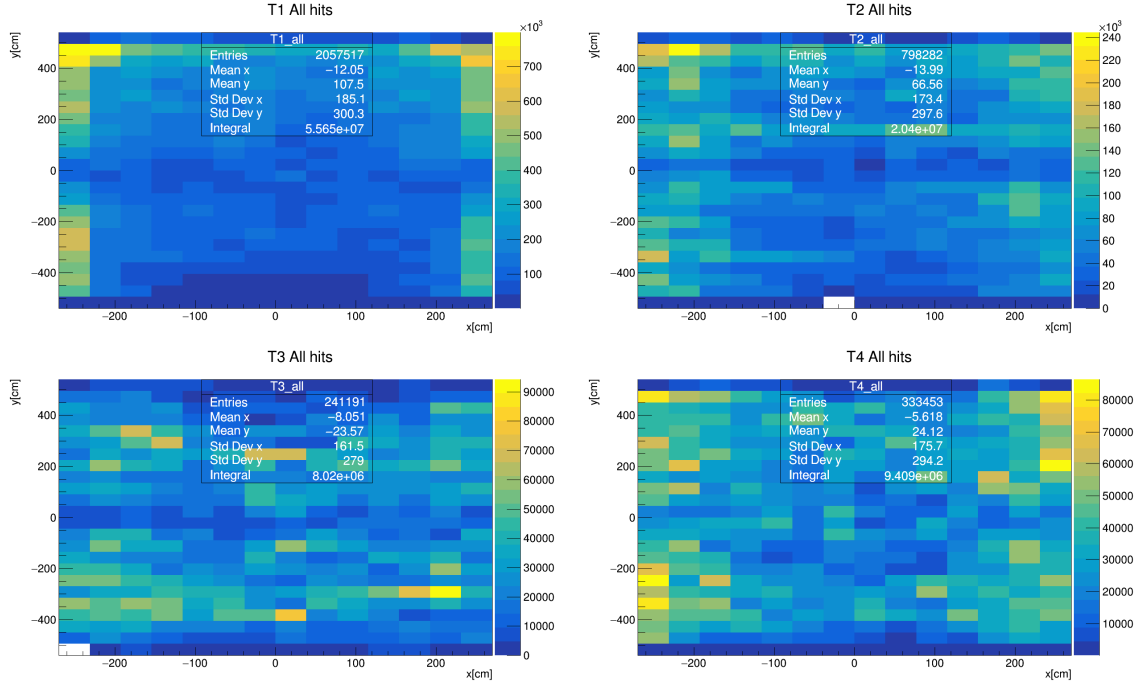
Figure 4.6: The geometrical volumes of the spectrometer magnet defined in the FairShip framework (obtained using Event Display script).

its corresponding momentum, and transport through the full SHiP setup is simulated in Geant4, with the active Muon Shield, the Scattering and Neutrino Detector, the vacuum tank and the straw tracker.

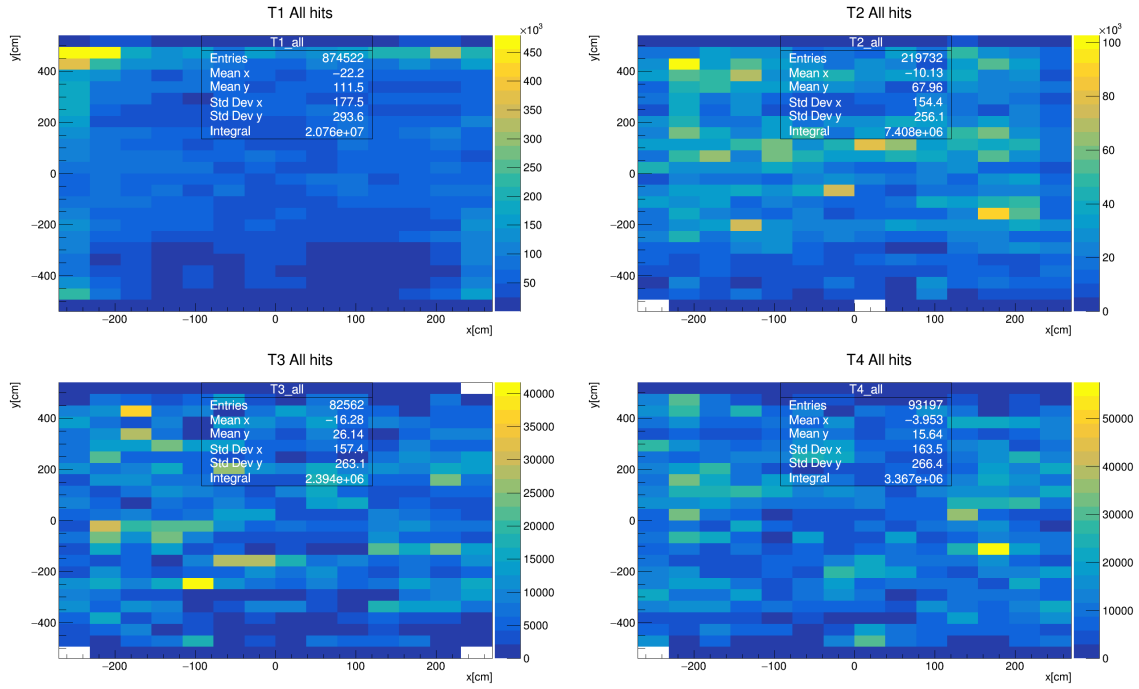
Each simulated muon in the file has a weight, which allows one to normalize the statistics to one SPS spill equivalent  $5 \cdot 10^{13}$  protons on target, while taking into account the enhancement factors for the production from charm and beauty cross sections, dimuon decays, etc. In simple terms, the trick with the weights enables the usage of the events from different sources in an uniform way, which means that some rare processes have larger probability in the simulation, but the muons produced by them have smaller weight. This also preserves the computational time of the simulation without losing too much in reliability of the results. The hits registered inside the straw tubes are scaled according to the weight of the original muon. The parameters used to run the simulation are the following:

```
python2 "$FAIRSHIPRUN"/macro/run_simScript.py --strawDesign 10
--tankDesign 6 --muShieldDesign 9 --MuonBack --nEvents $N
-f $MUONS --nuTauTargetDesign 3
```

where \$MUONS variable contains the path to the muon background input files, \$N is equal to the number of entries in the input file. After the simulation within the FairShip special analysis script was run. The goal of that script was to create the straw tube hits distributions per station of the SST. Each hit has its own global coordinates (X,Y,Z) and detector ID. According to those values the 2D histograms of each station are filled with X,Y coordinates and associated weights. The bin size of the histograms is  $45 \times 45 \text{ cm}^2$ . The resulting distributions of the hits in the tracking stations are shown in Figure 4.7 (a) for the old aluminum frames and Figure 4.7 (b) for the new steel frames. The maximum hit rate per straw tube is calculated in a following way.



(a) Old aluminum frames.



(b) New steel frames.

Figure 4.7: The simulated muon background hit rates inside the SST stations T1–T4 compared between aluminum (a) and steel (b) frames around the stations.

As it was described previously the tracking stations consist of views, views – of planes, planes – of layers and the layers are formed of the individual straw tubes (see Figure 4.2 and 4.3). Two layers of straw tubes (i.e. single plane) cover full geometrical acceptance with no gaps between the tubes and it can be also assumed that a single particle most likely creates only a single hit in the plane. For each plane of the station the 2D histogram with the hits is created with the same bin sizes per axis ( $45 \times 45 \text{ cm}^2$ ) as the histograms per station showed previously in Figure 4.7. Then, for every plane the projection onto  $Y$  coordinate axis is created and the bin with maximum amount of weighted hits in the projection is found. Then the  $Y$  coordinate of this bin is obtained. Afterwards, the value in this bin is scaled to the number of the straw tubes per bin (25):

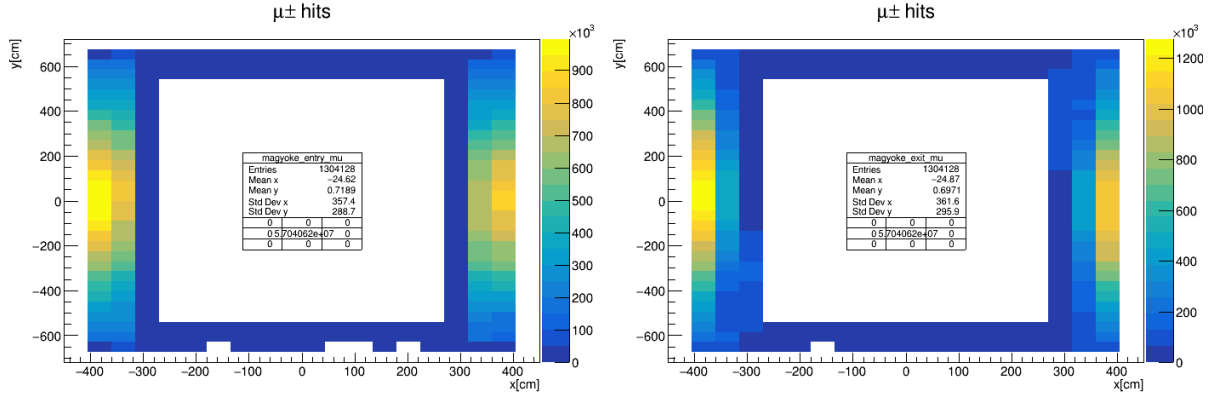
$$H_r = \max \left( \int_{-250 \text{ cm}}^{250 \text{ cm}} h_{r,i}(x) dx \right) / 55 \quad (4.1)$$

where  $h_{r,i}$  is the hit rate in the bins along  $X$  axis at  $i$  bin of  $Y$  coordinate, where  $i$  changes from the 1<sup>st</sup> to the last  $Y$  bin. The results of the simulations show that the replacement of the frames has caused a reduction of the maximum background rate in the stations by approximately 30%. The hottest station is T1, which has  $37.8 \pm 0.9 \text{ kHz}/(\text{tube})$  for the configuration with old aluminum material frames and  $26.6 \pm 0.7 \text{ kHz}/(\text{tube})$  for the configuration with the new steel frames (see Table 4.3 and 4.4). However, the background in the stations is not uniform. The highest rates are recorded in the corners of the stations. This effect is caused by the halo particles of the muon fluxes propagating on the left and the right sides of the tracker. Concerning the stations T3 and T4, the hit rates there decrease due to the same “shielding” effect of the steel frames as it is observed in T1 and T2. The hits in stations T1 and T2 are created by electrons and positrons for both aluminum and steel frames used (more than 97% and more than 94% respectively). However, as it is shown in Section 4.1.2 the composition of the hits in T3 and T4 stations is affected by the yoke iron and the return field in the SST magnet and contributes to muon domination instead of electrons and positrons in the current case (no field in the yoke of the magnet).

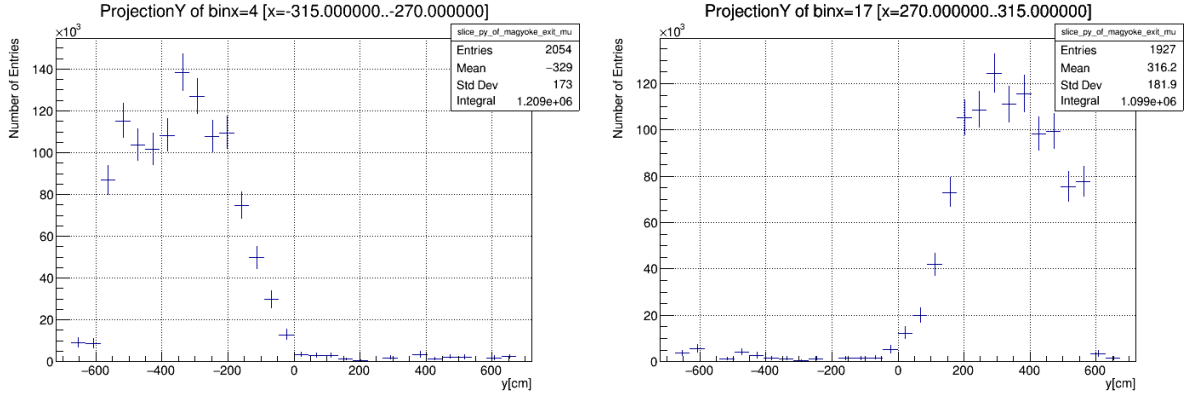
#### 4.1.2 The effects of the realistic magnetic field on the SST occupancy

Since June 2018 the magnetic field of the spectrometer magnet was changed to a more realistic one. This includes the simulation of the return field inside the geometrical volumes of the magnet yoke. There are 6 geometrical volumes declared within the FairShip framework belonging to the spectrometer magnet: magyoke, CV, MCoil1, MCoil2, MCoil3, MCoil4. They correspond to the yoke of the magnet, vertical and horizontal parts of the coil (see Figure 4.6). As noted in the previous section, some fraction of the particle fluxes on the sides of the SST do provoke hits in the straw tubes. A fraction of the particles are muons and some also penetrate through the magnet yoke volume of the spectrometer, which was not loaded with a magnetic field in the previous configuration of the simulation. In this simulation, with magnetic field in the yoke, part of the muons is bent back into the acceptance of the tracker. In order to confirm the statements above the geometrical





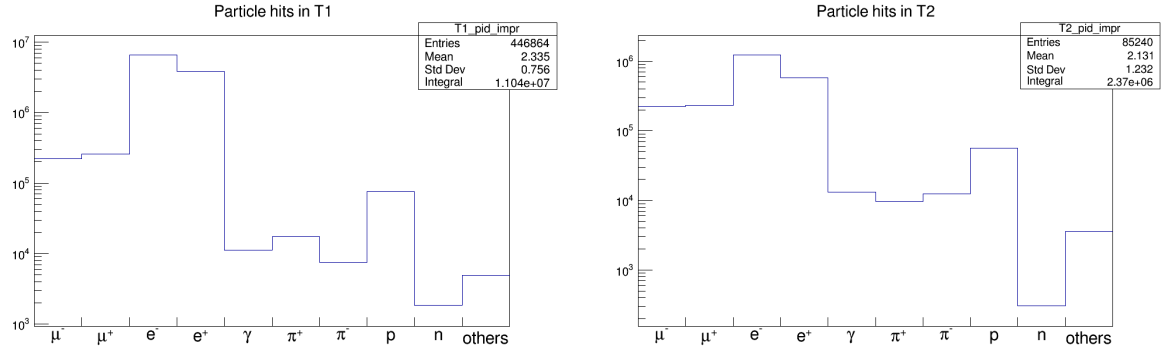
(a) In the left figure the muon hits created entering the magnet yoke are shown, in the right one – the muon hits created exiting the magnet yoke are shown.



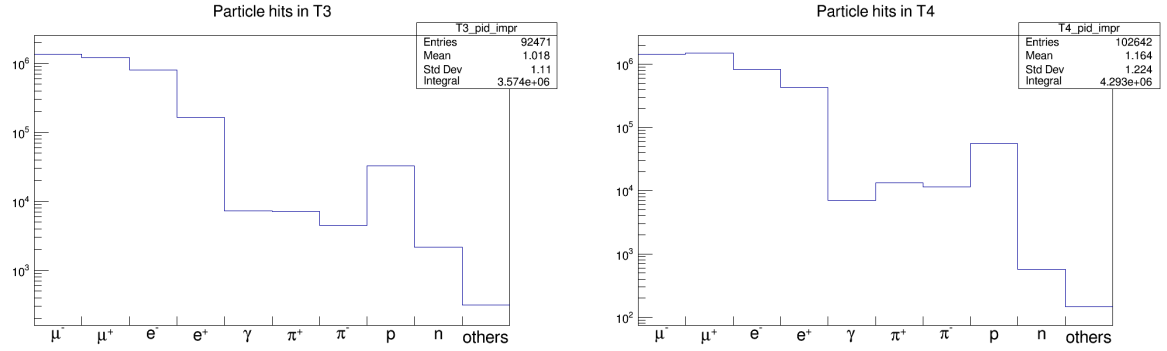
(b) In the left figure the fraction of bent muons at the left side of the SST acceptance is shown (projection from the top right histogram), in the right one - the fraction of bent muons at the right side of the SST acceptance is shown (another projection from the top right histogram).

Figure 4.8: The muon hit maps inside the magnet yoke.

volumes of the magnet were made artificially sensitive in order to be able to register particle hits at the entrance of the volume and at the exit. The hits in artificially sensitive magnet yoke can be observed in the occupancy maps in Figure 4.8. The distribution of hits exiting the yoke is reshaped with the magnetic field. Also, the return field of the magnet beyond the yoke defect can deflect the muons leading to the increased hot-spots on the top right and the bottom left corners of T3 and T4 stations of the SST (see Figure 4.10). The hit rate there goes up to  $\approx 6.7 \pm 0.4$  kHz/(tube) in T3 and  $\approx 5.7 \pm 0.4$  kHz/(tube) in T4 for the configuration with the steel frames and up to  $\approx 6.9 \pm 0.4$  kHz/(tube) in T3 and  $\approx 7.2 \pm 0.4$  kHz/(tube) in T4 for the old configuration with light aluminum frames. When there is no realistic return field the hit rate values become much lower:  $4.5 \pm 0.3 - 4.8 \pm 0.3$  kHz/(tube) with aluminum frames and  $2.0 \pm 0.2 - 1.5 \pm 0.2$  kHz/(tube) with steel frames around the stations (see Table 4.3 and 4.4). Another hint that the muons



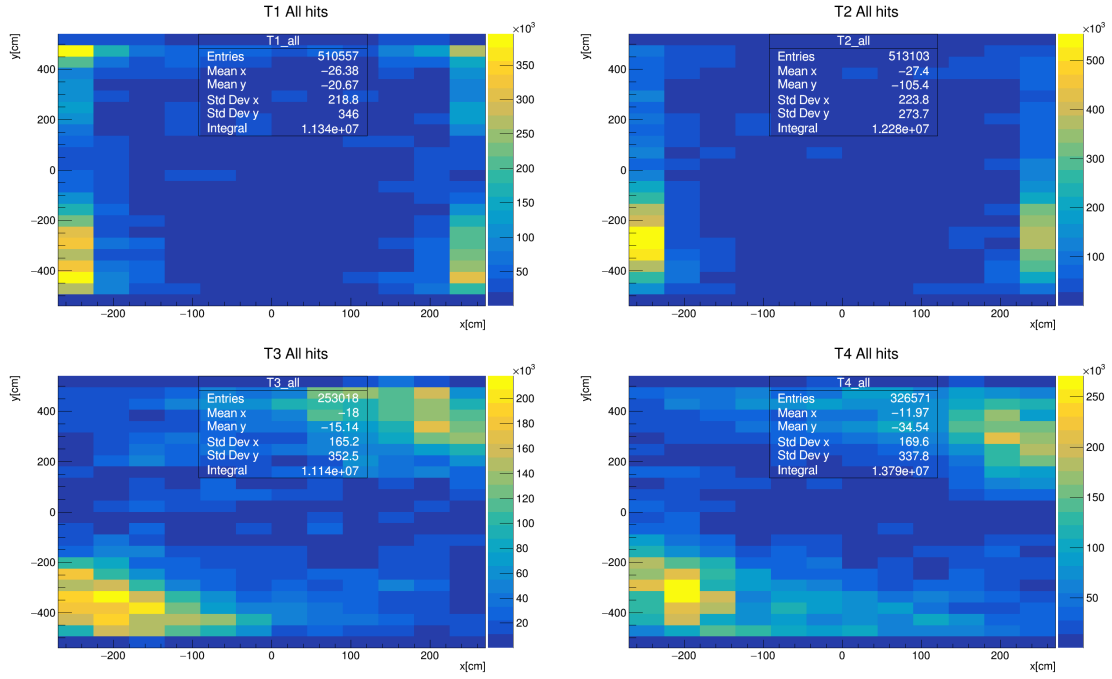
(a) Particle ID distributions in the T1 and T2 stations.



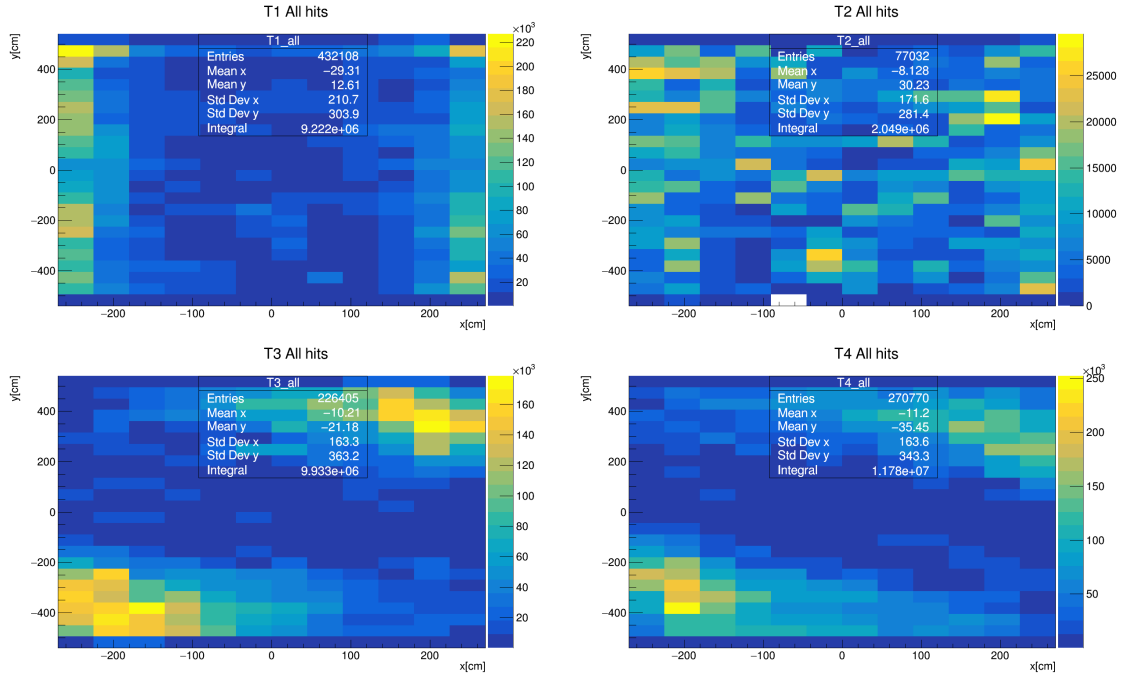
(b) Particle ID distributions in the T3 and T4 stations.

Figure 4.9: Particle ID distributions of the hits inside the tracking stations.

are indeed bent back into the stations are the particle ID distributions (see Figure 4.9). The muons dominate in the stations T3 and T4 by almost a factor of 10, T1 and T2 are dominated by electrons and positrons. Additionally, the absolute hit rate of muons in T3 and T4 is  $\approx 10$  times higher:  $\approx 1.5 \cdot 10^6$  kHz instead of  $\approx 2.5 \cdot 10^5$  kHz in T1 and T2 according to Figure 4.9. The momentum distributions for muons, electrons, positrons and photons are shown in Appendix E. Electrons and positrons, which created hits in the SST, have momenta smaller than 1 GeV/c, while muons have momenta up to 300 GeV/c. This means that some low energetic electrons can be deflected with the Spectrometer Magnet outside the acceptance of stations T3 and T4 leading to the muon hits dominance there. One can also see that there are hits caused by neutrons. They are produced due to photo nuclear reactions, muon nuclear reactions and pion hadronic inelastic interactions. Overall, the highest rate in the SST per tube for the June 2018 geometrical configuration, including the steel frame and the new field map, is  $\approx 6.7 \pm 0.4$  kHz/(tube) in T3 and  $\approx 6.6 \pm 0.4$  kHz/(tube) in T1 (see Table 4.3 and 4.4).



(a) Old aluminum frames.



(b) New steel frames.

Figure 4.10: The simulated muon background hit rates inside the SST stations T1–T4 compared between aluminum (a) and steel (b) frames around the stations and realistic field map for the spectrometer magnet in both cases.

### 4.1.3 The effects of the Scattering and Neutrino Detector magnetic field on the SST occupancy

The Scattering and Neutrino Detector (SND) of the SHiP experiment is located upstream the straw tracker, before the Decay Volume (See Figure 4.11). The most crucial and influential part of this subsystem for the SST occupancy is its magnet. According to the current geometrical setup (March 2019) used in the FairShip framework the magnitude of magnetic field inside the yoke can reach 1.9 T. This field is high enough to bend significantly high energetic particles, which pass through the yoke. In the end of 2018, a new detailed field map for the SND magnet was implemented into the FairShip, which includes its stray field too. In order to study the influence of the new field map alongside with the SST spectrometer map and including the new steel frames, new muon background simulations were performed with the updated SND magnetic field. The results are shown in Figure 4.12.

The shape of hit distributions in Figure 4.12 remained similar to the ones obtained for the configuration with only realistic field map for the SST spectrometer magnet (See Figure 4.10). The rates for T1 and T2 stations are comparable with the ones obtained previously:  $6.7 \pm 0.3$  kHz/tube and  $1.1 \pm 0.2$  kHz/tube respectively. The rates in the stations located downstream of the SST magnet decreased significantly. For T3 the maximum hit rate is equal to  $2.0 \pm 0.2$  kHz/tube and  $1.8 \pm 0.2$  kHz/tube for T4 (see Table 4.3 and 4.4). The reduction in the rates for the last two stations is caused by the fact that less muons reach the SST spectrometer, when the yoke return field of the SND is used (see Figure 4.13) comparing to the configuration without realistic SND map (see histogram projections in Figure 4.8).

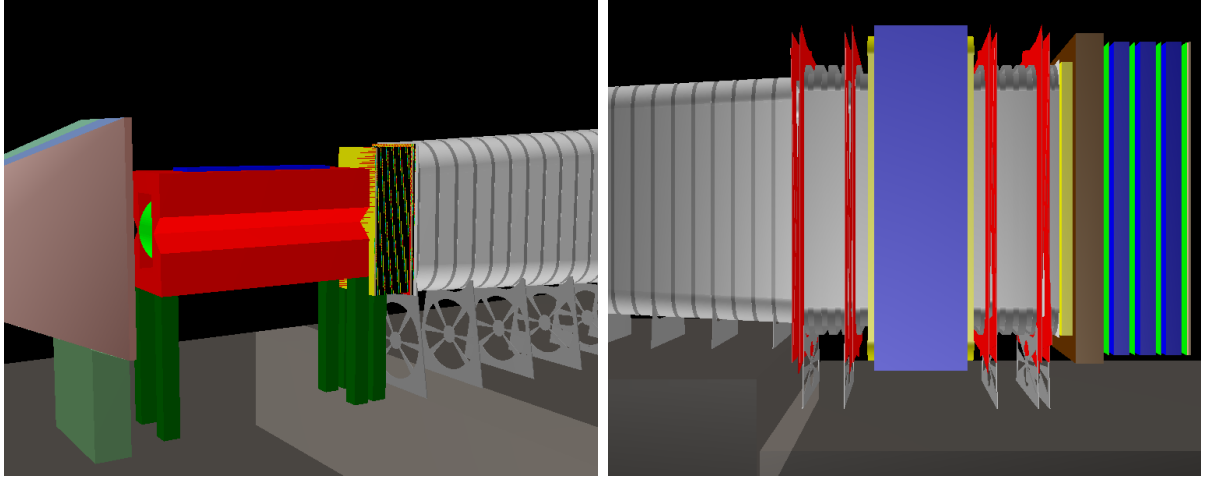


Figure 4.11: The location of the Scattering and Neutrino Detector in SHiP experiment with respect to the Decay Volume and the SST (obtained using Event Display script).

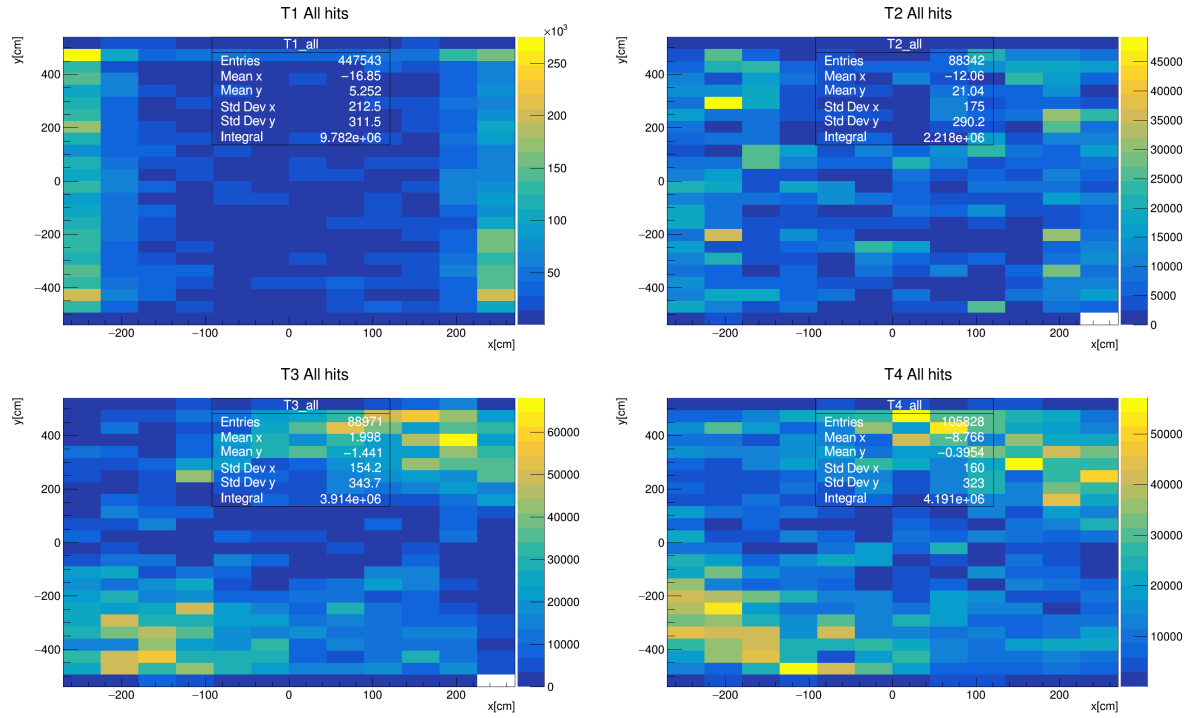
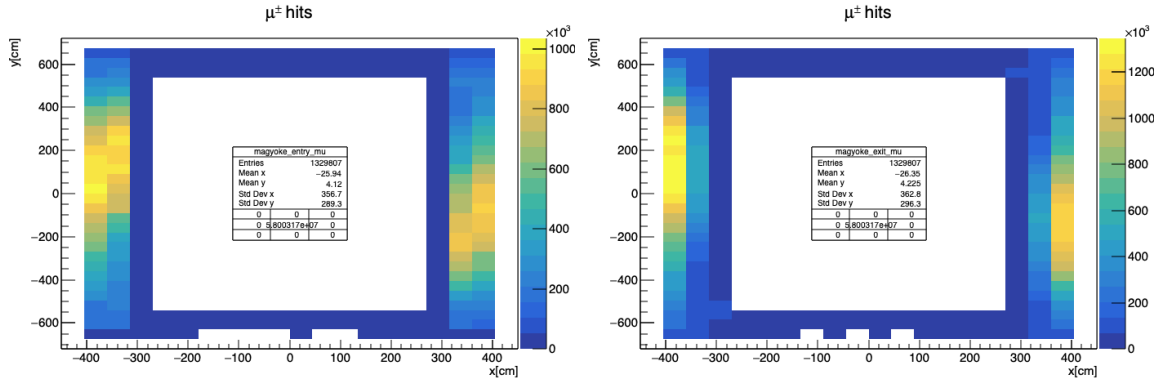
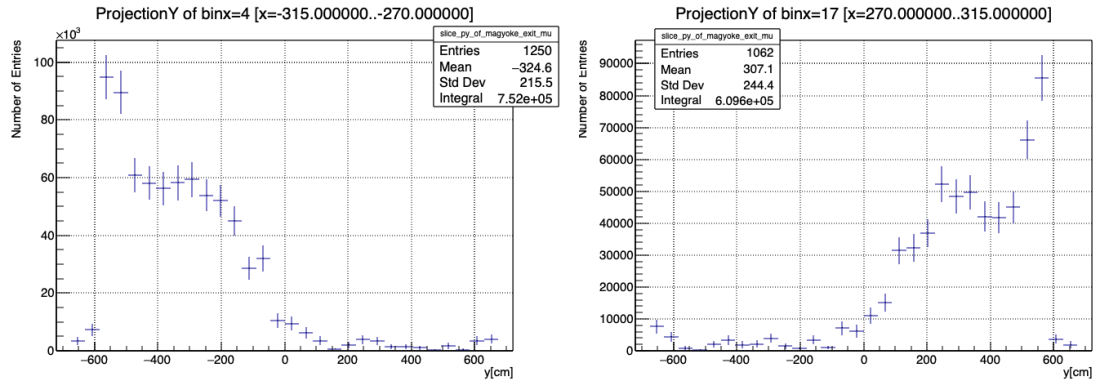


Figure 4.12: The hit rates inside the SST stations T1–T4 simulated using the geometry with realistic field maps for SST spectrometer magnet and SND magnet (March 2019).



(a) In the left figure the muon hits created entering the magnet yoke are shown, in the right one – the muon hits created exiting the magnet yoke are shown.



(b) In the left figure the fraction of bent muons at the left side of the SST acceptance is shown (projection from the top right histogram), in the right one - the fraction of bent muons at the right side of the SST acceptance is shown (another projection from the top right histogram).

Figure 4.13: The muon hit maps inside the magnet yoke with realistic SND field map.

#### 4.1.4 Expanding the size of the material frames around the views of the SST tracking stations

Muons propagating along the sides of the SST can cause non-negligible effect on the occupancies of tracking stations due to the interaction with the supporting material around the stations as it was shown in the previous sections. The lateral width of the frames is 1.2 m and it was observed that the hit rates inside the layers of the straw tubes became lower than for a setup without material frames due to shielding effect. The next step is to try to expand the lateral width of the frames in order to find the limits, where the occupancies of the stations can become intolerable. The simulations were performed for frames extended by 1 m, 2 m and 3 m in  $XY$ -plane. The results are shown in Figures 4.14, 4.15 and 4.16. They can be compared to the muon background hits distributions for the geometry with standard steel frames (see Figure 4.12).

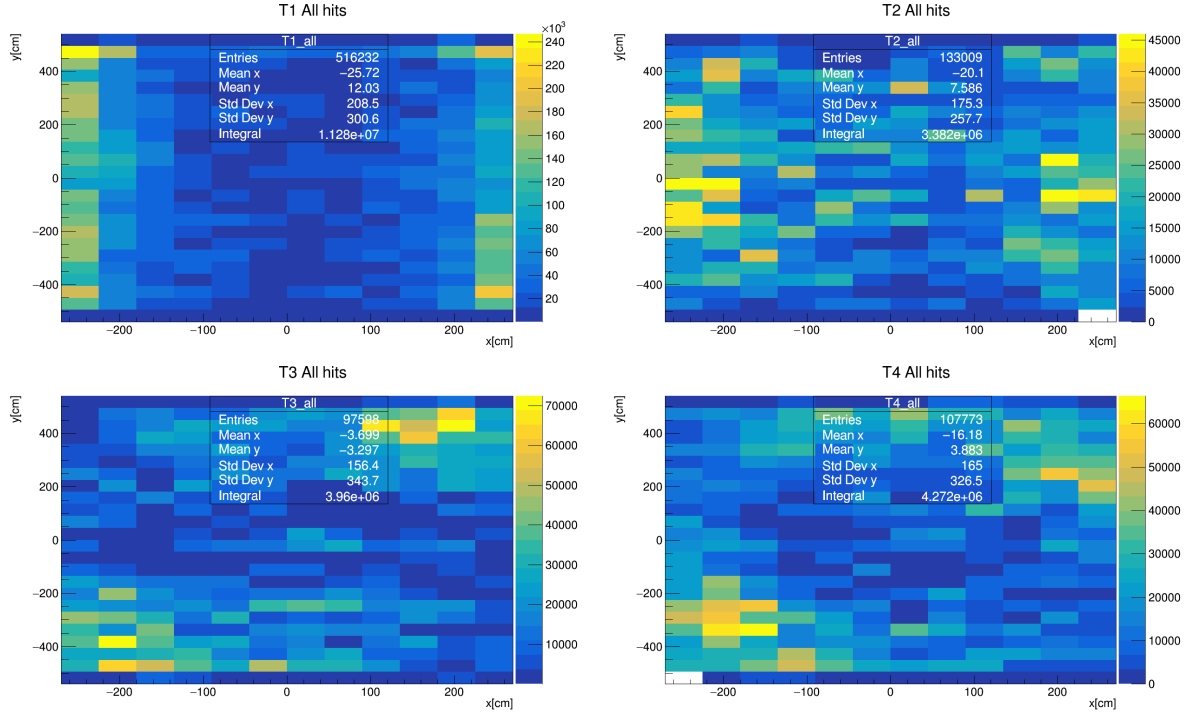


Figure 4.14: The muon background in the SST stations for the geometry with 1 m of extra lateral material frame width around the views and realistic field maps for the SST and the SND magnets.

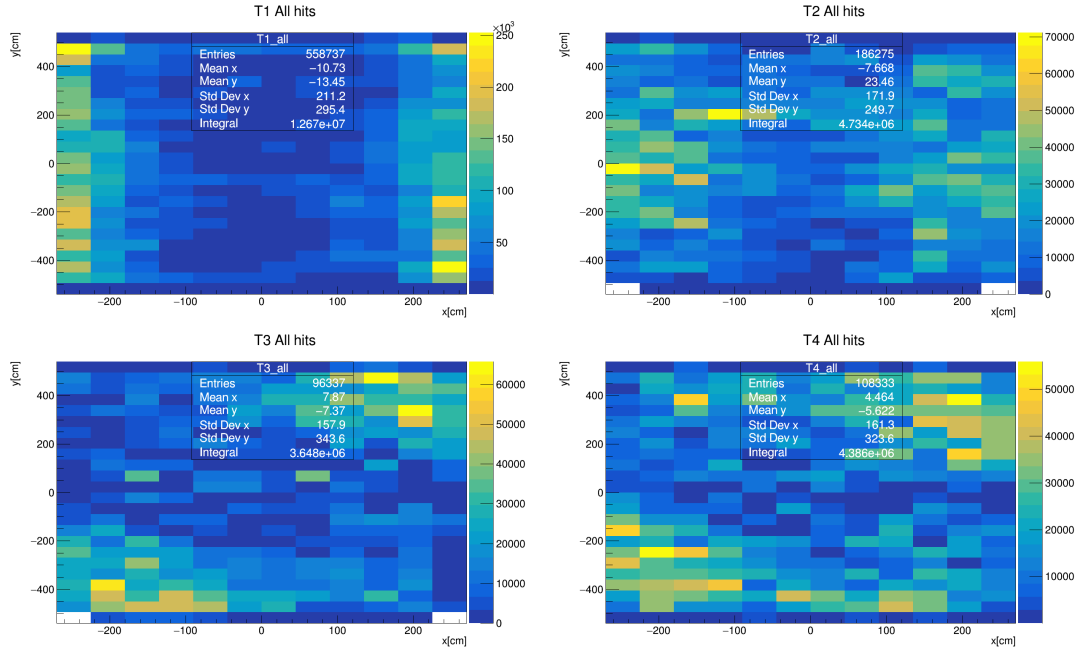


Figure 4.15: The muon background in the SST stations for the geometry with 2m of extra lateral material frame width around the views and realistic field maps for the SST and the SND magnets.

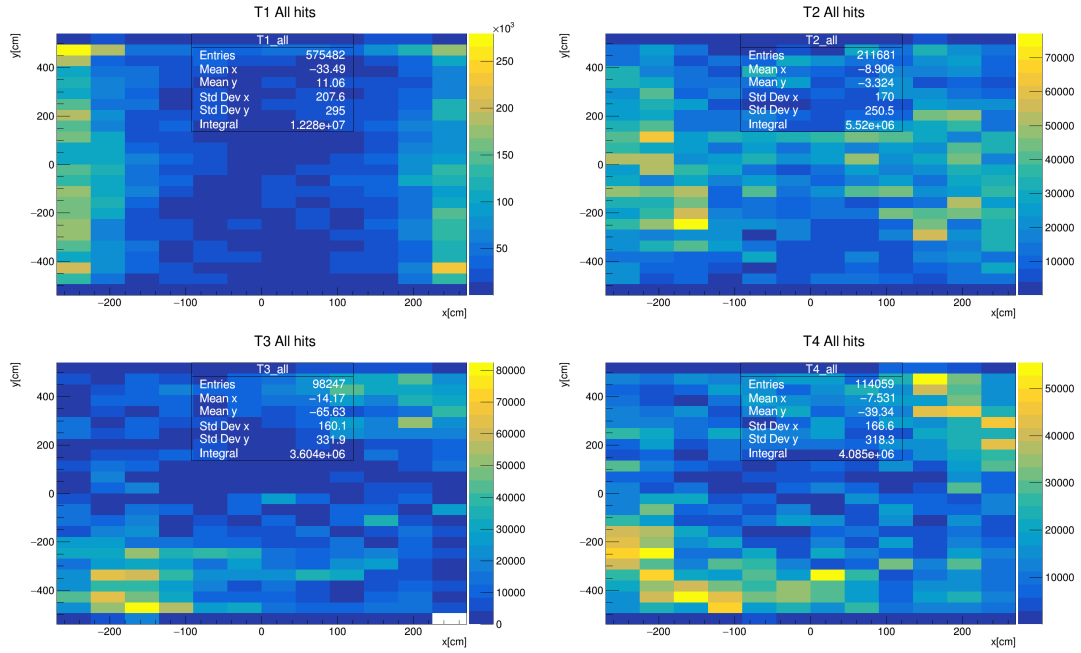


Figure 4.16: The muon background in the SST stations for the geometry with 3m of extra lateral material frame width around the views and realistic field maps for the SST and the SND magnets.



Table 4.1: The comparison between the maximum hit rates per station of the SST for different extra frame widths around the views of the stations.

Station	Hit rates (kHz/tube)			
	0 m	1 m	2 m	3 m
T1	6.8	7.6	7.9	7.5
T2	1.0	1.9	3.5	2.7
T3	1.5	2.0	1.9	2.4
T4	1.8	1.9	1.7	1.9

The hit rates did not grow drastically comparing to the ones discussed in the previous Section 4.1.3. The most affected station was T2, where the maximum rate grown up to  $3.4 \pm 0.3$  kHz/tube for 2 m of extra material. The rates in station T3 risen up to  $2.3 \pm 0.3$  kHz/tube for 3 m of extra lateral material width. The rates for station T1 increased by 16% maximum for 2 m of extra width and became  $7.7 \pm 0.4$  kHz/tube. The rates did not rise significantly due to the effect of the realistic magnetic field map of the SND on the muon fluxes on the sides of the SST (see Figure 4.13). The results can be observed and compared in Table 4.1. The complete information with average rates is available in Table 4.3 and 4.4.

#### 4.1.5 Symmetrical design

In the current geometrical arrangement of the SST in the FairShip framework (March 2019) the T1 station is situated right after the end of the Decay Volume. The distance between two volumes is 0.1 cm. This condition leads to a constraint on the width of the views (it should be no more than 10 cm). In order to avoid this situation and have the possibility to vary this parameter in larger range of values, a symmetrical arrangement of the whole SST was proposed. This means that the spectrometer magnet will be positioned in the geometrical center between the Decay Volume and the Timing Detector. The stations will be moved to new positions accordingly by keeping the same distance between each other and the magnet as it is in the current geometry. A separate FairShip branch was created to test this new geometrical configuration. The simulations of the muon background in the straw tubes showed that the shape of the distributions remained similar, but the absolute hit rate increased in all stations except T4:  $9.2 \pm 0.4$  kHz/tube in T1,  $1.5 \pm 0.2$  kHz/tube in T2,  $1.8 \pm 0.2$  kHz/tube in T3 and  $1.8 \pm 0.2$  kHz/tube in T4 respectively (see Figure 4.17), while moving the stations by less than 30 cm (see the rates comparison in Table 4.3 and 4.4). For now the reasons for increase of the rates in 3 stations deserves more studies and further understanding, but the difference is very close to statistical fluctuations for stations T2–T4. The comparison between the current positions of the SST volumes and symmetrical ones is shown in Table 4.2.

### 4.1.6 The occupancy of the SST for smaller magnetic fields of the Muon Shield

More crucial parameters can be extracted from the muon background simulations for weaker magnetic fields of the Muon Shield. If the  $B$ -field magnitude of the Muon Shield is getting smaller, then more muons can pass through the acceptance of the SST. Thus, the occupancy will grow. Such operational mode is interesting, in particular, for the SST alignment procedure. The alignment procedure requires massive amounts of tracks distributed across the geometrical acceptance as much as possible in order to have a high precision. These tracks also have to penetrate through all the tracking stations to be useful for the alignment. The limiting factor for the data taking in such operational mode is the capability of the DAQ system to read-out and disentangle all the hits from the straw tubes for every incoming spill of protons. To quantify the maximum possible hit rate in the SST and find the minimum  $B$ -field values of the Muon Shield, which can be used for the SST alignment runs without saturation of the front-end electronics, the muon background simulations for various magnitudes of the Muon Shield magnetic field gradient were performed. The total number of the SST hits in the first plane of the T1 station was used as the occupancy metric. This plane is the closest one to the Decay Volume and, according to the results of the muon background studies showed in Table 4.3, has the

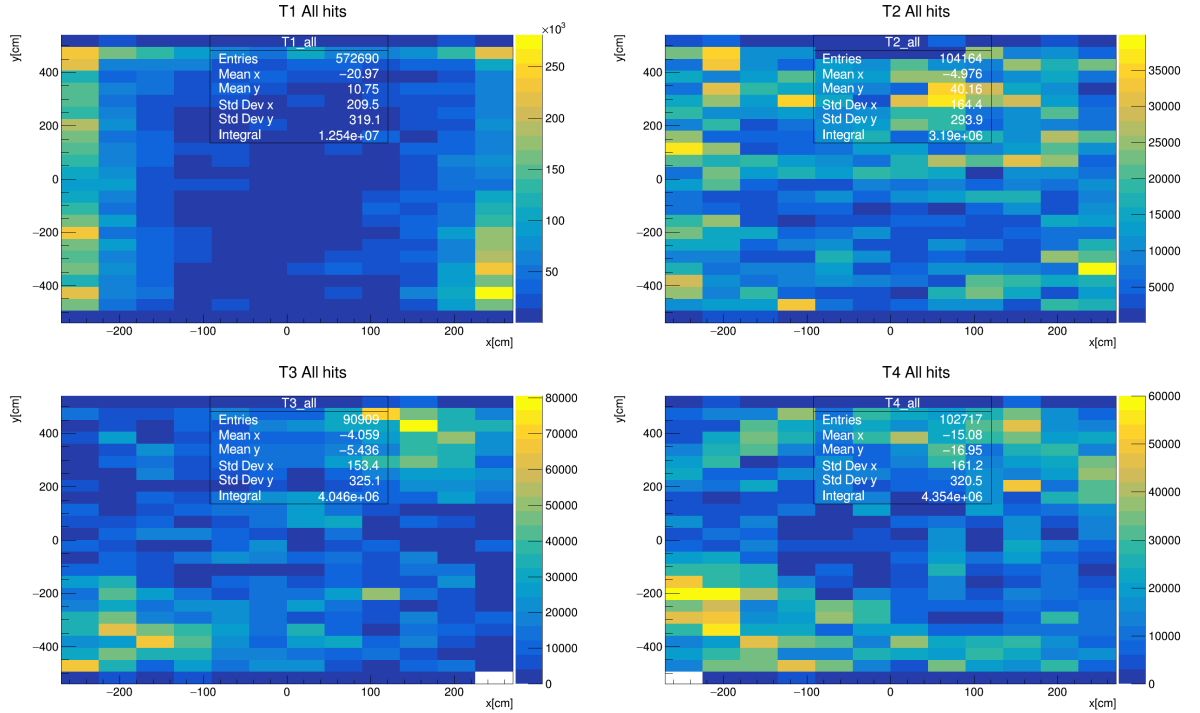


Figure 4.17: The hit rates inside the SST stations T1–T4 simulated using new geometry with material frames around stations with realistic magnetic field map and symmetrical arrangement between Decay Volume and Timing detector

Table 4.2: The comparison between the geometrical positions of the SST volumes inside the current version of FairShip and the symmetrical arrangement

Current geometry			
	Beginning (cm)	End (cm)	Middle (cm)
SST middle point	2578	3558	3068
	Beginning (cm)	End (cm)	Distance (cm)
DecayVolume and T1	2577.9	2578	0.1
T1 and T2 distance	2618	2778	160
T2 and ShiPMagnet	2818	2867	49
ShipMagnet and T3	3269	3318	49
T3 and T4 distance	3358	3518	160
T4 and Timing Detector	3558	3607.4	49.4
Symmetrical arrangement			
	Beginning (cm)	End (cm)	Middle (cm)
SST middle point	2602.65	3582.65	3092.65
	Beginning (cm)	End (cm)	Distance (cm)
DecayVolume and T1	2577.9	2602.65	24.75
T1 and T2 distance	2642.65	2802.65	160
T2 and ShiPMagnet	2842.65	2891.65	49
ShipMagnet and T3	3293.65	3342.65	49
T3 and T4 distance	3382.65	3542.65	160
T4 and Timing Detector	3582.65	3607.4	24.75

largest mean number of hits over all the rest of the tracking stations. This plane contains the two layers of the straw tubes arranged with the pitch of 36 mm located one after another with a certain relative vertical offset. Such arrangement of the tubes inside the plane allows to fully cover the geometrical acceptance with minimal overlaps. Thus, the straw tubes occupancy estimated for this particular plane gives the upper limit on possible hit rates and an estimate of the required read-out rate for the front-end electronics. The resulting numbers of the hits in the first plane of T1 station depending on the magnitude of the  $B$ -field of the Muon Shield are shown in Figure 4.18.

Recently obtained data for the current version of the FairShip framework with SST and SND magnetic field maps included is compared to the data obtained in 2017. In general, the hit rate significantly decreased for all  $B$ -field values in 2020 data comparing to the 2017 data. There are two possible sources of such discrepancy in the results. The first one is related to the fact that 2017 hit rate was acquired for SHiP TP geometry [2], which deviates significantly from the current SHiP geometry. Also the magnet of SND and Hadron absorber were switched off for 2017 studies, while in 2020 simulations they were kept at their nominal field values. If the Muon Shield is switched off in this case, then some fraction of muons will be deflected with the remaining magnets and will not reach T1 station. The second issue comes from the pre-generated muon data sample size

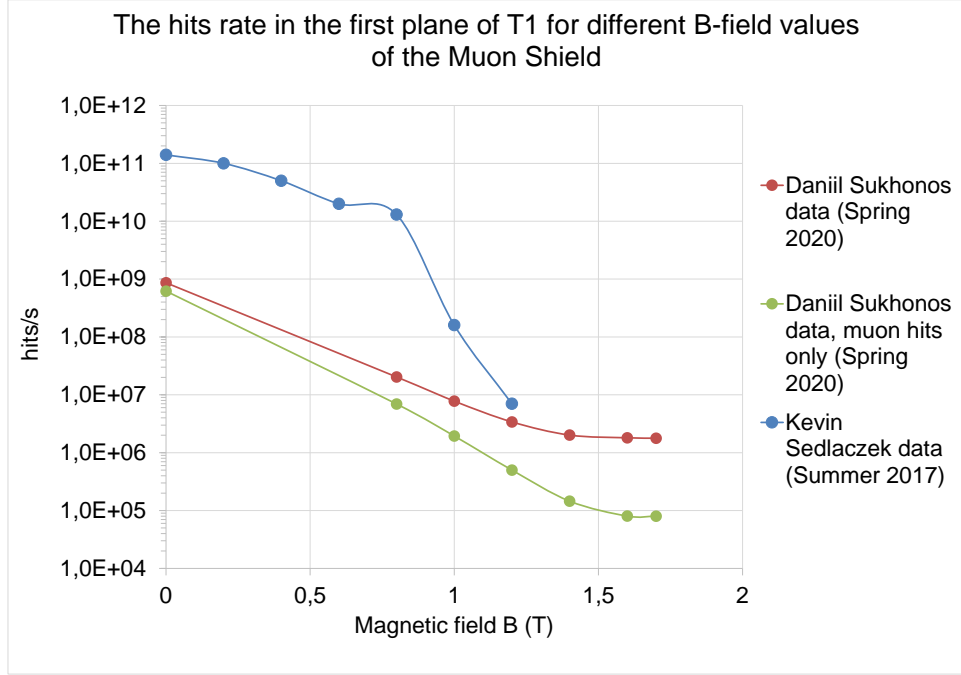


Figure 4.18: The hit rate in the first plane of the T1 tracking station depending on the magnitude of the Muon Shield  $B$ -field.

for 2017 analysis. It contained only 100 000 events, which were then scaled to match the requirement of  $4 \cdot 10^{13}$  protons on target. For 2020 muon background simulation a special background production was performed generating the full amount of events corresponding to  $4 \cdot 10^{13}$  protons on target.

The small values of the magnetic field of the Muon Shield allow more muons to pass through the geometrical acceptance of the SST leading to higher alignment accuracy. However, the tests of the DAQ system prototypes are required to ensure the stability of the signals read-out in the operational mode close to the technical limits of the front-end electronics.

#### 4.1.7 The summary tables with the results

The tables below illustrate the summary of the occupancies per station in the SST for different geometry and simulation options.

Table 4.3: The hit rates in T1 and T2 for different geometry setups.

Geometry variations	T1		T2	
	Average rate, kHz/tube	Maximum rate, kHz/tube	Average rate, kHz/tube	Maximum rate, kHz/tube
Al frames, no field maps	17.4(1)	37.8(9)	6.61(8)	12.5(5)
Steel frames, no field maps	6.47(7)	26.6(7)	2.05(4)	4.1(3)
Al frames, SST field map	4.72(6)	11.4(5)	5.11(7)	15.5(7)
Steel frames, SST field map	3.60(6)	6.6(4)	0.56(2)	1.0(1)
SST and SND field maps included				
Steel frames	3.88(6)	6.7(3)	0.63(2)	1.1(1)
Symmetrical arrangement	4.62(6)	9.2(4)	0.89(3)	1.5(2)
Extra 1 m around the views	4.13(6)	7.4(4)	1.08(3)	1.9(2)
Extra 2 m around the views	4.59(6)	7.7(4)	1.53(4)	3.4(3)
Extra 3 m around the views	4.39(6)	7.3(4)	1.66(4)	2.7(2)

Table 4.4: The hit rates in T3 and T4 for different geometry setups.

Geometry variations	T3		T4	
	Average rate, kHz/tube	Maximum rate, kHz/tube	Average rate, kHz/tube	Maximum rate, kHz/tube
Al frames, no field maps	2.47(5)	4.5(3)	2.86(5)	4.8(3)
Steel frames, no field maps	0.60(2)	1.98(2)	0.88(3)	1.5(2)
Al frames, SST field map	3.12(6)	6.9(4)	3.68(6)	7.2(4)
Steel frames, SST field map	2.75(5)	6.7(4)	3.09(6)	5.7(4)
SST and SND field maps included				
Steel frames	1.05(3)	1.97(2)	1.07(3)	1.8(2)
Symmetrical arrangement	1.00(3)	1.8(2)	1.11(3)	1.8(2)
Extra 1 m around the views	1.02(3)	2.3(2)	1.10(3)	1.9(2)
Extra 2 m around the views	0.96(3)	1.9(2)	1.10(3)	2.0(2)
Extra 3 m around the views	0.91(3)	2.3(3)	1.03(3)	2.3(2)

## 4.2 Misalignment simulation of the straw tubes

As it was shown in Chapters 2 and 3, the displacement of the wire inside the straw tube with respect to the tube axis affects the performance of the tube. The resulting value of this displacement is formed by the major contribution from the tube gravitational sagging (it bends more) and the minor from the wire sagging. The main consequence of such displacement is that the drift time of the charges created after the ionization of the gas by the charged particle penetrating the tube will change. The drift time decreases or increases depending on the magnitude of the wire displacement and the location of the particle track with respect to the wire. This means that for some fraction of particles the reconstructed distance to the track from the displaced wire becomes larger than the radius of the straw tube. The hits in the tubes belonging to the this track will be displaced further from the intercept of the fitted track, thus, the quality of the reconstructed tracks can degrade. In order to quantify the effects caused by the wire displacements inside the straw tubes, the SST misalignment studies were performed. These studies were carried out together with a CERN Summer student, Kwing Lam Leung, whom the author of the thesis supervised. His detailed report can be found following this reference [87].

### 4.2.1 Straw tube wire sagging profile

The precise sagging profile for the wire inside the tube has not been experimentally measured yet. The theoretical calculation faces some obstacles too, because the wire is a subject to the combination of the external electrical and gravitational forces, and the internal elastic response due to the pretensioning from the sides. Some attempts to calculate the resulting magnitude of the wire displacement were taken in [43, 49] and also performed in Section 1.3.

For the misalignment studies within the scope of this thesis few simplifications were applied. As it was mentioned above, the straw tube sagging has the main contribution to the resulting displacement of the wire with respect to the tube center, but, from the straw tube detector simulation point of view, only the final value of the displacement matters. The tube was assumed to be ideally horizontal and the wire was assigned to have the resulting displacement. Later in the text of the section this feature is discussed. The wire was assumed to have a parabolic sagging profile in  $XY$ -plane with the maximum magnitude of sagging located in the middle of the straw tube along  $X$ -coordinate and no displacement at the ends of the tube. Then, the distance to the wire ( $\Delta r$ ) inside the straw tube from the particle hit point ( $x_p$ ,  $y_p$  and  $z_p$ ) is equal to [87]:

$$\Delta r = \sqrt{(x_w - x_p)^2 + (y_w(x_w) - y_p)^2 + (z_w - z_p)^2}, \quad (4.2)$$

where  $x_w$ ,  $y_w$  and  $z_w$  are the coordinates of the wire.  $y_w$  depends on  $x_w$  and has a parabolic shape:  $y_w = a(x_w - x_{w,mid})^2 - \Delta y_w$ .  $x_{w,mid}$  is the coordinate of the middle of the wire,  $\Delta y_w$  is the maximum magnitude of the wire displacement at  $x_{w,mid}$ . The hit point ( $x_p$ ,  $y_p$  and  $z_p$ ) of the impinging particle in each straw tube in the FairShip framework

simulation is calculated as the middle point between the entry point of the particle track inside the tube volume and the exit point of this track. The coordinate  $x_w$  of the wire, where the distance from the hit point to the wire of the tube is minimal  $\Delta r_{min}$ , can be found from the derivative of the equation (4.2):

$$\frac{d\Delta r}{dx_w} = \frac{x_w - x_p + (y_w(x_w) - y_p)y'_w(x_w)}{\Delta r} = 0 \quad (4.3)$$

The equation (4.3) is a third order polynomial and can be solved only numerically. In order to simplify the task, the sagging profile of the tube can be linearized locally in the vicinity of the  $x_p$  coordinate. The local linearization causes negligible error, because the length of the wire is 5 m and the maximum magnitude of sagging is of the order of a few millimeters. This means that the slopes of the line and the parabolic curve are similar within the range of few millimeters along  $X$ -axis. The locally linearized wire profile  $y_w$  obtained after taking the first two terms of a Tailor expansion is:

$$y_w(x_w) \approx y_w(x_p) + y'_w(x_p)(x_w - x_p) \quad (4.4)$$

After the substitution of the  $y_w$  from the equation (4.4) into the equation (4.3), the coordinate  $x_{w,min}$ , where the distance from the hit point to the wire is minimal, can be obtained analytically. The obtained  $x_{w,min}$  value is inserted into the equation (4.2). The final value of the minimal distance from the hit point to the wire  $\Delta r_{min}$  is equal to:

$$\Delta r_{min} = \sqrt{\frac{y_p - y_w(x_p)}{1 + (y'_w(x_p))^2} + (z_w - z_p)^2} \quad (4.5)$$

There are two possibilities within the FairShip framework, where the modified distances from the hit points to the wires of the straw tubes calculated using the equation (4.5) can be implemented. The first one, the most precise and appropriate, is to directly modify the geometrical volumes of the SST replacing the straight wires inside the tubes with the sagged ones. However, such implementation has a major drawback: FairShip has to rerun and rebuild the detectors geometry each time, when the parameters of the wire displacements are changed. The run time of every FairShip simulation can exceed several hours in order to simulate the significant amount of events, meaning that it can take too much time to generate the data samples to compare the track fitting performance for a set of different wire displacement values. The solution to this issue is to update at the digitization step already simulated collections of the SST hits. The coordinates of the closest points on the wires inside the tubes to the MC generated hits are recalculated taking into account the sagging parametrization (a parabolic shape in our case) and the new distances between the wires and the hit positions are obtained. These distances are then converted to the drift times and added to the final TDC values produced with the digitization algorithm of the FairShip framework. The collections of the digitized SST hits are propagated to the pattern recognition algorithm and finally the selected sets of hits (track candidates) are used as an input for the track fitting procedure performed with GENFIT [88] subroutine.

As it was mentioned earlier, during the misalignment simulation only the shape of the wire is changed to the parabolic profile, but the tube is left horizontal. From a straw tube performance point of view, only the final value of a displacement has the influence on a drift time obtained for each tube. If the wire is straight and only the tube has a parabolic profile or both are sagged, but the total displacement magnitude is the same, then the response of a given straw tube will be the same. As it was mentioned above the misalignment simulation due to sagging is implemented at the digitization step of the FairShip routine. This means that the sagging of a particular straw tube (not the wire) changes only the total number of hits generated in it, because some of them will be outside of the tube acceptance, but the new fiducial region appeared due to the sagging will not contain any hits, because they were not generated at the simulation step. To prove that loosing the hits does not hide any effect in the performance of a straw tube (tracks quality) except of loosing the statistics, additional FairShip simulation were performed (see [87]). The results showed that the displacement of tubes (not the wires) has a major influence only on the total number of hits in tubes and the number of corresponding tracks, but not on their quality.

#### 4.2.2 The track fitting performance for displaced wires

The default HNL simulation engine of the FairShip was used to produce the MC hits and tracks in the SST. The output simulation files were used as the input for the modified digitization algorithm of FairShip. The default “cheating” pattern recognition, which has access to MC tracks and hits and, thus, has a 100% efficiency, and track fitting algorithms were used for the reconstruction procedure. In order to compare the track fitting performance of the SST, when the wires are misaligned with respect to the straw

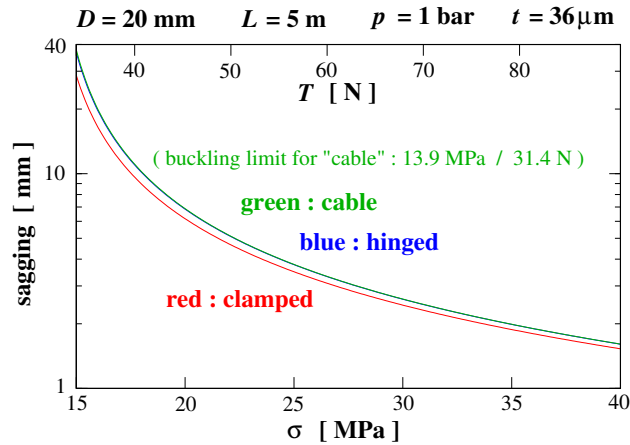


Figure 4.19: Sagging of the tube *vs.* the longitudinal wall stress. The figure is adapted from [49].



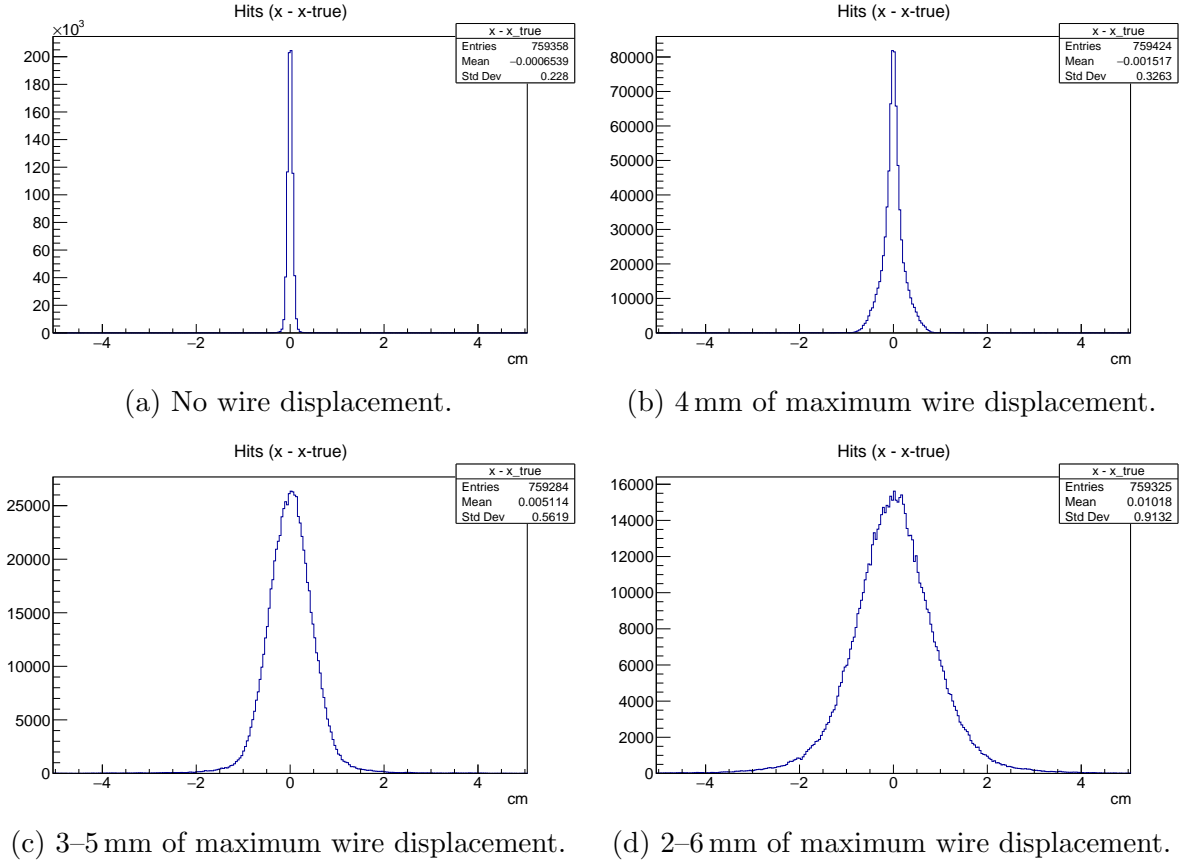


Figure 4.20: The absolute error  $x - x_{true}$  of the  $X$ -coordinates of the fitted tracks.

tube axes, the following metrics were chosen: the absolute error of the reconstructed track coordinates in the  $XY$ -plane, the  $\chi^2/\text{NDOF}$  for the fitted tracks and the corresponding p-values, the relative error of the reconstructed momentum of the fitted tracks. The performance of the track fitting was compared to the parameters of MC tracks obtained during the simulation step, where misalignment algorithms were not implemented. As a reference value the maximum wire displacement value of 4 mm was taken. According to theoretical predictions in [49], the maximum possible magnitude of the tube sagging (hence, the wire displacement), when the tube is pretensioned with 20 MPa load at the ends can reach 7 mm (see Figure 4.19). This is an extreme case and there are no experimental evidences, if the tube would be able to operate with such large wire displacement value without any discharges happening. That is why the intermediate value of 4 mm for the maximum wire displacement was selected, which is more tolerable and is enough significant to already show the observable effects on the track fitting quality.

The first set of histograms in Figure 4.20 shows the absolute  $X$ -coordinate errors for the reconstructed tracks. The “true” values are extracted from the Monte Carlo tracks created during the simulation step in the FairShip framework. The first test was to apply the 4 mm maximum wire displacement value in positive  $Y$  direction (the wire would be

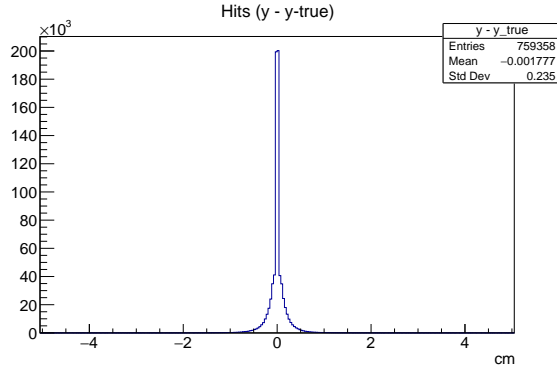
closer to the top side of the tubes emulating the fact that the tube sags more than the wire) equally for all the straw tubes in the SST. The second test was to use randomly generated maximum wire displacement values uniformly distributed for all the tubes within the range 3–5 mm. The third test was to increase the range of uniformly distributed random values of maximum wire displacements to 2–6 mm and apply them to all tubes.

One can observe that the standard deviation calculated for 4 histograms in Figure 4.20 increases with the magnitude of the maximum wire displacements and with the width of their range in Figure 4.20 (c) and (d). When all wires were misaligned equally to the maximum displacement of 4 mm, the standard deviation changed by 30% (see Figure 4.20 (b)) comparing to the histogram, where the misalignment algorithm was not applied (see Figure 4.20 (a)). More significant changes in the standard deviation appear, when the maximum wire displacement values are uniformly distributed within a certain range and then are randomly assigned to the straw tubes of the SST. The wider the variation range is, the larger standard deviation of the absolute  $X$ -errors distribution becomes. For the 3–5 mm maximum wire displacement range (see Figure 4.20 (c)) the standard deviation increased in 2.46 times comparing to the case, where the misalignment was not applied (see Figure 4.20 (a)). When the range of possible magnitudes of the wire displacements was further increased to 2–6 mm, the standard deviation increased in 4 times (see Figure 4.20 (d)). Such large contribution to the standard deviation of the distributions of the  $X$  absolute errors for the fitted tracks comes from the misaligned reconstructed hits in the stereo views of the SST tracking stations. These stereo views are rotated by  $\pm 5^\circ$  around  $Z$ -axis parallel to the primary proton beam direction. When the minimal distances to the wire are changed randomly with the misalignment algorithm, the contribution to the change of the reconstructed  $x_p$  coordinate of the hit inside the straw tube will always be larger than the contribution to the change of the reconstructed  $y_p$  coordinate. The  $x_p$  coordinate of the reconstructed hits in the stereo views is calculated as  $x_p = \Delta r_{min} \cdot \sin(\alpha)$  and the  $y_p$  coordinate – as  $y_p = \Delta r_{min} \cdot (1 - \cos(\alpha))$ , where  $\alpha = \pm 5^\circ$  is a stereo angle. The inequality  $\sin(\alpha) > 1 - \cos(\alpha)$  is satisfied for  $0 < \alpha < \pi/2$ , proving that for the stereo angle of  $5^\circ$  the relative change of  $x_p$  coordinates due to the misalignment will be up to 23 times larger than the relative change of  $y_p$  coordinates of the reconstructed hits.

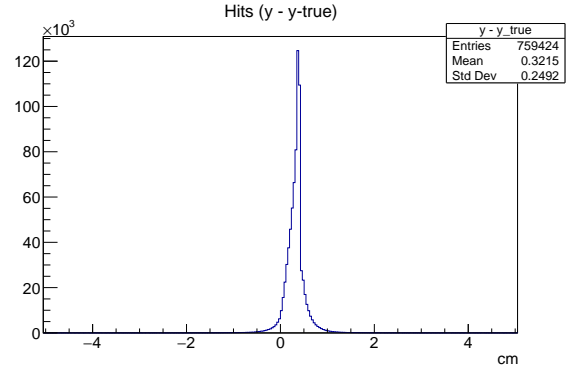
The second set of histograms in Figure 4.21 shows the absolute  $Y$ -coordinate errors for the reconstructed tracks.

The distributions of the  $Y$ -coordinate absolute errors of the fitted tracks showed in Figure 4.21 (b), (c) and (d), where the misalignment algorithm was applied, have the shifted mean value within the range of 3.1–3.2 cm comparing to the distribution in Figure 4.21 (a), where the mean value is at -0.002 cm. This shift is caused by the maximum magnitude of the wire displacement of 4 cm (applied to the  $Y$  coordinates of the wires of the tubes). In cases, where the range of random maximum wire displacement values was used (see Figure 4.21 (c) and (d)), the mean value remained within the 3.1–3.2 cm range, but the standard deviation increased by 7% and 9% respectively. Overall, the distributions of  $Y$ -coordinate absolute errors became more symmetric, when the range of random maximum wire displacement values was used.

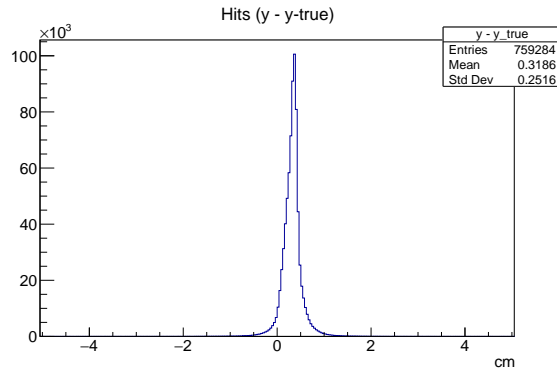
In Figure 4.22 the  $\chi^2/\text{NDOF}$  distributions of the fitted tracks are compared for the



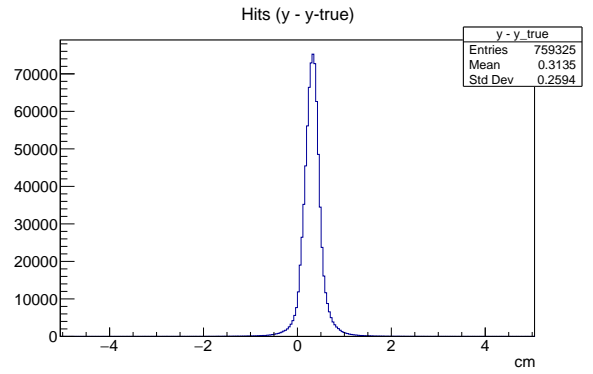
(a) No wire misalignment.



(b) 4 mm of maximum wire displacement.



(c) 3-5 mm of maximum wire displacement.

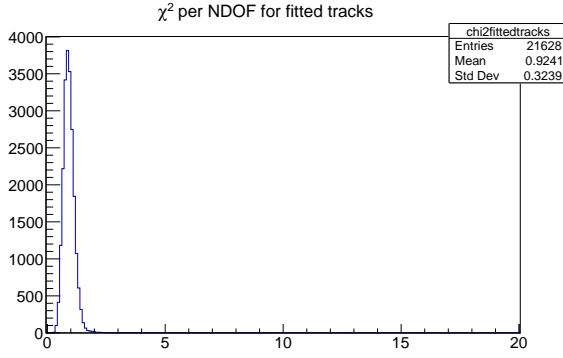


(d) 2-6 mm of maximum wire displacement.

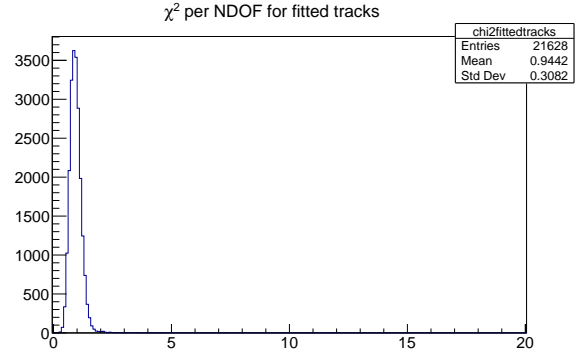
Figure 4.21: The absolute error  $y - y_{true}$  of the  $Y$ -coordinates of the fitted tracks.

FairShip reconstruction runs with non-misaligned (original) hit collections showed in Figure 4.22 (a) and the misaligned ones presented in Figure 4.22.

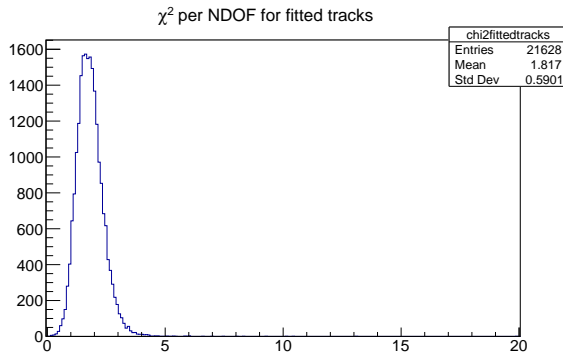
In order to make a quantitative statement on the quality of the fitted tracks, an arbitrary statistical significance level  $\alpha_s$  should be defined. The commonly used value of the significance level is  $\alpha_s = 0.05$  [37]. The top row of histograms in Fig 4.22 has the mean value of 0.9241 and 0.9442 for the fitted tracks, when the wires of the tubes were not misaligned and when all wires had the maximum wire displacement magnitude of 4 mm. The average number of hits per reconstructed track is 35 meaning that the mean number of degrees of freedom is 34. So, the p-values for the  $\chi^2$  values calculated at the mean values of the distributions in the first row of Figure 4.22 are 0.64 and 0.61, which is much larger than the significance level  $\alpha_s$ . The tracks with  $\chi^2/\text{NDOF}$  values from the core of these distributions have statistically good quality having p-value higher than  $\alpha_s$ . Only 1.7% of the fitted tracks for the non-misaligned hits have the p-value smaller than  $\alpha_s$  and 2.1% of the fitted tracks for the misaligned hits, when all wires had 4 mm maximum magnitude of the wire displacements, have the p-value smaller than  $\alpha_s$ . This means that for those fractions of tracks the hypothesis that the chosen fit model (linear in our case) can be used to approximate the set of given hits is rejected. These tracks are called badly fitted



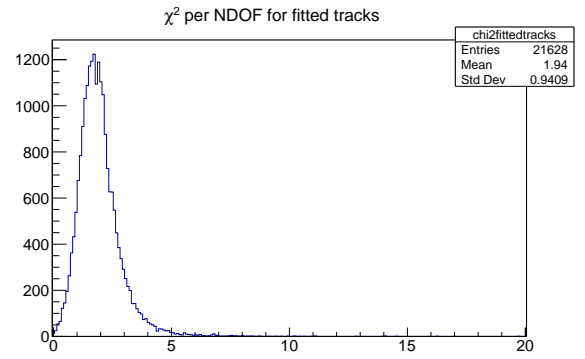
(a) No wire misalignment.



(b) 4 mm of maximum wire displacement.



(c) 3–5 mm of maximum wire displacement.



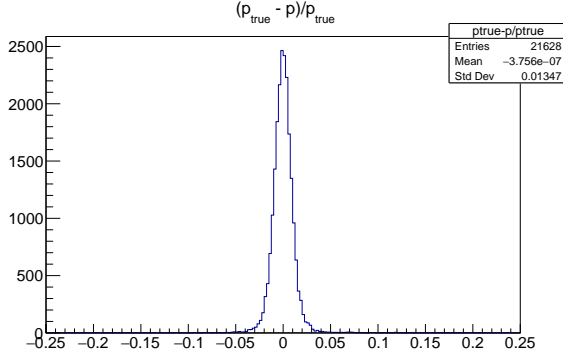
(d) 2–6 mm of maximum wire displacement.

Figure 4.22: The  $\chi^2/\text{NDOF}$  distributions of the fitted tracks.

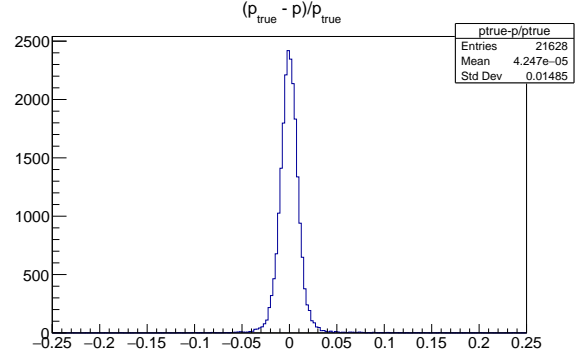
further in the text. The quality of the track fits becomes worse for the cases, where the wires had randomly generated maximum displacement values within the defined ranges. The mean values of the  $\chi^2/\text{NDOF}$  distributions in the bottom row of Figure 4.22 are 1.817 and 1.94, which correspond to the p-values of 0.003 and 0.001. These p-values are much smaller than the significance level  $\alpha_s$ , meaning that the majority of tracks had statistically bad fits. The precise number of badly fitted tracks for the range 3–5 mm of the maximum magnitude of the wire displacements is 56.1% and for the range 2–6 mm is 45.0%.

One of the crucial parameters calculated using the fitted tracks in the SST is the momentum of the tracks and its uncertainty. The set of histograms with relative errors of the magnitude of the momenta of the fitted tracks  $(p_{true} - p)/p_{true}$  for the non-displaced wires and displaced ones are shown in Figure 4.23.

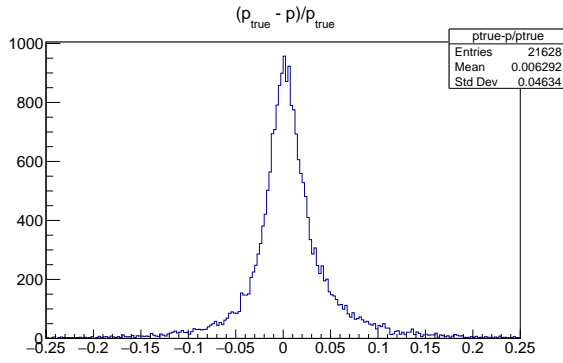
The influence on the standard deviation of the relative error of the magnitude of the fitted tracks momenta  $(p_{true} - p)/p_{true}$  for the case, when all wires are equally displaced with the maximum sagging magnitude of 4 mm, is small. The standard deviation for the non-misaligned hits showed in Figure 4.23 (a) is equal to 0.0135 and for the ones with equally displaced wires (4 mm maximum) is 0.0149, see Figure 4.23 (b). The increase for the standard deviation is 9%. For the case of the randomly distributed maximum values



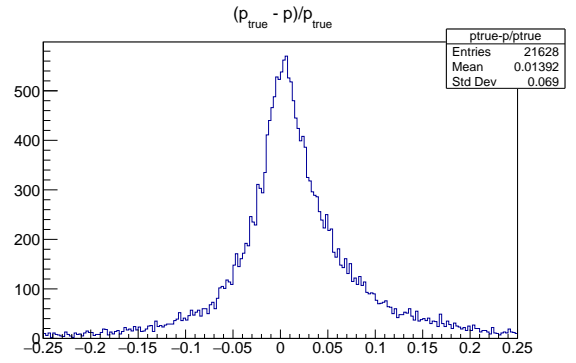
(a) No wire misalignment.



(b) 4 mm of maximum wire displacement.



(c) 3–5 mm of maximum wire displacement.



(d) 2–6 mm of maximum wire displacement.

Figure 4.23: The relative error  $(p_{true} - p)/p_{true}$  of the momentum magnitudes for the fitted tracks.

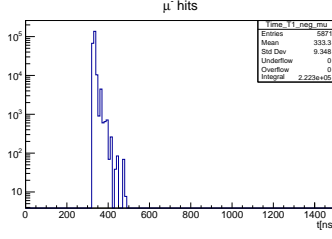
of the wire displacements within the range of 3–5 mm (see Figure 4.23 (c)) the standard deviation is 3.4 times larger than for the histogram in Figure 4.23 (a). For the maximum wire displacement range of 2–6 mm showed in Figure 4.23 (d) the standard deviation is 5.1 times larger. The significant influence on the distributions of the relative momenta errors is made by the relatively large  $X$ -coordinate uncertainties showed previously in Figure 4.20 (c) and (d). The  $Y$ -coordinate uncertainties made a minor contribution to the relative momenta errors and  $Z$ -coordinate uncertainties were not affected at all with the misalignment algorithm.

In general, 0.9% of all fitted tracks without applying the misalignment algorithm have the relative momentum errors larger than 5%. For the case, when all wires have equal maximum displacement value of 4 mm, 1.2% of all fitted tracks have the relative momentum error larger than 5%. In case of the random distribution of the maximum wire displacement values within the range of 3–5 mm the 17.6% of the fitted tracks exceeded the 5% limit for the relative momentum error. For the range of 2–6 mm the 35.5% of the fitted tracks exceeded the error limit. Also, the fit quality degraded significantly for the tests, where the ranges of random maximum wire displacement values were applied, having only

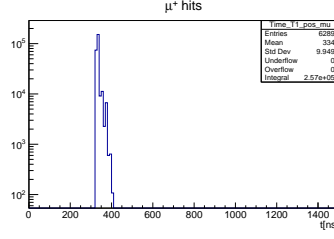
43.9% of the tracks with satisfying quality (p-value larger than  $\alpha_s$ ) for 3–5 mm range and 55.0% for 2–6 mm range respectively. The span of the variation range for the maximum wire displacement values has more significant impact on the track fitting performance than the mean value of the maximum wire displacement (4 mm in our studies). More studies and investigations need to be performed to find precisely the tolerable limit for the variation span of the maximum wire displacement values. According to the obtained results, the current limit on the variation of the sagging magnitude is 1 mm. Additional histograms and plots related to the track fitting performance for the misaligned hits can be found in [87].

### 4.3 Hits pile-up simulation in the SST

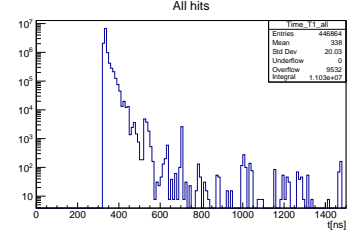
According to the muon background studies described in Section 4.1 the number of events, when at least one hit in any straw tube of the SST was created, is 2.3 million (for the nominal 1.7 T magnetic field of the Muon Shield) out of 32.1 million of the total number of events in the muon background simulation files. All initial particles (muons) in the muon background simulation files were created either after the primary proton interactions with the SHiP Target or after the secondary interactions and decays of the shortly living particles in the magnetized Hadron Absorber. In the FairShip framework it is currently defined that the time of each primary proton interaction is 0 s and the total number of such interactions is scaled to match the intensity of the SPS spill ( $5 \cdot 10^{13} \text{ s}^{-1}$ ) in the Beam Dump Facility [20]. The expected duration of the extracted SPS spill is 1 s. The slow beam extraction technique [18] allows to spread uniformly the extracted beam with a constant intensity over the spill duration. This means that each primary proton interaction will have its own time of the interaction in the temporal spill profile. Another important fact is that the SHiP DAQ system will have the continuous time framed read-out [89] of the registered hits from each subdetector without using any hardware triggering systems. This means that the events in the output data files will be formed according to the individual TDC hits of each subdetector and to the selection of the arbitrary time windows contrary to the current general simulation approach in the FairShip framework, where each event corresponds to a single primary proton interaction with the SHiP Target. In the Fairship muon background simulation output files each event corresponds to a single muon coming from the Hadron Absorber and contains all hits created by this muon and its daughter particles until their tracking with Geant4 [80] is stopped, when their energy is lower than an arbitrary chosen cut.



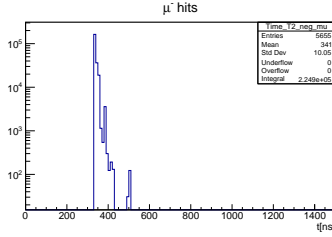
(a)  $\mu^-$  hits in the T1 tracking station.



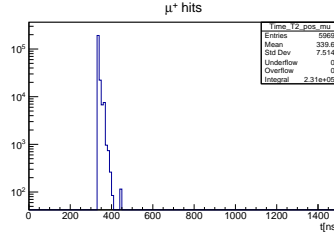
(b)  $\mu^+$  hits in the T1 tracking station.



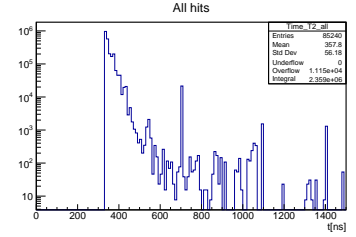
(c) All hits in T1 tracking station.



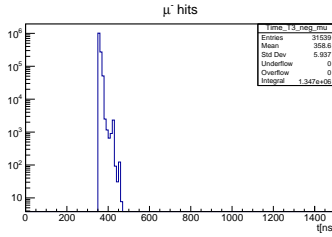
(d)  $\mu^-$  hits in the T2 tracking station.



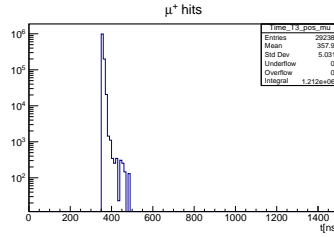
(e)  $\mu^+$  hits in the T2 tracking station.



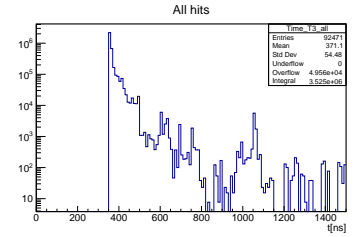
(f) All hits in T2 tracking station.



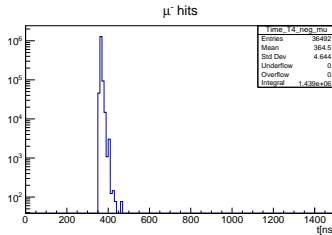
(g)  $\mu^-$  hits in the T3 tracking station.



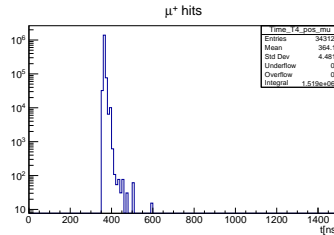
(h)  $\mu^+$  hits in the T3 tracking station.



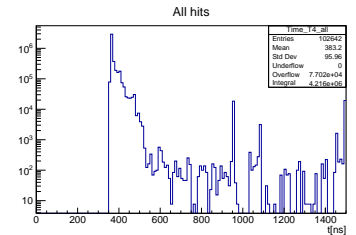
(i) All hits in T3 tracking station.



(j)  $\mu^-$  hits in the T4 tracking station.



(k)  $\mu^+$  hits in the T4 tracking station.



(l) All hits in T4 tracking station.

Figure 4.24: The hit time (the time-of-flight) distributions for separately muons ( $\mu^-$ ,  $\mu^+$ ) and for all particles leaving the hits in the SST tracking stations (T1, T2, T3 and T4) obtained from the simulation of the muon background in SHiP experiment using the FairShip framework.

The time of the hits created in the SST (the time-of-flight) varies from a few hundreds of nanoseconds for muon hits and up to few microseconds and more for low energetic electron and positron hits (see Figure 4.24). The hits generated in the tubes are then delayed within a  $\mathcal{O}(1\ \mu\text{s})$  time window depending on the distance from the hit point to the wire of the straw tube. The signal propagation time is of the order of  $\mathcal{O}(10\ \text{ns})$  and is also added to a final TDC value. Depending on the selected time frame width for the DAQ system read-out, the TDC hits created with the particles originating from a single initial muon can mix in time with the hits from another muon event due to the time delays generated in the SST. This effect is known as a pile-up of hits and its influence can be estimated for a given value of the time frame width. The pile-up effect has a major influence on the performance of the pattern recognition algorithms [36], which potentially reduces the efficiency of the SST. The idea of the following studies is to check the influence of piled-up hits on the current (unmodified) pattern recognition algorithms efficiency and the tracks fitting quality.

The size of the time frames for the DAQ system read-out is not yet finally defined, so, for the studies described in this section, the arbitrary value for the time frame width of  $3\ \mu\text{s}$  was chosen. Such choice of the time frame width was motivated by the time-of-flight distributions of the particles showed in Figure 4.24. The minimum time needed for the particles to reach the first tracking station is  $\approx 320\ \text{ns}$ , but the tails of the distributions spread beyond the  $1.5\ \mu\text{s}$  time scale. So, a  $3\ \mu\text{s}$  time frame width is the significant choice covering 97% of the hit times for all events. For the given time frame width  $\Delta t = 3\ \mu\text{s}$ , the mean number of muon background events  $\lambda$ , when at least one hit in the SST was created, is equal to:

$$\lambda = R_{SST} \cdot \Delta t = 2.3\ \text{MHz} \cdot 3\ \mu\text{s} = 6.9, \quad (4.6)$$

where  $R_{SST}$  is the total number of events in all muon background files, when at least one hit in the SST was created;  $\Delta t$  is the time frame width. As it was mentioned earlier in this section, the particles in the spill of the extracted beam are distributed uniformly in time with constant intensity, thus, the probabilities of getting a certain number  $k$  of the events (muons) within the  $\Delta t$  time frame, when at least one hit in the SST was created, follow the Poisson law:

$$p(k) = \frac{\lambda^k}{k!} \exp(-\lambda) = \frac{(R_{SST}\Delta t)^k}{k!} \exp(-R_{SST}\Delta t) \quad (4.7)$$

Using the equation (4.7) the one can calculate the probability of getting no events during the waiting time  $t$ :

$$p(0, t) = \exp(-R_{SST}t) \quad (4.8)$$

On the other hand, the probability of getting an event within the infinitesimal time window  $dt$  is equal to  $p = R_{SST}dt$ . Thus, the probability of getting an event within the time interval  $[t, t + dt]$  is equal to the product of the probability to have no events during



the waiting time  $t$  and the probability of getting a single event within the infinitesimal time window  $dt$ :

$$p(t) = R_{SST} \exp(-R_{SST}t)dt \quad (4.9)$$

The equation (4.9) is a fundamental formula describing the Poisson sequences in a single dimension. More details on this formula and other features of the Poisson distribution can be found in [90]. In the case of event pile-up studies, the equation (4.9) can be used to generate the probability distribution within the  $\Delta t$  time window of  $3\mu\text{s}$ , which was chosen previously. The  $dt$  size was selected to be  $2.5\text{ ns}$  – a typical least significant bit TDC value for the SST read-out electronics prototypes. So, the global time of each next event inside the time frame can be taken as a random variable with a probability density function generated according to the equation (4.9). This is one of the crucial steps in the pile-up simulation algorithm. The step-by-step description of the algorithm is given below:

1. As an input the FairShip muon background simulation files are taken. As it was mentioned earlier, the global time of each event in these files is set to  $0\text{ s}$  (the time of the primary proton interaction with the SHiP Target).
2. The event pile-up simulation runs over the events within the input file. The time of the first event is left intact (remains  $0\text{ s}$ ). All hits registered in the SST, which have the time less than the time frame width ( $3\mu\text{s}$  in our case) are added to the united *strawtubesPoint* collection. If any SST hit in the current muon background event has a time larger than the time frame width, it is saved to the temporary buffer. Later the hits from this temporary buffer can be added to the subsequent time frames. The Monte Carlo tracks associated with the selected hits from the united *strawtubesPoint* collection are also saved to the united *MCTrack* collection, in order to use them later for the pattern recognition performance studies. The MC tracks for the hits, which were put into the temporary buffer, are saved into the separate temporary buffer for the usage in the subsequent time frames, because the hits from the same track can be split across the neighboring frames in time.
3. The global time of each next event in the muon background simulation file is calculated as a sum of global times of the previous events and a randomly picked value from the distribution generated with the equation (4.9). This sum is added to the hit time of the SST hits. The same procedure regarding saving the hits and the MC tracks is applied as in the step 2. If the global time exceeds the time frame width ( $3\mu\text{s}$ ), the united *strawtubesPoint* and *MCTrack* collections are saved to the output file forming the piled-up event in the new ROOT [66] tree.
4. The frame time is increased by the time frame width value ( $3\mu\text{s}$ ). The piled-up event counter is increased by 1. The time of the hits saved during the step 2 in the temporary buffers is checked. If there are any hits with the time smaller than the current maximum frame time, then these hits and the corresponding MC tracks are added to the new united *strawtubesPoint* and *MCTrack* collections. The selected

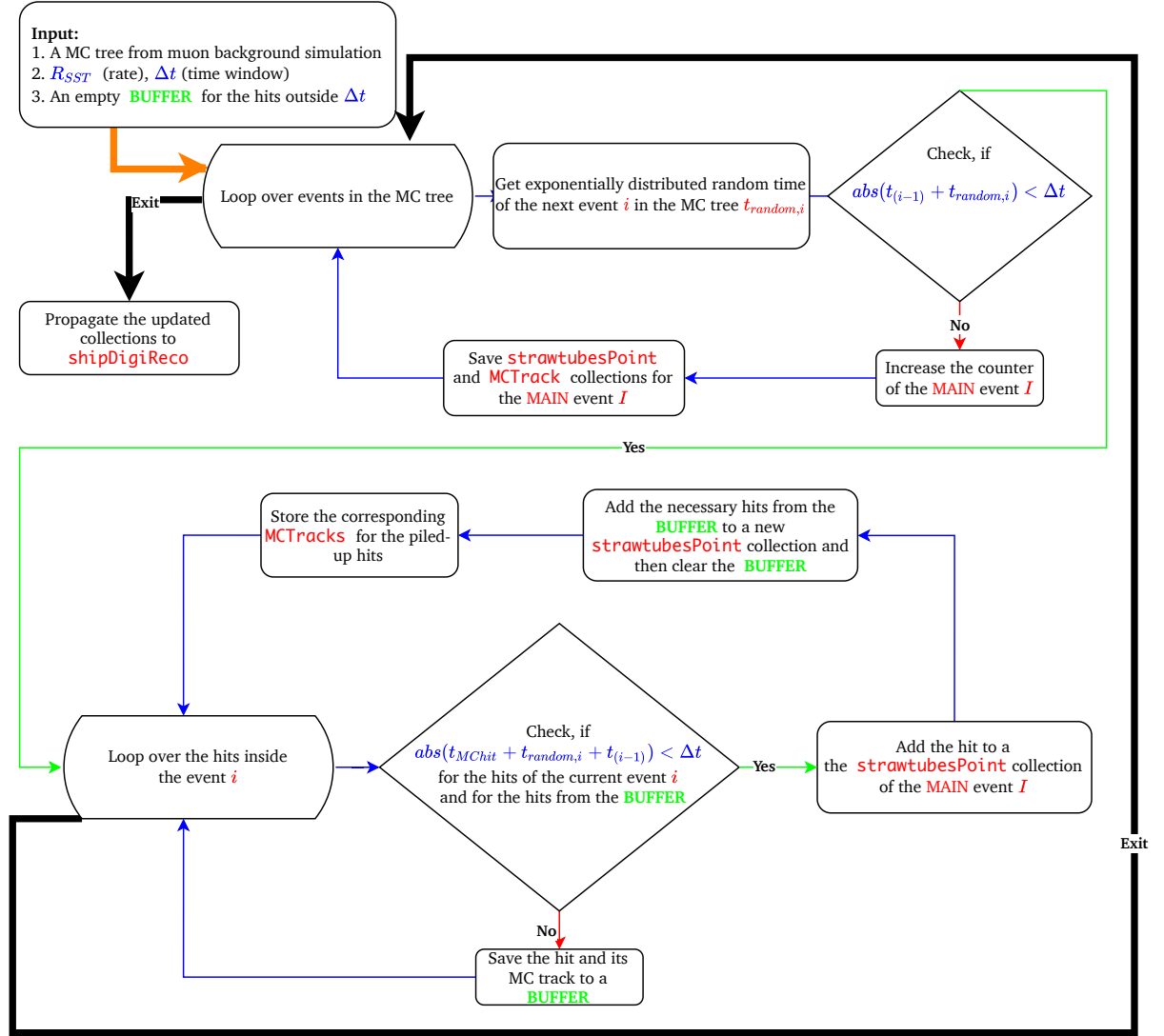


Figure 4.25: The schematic description of the pile-up simulation algorithm in the SST.

hits and tracks are removed from the temporary buffers, the rest are kept for the checks in the subsequent time frames.

5. After dealing with the hits saved in the temporary buffers, the hits from the next events of the muon background files are treated in a way, which was described in the steps 2 and 3.
6. In the end of the loop over all events in muon background simulation files, the new piled-up tree is saved to the final ROOT file.

The number of created piled-up events in the output file is smaller than the original number of the muon background events and it depends on the size of the time frame. The

larger the width of the time frame is, the smaller is the number of the piled-up events and vice versa. The schematic description of the pile-up simulation algorithm described above is shown in Figure 4.25.

The output files with the piled-up events are used as the input files for the digitization and reconstruction algorithms of the FairShip framework. The pattern recognition and the track fitting algorithms were not changed. The only difference was that the digitized collections of the SST hits were created using the united *strawtubesPoint* collections obtained after applying the pile-up simulation algorithm. Three pattern recognition methods, a template matching, a Hough transform and an Artificial retina, were tested on the muon background simulation files with applied event pile-up algorithm. The details on the pattern recognition algorithms theoretical concepts for the SST can be found in [36]. The pattern recognition and track fitting performance metrics are shown in Figure 4.26, 4.27, 4.28. The reconstructible tracks (labeled as “N total” in histograms) are the MC tracks, which were created before the first station T1 of the SST and have hits in all SST stations. The “other” tracks are the tracks, which were recognized by the pattern recognition algorithms, but have the track IDs, which are not available in the list of reconstructible tracks. The recognized tracks are the tracks recognized by the pattern recognition algorithms, which satisfy the conditions for the reconstructible tracks and have the same track IDs as the reconstructible tracks for the given piled-up event. The clone tracks are the tracks from the recognized tracks collection, which have equal track IDs to any other track in this collection for the given pile-up event. The “ghost” (labeled on histograms) or mismatched tracks are the tracks, which were accidentally made of two tracklets (the halves of the track before and after the Spectrometer magnet) with different track IDs, but both track IDs are from the reconstructible tracks collection for a given piled-up event.

The number of reconstructible tracks decreased in the piled-up muon background reconstruction files from 1310 tracks to 1301. This happened, because some fraction of the MC tracks after applying the pile-up simulation algorithms turned out split between the neighboring frames, thus, belonging to different piled-up events. The efficiency of the template matching pattern recognition algorithm (the number of recognized tracks divided by the number of the reconstructible ones) is 87.3% for the standard muon background simulation files without the SST hits pile-up simulation (see Figure 4.26 (a)). The statistical significance level  $\alpha_s$  introduced in the previous section and equal to 0.05 is used to determine the goodness of track fits. The fraction of the reconstructed tracks having the  $\chi^2/\text{NDOF}$  value smaller than 1.487 (the p-value is larger  $\alpha_s$ ) is 93.0% for the standard files without the pile-up simulation (see Figure 4.26 (b)). The efficiency of the template matching pattern recognition algorithm for the files with simulated pile-up of the hits is 80.6% (see Figure 4.26 (c)). The fraction of the reconstructed tracks having the  $\chi^2/\text{NDOF}$  value smaller than 1.487 (the p-value is larger  $\alpha_s$ ) is 92.4% for the muon background files with simulated pile-up of the hits (see Figure 4.26 (d)).

The efficiency of the Hough transform pattern recognition algorithm is 86.3% for the standard muon background simulation files without the pile-up simulation (see Figure 4.27 (a)). The fraction of the reconstructed tracks having the  $\chi^2/\text{NDOF}$  value smaller than

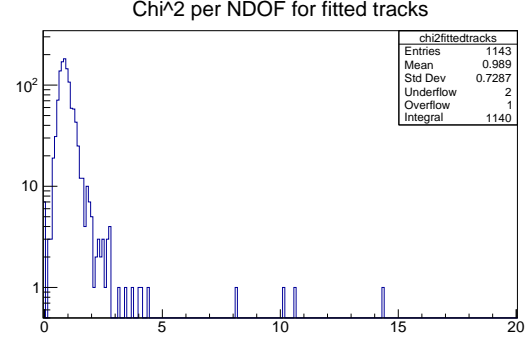
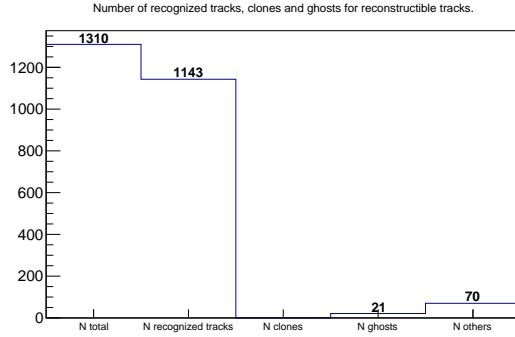
Table 4.5: The performance comparison between there pattern recognition methods applied to the collections of the SST hits from the standard muon background simulation and the collections of hits modified with the pile-up algorithm.

Standard muon background reconstruction files						
PR method	Reconstructible tracks	Recognized tracks	Efficiency (%)	Fraction of ghost tracks (%)	Fraction of other tracks (%)	Fraction of tracks with good fit quality ( $p > 0.05$ )
Template matching	1310	1143	87.3	1.7	5.7	93.0
Hough transform	1310	1130	86.3	1.1	4.9	93.8
Artificial retina	1310	1120	85.5	1.2	5.7	93.9
Muon background files with SST hits pile-up simulation						
PR method	Reconstructible tracks	Recognized tracks	Efficiency (%)	Fraction of ghost tracks (%)	Fraction of other tracks (%)	Fraction of tracks with good fit quality ( $p > 0.05$ )
Template matching	1301	1048	80.6	1.9	5.8	92.4
Hough transform	1301	1046	80.4	1.5	5.0	93.4
Artificial retina	1301	1015	78.0	1.2	5.6	93.4

1.496 (the p-value is larger  $\alpha_s$ ) is 93.8% for the standard muon background simulation files without the pile-up simulation (see Figure 4.27 (b)). The efficiency of the Hough transform pattern recognition algorithm for the files with simulated pile-up of the hits is 80.4% (see Figure 4.27 (c)). The fraction of the reconstructed tracks having the  $\chi^2/\text{NDOF}$  value smaller than 1.496 (the p-value is larger  $\alpha_s$ ) is 93.4% for the muon background simulation files with simulated pile-up of the hits (see Figure 4.27 (d)).

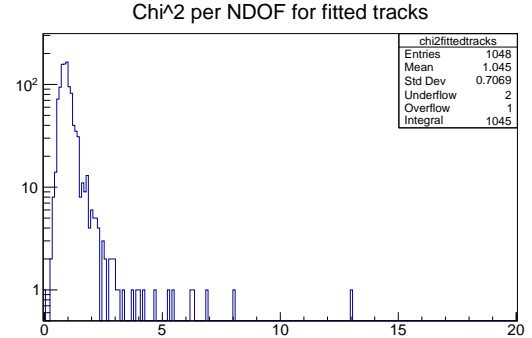
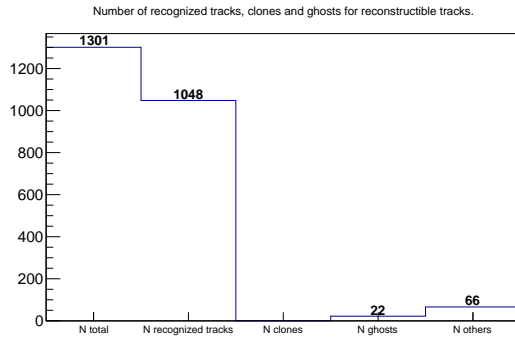
The efficiency of the Artificial retina pattern recognition algorithm is 85.5% for the standard muon background simulation files without the pile-up simulation (see Figure 4.28 (a)). The fraction of the reconstructed tracks having the  $\chi^2/\text{NDOF}$  value smaller than 1.487 (the p-value is larger than  $\alpha_s$ ) is 93.9% for the standard muon background simulation files without the pile-up simulation (see Figure 4.28 (b)). The efficiency of the Artificial retina pattern recognition algorithm for the files with simulated pile-up of the hits is 78.0% (see Figure 4.28 (c)). The fraction of the reconstructed tracks having the  $\chi^2/\text{NDOF}$  value smaller than 1.487 (the p-value is larger than  $\alpha_s$ ) is 93.4% for the muon background simulation files with simulated pile-up of the hits (see Figure 4.28 (d)).

Overall, all pattern recognition methods available in the FairShip framework had different values of the efficiency both for standard muon background files 85.5–87.3% and for the ones with simulated pile-up of the SST hits 78.0–80.6%. The drop of the pattern recognition efficiency is not dramatical with the maximum degradation of 7.5% for the Artificial retina algorithm. The change of the fitting quality of the reconstructed tracks is negligible for both standard muon background files and for the ones with simulated pile-up of the SST hits. The fraction of the fitted tracks having the p-value larger than  $\alpha_s$  did not drop lower than 92.4%. The summary with all the results is shown in Table 4.5. The table does not contain the values for fractions of clone track, because they were not observed in all tests.



(a) The histogram shows the total number of recognized tracks, clones of the tracks, ghost tracks and other tracks (non-reconstructible) obtained for the template matching pattern recognition algorithm compared to the total number of reconstructible tracks. The original muon background files are used (no pile-up).

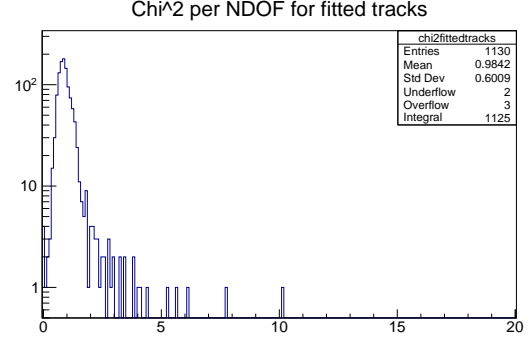
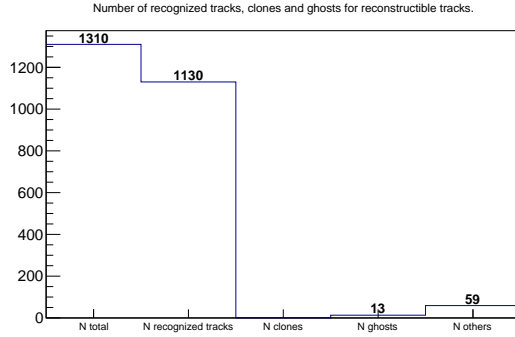
(b) The  $\chi^2/\text{NDOF}$  distribution of the fitted tracks after applying the template matching pattern recognition algorithm. The original muon background files are used (no pile-up).



(c) The histogram shows the total number of recognized tracks, clones of the tracks, ghost tracks and other tracks (non-reconstructible) obtained for the template matching pattern recognition algorithm compared to the total number of reconstructible tracks. The muon background files with the pile-up simulation are used.

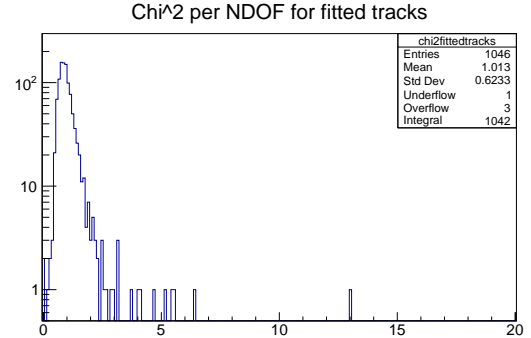
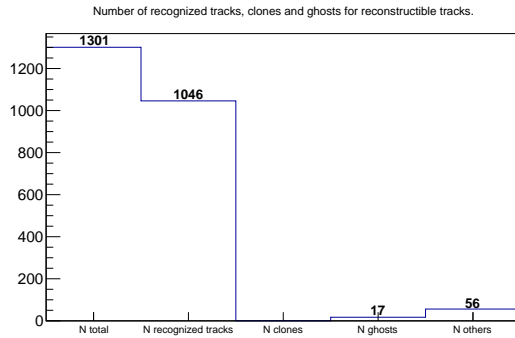
(d) The  $\chi^2/\text{NDOF}$  distribution of the fitted tracks after applying the template matching pattern recognition algorithm. The muon background files with pile-up simulation are used.

Figure 4.26: The top row of histograms reflects the efficiency of the template matching pattern recognition algorithm and the quality of the track fitting procedure applied on the recognized track patterns.



(a) The histogram shows the total number of recognized tracks, clones of the tracks, ghost tracks and other tracks (non-reconstructible) obtained for the Hough transform pattern recognition algorithm compared to the total number of reconstructible tracks. The original muon background files are used (no pile-up).

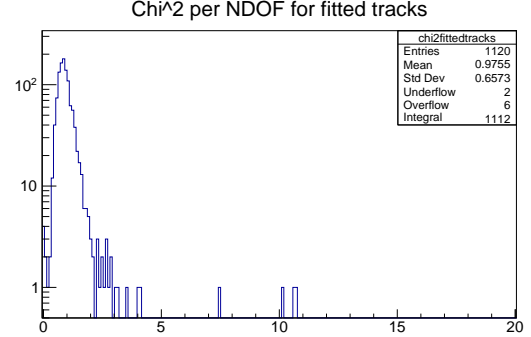
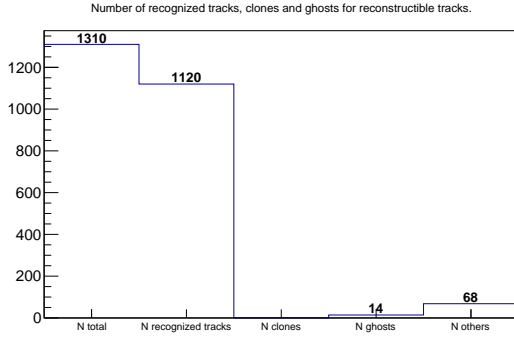
(b) The  $\chi^2/\text{NDOF}$  distribution of the fitted tracks after applying the Hough transform pattern recognition algorithm. The original muon background files are used (no pile-up).



(c) The histogram shows the total number of recognized tracks, clones of the tracks, ghost tracks and other tracks (non-reconstructible) obtained for the Hough transform pattern recognition algorithm compared to the total number of reconstructible tracks. The muon background files with the pile-up simulation are used.

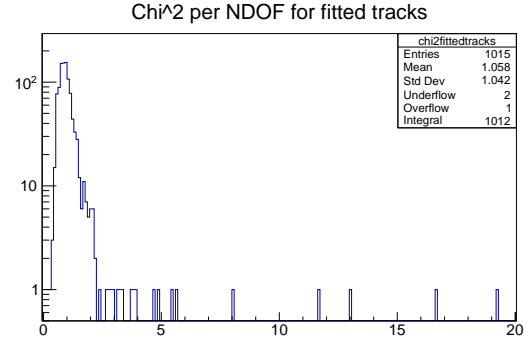
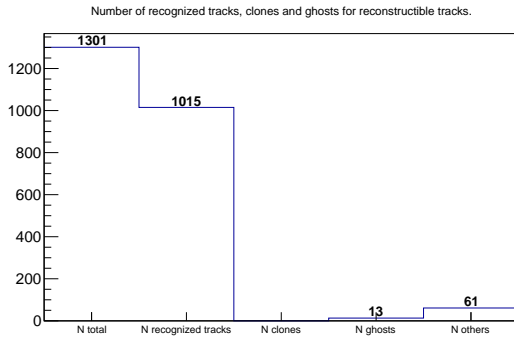
(d) The  $\chi^2/\text{NDOF}$  distribution of the fitted tracks after applying the Hough transform pattern recognition algorithm. The muon background files with pile-up simulation are used.

Figure 4.27: The top row of histograms reflects the efficiency of the Hough transform pattern recognition algorithm and the quality of the track fitting procedure applied on the recognized track patterns.



(a) The histogram shows the total number of recognized tracks, clones of the tracks, ghost tracks and other tracks (non-reconstructible) obtained for the Artificial retina pattern recognition algorithm compared to the total number of reconstructible tracks. The original muon background files are used (no pile-up).

(b) The  $\chi^2/\text{NDOF}$  distribution of the fitted tracks after applying the Artificial retina pattern recognition algorithm. The original muon background files are used (no pile-up).



(c) The histogram shows the total number of recognized tracks, clones of the tracks, ghost tracks and other tracks (non-reconstructible) obtained for the Artificial retina pattern recognition algorithm compared to the total number of reconstructible tracks. The muon background files with the pile-up simulation are used.

(d) The  $\chi^2/\text{NDOF}$  distribution of the fitted tracks after applying the Artificial retina pattern recognition algorithm. The muon background files with pile-up simulation are used.

Figure 4.28: The top row of histograms reflects the efficiency of the Artificial retina pattern recognition algorithm and the quality of the track fitting procedure applied on the recognized track patterns.





# Conclusions

The objects of the studies in this thesis were the straw tubes of the Spectrometer Straw Tracker (SST) of the future SHiP experiment. The measurements of the mechanical and electrical properties of the straw tubes presented in Chapter 2 provide information that could prove useful for the development of the SST design and confirmed various theoretical predictions. It was found that the sagging magnitude of the pressurized straw tubes under their own weight (without pretensioning) depends on the position of the welding seam of the tube with respect to the gravitational force direction. It turned out that the seam is stiffer than the rest of the tube for compression stresses and, if the tube is positioned with the welding seam on top, can help to counter sagging (5.5% sagging magnitude reduction). Additionally, during the straw tube elongation measurements an axial torsion of the tube was observed. This effect was not expected and is probably related to the BoPET material features, which is used to make the tubes. The magnitude of the relative rotation angle of the tube has a similar dependence on the gas pressure values inside the tube as the longitudinal strain (elastic deformation up to 2 bar) and reaches  $14^\circ$  at 2 bar. The longitudinal strain of the tube grows with the internal gas pressure linearly up to 2 bar with a slope of  $(1.11 \pm 0.02) \text{ mm}/(\text{m} \cdot \text{bar})$ . The elastic modulus of the straw tubes was calculated too and it is consistent within the uncertainties of the measurements with the data sheet value of 4.5 GPa for the machine direction of the BoPET roll in the elastic deformation region. The shape of the fully assembled tube (pressurized with the pretensioned wire inside) was studied using the laser scanning technique. The results showed that the vertically freely hanging pressurized straw tube bends towards the location of the welding seam. The magnitude of the bending reaches 4 mm for 1.28 bar of internal gas overpressure. The radius of the tube increases by 3.5% in the middle of the tube for 1.28 bar of internal gas overpressure. These observations should be considered during the development of the SST tracking station and module design. The rupture tests for the straw tubes showed that the tubes fail at  $\approx 4.7$  bar of gas pressure, if the test is performed within few minutes. However, the tubes are made of polymer and, hence, are a subject to the creep under the continuous loads. The creep tests showed that the elastic modulus of the straw tubes under 2.5 bar of pressure drops by almost 2 GPa from the data sheet value of 4.5 GPa after 17 hours of measurements. Such behavior of the straw tubes needs to be more thoroughly investigated.

The second part of Chapter 2 is dedicated to the simulation and measurements of the electrical properties of the straw tubes. The  $S_{11}$  parameter of the straw tube and the characteristic impedance  $Z_0$  were simulated using the ANSYS HFSS software. The  $S_{11}$  and

the signal attenuation per unit length were also experimentally measured and compared to the simulation results. The experimental value  $S_{11} = (-8.4 \pm 0.4)$  dB corresponds to the  $S_{11}$  value at  $\approx 1.5$  MHz from the HFSS simulation. The measured maximal signal attenuation at 2 m from the read-out electronics side is  $(-5.3 \pm 0.8)$  dB or, alternatively, the attenuation length  $\lambda$  is  $(370.4 \pm 25.6)$  cm. The characteristic impedance of the straw tube was not measured experimentally, because it requires the usage of the vector network analyzer, but could be conducted in the future. The  $Z_0$  value from the simulation is  $395 \Omega$  for the frequencies higher than 200 MHz. The information about the signal attenuation and the characteristic impedance of the straw tube is essential for the development of the front-end read-out electronics.

The major part of this thesis (Chapter 3) is devoted to the analysis of the 2017 test beam data, where two straw tube prototypes were tested (with 1 cm and 2 cm diameter). Measurements were carried out with a high energy pion test beam at the SPS H2 beam line to investigate the spatial resolution of the prototype straw tube detector for the SHiP experiment for different wire eccentricities. The emphasis was put on the analysis of the short straw tube (2 m length, 2 cm diameter), as this diameter is the baseline for the SST. The main goal was to study the wire eccentricity dependence of the spatial resolution, a dedicated measurement was performed with an optical method to cross check the wire eccentricity obtained from the V-shape analysis. The resolution calculation approach used the spatial distributions of the track hits inside the tube and extracted the resolution from the coordinate residuals. It had three options for the V-shape (isochrone relation) parametrization: a parabolic function fit, a degree 6 polynomial fit and an interpolation of the V-shape data points. All of them showed consistent results. The contribution from the systematic effects, including the bin size effects, the hit selection influence and the track extrapolation were considered. Averaged over the full straw diameter, the raw values for the spatial resolution range from  $(104.0 \pm 7.8) \mu\text{m}$  to  $(118.0 \pm 8.9) \mu\text{m}$  and, after subtraction of the telescope extrapolation error, from  $(85.0 \pm 6.4) \mu\text{m}$  to  $(102.0 \pm 7.7) \mu\text{m}$ . The spatial resolution shows a very weak dependence on the wire eccentricity within the measured experimental range from 0 mm to 2.1 mm and assumed to be constant for achieved precision of measurements. The other important effect observed is the dependence of a shape of the isochrone relation (V-shape parametrization) on the wire eccentricity. The perturbed electric field induced by the wire displacement has non-negligible effect on the drift velocity of the charges inside the straw tube. In the same chapter the possibility to extract the wire eccentricity of the straw tube using only the information about the shape of the drift time spectrum was considered. In order to detect the steps in the drift time distribution various edge detection techniques were utilized. Four edge detection methods were compared, which showed a competitive performance in terms of detection of the edges of the drift time distribution. The most promising methods are the improved Canny's and the Laplacian of Gaussian (LoG), as they are capable of distinguishing the positions of steps in the drift time distribution with sufficient precision and extract a wire eccentricity down to about 0.1 mm with a precision better than  $100 \mu\text{m}$ , if at least  $\sim 10\,000$  events are available. A common issue of the methods is that they can predict only the absolute value of the wire eccentricity, but the direction of it remains unknown

(positive or negative in the vertical direction orthogonal to the straw tube axis, in the case of the SST). This information can be extracted from track fitting techniques, if track hits from several tubes are studied. This feature will be studied further, when a larger SST prototype with a few straw tubes (a module) will be designed and built. The methods of the edge detection showed also a good applicability for calculation of the  $r(t)$  relation using a numerical integration of the drift time spectrum, provided the effect of the non-flat beam profile is properly taken into account.

The last chapter is dedicated to the studies of the straw tubes parameters in the FairShip framework, which affect the performance of the SST. The expected occupancy of the SST tracking stations is an important information, which gives the estimate of the read-out speed needed for the front-end electronics. The hit rates in the straw tubes were calculated for the muon background simulation depending on the amount of heavy supporting material around the stations (steel frames) and the availability of the implemented field maps for the SST Spectrometer Magnet and the Scattering and Neutrino Detector magnet instead of standard uniform fields existing only within the geometrical acceptance of SHiP. The implemented field maps reduced the average hit rate in the first two stations (especially in T2 by a factor of 2) of the SST, but increased the average hit rate in the last two stations T3 and T4 by 10–40%. The particle hits composition changed too. The stations T1 and T2 are dominated by  $e^+/e^-$  hits, but the stations T3 and T4 register mostly muon hits. The main reason for all the mentioned changes is the addition of the return field of the magnets, which bends back some fraction of background muons to the geometrical acceptance of the stations. The addition of the extra supporting material around the stations had significant influence on the average rates in the first two stations (1.5–2.5 times larger average hit rates in T1 and T2), but the influence on the last two stations was negligible. Additionally, in this chapter the results were shown from a simulation of the wire displacement inside the straw tube and how this affects the track fitting quality in the FairShip framework. The studies showed that the misalignment of the wire with respect to the tube axis in  $XY$ -plane orthogonal to the proton beam direction  $Z$  has significant influence on the  $X$ -coordinate of the reconstructed tracks. This is happening, because of the large contribution to the  $X$ -coordinate track error from the stereo views of the tracking stations rotated by  $\pm 5^\circ$ . This contribution to the error becomes even larger, if the magnitudes of the wire displacements inside the straw tubes are randomly distributed within a certain range. The last section of this chapter was devoted to the simulation of the hits pile-up in the SST, due to the fact that the incoming proton beam is spread with uniform intensity over 1 s spill duration. The pile-up affects mainly the tracks pattern recognition efficiency, because the hits from neighboring events are getting merged and the number of SST hits per time frame increases. It was shown that, without any attempt to adapt the algorithm, the pattern recognition efficiency suffered a relative drop of about 9%, when the hit pile-up was introduced.

In general, all the studies presented in this thesis contributed to the development of the SST design, improved the understanding of various features of straw tubes and provided the quantitative description of them either using the simulations or experimental measurements. The investigations from this thesis can be used as a starting point for

further more detailed simulations, measurements and studies related to the research and development of the Spectrometer Straw Tracker of SHiP.

# Bibliography

- [1] S. Alekhin, W. Altmannshofer, T. Asaka, B. Batell, F. Bezrukov, K. Bondarenko, A. Boyarsky, K.-Y. Choi, C. Corral, N. Craig *et al.*, “A facility to search for hidden particles at the CERN SPS: the SHiP physics case,” *Reports on Progress in Physics*, vol. 79, no. 12, p. 124201, Oct 2016. [Online]. Available: <http://dx.doi.org/10.1088/0034-4885/79/12/124201>
- [2] M. Anelli, S. Aoki, G. Arduini, J. Back, A. Bagulya, W. Baldini, A. Baranov, G. Barker, S. Barsuk, M. Battistin *et al.*, “A Facility to Search for Hidden Particles (SHiP) at the CERN SPS,” CERN, Geneva, Tech. Rep. CERN-SPSC-2015-016. SPSC-P-350. arXiv:1504.04956, Apr 2015, technical Proposal. [Online]. Available: <https://cds.cern.ch/record/2007512>
- [3] SHiP Collaboration, “Addendum to Technical Proposal: A Facility to Search for Hidden Particles (SHiP) at the CERN SPS,” CERN, Geneva, Tech. Rep. CERN-SPSC-2015-040. SPSC-P-350-ADD-2, Oct 2015. [Online]. Available: <https://cds.cern.ch/record/2060742>
- [4] W. Bonivento, A. Boyarsky, H. Dijkstra, U. Egede, M. Ferro-Luzzi, B. Goddard, A. Golutvin, D. Gorbunov, R. Jacobsson, J. Panman, M. Patel, O. Ruchayskiy, T. Ruf, N. Serra, M. Shaposhnikov, and D. Treille, “Proposal to Search for Heavy Neutral Leptons at the SPS,” CERN, Geneva, Tech. Rep. CERN-SPSC-2013-024. SPSC-EOI-010, Oct 2013. [Online]. Available: <https://cds.cern.ch/record/1606085>
- [5] C. Ahdida *et al.*, “SHiP Experiment - Comprehensive Design Study report,” CERN, Geneva, Tech. Rep. CERN-SPSC-2019-049. SPSC-SR-263, Dec 2019. [Online]. Available: <https://cds.cern.ch/record/2704147>
- [6] D. Sukhonos, M. Ferro-Luzzi, and T. Ruf, “Hit Rates in the Spectrometer Straw Tracker from Simulation,” no. CERN-SHiP-INT-2019-002, Jun 2019. [Online]. Available: <https://cds.cern.ch/record/2680288>
- [7] D. Sukhonos, “SST 2017 test beam: drift time distribution analysis,” no. CERN-SHiP-INT-2020-002, Oct 2020. [Online]. Available: <https://cds.cern.ch/record/2741314>
- [8] D. Sukhonos, “SST 2017 test beam: spatial resolution results,” no. CERN-SHiP-INT-2019-005, Dec 2019. [Online]. Available: <https://cds.cern.ch/record/2702526>

- [9] M. D. Schwartz, *Quantum field theory and the standard model*. Cambridge University Press, 2014.
- [10] J. Abdallah, H. Araujo, A. Arbey, A. Ashkenazi, A. Belyaev, J. Berger, C. Boehm, A. Boveia, A. Brennan, J. Brooke, and et al., “Simplified models for dark matter searches at the LHC,” *Physics of the Dark Universe*, vol. 9-10, p. 8–23, Sep 2015. [Online]. Available: <http://dx.doi.org/10.1016/j.dark.2015.08.001>
- [11] Apollinari G. and Béjar Alonso I. and Brüning O. and Fessia P. and Lamont M. and Rossi L. and Tavian L., *High-Luminosity Large Hadron Collider (HL-LHC): Technical Design Report V. 0.1*, ser. CERN Yellow Reports: Monographs. Geneva: CERN, 2017. [Online]. Available: <https://cds.cern.ch/record/2284929>
- [12] M. Battaglieri *et al.*, “US Cosmic Visions: New Ideas in Dark Matter 2017: Community Report,” in *U.S. Cosmic Visions: New Ideas in Dark Matter*, no. FERMILAB-CONF-17-282-AE-PPD-T, 7 2017.
- [13] T. Yanagida, “Horizontal gauge symmetry and masses of neutrinos,” *Conf. Proc. C*, vol. 7902131, pp. 95–99, 1979.
- [14] SHiP Collaboration, “SHiP sensitivity to Dark Photons,” no. CERN-SHiP-NOTE-2016-004, Sep 2016. [Online]. Available: <https://cds.cern.ch/record/2214092>
- [15] G. Lanfranchi, “Sensitivity of the SHiP experiment to a light scalar particle mixing with the Higgs,” no. CERN-SHiP-NOTE-2017-001, Jan 2017. [Online]. Available: <https://cds.cern.ch/record/2243034>
- [16] J. Beacham, C. Burrage, D. Curtin, A. De Roeck, J. Evans, J. L. Feng, C. Gatto, S. Gninenko, A. Hartin, I. Irastorza, and others., “Physics beyond colliders at cern: beyond the standard model working group report,” *Journal of Physics G: Nuclear and Particle Physics*, vol. 47, no. 1, p. 010501, Dec 2019. [Online]. Available: <http://dx.doi.org/10.1088/1361-6471/ab4cd2>
- [17] SHiP collaboration, “FairShip framework,” <https://github.com/ShipSoft/FairShip>.
- [18] Ambrosini, G and NA56/SPY collaboration and others, “Measurement of charged particle production from 450 GeV/c protons on beryllium,” *The European Physical Journal C-Particles and Fields*, vol. 10, no. 4, pp. 605–627, 1999.
- [19] C. Ahdida *et al.*, “Measurement of the muon flux for the SHiP experiment,” no. CERN-EP-2020-006, 1 2020.
- [20] ———, *SPS Beam Dump Facility - Comprehensive Design Study*, ser. CERN Yellow Reports: Monographs, M. Calviani, B. Goddard, R. Jacobsson, and M. Lamont, Eds., 2020, vol. 2/2020, no. CERN-PBC-REPORT-2019-005, CERN-2020-002.

- [21] V. Bayliss and J. Boehm, “Development of a magnet system for the CERN BDF/SHiP Facility,” no. CERN-SHiP-NOTE-2019-004, Oct 2019. [Online]. Available: <https://cds.cern.ch/record/2704042>
- [22] A. Akmete and others., “The active muon shield in the SHiP experiment,” *Journal of Instrumentation*, vol. 12, no. 05, pp. P05 011–P05 011, may 2017. [Online]. Available: <https://doi.org/10.1088%2F1748-0221%2F12%2F05%2Fp05011>
- [23] A. Baranov, E. Burnaev, D. Derkach, A. Filatov, N. Klyuchnikov, O. Lantwin, F. Ratnikov, A. Ustyuzhanin, and A. Zaitsev, “Optimising the active muon shield for the SHiP experiment at CERN,” *J. Phys. Conf. Ser.*, vol. 934, no. 1, p. 012050, 2017.
- [24] K. Gunther, G. Abbruzzese, S. Fortunati, and G. Ligi, “Recent Technology Developments in the Production of Grain-Oriented Electrical Steel,” *steel research international*, vol. 76, no. 6, pp. 413–421, 2005. [Online]. Available: <https://onlinelibrary.wiley.com/doi/abs/10.1002/srin.200506030>
- [25] “LHCb Tracker Upgrade Technical Design Report,” no. CERN-LHCC-2014-001, LHCb-TDR-015, 2 2014.
- [26] P. Wertelaers and A. P. Perez, “SHiP Hidden Sector spectrometer magnet,” no. CERN-SHiP-INT-2019-008, Dec 2019. [Online]. Available: <https://cds.cern.ch/record/2704120>
- [27] G. Lanfranchi, A. Montanari, N. Tosi, G. Felici, P. Ciambrone, T. Rovelli, A. Saputi, A. Calcaterra, and A. Paoloni, “SHiP Hidden Sector Muon System: Progress report.” no. CERN-SHiP-NOTE-2019-002, Nov 2019. [Online]. Available: <https://cds.cern.ch/record/2702955>
- [28] D. R. Breton, M. Jonker, and J. Maalmi, “SHiP Common Detector Electronics,” no. CERN-SHiP-INT-2020-001, Jan 2020. [Online]. Available: <https://cds.cern.ch/record/2706968>
- [29] E. Van Herwijnen, H. Dijkstra, M. Ferro-Luzzi, and T. Ruf, “Simulation and pattern recognition for the SHiP Spectrometer Tracker,” no. CERN-SHiP-NOTE-2015-002, Mar 2015. [Online]. Available: <https://cds.cern.ch/record/2005715>
- [30] F. Hahn, F. Ambrosino, A. Ceccucci, H. Danielsson, N. Doble, F. Fantechi, A. Kluge, C. Lazzeroni, M. Lenti, G. Ruggiero, M. Sozzi, P. Valente, and R. Wanke, “NA62: Technical Design Document,” CERN, Geneva, Tech. Rep. NA62-10-07, Dec 2010. [Online]. Available: <https://cds.cern.ch/record/1404985>
- [31] N. I. Azorskii, Y. V. Gusakov, V. V. Elsha, T. L. Enik, Y. V. Ershov, V. D. Kekelidze, E. M. Kislov, A. O. Kolesnikov, D. T. Madigozhin, S. A. Movchan, I. A. Polenkevich, Y. K. Potrebenikov, V. A. Samsonov, S. N. Shkarovskiy, A. N. Sotnikov, A. D. Volkov, and A. I. Zinchenko, “New type of drift tubes for gas-discharge

- detectors operating in vacuum: Production technology and quality control,” *Physics of Particles and Nuclei Letters*, vol. 14, no. 1, pp. 144–149, Jan 2017. [Online]. Available: <https://doi.org/10.1134/S1547477117010071>
- [32] P. Wertelaers and A. Perez, “Expanding piano frame for Straw Tracker,” no. CERN-SHiP-INT-2019-007, Dec 2019. [Online]. Available: <https://cds.cern.ch/record/2703481>
  - [33] D. Bick, S. Bieschke, C. Hagner, B. Kaiser, and W. Schmidt-Parzefall, “The Suspended Bridge Design Concept for the SHiP Spectrometer Straw Tracker,” no. CERN-SHiP-INT-2019-006, Dec 2019. [Online]. Available: <https://cds.cern.ch/record/2702653>
  - [34] M. Ferro-Luzzi, “Cemented pack concept for the SHiP spectrometer straw tracker,” Oct 2020. [Online]. Available: <https://cds.cern.ch/record/2741489>
  - [35] A. Zelenov, “Implementation of signal digitization for the SHiP Spectrometer Straw Tracker simulation,” no. CERN-STUDENTS-Note-2020-008, Mar 2020. [Online]. Available: <https://cds.cern.ch/record/2713503>
  - [36] M. Hushchyn, A. Ustyuzhanin, O. Alenkin, and E. van Herwijnen, “Track pattern recognition for the SHiP spectrometer tracker,” *Journal of Physics: Conference Series*, vol. 898, p. 042027, oct 2017. [Online]. Available: <https://doi.org/10.1088%2F1742-6596%2F898%2F4%2F042027>
  - [37] P. D. Group *et al.*, “Review of Particle Physics,” *Progress of Theoretical and Experimental Physics*, vol. 2020, no. 8, 08 2020, 083C01. [Online]. Available: <https://doi.org/10.1093/ptep/ptaa104>
  - [38] A. D. Girolamo, “Studies on the performances of the Monitored Drift Tubes of the Atlas detector,” 2004. [Online]. Available: <http://diggi.web.cern.ch/diggi-phd-thesis.pdf>
  - [39] F. Sauli, “Principles of operation of multiwire proportional and drift chambers,” CERN. Geneva: CERN, 1977, p. 92 p, cERN, Geneva, 1975 - 1976. [Online]. Available: <https://cds.cern.ch/record/117989>
  - [40] S. Biagi, “A multiterm boltzmann analysis of drift velocity, diffusion, gain and magnetic-field effects in argon-methane-water-vapour mixtures,” *Nuclear Instruments and Methods in Physics Research Section A: Accelerators, Spectrometers, Detectors and Associated Equipment*, vol. 283, no. 3, pp. 716 – 722, 1989. [Online]. Available: <http://www.sciencedirect.com/science/article/pii/0168900289914460>
  - [41] F. Penning, “Über ionisation durch metastabile atome,” *NW*, vol. 15, no. 40, pp. 818–818, 1927.



- [42] Özkan Şahin and Tadeusz Z. Kowalski and Rob Veenhof, “High-precision gas gain and energy transfer measurements in Ar–CO<sub>2</sub> mixtures,” *Nuclear Instruments and Methods in Physics Research Section A: Accelerators, Spectrometers, Detectors and Associated Equipment*, vol. 768, pp. 104 – 111, 2014. [Online]. Available: <http://www.sciencedirect.com/science/article/pii/S0168900214010924>
- [43] W. Blum, W. Riegler, and L. Rolandi, *Particle detection with drift chambers; 2nd ed.* Berlin: Springer, 2008. [Online]. Available: <https://cds.cern.ch/record/1105920>
- [44] National Nuclear Data Center. Information extracted from the NuDat 2 database, <https://www.nndc.bnl.gov/nudat2/>.
- [45] M. Berger, “XCOM: photon cross sections database,” 2010. [Online]. Available: <http://www.nist.gov/pml/data/xcom/index.cfm>
- [46] M. J. Berger, J. S. Coursey, and M. A. Zucker, “ESTAR, PSTAR, and ASTAR: computer programs for calculating stopping-power and range tables for electrons, protons, and helium ions (version 1.21),” Tech. Rep., 1999.
- [47] I. Bereziuk, O. Bezshyyko, and M. Ferro-Luzzi, “Initial design studies of the SHiP straw detector,” no. CERN-SHiP-NOTE-2015-001, Mar 2015. [Online]. Available: <https://cds.cern.ch/record/2005286>
- [48] Hostaphan, “RNK,” <https://www.m-petfilm.de/wp-content/uploads/RNKe.pdf>, Oct 2011, accessed on 2020/10/03.
- [49] P. Wertelaers, A. Perez, and M. Ferro-Luzzi, “The CERN-2017 engineering design concept of a generic straw station for the Spectrometer Tracker,” no. CERN-SHiP-INT-2018-001, Dec 2018. [Online]. Available: <https://cds.cern.ch/record/2652629>
- [50] W. Erni *et al.*, “Technical design report for the PANDA (AntiProton Annihilations at Darmstadt) Straw Tube Tracker,” *Eur. Phys. J. A*, vol. 49, p. 25, 2013.
- [51] V. BATUSOV, “SHiP - Control of the sag of horizontal STRAW ”N3” in different rotations (NATIVES) Measurement of 07th October 2019,” [https://edms.cern.ch/ui/file/2249748/1/20191007\\_STRAW\\_N3.pdf](https://edms.cern.ch/ui/file/2249748/1/20191007_STRAW_N3.pdf), Oct 2019, accessed on 2020/10/03.
- [52] Leica, “NA2,” <http://rentals.leica-geosystems.com/support/F7F2D6C1-5056-8236-9A0B5DFC14539F8F.pdf>, 2004, accessed on 2020/10/03.
- [53] “Dino-Lite: powerful, portable, versatile,” Dino-Lite Digital Microscope. The Industry Standard. [Online]. Available: [http://www.dino-lite.eu/images/pdfs/Dino-Lite.General.Brochure.EN\\_2015Q3.pdf](http://www.dino-lite.eu/images/pdfs/Dino-Lite.General.Brochure.EN_2015Q3.pdf)
- [54] Leica, “ABSOLUTE TRACKER AT960,” <https://metrology.precizika.lt/uploads/Downloads/Leica%20AT960%20brochure.en.pdf>, Jul 2015, accessed on 2020/10/03.

- [55] K. NIKOLITSAS, “SHiP - STRAW 3D Scan of the Straw N3 in vertical position Measurement of 20th November 2019,” [https://edms.cern.ch/ui/file/2293647/1/2019.11.20\\_Scanning\\_of\\_STRAW\\_N3.pdf](https://edms.cern.ch/ui/file/2293647/1/2019.11.20_Scanning_of_STRAW_N3.pdf), Nov 2019, accessed on 2020/10/03.
- [56] X. Pan, “cylinder-fitting python module,” <https://github.com/xingjiepan/cylinder-fitting>, Jun 2017, accessed on 2020/10/03.
- [57] D. Eberly, “Fitting 3D data with a cylinder,” *Online, February*, 2008. [Online]. Available: <http://www.geometrictools.com/Documentation/CylinderFitting.pdf>
- [58] A. CARVALHOSA, “DIC measurements on straws for the SHiP experiment,” [https://edms.cern.ch/ui/file/2392744/1/SHIP\\_Straws\\_Pressure\\_Tests\\_Analysis.html](https://edms.cern.ch/ui/file/2392744/1/SHIP_Straws_Pressure_Tests_Analysis.html), Sep 2020, accessed on 2020/10/03.
- [59] First Sensor, “CTE9000 / CTU9000 Series,” [https://twiki.cern.ch/twiki/pub/Ship/TestbeamIn2016/DS\\_Standard-CTE-CTU9000\\_E\\_11509.pdf](https://twiki.cern.ch/twiki/pub/Ship/TestbeamIn2016/DS_Standard-CTE-CTU9000_E_11509.pdf), 2016, accessed on 2020/10/03.
- [60] T. Siebert and M. J. Crompton, “Application of high speed digital image correlation for vibration mode shape analysis,” in *Application of Imaging Techniques to Mechanics of Materials and Structures, Volume 4*. Springer, 2013, pp. 291–298.
- [61] *Luma Tungsten Wire alloyed with 3% Rhenium*, [https://luma-metall.com/wp-content/uploads/2017/01/LUMA-Tungsten-alloyed-with-rhenium\\_march2014.pdf](https://luma-metall.com/wp-content/uploads/2017/01/LUMA-Tungsten-alloyed-with-rhenium_march2014.pdf), Luma Metall, Mar 2014, accessed on 2020/10/03.
- [62] F. Cemin, D. Lundin, D. Cammilleri, T. Maroutian, P. Lecoeur, and T. Minea, “Low electrical resistivity in thin and ultrathin copper layers grown by high power impulse magnetron sputtering,” *Journal of Vacuum Science & Technology A*, vol. 34, no. 5, p. 051506, 2016. [Online]. Available: <https://doi.org/10.1116/1.4959555>
- [63] T. Gilani and D. Rabchuk, “Electrical resistivity of gold thin film as a function of film thickness,” *Canadian Journal of Physics*, vol. 96, no. 3, pp. 272–274, 2018. [Online]. Available: <https://doi.org/10.1139/cjp-2017-0484>
- [64] Ansys®, “Electronics Desktop 2019 R1,” <https://www.ansys.com/products/electronics>, accessed on 2020/10/03.
- [65] W. Verkerke and D. P. Kirkby, “The RooFit toolkit for data modeling,” *eConf*, vol. C0303241, p. MOLT007, 2003.
- [66] R. Brun and F. Rademakers, “ROOT: An object oriented data analysis framework,” *Nucl. Instrum. Meth. A*, vol. 389, pp. 81–86, 1997.
- [67] A. Abba, F. Caponio, M. Citterio, S. Coelli, J. Fu, M. Lazzaroni, A. Merli, M. Monti, N. Neri, M. Petruzzo, I. Rachevskaia, and D. Terzi, “Silicon telescope for prototype sensor characterization using particle beams and cosmic rays,”

- Journal of Instrumentation*, vol. 12, no. 03, p. C03060, 2017. [Online]. Available: <http://stacks.iop.org/1748-0221/12/i=03/a=C03060>
- [68] M. Agari, N. van Bakel, C. Bauer, D. Baumeister, M. van Beuzekom, M. Feuerstack-Raible, N. Harnew, W. Hofmann, E. Jans, S. Klous *et al.*, “Beetle—a radiation hard readout chip for the lhcb experiment,” *Nuclear Instruments and Methods in Physics Research Section A: Accelerators, Spectrometers, Detectors and Associated Equipment*, vol. 518, no. 1-2, pp. 468–469, 2004.
  - [69] L. Glonti, T. Enik, V. Kekelidze, A. Kolesnikov, D. Madigozhin, N. Molokanova, S. Movchan, Y. Potrebenikov, and S. Shkarovskiy, “Longitudinal tension and mechanical stability of a pressurized straw tube,” *Instruments*, vol. 2, no. 4, p. 27, Nov 2018. [Online]. Available: <http://dx.doi.org/10.3390/instruments2040027>
  - [70] L. Glonti, M. Misheva, Y. Potrebenikov, V. Samsonov, S. Movchan, T. Enik, and A. Kolesnikov, “Determination of the anode wire position by visible light in a new type straw for na62 experiment tracker,” *Nuclear Instruments and Methods in Physics Research Section A: Accelerators, Spectrometers, Detectors and Associated Equipment*, vol. 824, pp. 532 – 534, 2016, frontier Detectors for Frontier Physics: Proceedings of the 13th Pisa Meeting on Advanced Detectors. [Online]. Available: <http://www.sciencedirect.com/science/article/pii/S0168900215015569>
  - [71] N. Azorskiy, L. Glonti, Y. Gusakov, V. Elsha, T. Enik, S. Kakurin, V. Kekelidze, E. Kislov, A. Kolesnikov, D. Madigozhin, S. Movchan, I. Polenkevich, Y. Potrebenikov, V. Samsonov, S. Shkarovskiy, S. Sotnikov, A. Zinchenko, H. Danielsson, J. Bendotti, J. Degrange, N. Dixon, P. Lichard, J. Morant, V. Palladino, F. P. Gomez, G. Ruggiero, and M. Vergain, “A drift chamber with a new type of straws for operation in vacuum,” *Nuclear Instruments and Methods in Physics Research Section A: Accelerators, Spectrometers, Detectors and Associated Equipment*, vol. 824, pp. 569 – 570, 2016, frontier Detectors for Frontier Physics: Proceedings of the 13th Pisa Meeting on Advanced Detectors. [Online]. Available: <http://www.sciencedirect.com/science/article/pii/S0168900215014990>
  - [72] R. Brun and F. Rademakers, “ROOT: An object oriented data analysis framework,” *Nucl. Instrum. Meth. A*, vol. 389, pp. 81–86, 1997.
  - [73] A. Abba, F. Bedeschi, F. Caponio, R. Cenci, M. Citterio, S. Coelli, J. Fu, A. Geraci, M. Grizzuti, N. Lusardi *et al.*, “Real time tracking with a silicon telescope prototype using the “artificial retina” algorithm,” *Nuclear Instruments and Methods in Physics Research Section A: Accelerators, Spectrometers, Detectors and Associated Equipment*, vol. 824, pp. 343–345, 2016.
  - [74] A. Lechner, “Particle interactions with matter,” *CERN Yellow Rep. School Proc.*, vol. 5, p. 47. 22 p, 2018. [Online]. Available: <https://cds.cern.ch/record/2674116>

- [75] Şahin, Ö and Tapan, I and Özmutlu, Emin N and Veenhof, R, “Penning transfer in argon-based gas mixtures,” *Journal of Instrumentation*, vol. 5, no. 05, p. P05002, 2010.
- [76] J. Canny, “A computational approach to edge detection,” *IEEE Transactions on Pattern Analysis and Machine Intelligence*, vol. PAMI-8, no. 6, pp. 679–698, Nov 1986.
- [77] A. Huertas and G. Medioni, “Detection of intensity changes with subpixel accuracy using laplacian-gaussian masks,” *IEEE Transactions on Pattern Analysis and Machine Intelligence*, vol. PAMI-8, no. 5, pp. 651–664, Sept 1986.
- [78] Wikipedia contributors, “Bisection method — Wikipedia, the free encyclopedia,” [https://en.wikipedia.org/w/index.php?title=Bisection\\_method&oldid=981021314](https://en.wikipedia.org/w/index.php?title=Bisection_method&oldid=981021314), 2020, [Online; accessed 13-October-2020].
- [79] M. Al-Turany, D. Bertini, R. Karabowicz, D. Kresan, P. Malzacher, T. Stockmanns, and F. Uhlig, “The FairRoot framework,” *Journal of Physics: Conference Series*, vol. 396, no. 2, p. 022001, dec 2012. [Online]. Available: <https://doi.org/10.1088%2F1742-6596%2F396%2F2%2F022001>
- [80] S. Agostinelli, J. Allison, K. a. Amako, J. Apostolakis, H. Araujo, P. Arce, M. Asai, D. Axen, S. Banerjee, G. . Barrand *et al.*, “Geant4—a simulation toolkit,” *Nuclear instruments and methods in physics research section A: Accelerators, Spectrometers, Detectors and Associated Equipment*, vol. 506, no. 3, pp. 250–303, 2003.
- [81] *OPERA-3d Reference Manual*, Vector Fields Limited, 1999. [Online]. Available: <http://epp.phys.kyushu-u.ac.jp/~oda/cns/GEM/man/ref-3d.pdf>
- [82] T. Sjöstrand, S. Ask, J. R. Christiansen, R. Corke, N. Desai, P. Ilten, S. Mrenna, S. Prestel, C. O. Rasmussen, and P. Z. Skands, “An introduction to pythia 8.2,” *Computer Physics Communications*, vol. 191, p. 159–177, Jun 2015. [Online]. Available: <http://dx.doi.org/10.1016/j.cpc.2015.01.024>
- [83] T. Sjöstrand, S. Mrenna, and P. Skands, “Pythia 6.4 physics and manual,” *Journal of High Energy Physics*, vol. 2006, no. 05, p. 026–026, May 2006. [Online]. Available: <http://dx.doi.org/10.1088/1126-6708/2006/05/026>
- [84] C. Andreopoulos *et al.*, “The GENIE Neutrino Monte Carlo Generator,” *Nucl. Instrum. Meth. A*, vol. 614, pp. 87–104, 2010.
- [85] SHiP Collaboration, “Heavy Flavour Cascade Production in a Beam Dump.” no. CERN-SHiP-NOTE-2015-009, Dec 2015. [Online]. Available: <https://cds.cern.ch/record/2115534>

- [86] T. Ruf and E. Van Herwijnen, “Description of the SHiP FixedTargetGenerator.” CERN-SHiP-INT-2017-001,” Aug 2017. [Online]. Available: <https://cds.cern.ch/record/2280572>
- [87] K. L. Leung, “Influence of the straw tube sagging on the SHiP Spectrometer Straw Tracker performance,” no. CERN-STUDENTS-Note-2019-261, Dec 2019. [Online]. Available: <https://cds.cern.ch/record/2703438>
- [88] C. Höppner, S. Neubert, B. Ketzer, and S. Paul, “A novel generic framework for track fitting in complex detector systems,” *Nuclear Instruments and Methods in Physics Research Section A: Accelerators, Spectrometers, Detectors and Associated Equipment*, vol. 620, no. 2-3, pp. 518–525, 2010.
- [89] M. Jonker, “Readout Control Specifications for the Front-End and Back-End of SHiP,” no. CERN-SHiP-INT-2016-001, Jun 2016. [Online]. Available: <https://cds.cern.ch/record/2162870>
- [90] J. Ogborn, S. Collins, and M. Brown, “Randomness at the root of things 2: Poisson sequences,” *Physics Education*, vol. 38, no. 5, pp. 398–405, sep 2003. [Online]. Available: <https://doi.org/10.1088%2F0031-9120%2F38%2F5%2F303>
- [91] pco., “pco.dimax cs,” Nov. 2019. [Online]. Available: [https://www.pco.de/fileadmin/user\\_upload/pco-product\\_sheets/pco.dimax\\_cs\\_data\\_sheet.pdf](https://www.pco.de/fileadmin/user_upload/pco-product_sheets/pco.dimax_cs_data_sheet.pdf)
- [92] D. Breton, E. Delagnes, J. Maalmi, and P. Rusquart, “The wavecatcher family of sca-based 12-bit 3.2-gs/s fast digitizers,” in *2014 19th IEEE-NPSS Real Time Conference*, 2014, pp. 1–8.
- [93] Bondar, N. and Ferguson, T. and Golyash, A. and Sedov, V. and Terentev, N., “Anode front-end electronics for the cathode strip chambers of the CMS endcap muon detector,” in *7th Workshop on Electronics for LHC Experiments*, 9 2001, pp. 190–194.
- [94] A. Korzenev *et al.*, “Plastic scintillator detector with the readout based on an array of large-area SiPMs for the ND280/T2K upgrade and SHiP experiments,” *JPS Conf. Proc.*, vol. 27, p. 011005, 2019.
- [95] S. Gomez, D. Gascon, G. Fernandez, A. Sanuy, J. Mauricio, R. Graciani, and D. Sanchez, “MUSIC: An 8 channel readout ASIC for SiPM arrays,” in *Optical Sensing and Detection IV*, F. Berghmans and A. G. Mignani, Eds., vol. 9899, International Society for Optics and Photonics. SPIE, 2016, pp. 85 – 94. [Online]. Available: <https://doi.org/10.1117/12.2231095>
- [96] *WaveCatcher Family User’s Manual*, LAL, 2017. [Online]. Available: <https://owncloud.lal.in2p3.fr/index.php/s/56e4a2c53a991cb08f73d03f1ce58ba2?path=%2FSystem%20documentation#pdfviewer>

- [97] D. Breton and E. Delagnes, “Fast analog sampler with great memory depth,” *FR2824177 and US*, no. 6859375.

# List of acronyms

ADC	Analog-to-digital converter
ASIC	Application-specific integrated circuit
ATLAS	A Toroidal LHC Apparatus
BDF	Beam Dump Facility
BoPET	Biaxially-oriented PET
CDF	Cumulative distribution function
CERN	European Organization for Nuclear Research
CES	Compact emulsion spectrometer
CFD	Constant fraction discriminator
CMS	Compact Muon Solenoid
CTC	Control distribution, data Transport and Concentration
DAC	Digital-to-analog converter
DAQ	Data acquisition
DC	Direct current
DIC	Digital image correlation
DOCA	Distance of closest approach
DUT	Device under test
ECC	Emulsion cloud chamber
FPGA	Field-programmable gate array
FWHM	Full width at half maximum
GUI	Graphical user interface
HNL	Heavy neutral lepton
HS	Hidden Sector
HV	High voltage
ID	Identifier
LDM	Light dark matter
LED	Light emitting diode
LHC	Large Hadron Collider
MC	Monte Carlo
MIP	Minimum-ionizing particle
MRPC	Multi-gap Resistive Plate Chamber
NDF (NDOF)	Number of degrees of freedom
NIM	Nuclear Instrumentation Module

NTP	Normal temperature and pressure
PC	Personal computer
PCB	Printed circuit board
PDF	Probability density function
PET	Polyethylene terephthalate
PMT	Photomultiplier tube
PNPI	Petersburg Nuclear Physics Institute
R&D	Research and design
RF	Radio frequency
RMS	Root mean square
RMSD	Root mean square of distances
RPC	Resistive Plate Chamber
SBT	Surround Background Tagger
SHiP	Search for Hidden Particles
SiPM	Silicon photomultiplier
SM	Standard Model
SND	Scattering and Neutrino Detector
SplitCal	Split Calorimeter
SPS	Super Proton Synchrotron
SST	Spectrometer Straw Tracker
STT	Straw tubes tracker
TD	Timing Detector
TDC	Time-to-digital converter
TFC	Timing and Fast Control
TP	Technical Proposal
tRPC	Time measuring RPC
TT	Target tracker



## Appendix A

### The evolution of the straw tube rupture process

The process of the straw tube rupture was filmed with a high speed camera PCO dimax cs3 [91]. This camera is capable of achieving the frame rate of 2128 fps at Full HD resolution. The rupture of the straw tube happens at more than 4 bar overpressure (if the test is carried out within few minutes). The weak point of the tube is the welding seam. After reaching the critical values of the overpressure the tube eventually fails at some point along the seam. The speed of unfolding the straw tube is high. The process happens within the fractions of a millisecond. Thus, the frame rate of the camera was increased to 64180 fps, but the resolution was lowered to  $360 \times 68$  pixels. This setting of the camera allowed us to film the process of the rupture within the 10 frames. The frames in chronological order are showed in Fig. A.1.

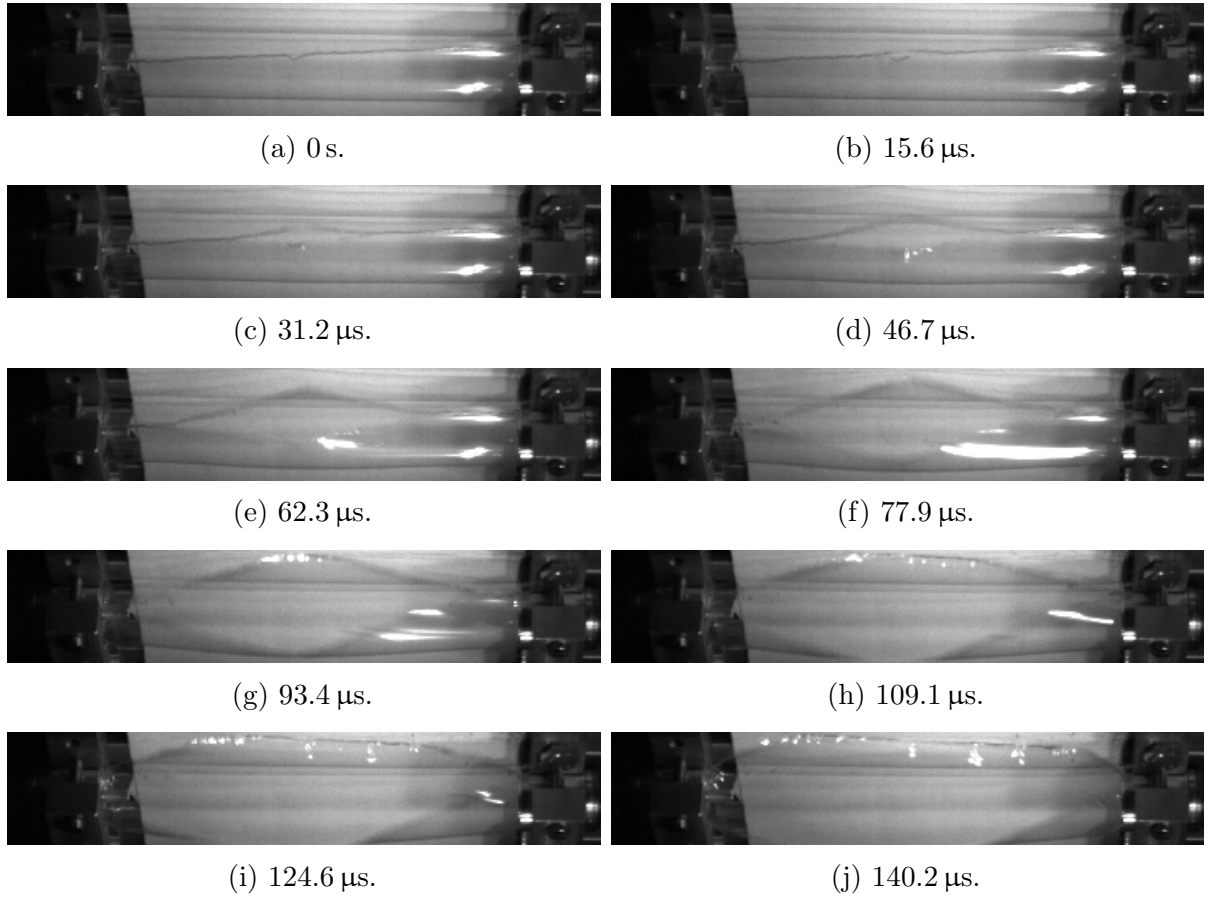


Figure A.1: The evolution of the straw tube rupture process captured with the high speed camera.

# Appendix B

## Read-out electronics tests

The final concept of the read-out electronics for the SST is not yet approved and design studies are still ongoing. In this thesis two prototype solutions for the DAQ system for the straw tubes are investigated. These solutions are suitable for using with either a single straw tube or with small modules (up to 16 tubes). The first DAQ system prototype is proposed by the collaborators from PNPI (Petersburg Nuclear Physics Institute). It consists of front-end cards and concentrator boards, which are linked with a PC or higher level concentrators. The second DAQ solution is using a WaveCatcher digitizer [92]. It is a multifunctional compact digitizer capable of recording the entire waveforms of the signals and simultaneously performing the variety of signal measurements (*e.g.*, finding the baseline, the amplitude, the charge *etc.*). The main design features of both DAQ solutions and their tests performed using the straw tubes prototypes are described in the following subsections.

### B.1 PNPI electronics tests

A read-out electronics concept proposed by the collaborating group from PNPI consists of an AD16 [93] front-end card with 2 ASDQ ASICs and Spartan 3 FPGA, which connects directly to the straw tubes output signal terminals, and a CCB16 concentrator with TE0720/Zyng XCZ020/TE0703 daughter board, which collects data from up to 16 AD16 boards and re-routes it to the top-level concentrator or directly to the PC. Images of the boards and the connection scheme are shown in Figure B.1.

The AD16 front-end card is a 16 channel amplifier-digitizer (only 8 channels were available for the tests, because of the Spartan 3 FPGA resources limitation) providing the gain of 7 mV/fC, 6 ns signal shaping time and variable thresholds per channel between 5 fC and 150 fC. The data digitizing rate is up to 400 MHz and the card is connected to the concentrator board through the 100 Mbps serial link (CAT5 cable). The CCB16 concentrator board contains 16 serial ports for CAT5 cables from AD16 cards and Finisar's FTLX8571D3BCL 10Gb/s SFP+ transceiver for links with optical fibers.

In order to conduct tests with the straw tubes using the described above system, a special firmware dedicated for the read-out of straw tube signals was developed. The SHiP

Table B.1: The word types of the data stream recorded with the PNPI DAQ system. The top row of the table represents the order of bytes. The left column shows the type of words.

W	31	30	29	28	27	26	25	24	23	22	21	20	19	18	17	16	15	14	13	12	11	10	9	8	7	6	5	4	3	2	1	0
1	0x8				0x006												StartStreamID															
2	0x9				FrameTime [19:0]																ChDisMap (0-7)											
3	0xA				LostSynch				LostFrameCnt [15:0]																ChDisMap (0-7) = 0x3F							
4	0xB				HitTime [11:0]												HitWidth [7:0]								ChID (0-7)							
5	0xC				HitTime [11:0]												HitWidth [7:0]								ChID (0-7)							
6	0xD				LostHitCnt[11:0]												0								ChID (0-7)							
7	0xF				0x007												StopStreamID															

experiment is planned to have a triggerless concept of data taking [89], meaning that all the data recored with the subsystems will be merged into the continuous data flow divided by the time frames of an arbitrary width. This concept was implemented into the firmware for the PNPI electronics tests at CERN. The TDC hits formed with the AD16 front-end card from the incoming signals are recorded continuously into the time line divided by the time frames of 10.24  $\mu$ s width. The counter of the time frames is reset after the start of each data acquisition run. The time of the digital TDC hits is recorded relative to the frame time with an accuracy of 2.5 ns. The digital hit width is also recorded with the same accuracy of 2.5 ns. The hit width is the absolute difference between the time of the first threshold crossing of the input analog signal and the second crossing. Due to the short shaping time of the AD16 card (6 ns) the recorded hit width is smaller than the real signal width (the tail of the signal is suppressed after the amplification), which can be up to few hundreds of nanoseconds. The minimal digital hit width is 10 ns. In the output data stream the hit time, the hit width and the channel ID are formed into a 28-bit word



Figure B.1: The images of the AD16 front-end card and the CCB16 concentrator board. The interface connections between the boards are shown schematically too<sup>1</sup>.

<sup>1</sup>The figure is adapted from slides:[https://indico.cern.ch/event/714498/contributions/3005937/attachments/1655256/2649481/SHiP\\_Readout\\_24\\_05\\_2018\\_01\\_LU.pdf](https://indico.cern.ch/event/714498/contributions/3005937/attachments/1655256/2649481/SHiP_Readout_24_05_2018_01_LU.pdf)

with a unique 4-bit ID making a 32-bit data stream entry. There are additional counters in the output binary file: the *LostHitsCnt*, which counts the number of lost hits due to the channel buffer being full, and the *LostFramesCnt*, which counts the number of the lost frames due to the back-pressure from the concentrator board during the data taking. The frame time counter wraps after 10 s, which is much larger than the expected duration of the SPS spill (1 s) extracted to the Beam Dump Facility [20]. If no hits are registered inside the particular time frame, only the frame time is recorded into the output binary file. The table illustrating the description of the data format is shown in Table B.1.

The experimental setup constructed in the laboratory 15/S-006 at CERN for the tests of PNPI electronics consists of two straw tube prototypes, two plastic scintillators with SiPM read-out [94] acting as a T0 detector for the tubes, a radioactive source of  $^{90}\text{Sr}$  and a NIM crate with a discriminator, a coincidence and delay units. The first straw tube is the one used for 2017 test beam at H2 beam line in the North Area at CERN (see Chapter 3). It has a diameter of 2 cm and a length of 2 m. It is pretensioned and covered with an RF shielding made of steel. The second tube was assembled in the lab 15/S-006 at CERN. It has the same diameter (2 cm), but its length is 2.4 m. It is covered with an RF shielding made of aluminum profiles with technical holes in it (to let the electrons from the source penetrate the tube). The two plastic scintillators are bars of 168 cm length, 6 cm width and 1 cm thickness made of polyvinyltoluene (EJ-200). The photons created inside the scintillating material are registered with arrays of 8 SiPMs mounted at each of the opposing ends of the plastic bar. The PCB with SiPMs is connected to the eMUSIC board [95]. The eMUSIC board amplifies the signals from 8 SiPMs and makes the analog sum of them. The parameters of the eMUSIC ASIC are configurable through the external UART-to-USB adapter. The 2 output signals from every bar are sent to the input of a discriminator unit of the NIM crate and then to the coincidence unit. Depending on the test performed in the laboratory, the two plastic scintillators can be put into coincidence scheme or operate separately.

The radioactive source of  $^{90}\text{Sr}$  according to [44] has a pure  $\beta^-$  decay mode with a half-life of 28.79 years emitting electrons with an average energy of 195.8 keV and a maximum energy of 546 keV. The decay product of  $^{90}\text{Sr}$  is  $^{90}\text{Y}$ , which is radioactive and also has

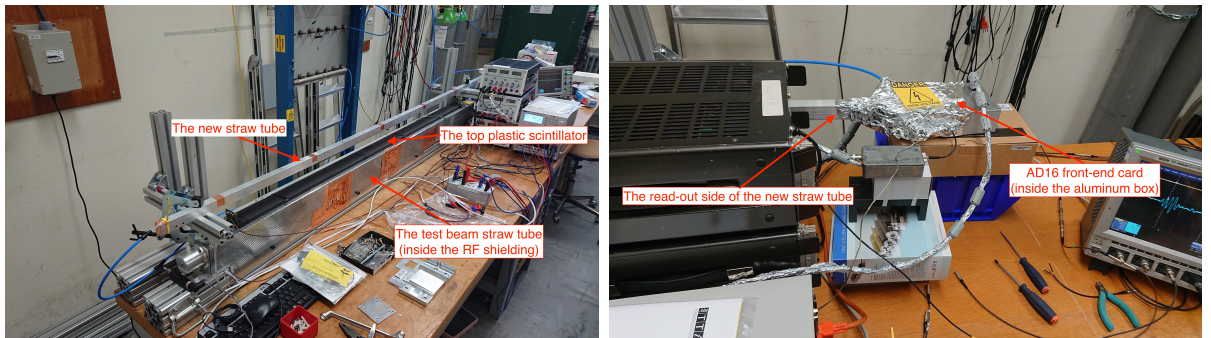


Figure B.2: The photos of the test setup built for the DAQ systems tests in the laboratory 15/S-006 at CERN.

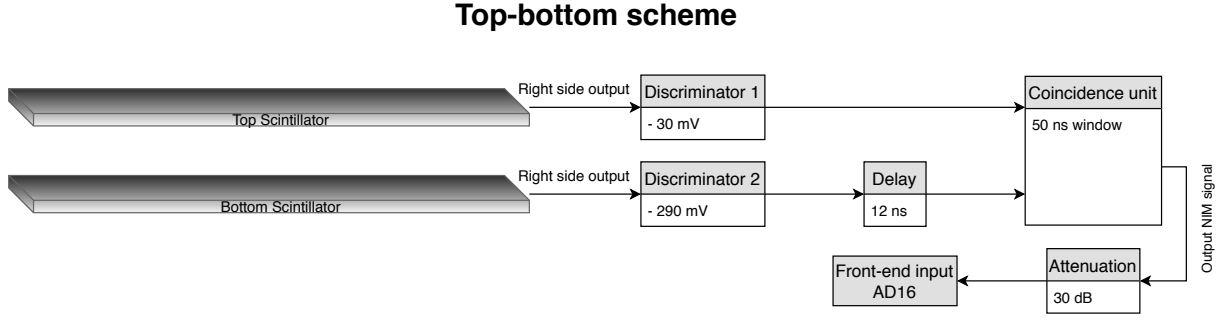


Figure B.3: The coincidence scheme for the plastic scintillators used for cosmic rays measurements.

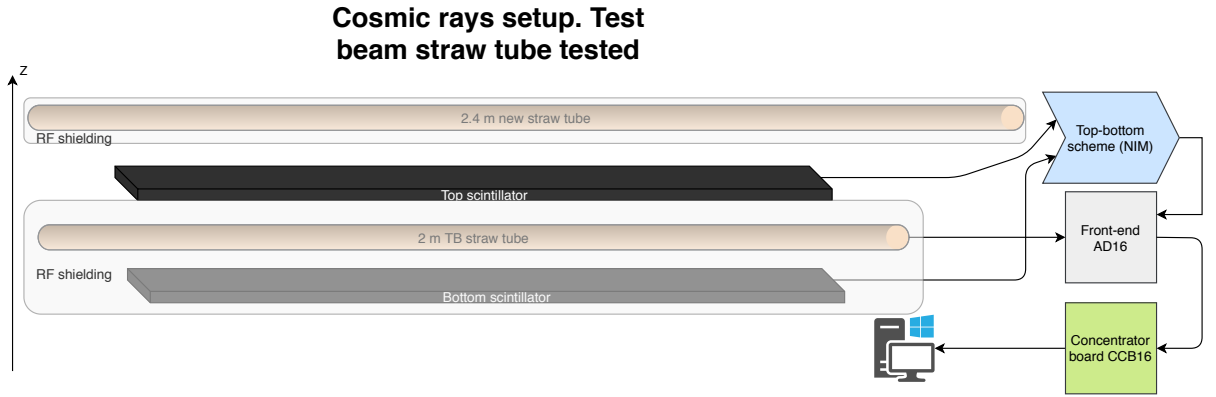


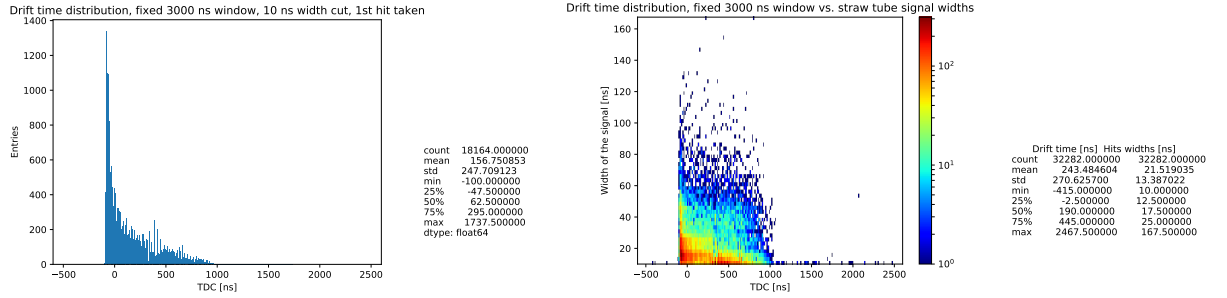
Figure B.4: The experimental setup configuration used for PNPI DAQ system tests with cosmic rays.

dominant  $\beta^-$  decay mode with a half-life of 64 hours emitting electrons with an average energy of 933.7 keV and a maximum energy of 2280.1 keV. Thus, the radioactive source of  $^{90}\text{Sr}$  provides electrons in the wide energy range up to 2280.1 keV. The photos of one of the experimental configurations built in the lab are shown in Figure B.2.

The aim of the read-out electronics tests was to check the functionality and robustness of the developed DAQ system working with the real detector prototypes, debug and optimize the firmware and find out what can be improved in the system. The first configuration of the experimental setup was built to work with cosmic rays. The first plastic scintillator was put under the first straw tube (the test beam straw tube), inside its RF shielding, the second scintillator was fixed on top of the RF shielding. The second straw tube was mounted 12 cm higher than the top plastic scintillator. It was fixed with clamps to the supporting frame. A schematic view of the setup is shown in Figure B.4. The output signals from the right sides of the top and the bottom scintillators were sent to the discriminator unit in the NIM crate. They were not sent directly to the AD16 card, because the analog signals were already amplified by the eMUSIC boards and would saturate the input of the front-end card. The discriminator thresholds of the NIM unit

were set individually for each scintillator output channel in order to have equal trigger rate. The threshold for the top scintillator right side was -30 mV, for the bottom scintillator right side -290 mV. The digital signal after the discrimination from the bottom scintillator was artificially delayed by 12 ns to compensate for the length of the plastic bars and to reduce the jitter influence. Then the two digital signals were sent to the coincidence unit with a time window width of 50 ns. The output signal from the coincidence unit was attenuated (30 dB) and sent to the AD16 front-end in order to register TDC hits and write them alongside with the straw tube hits into the common data stream. The signal was attenuated, because the standard NIM signal (-0.8 V) was too high for the AD16 input. The threshold for the straw tube signal was set to 40 fC, for the coincidence signal – to 128 fC. The high voltage for the test beam straw tube was set at 2400 V and the absolute pressure of Ar/CO<sub>2</sub> gas mixture (70%/30%) – to 1.1 bar. The bias voltage for the SiPMs of the plastic scintillators was set to 57 V. A schematic image of the coincidence chain is shown in Figure B.3.

As control plots for the measurement the drift time spectrum and the signal widths distributions were used. The shape of the drift time spectrum can be compared to the real one from the test beam analysis performed in Chapter 3. The drift time distribution was calculated as the difference between the TDC hit time from the coincidence signal of the plastic scintillators and the TDC hit time of the straw tube within a 3  $\mu$ s time window. If there were more than a single straw tube hit within this time window, only the first hit was taken to calculate the drift time. The cut on the signal width  $w > 10$  ns was applied too, in order to reject the majority of the noise hits. The obtained drift time distribution and the dependence between the calculated drift time and the signal widths are shown in Figure B.5. From the histograms one can observe that the signals from the real tracks

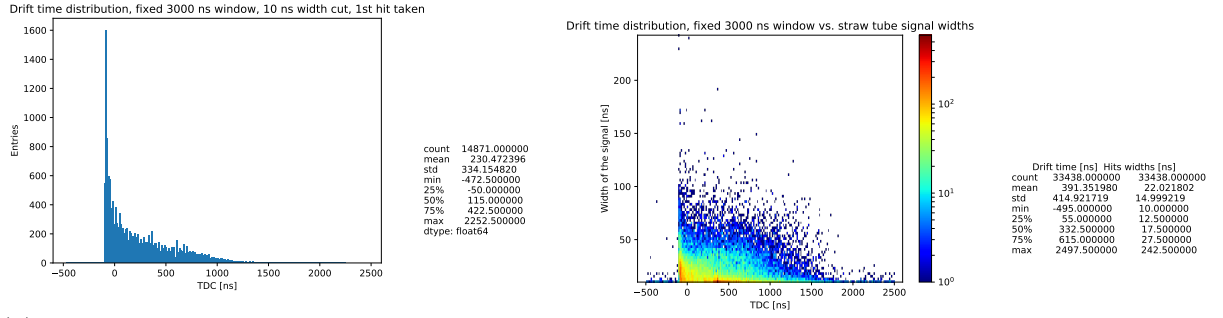


(a) The drift time distribution of the test beam straw tube acquired with PNPI DAQ system. The time window of 3  $\mu$ s was used. Only the first straw tube hit was considered and the straw tube hit width cut of  $w > 10$  ns was applied.

(b) The 2-dimensional histogram of the straw tube hit widths *vs.* the drift time. The time window of 3  $\mu$ s was used. No additional cuts were applied, all straw tube hits within the time window were used for the drift time calculation.

Figure B.5: The results of PNPI electronics tests for the test beam straw tube with the cosmic rays.





(a) The drift time distribution of the newly assembled straw tube acquired with PNPI DAQ system. The time window of  $3\mu\text{s}$  was used. Only the first straw tube hit was considered and the straw tube hit width cut of  $w > 10\text{ ns}$  was applied.

(b) The 2-dimensional histogram of the straw tube hit widths *vs.* the drift time. The time window of  $3\mu\text{s}$  was used. No additional cuts were applied, all straw tube hits within the time window were used for the drift time calculation.

Figure B.6: The results of PNPI electronics tests for the new straw tube with the cosmic rays.

passing through the tube have a mean width of  $\approx 21\text{ ns}$ . The noise hits have mostly  $10\text{ ns}$  width.

The same experimental setup configuration (see Figure B.4) was used for performing the electronics tests for the second (new) straw tube, which was assembled in the laboratory 15/S-006 at CERN. The output signal from the tube was connected through the decoupling circuit to one of the input channels of the AD16 front-end card. The same coincidence scheme for the plastic scintillators was used as previously (see Figure B.3). The straw tube was filled with the same gas mixture ( $\text{Ar}/\text{CO}_2 : 70\%/30\%$ ), but at  $2\text{ bar}$  absolute pressure. This tube was designed to operate in vacuum and the wire was pretensioned and crimped at  $1\text{ bar}$  overpressure, when the tube was elongated. That is why, the new straw tube should operate at  $2\text{ bar}$  absolute pressure. As the gas pressure inside the tube is higher, the applied high voltage is increased. The high voltage used for the measurements was set to  $2550\text{ V}$  and the input channel threshold for the AD16 card was set to  $20\text{ fC}$ . The threshold for the coincidence signal of the two scintillators remained the same as for the previous test:  $128\text{ fC}$ . The obtained for  $3\mu\text{s}$  time window drift time distribution with  $10\text{ ns}$  signal width cut applied is shown in Figure B.6. The 2-dimensional histogram showing the drift time *vs.* the signal widths is also shown in Figure B.6. Despite having the same diameter as the test beam tube, the new straw tube has significantly longer tail in the drift time distribution. The drift time increased because of higher pressure inside the tube, thus the drifting charges are more likely to interact with the atoms of the gas and slow down on their way to anode and cathode.

The second configuration of the experimental setup was built for the measurements with a  $^{90}\text{Sr}$  radioactive source. According to the data from [46], electrons with kinetic energy smaller than  $2\text{ MeV}$  will not penetrate through a  $1\text{ cm}$  thick plastic scintillator. The



maximum energy of the electrons from  $^{90}\text{Sr}$  source is 2.2801 MeV, which means that more than 90% of the particles won't reach the second scintillator after penetrating through the straw tube and the first plastic scintillator. That is why, for the measurements with electrons source only a single plastic scintillator was used. In order to suppress the noise rate in the scintillator, the coincidence scheme for the left and the right side output signals was used (see Figure B.7). The signals from both eMUSIC boards of the scintillator were sent to the discriminator input with the channel thresholds set at -80 mV for the left signal and -30 mV for the right one. The right side signal was delayed by 24 ns in order to always trigger coincidence signal on the arrival of the input signal from the right side output. The coincidence window width was set to 50 ns. The output signal of the coincidence unit was attenuated (30 dB) and then transferred to one of the input channels of the AD16 front-end card. The threshold was set to 128 fC. The plastic scintillator was positioned behind the test beam straw tube and the radioactive source was placed inside the technical hole of the tube's RF shielding. The aluminum 7 mm thick collimator with a hole of 1 mm diameter was attached to the source in order to select the electrons, which travel perpendicularly to the tube's surface. The schematic image illustrating the described experimental configuration is shown in Figure B.8. The operational conditions for the test beam tube were the same as for the cosmic rays measurement: the applied high voltage – 2400 V, the gas absolute pressure – 1.1 bar, the AD16 discriminator threshold – 40 fC.

For the new straw tube (assembled in the laboratory) the same coincidence scheme for the scintillator signals was used (see Figure B.7). The scintillator was moved up and attached to the aluminum RF shielding at the back of the straw tube. The radioactive source with the attached aluminum collimator (1 mm hole and 7 mm thickness) was aligned with respect to the position of the technical window in the tube's RF shielding (see Figure B.9). The operational conditions for the straw tube changed comparing to the test with the cosmic rays. The discriminator threshold of the AD16 input channel was set to 20 fC, the applied high voltage – to 2400 V, the gas pressure and the mixture itself remained the same – 2 bar of Ar/CO<sub>2</sub>. The obtained drift time distributions for both tubes (see Figure B.10 and B.11) have slightly different shapes of the drift time distributions comparing to the tests performed with the cosmic rays. The large peak in the drift time distribution, which corresponds to the smallest possible drift time in the tube, is more populated. This effect is caused by the collimator attached to the source: major fraction of electrons penetrated the tubes in the middle, close to the wire. The tails of the distributions are less pronounced, because only a small fraction of electrons were deflected into the tube walls direction. The distributions of the signal widths for both tubes remained similar to cosmic tests showing that the mean width of signals from the real tracks is  $\approx 20$  ns.

In general, the tests of the DAQ system developed in PNPI were successfully done. The whole system showed the potential of using the time framed continuous data stream read-out of the hits from both straw tubes and scintillators. The capacity of the front-end was enough large to handle high data rates from the radioactive source without losing the hits. There were several issues with stability of the DAQ system over long periods of data taking (the system required few restarts), but it can be fixed with the firmware

### Left-right scheme

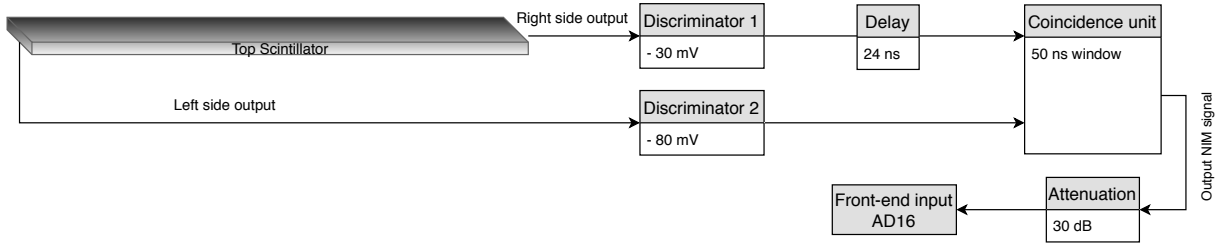


Figure B.7: The coincidence scheme for the plastic scintillator used for the  $^{90}\text{Sr}$  radioactive source measurements.

### Sr90 setup. Test beam straw tube tested

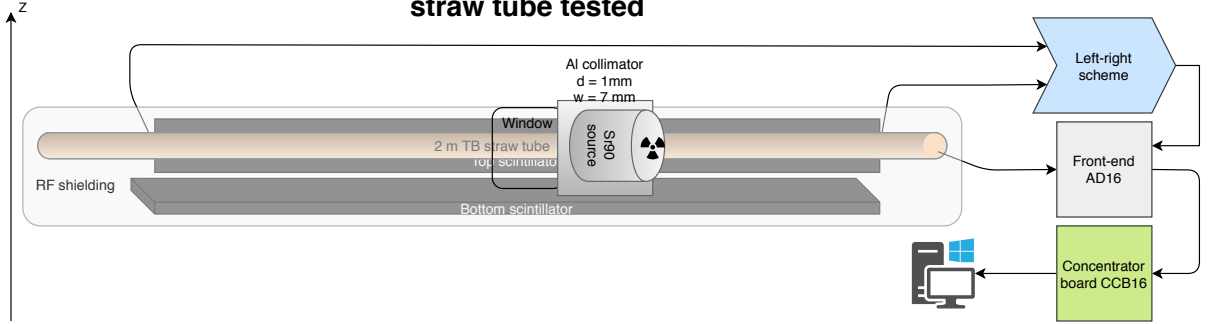


Figure B.8: The experimental setup configuration used for PNPI DAQ system tests of the test beam straw tube with the  $^{90}\text{Sr}$  radioactive source.

upgrades in future. The DAQ was tested only for single tubes. The next major task for this electronics will be the reading out the data from the module of few tubes.

## B.2 WaveCatcher tests

One of the alternatives for the DAQ system developed in PNPI for the laboratory tests of the straw tubes is the WaveCatcher digitizer [96] designed by CEA/IRFU & CNRS/IN2P3/LAL institutions. The WaveCatcher is a 12-bit 3.2 GS/s switched capacitor digitizer based on the SAMLONG chip [97]. There are 2, 8, 16 and 64 channel versions of the WaveCatcher digitizer. The one used for the straw tube tests in the laboratory 15/S-006 at CERN has 16 input channels (see Figure B.12). The input dynamic range of the WaveCatcher is 2.5 Vpp with the possibility to apply the DC offset to the input signal up to  $\pm 1.25$  V using a 16-bit DAC. One of the remarkable features of the WaveCatcher digitizer is its ability to record the entire waveforms of the input signals with maximum sampling rate of 3.2 GS/s over 1024 analog memory cells available in the SAMLONG chip using a 12-bit ADC to get digital values for the voltage of the input signal. As the entire waveforms

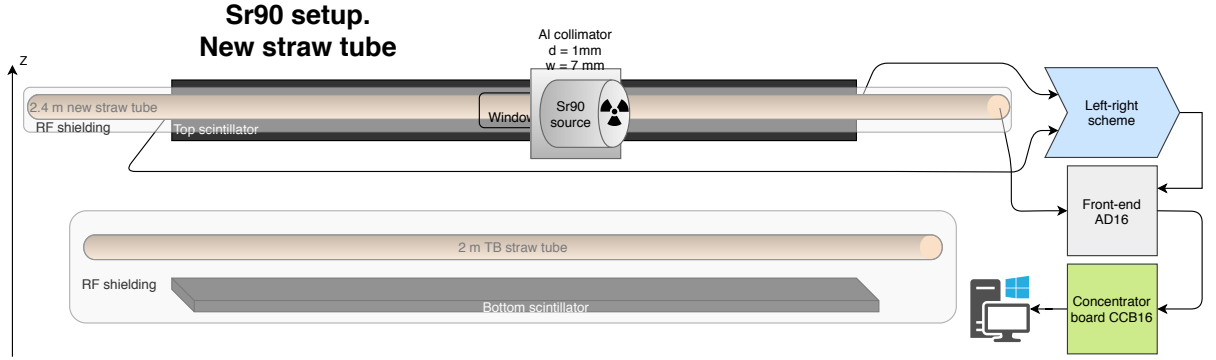
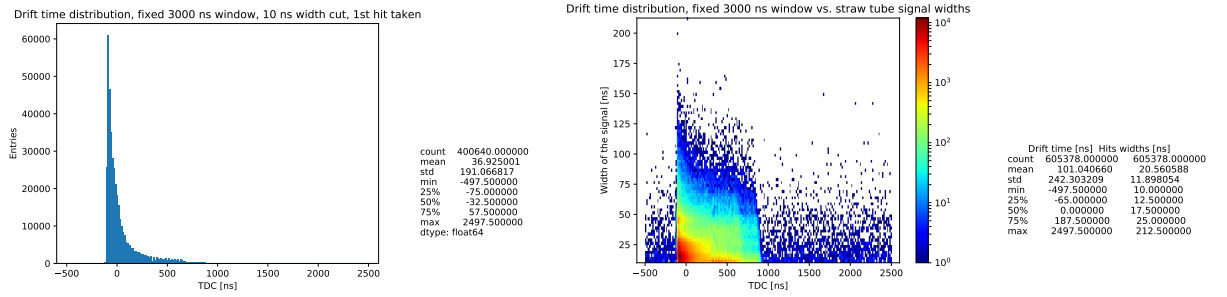


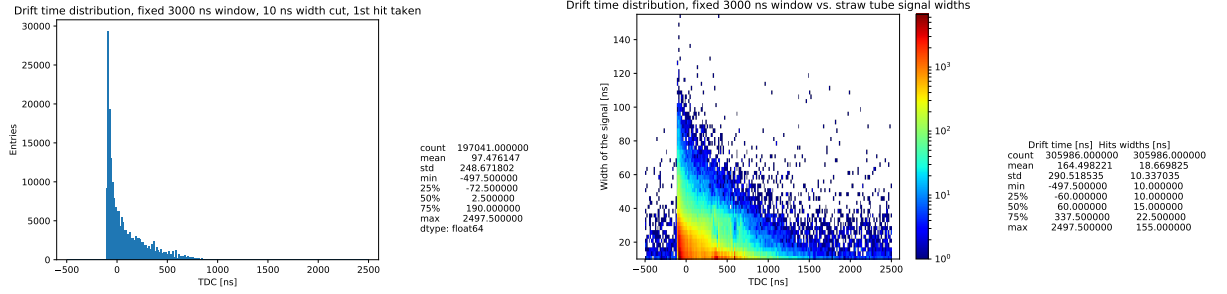
Figure B.9: The experimental setup configuration used for PNPI DAQ system tests of the new straw tube with the  $^{90}\text{Sr}$  radioactive source.



- (a) The drift time distribution of the test beam straw tube acquired with PNPI DAQ system. The time window of  $3\ \mu\text{s}$  was used. Only the first straw tube hit was considered and the straw tube hit width cut of  $w > 10\ \text{ns}$  was applied.
- (b) The 2-dimensional histogram of the straw tube hit widths *vs.* the drift time. The time window of  $3\ \mu\text{s}$  was used. No additional cuts were applied, all straw tube hits within the time window were used for the drift time calculation.

Figure B.10: The results of PNPI electronics tests for the test beam straw tube with the  $^{90}\text{Sr}$  radioactive source.

of the signals can be saved per trigger event, the firmware and software measurement over those waveforms can be performed simultaneously and recorded alongside the waveform data into the output files. The available firmware-based (using the front-end FPGA) signal measurements are: the baseline of the signal, the peak amplitude, the peak time, the charge of the signal, the rising and the falling edges of the signal (either for a fixed threshold or a constant fraction). These measurements are illustrated in Figure B.13 where an example of an arbitrary input signal is showed. Each input channel of the WaveCatcher has its own firmware implemented hit rate monitor with the maximum occupancy of 400 MHz. The counting rate does not depend on the occupancy of the rest of the system and the values acquired with the hit rate monitors are always valid. Each pair of the input channels are



(a) The drift time distribution of the newly assembled straw tube acquired with PNPI DAQ system. The time window of  $3\text{ }\mu\text{s}$  was used. Only the first straw tube hit was considered and the straw tube hit width cut of  $w > 10\text{ ns}$  was applied.

(b) The 2-dimensional histogram of the straw tube hit widths *vs.* the drift time. The time window of  $3\text{ }\mu\text{s}$  was used. No additional cuts were applied, all straw tube hits within the time window were used for the drift time calculation.

Figure B.11: The results of PNPI electronics tests for the new straw tube with the  $^{90}\text{Sr}$  radioactive source.



Figure B.12: The photo of the 16 channel WaveCatcher digitizer used for the tests of the straw tubes. The figure is adapted from [96].

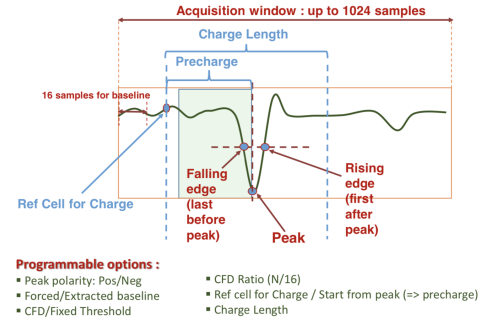


Figure B.13: The example of an arbitrary input signal at one of the channels of the WaveCatcher with the available measurements of its waveform. The figure is adapted from [96].

also equipped with 40-bit TDC capable of associating the trigger events with the clock provided by the SAMLONG chips (from 200 MHz to 25 MHz depending on the sampling frequency selected).

The test of the WaveCatcher digitizer was performed for the test beam straw tube (2 cm diameter and 2 m length) using the cosmic rays. The output signal from the tube was amplified with a fast pre-amplifier (5 ns leading edge time and the amplification factor of 11) and then transferred via coaxial cable to one of the WaveCatcher input channels. The output signals from both sides of each plastic scintillator were transferred directly to the

WaveCatcher input channels as they were already amplified with the ASIC of the eMUSIC board. The sampling frequency of the WaveCatcher was set to 0.8 GS/s in order to have the acquisition time window of 1.28  $\mu$ s, because the signals from the straw tube are delayed due to the drift time depending on the distance to the primary ionization clusters. The position of the plastic scintillators with respect to the test beam straw tube remained the same as for PNPI electronics tests. The schematic image showing the experimental setup is presented in Figure B.14. The event during the data acquisition with the WaveCatcher is formed, when the trigger signal is generated. The trigger signal is formed out of the coincidence of 4 input signals from the plastic scintillators within a 60 ns time window in order to compensate for the length of the plastic bars and possible jitter. Due to the available on-the-flight firmware measurements of the recorded signal waveforms the drift time distribution can be acquired simultaneously with the data taking procedure. The drift time, in this case, is equal to the difference between the TDC time of the trigger signal and the leading edge time of the straw tube signal waveform. In order to skip the events, when the signal in the tube was not induced (the particle didn't pass through the tube, but passed through the scintillators, which are wider than the diameter of the tube (6cm > 2cm)), the cut-off threshold of -30 mV was applied for the straw tube input channel of the WaveCatcher. The resulting drift time distribution is shown in Figure B.15.

The resulting shape of the drift time distribution shown in Figure B.15 is similar to the one obtained during the tests of PNPI electronics with the cosmic rays (see Figure B.5). A total of 50 000 trigger events were recorded, 24041 out of the total amount were used to produce the drift time distribution. The WaveCatcher firmware is not designed to work in triggerless mode like PNPI DAQ system does, but it allows to perform more on-the-flight firmware measurements of the signal waveform and save the entire waveform into the output files giving the possibility for more detailed off-line data analysis. The major drawback of having such advanced firmware features is the trigger rate limitation. The maximum dead time of the SAMLONG chip is 125  $\mu$ s decreasing with the recording depth. The second limiting factor is the USB 2.0 connection of the WaveCatcher to the PC, which can handle only up to 50 Mb/s of data transfer speed. The 16 channel model of the WaveCatcher has also a UDP interface capable of transferring the data with speeds up to 100 Mb/s, but it was not used during the test. In general, the WaveCatcher digitizer showed a great potential for laboratory usage, when the data rates are small compared to the beam test facilities. The WaveCatcher digitizer is a standalone plug-end-play device with available GUI and manuals, which can be easily configured and operated making it a convenient alternative to the PNPI DAQ system for the laboratory usage.

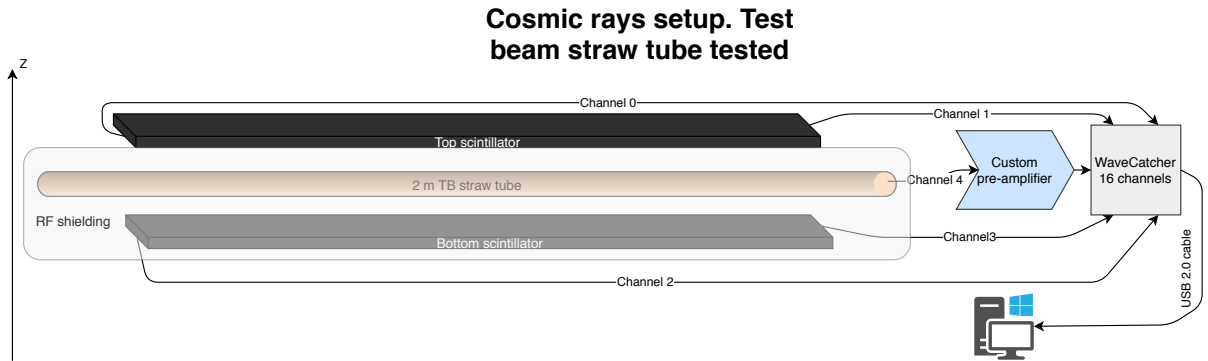


Figure B.14: The experimental setup configuration used for WaveCatcher DAQ system test with the cosmic rays.

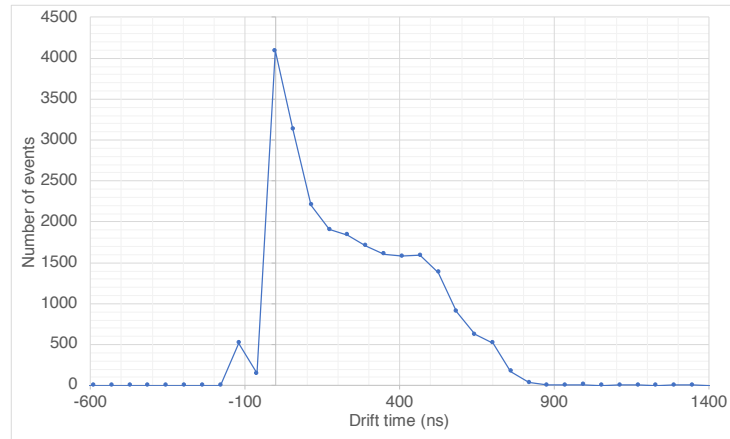


Figure B.15: The drift time distribution of the test beam straw tube acquired with WaveCatcher DAQ system.

# Appendix C

## Synchronization algorithms

Conceptually, the algorithm is based on a simple approach. Each DAQ board has its own clock. The clock of VME board has smaller period than the one of MAMBA. After  $\approx 108$  s it starts from 0 counts. The duration of the measurements is larger than the VME clock refresh period, so the converted time from VME clock needs to be adjusted according to the number of cycles it passed. The other obstacle is that the beam itself has periodic structure in time. Approximately every 46 s (in case of double spill from SPS – 23 s) the particles of the beam impinge the experimental setup. Also sometimes the duration of the beam cycle can be stretched in time due to various technical reasons. On the other hand the events are recorded only if the telescope receives a trigger event from front and backward scintillators, but the clocks of DAQ boards are running in any case despite the fact whether the trigger occurred or not. This means that during the “dead” time of the beamline VME clock can run over few additional cycles. This problem is solved by introducing the extra PC clock value to the event tree created by VME DAQ software. PC clock has very large refresh period and can help to calibrate VME clock comparing the last clock value from VME with PC one.

The resulting synchronization plots are shown in Fig. C.1. The procedure of synchronization is following:

1. Loop over first 10 events from telescope in order to find the first one which has respective event in VME tree that satisfies the timing window requirements for time residuals (differences) between VME, PC clocks and MAMBA clock. For test beam data both timing windows are set to 500 ns<sup>1</sup>.
2. Set the number of previously found telescope event as a starting point for the loop over the whole MAMBA tree.
3. Loop over the rest of MAMBA and VME events, select the ones, which satisfy the timing window requirements and `pattern` value constrain. If the difference between clocks exceeds the dedicated timing window, the number of event in VME tree changes by 1. In the next cycle MAMBA event is compared with the modified VME event and the procedure is then repeated.

4. The number of VME clock cycles is checked after each iteration using the converted PC clock value.
5. The clocks themselves do not have stable periods. They have a small timestamp jitter, which modifies the ratio between MAMBA and VME (PC) clocks. The jitter has a nanosecond scale, so it affects strongly the ratio MAMBA/PC, because MAMBA clock has a precision of the order of few nanoseconds. The ratio is periodically corrected using the averaged result over the last 100 events.
6. The termination condition i.e. the signature of totally desynchronized files occurs when the difference between numbers of two trees is larger than 11.

When the synchronization iterations reach the end of MAMBA tree, the united synchronized ROOT file is produced. It contains two separated trees **tree** and **ADC1** (MAMBA and VME trees respectively) with reduced number of branches according to the needs of future analysis. The event numbers of each tree are the same and they are synchronized in time.

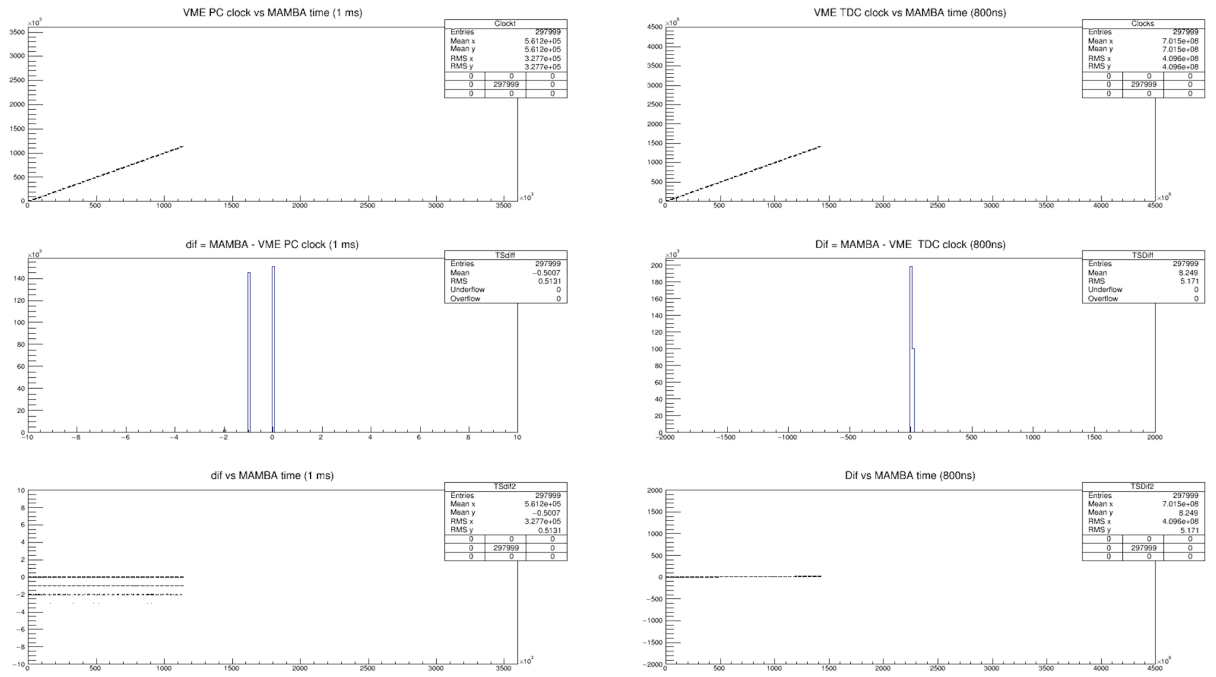


Figure C.1: Plots showing the dependence between VME, PC clocks and MAMBA clock. The trend of two top plots is a line with blanks, because of periodic beam structure. Two histograms in the middle represent the residuals of the clocks in ms and ns time scales. The bottom plots show the evolution in time of those residuals.

<sup>1</sup>In the middle of the test beam for a short time the calorimeter triggers were connected to the channels of the VME board. The values of the branch **pattern** represent this change of the board configuration. The events related to straw tubes have the **pattern** equal to 0



## Appendix D

# Geometry configuration script for muon background studies

The part of the geometry configuration script of the FairShip, where the parameters of the straw tubes layout are defined:

```
c.strawtubes = AttrDict(z=0*u.cm)
if strawDesign==4:
c.strawtubes.InnerStrawDiameter = 0.975*u.cm
c.strawtubes.StrawPitch          = 1.76*u.cm
c.strawtubes.DeltazLayer         = 1.1*u.cm
c.strawtubes.DeltazPlane         = 2.6*u.cm
c.strawtubes.YLayerOffset = c.strawtubes.StrawPitch/2.
c.strawtubes.YPlaneOffset = c.strawtubes.StrawPitch/4.
c.strawtubes.FrameMaterial       = "aluminium"
c.strawtubes.FrameLateralWidth   = 1.*u.cm
c.strawtubes.DeltazFrame         = 10.*u.cm
elif strawDesign==10: # 10 - baseline for 2018
c.strawtubes.InnerStrawDiameter = 1.975*u.cm
c.strawtubes.StrawPitch          = 3.60*u.cm
c.strawtubes.DeltazLayer         = 2.1*u.cm
c.strawtubes.DeltazPlane         = 4.2*u.cm
c.strawtubes.YLayerOffset = 1.9*u.cm
c.strawtubes.YPlaneOffset = 1.3*u.cm
c.strawtubes.FrameMaterial       = "steel"
c.strawtubes.FrameLateralWidth   = 1.2*u.m
c.strawtubes.DeltazFrame         = 2.5*u.cm
```



## Appendix E

# Momentum distributions of the the SST hits in muon background simulations

The momentum  $p$  and transverse momentum  $p_T$  distributions of hits created in the SST stations by muons, electrons, positrons and gamma rays. The original muon momentum  $p$  and transverse momentum  $p_T$  distributions are created for muons that created at least one hit in the SST. In the histograms the initial momenta of those muons is shown (not the momenta at the hit point).

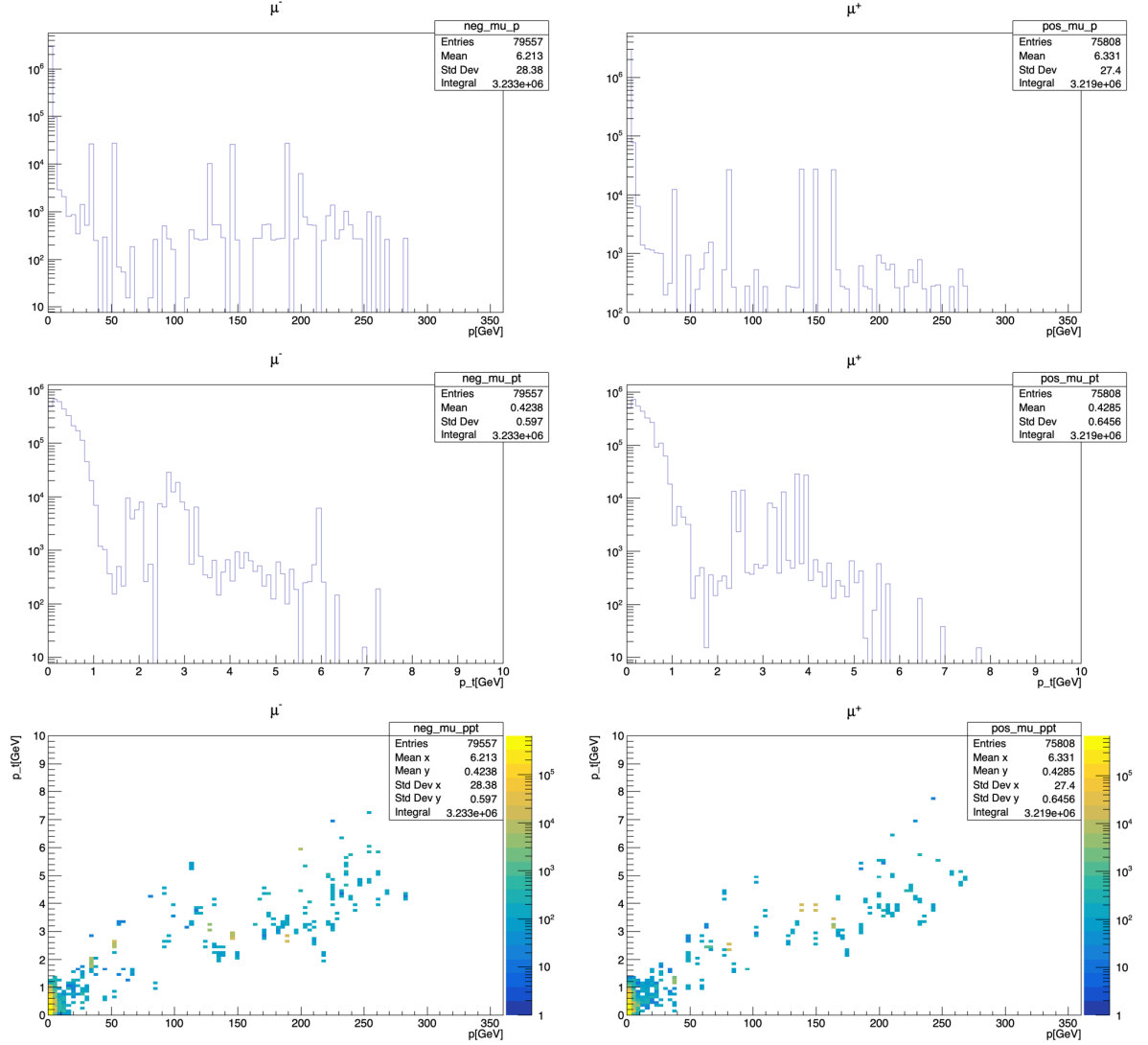


Figure E.1: Muons momentum  $p$  and transverse momentum  $p_T$  distributions of hits, separated by charge.

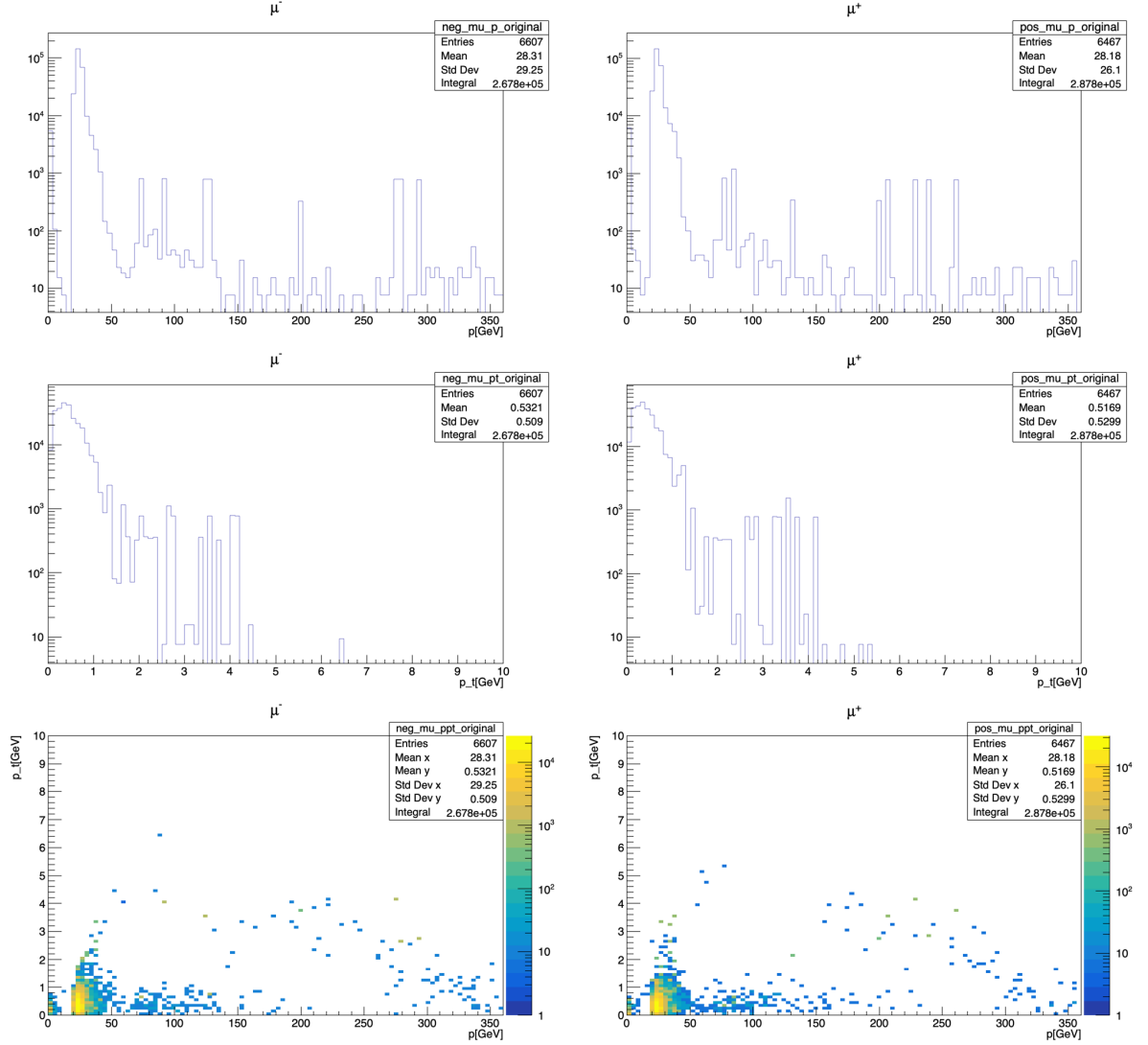


Figure E.2: Original muons momentum  $p$  and transverse momentum  $p_T$  distributions, separated by charge.

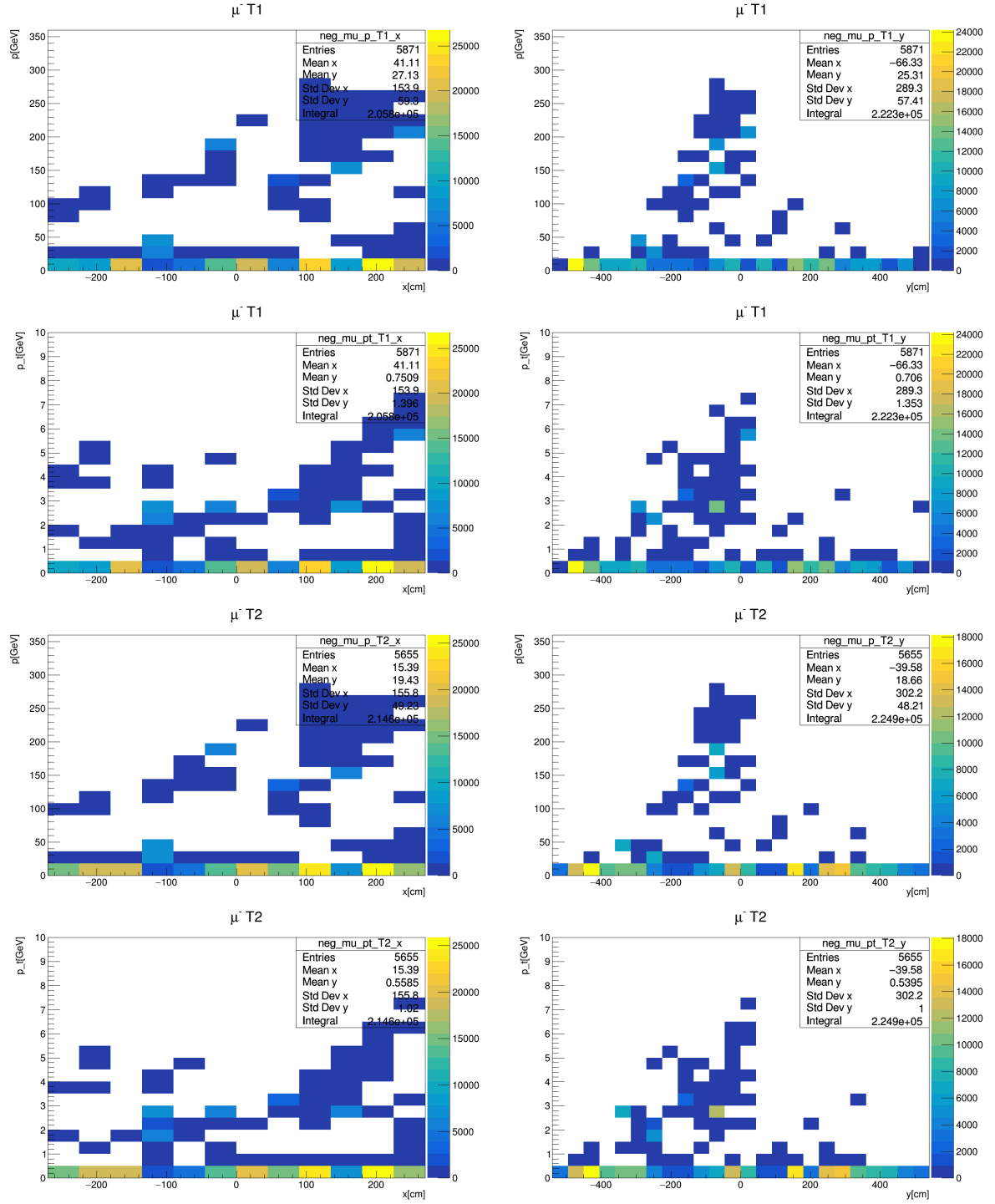


Figure E.3: Negative muons momentum  $p$  and transverse momentum  $p_T$  distributions of hits in stations T1 and T2.

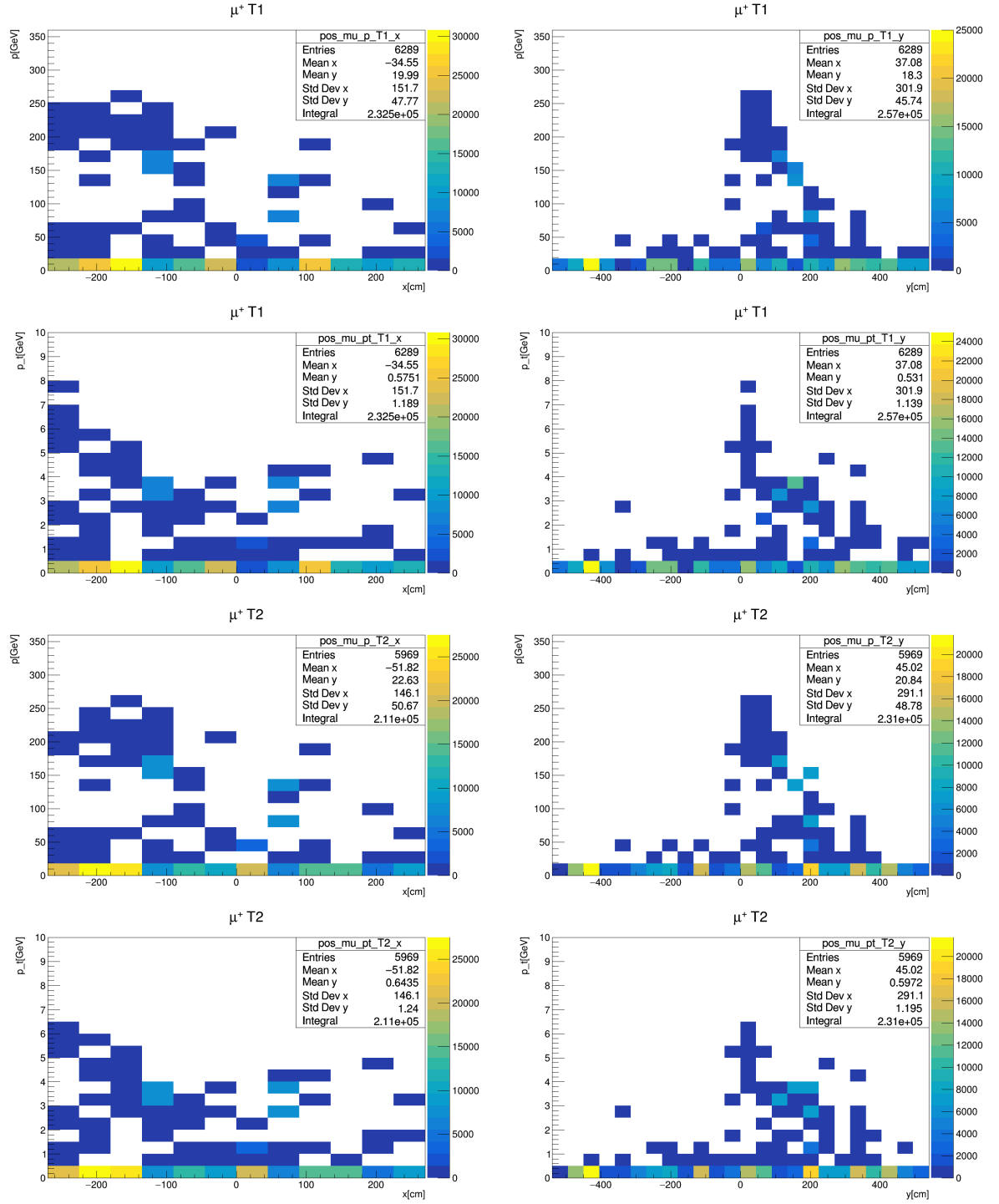


Figure E.4: Positive muons momentum  $p$  and transverse momentum  $p_T$  distributions of hits in stations T1 and T2.

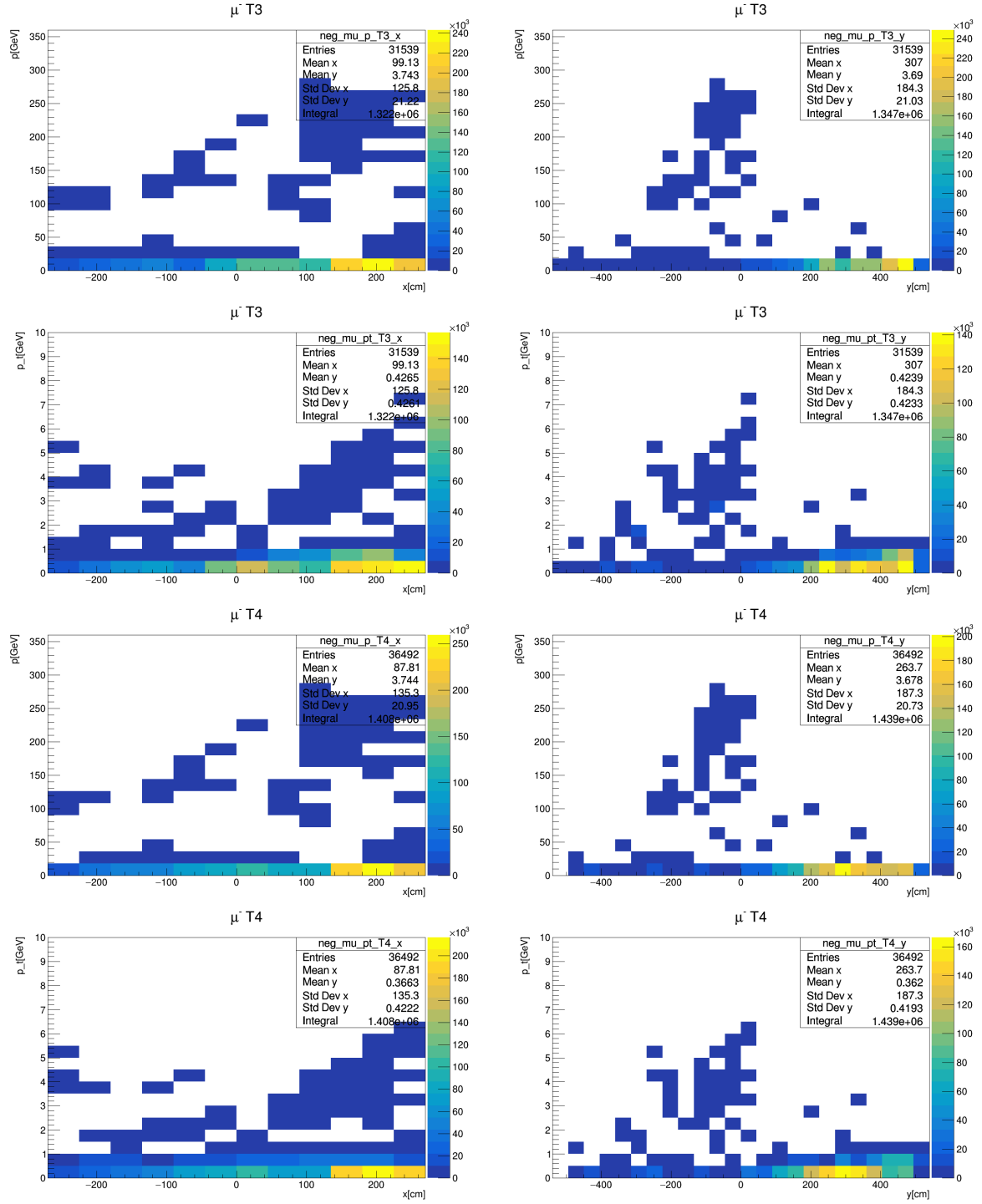


Figure E.5: Negative muons momentum  $p$  and transverse momentum  $p_T$  distributions of hits per stations T3 and T4.



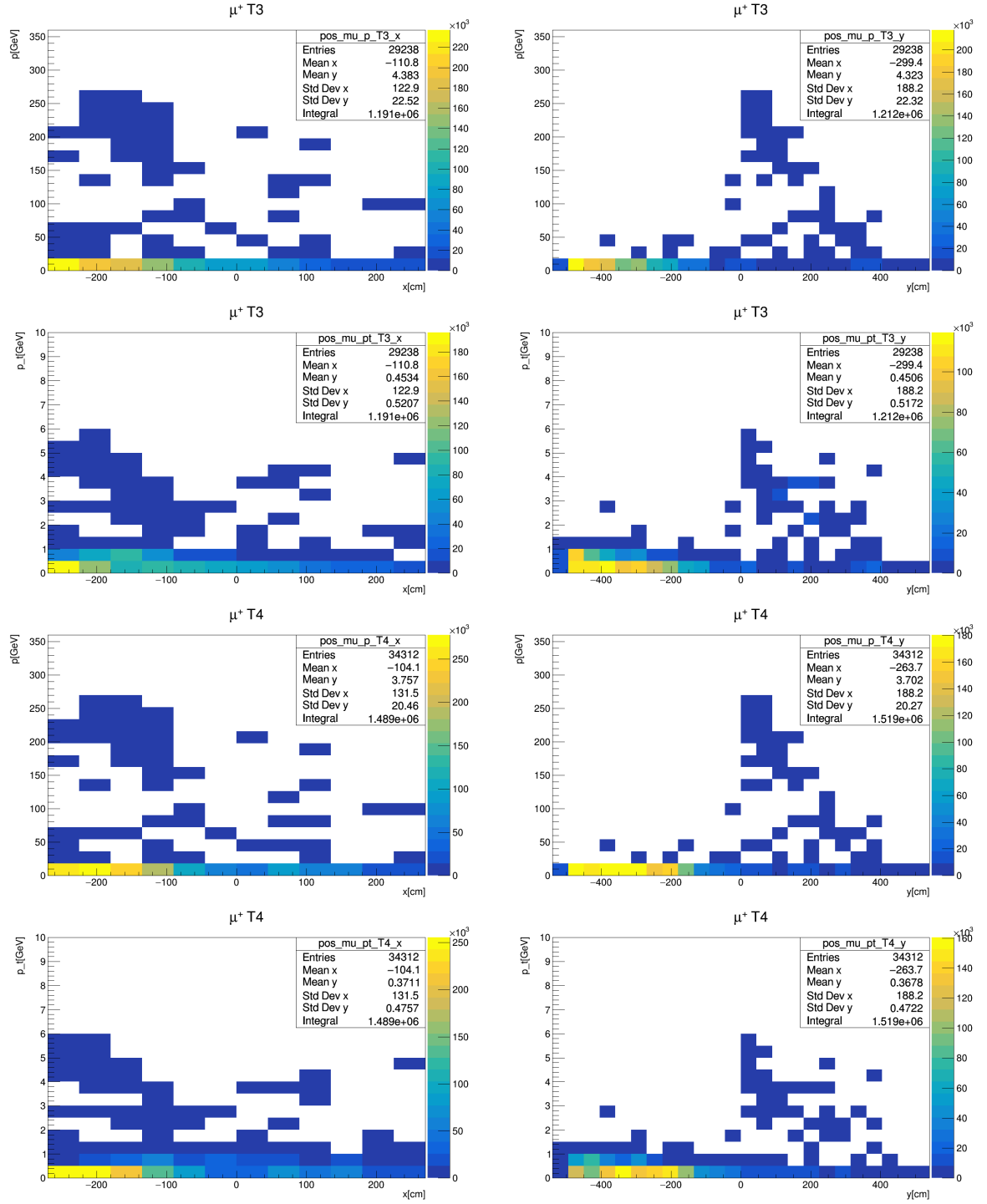


Figure E.6: Positive muons momentum  $p$  and transverse momentum  $p_T$  distributions of hits per stations T3 and T4.

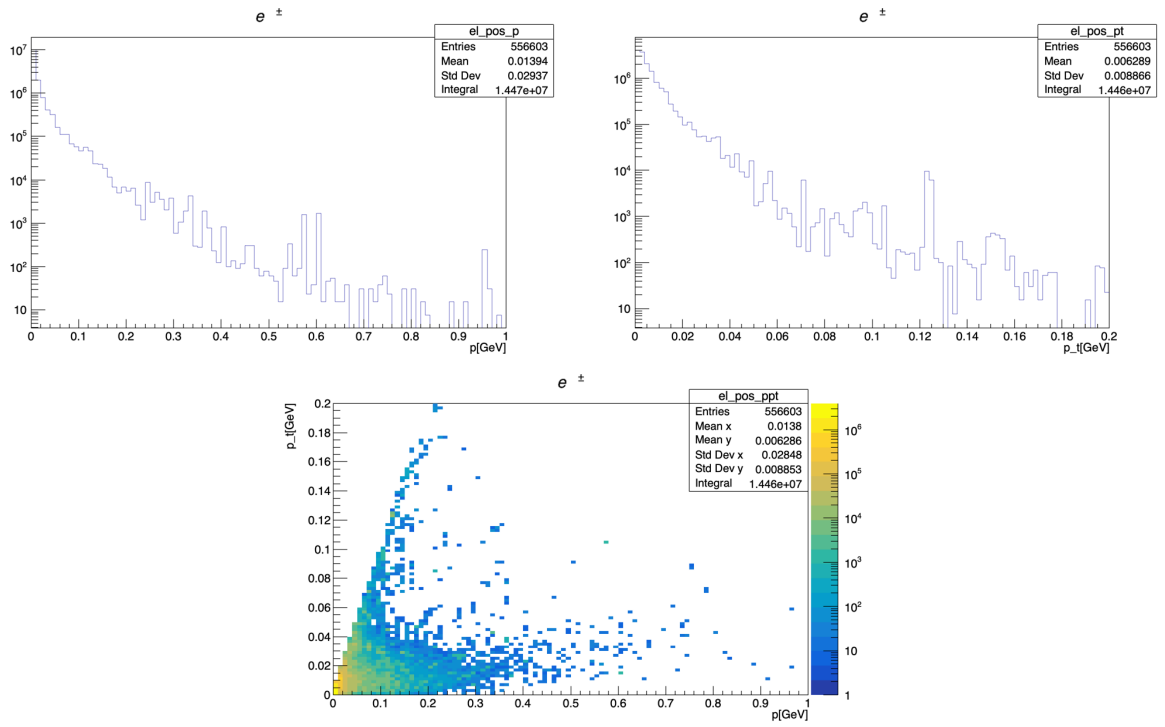


Figure E.7: Electrons and positrons momentum  $p$  and transverse momentum  $p_T$  distributions of hits in all SST stations.

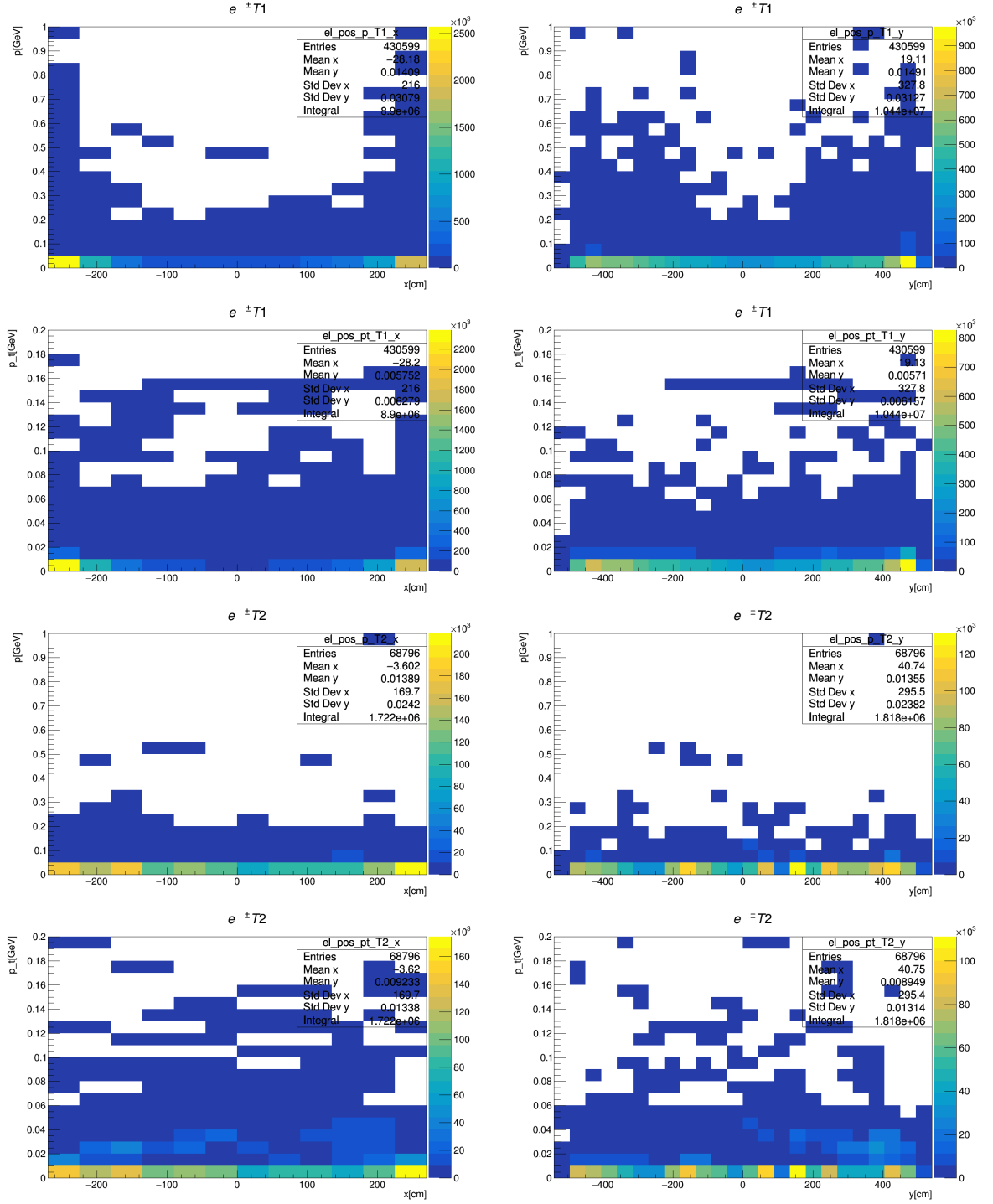


Figure E.8: Electrons and positrons momentum  $p$  and transverse momentum  $p_T$  distributions of hits in T1 and T2 stations.

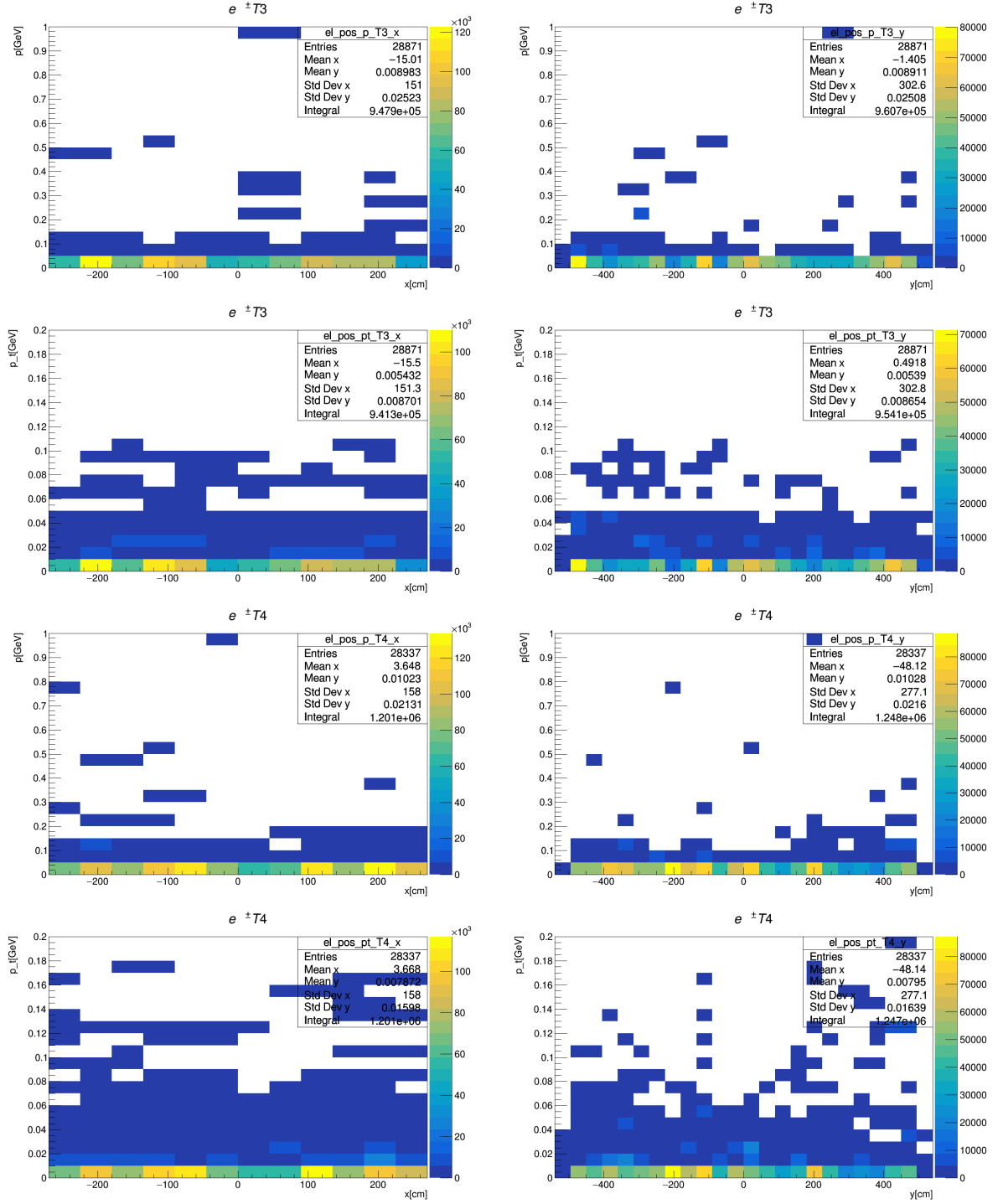


Figure E.9: Electrons and positrons momentum  $p$  and transverse momentum  $p_T$  distributions of hits in T3 and T4 stations.

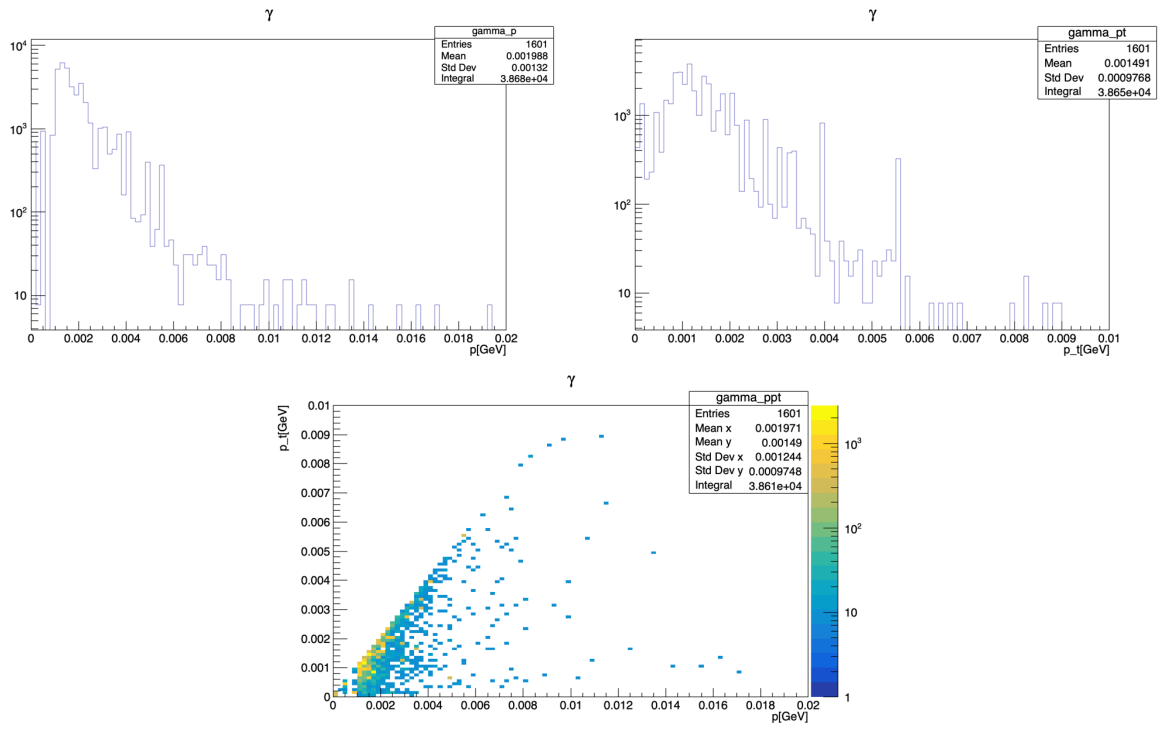


Figure E.10: Gamma rays momentum  $p$  and transverse momentum  $p_T$  distributions of hits in all SST stations.

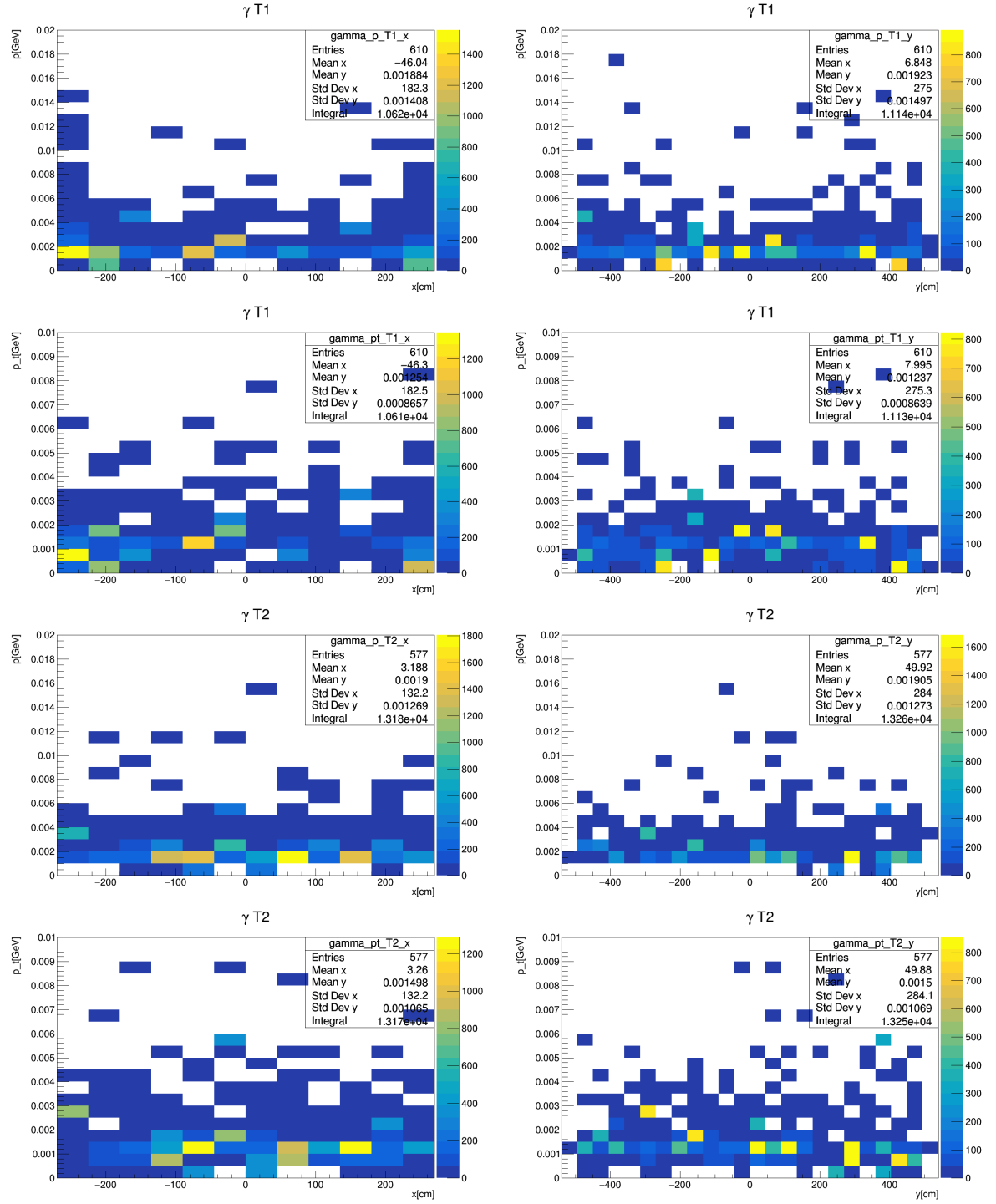


Figure E.11: Gamma rays momentum  $p$  and transverse momentum  $p_T$  distributions of hits in T1 and T2 stations.

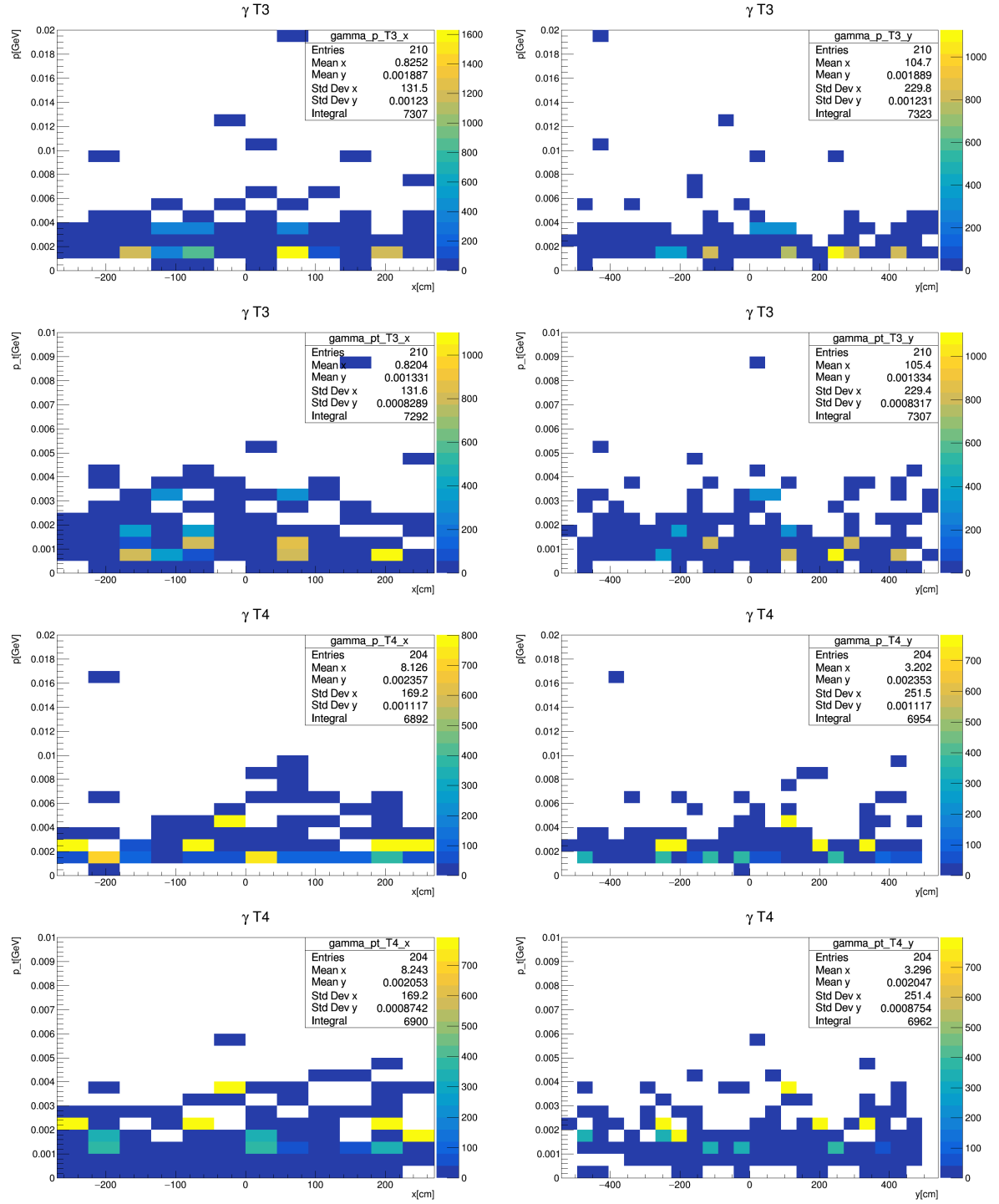


Figure E.12: Gamma rays momentum  $p$  and transverse momentum  $p_T$  distributions of hits in T3 and T4 stations.





# Acknowledgements

I would like to thank my CERN supervisor Dr. Massimiliano Ferro-Luzzi, who was extremely supportive during three years of my doctoral studies at CERN. His guidance, advices and persistence helped me to perform all the studies, learn new things and sum up everything in this thesis. Also, I appreciate the support from other members of SHiP collaboration, with whom I had a chance to work closely during my stay at CERN: Katerina Kuznetsova, Thomas Ruf, Eric van Herwijnen, Nikolay Azorskiy, Temur Enik, Nikolai Gruzinskii, Valerii Yatsura and Oliver Lantwin. Special thanks are delivered to Dirk Mergelkuhl (CERN, EN-SMM), Vitali Batusov (CERN, EP-UAT), Kostantinos Nikolitsas (CERN, EN-SMM), Antonio Carvalhosa (CERN, EN-MME) and Óscar Sacristan de Frutos (CERN, EN-MME) for helping with mechanical measurements on the straw tubes.

In 2017 the neutrino physics research group of Prof. Dr. Caren Hagner from Hamburg University accepted me as a doctoral student. I am grateful to Prof. Dr. Caren Hagner for believing in me and giving a chance to become a doctoral researcher. I would like to award with special thanks Dr. Daniel Bick, who was always in touch with me during past years helping to overcome any problems, which I faced during my doctoral studies. Each time, when I visited Hamburg to give a seminar and make a progress report, all neutrino physics group members were very friendly and nice to me. I highly appreciate this.

I respect the efforts of Dr. Massimiliano Ferro-Luzzi and Dr. Daniel Bick in reading my thesis. Their valuable and useful comments helped to increase its quality.

I am endlessly grateful to my lovely fiancée Mariia Bilous. It is impossible to list everything, what she has done for me during these three years. Despite being involved in her own doctoral research, she found the time to read my thesis too. Her view from the side helped to make this manuscript more clear and explicit.

I would like to address the thanks to my friends: Dr. Andrii Natochii, Dr. Mykyta Haranko and Andrii Pastushenko. Their moral support and advices helped me to always push forward and never give up my scientific investigations.

It is worth to mention the support I received from my parents and my younger brother. We met rarely during the past three years, but every time we saw each other, they shared huge amounts of positive emotions and love. These meetings were always of a great importance for me.